UCLouvain

École polytechnique de Louvain

Design of a new bone implant and its instrumentation for spinal fusion via transforaminal approach.

Author: **William Forster**
Supervisors: **Greet Kerckhofs, Olivier Cornu**
Readers: **Greet Kerckhofs, Olivier Cornu, Benoît Herman, Laurent Delanay**
Academic year 2019–2020
Master [120] in Biomedical Engineering

UNIVERSITÉ CATHOLIQUE DE LOUVAIN
École polytechnique de Louvain
Rue Archimède, 1 bte L6.11.01, 1348 Louvain-la-Neuve, Belgique | **www.uclouvain.be/epl**

Abstract

Intervertebral fusion is a common procedure in case of disc disease, and especially in case of disc degeneration. A lumbar intervertebral fusion can be achieved via the insertion of a cage between the vertebrae that need to be fused. This insertion can be done via a transforaminal approach, which is a recent promising insertion approach reducing the risk of the operation and decreasing the length of the patient's recovery period. The cages which are currently available do not integrate into the bony junction or degrades once the junction done. Therefore, the aim of this thesis is to develop an appropriate design of a cage made of cortical bone and to provide the tools in order to implement it. So, it is hypothesized that the cage would integrate into the bony junction. The cage was designed using a systematic design approach, from which multiple possible solutions were generated, and the best ones were combined. Then, using finite element modelling, the cage was optimized in term of porosity regarding its strength and stiffness under axial compression. Additionally, a design of its instrumentation is provided, in order to evaluate the appropriate cage dimensions and insert it. All together, this thesis provides a design for a cage made of cortical bone and its instrumentation for spinal fusion. The cage design and implementation tools, however, still needs to be clinically validated. Eventually, some insight for future perspective are provided.

Acknowledgements

First of all, I would like to thank my promoter, Professor Greet Kerckhofs, for her guidance, advice and support, both technical and moral, throughout the preparation of this thesis. Also, I would like to thank her for agreeing to help me on this subject that she did not propose and for all her efforts, both to help me as much as possible but also to reorient of this thesis consequently to the COVID-19 situation.

I would also like to thank my co-promoter, Dr. Olivier Cornu, for allowing me to work on this subject. I thank him for his confidence in me but also for his support, which enabled me to obtain pragmatic information directly from the user. Also, I thank him for having allowed me to meet the people responsible for the manufacture and use of the object, what made me realizing the concrete and pragmatic interest of this thesis.

Thanks also to Professor Benoît Herman, who helped me through all the key design steps. His insights were helpful to find solutions to problem, which saved me a lot of time.

A huge thank you to Michel Joie. Thank you for his advice, for the time he devoted to creating solutions and to understand me and giving me his advice, without which some possibilities would not have been considered.

A special thanks to Michel Verhelpen, who is responsible for the production of the cage. The information on the production of the cage was indispensable to me so that the cage could be produced with the material available with the necessary delay.

Many thank to Laurent Delannay, who is helped through the modelization process and guided me to take the necessary decisions. his background were welcomed to bring some insights and knowledge that was missing.

A special thanks to Greet Kerckhofs and Michel Joie, for the time they devoted to proofreading and correcting from memory. Their help was necessary in order to obtain a quality writing.

Eventually, a huge thank you to those close to me for supporting me during these five years at university and, more particularly, during the completion of this dissertation. Thank you for believing in me and motivating me when I needed it.

The completion of this thesis would not have been possible without all their contributions.

Contents

List of Figures

List of Tables

List of Abbreviations

DOF	**D**egree(s) **O**f **F**reedom
FSU	**F**unctionnal **S**pinal **U**nit
LF	**L**igamentum **F**lavum
PLL	**P**osterior **L**ongitudinal **L**igament
ALL	**A**anterior **L**ongitudinal **L**igament
CL	**C**apsular **L**igament
ISL	**I**nterspinous **L**igament
SSL	**S**upraspinous **L**igament
IAR	**I**nstantaneous **A**xe(s) of **R**otation
MRI	**M**agnetic **R**esonance **I**maging
PLIF	**P**osterior **L**umbar **I**nterbody **F**usion
PCIF	**P**osterior **C**ervical **I**nterbody **F**usion
ALIF	**A**nterior **L**umbar **I**nterbody **F**usion
ACIF	**A**nterior **C**ervical **I**nterbody **F**usion
OLIF	**O**blique **L**ateral **I**nterbody **F**usion
TLIF	**T**ransforaminal **L**umbar **I**nterbody **F**usion
TCIF	**T**ransforaminal **C**ervical **I**nterbody **F**usion
PLF	**P**oster**o**lateral **F**usion
LLIF	**L**ateral **L**umbar **I**nterbody **F**usion
LCIF	**L**ateral **C**ervical **I**nterbody **F**usion
CT	**C**omputed **T**omography
OR	**O**perating **T**able
MAST	**M**inimal **A**ccess **S**pinal **T**echnologies
Ti	**Ti**tanium
PEEK	**P**oly**e**ther**e**ther**k**etone

LD	**L**onditudinal **D**irection
TD	**T**ransverse **D**irection
YCS	**Y**ield **C**ompressive **S**tress
UCS	**U**ltimate **C**ompressive **S**tress
YTS	**Y**ield **T**ensile **S**tress
UTS	**U**ltimate **T**ensile **S**tress
YSS	**Y**ield **S**hear **S**tress
USS	**U**ltimate **S**hear **S**tress
IDP	**I**ntra**d**iscal **P**ressure
EMG	**E**lectro**m**yo**g**raphy
ASTM	**A**merican **S**ociety for **T**esting and **M**aterials
FDA	**F**ood and **D**rug **A**dministration
MF	**M**ain **F**unction
CF	**C**onstrain **F**unction
rhBMP-2 or BMP	**R**ecombinant **H**uman **B**one **M**orphogenetic **P**rotein
MSCs	**M**esenchymal **s**tem **c**ells
Titanium	**Ti**tanium
SolidWorks	**S**olid**W**orks
UCM	**U**nit **C**ell **M**odel
FoS	**F**actor **o**f **S**afety
OAP	**O**ne **A**xial **P**ore
FAP	**F**ew **A**xial **P**ore
OLP	**O**ne **L**ongitudinal **P**ore
FLP	**F**ew **L**ongitudinal **P**ore
OFP	**O**ne **F**rontal **P**ore
FFP	**F**ew **F**rontal **P**ore
FD	**F**inal **D**esign

List of Symbols

Please note that given units are default units, these could be different if explicitly precised.

E	Young modulus	$\frac{N}{m^2}$
ϵ	Strain	$-$
σ	Stress	$\frac{N}{m^2}$
ρ	Density	$\frac{kg}{m^3}$
F	Force	N
I	Moment of inertia	$kg * m^2$
δ	Deflection	m
p	Porosity	%
ν	Poisson ration	$-$
G	Shear modulus	$\frac{N}{m^2}$
K	Bulk modulus	$\frac{N}{m^2}$

Chapter 1

Context

1.1 Discopathy

The spinal cord is built of a stack of vertebrae (Figure 1.1a). Between each pair of vertebrae, there is one disc that serves as damper. Briefly, each disk is composed of 2 parts: the central part or the nucleus, and the peripheral part or the annulus that encircles the nucleus (Figure 1.1b). A disc can degenerate, and this is referred to as discopathy. Although discopathy mostly does not lead to damage of the annulus, sometimes it does [1]. Intervertebral disc disease is estimated to affect about 5% of the population in developed countries each year [2]. When the annulus ruptures (mostly by wear and tear), a part of the nucleus escapes from the disc and compresses the nerve(s), which is referred as a hernia (very painful for the patient). If the discopathy is very advanced, this could lead to local arthrosis or static trouble in the spinal cord that can result in chronic pain. A more detailed description of the anatomy and biomechanics of the spine can be found in Appendix A and Appendix B respectively.

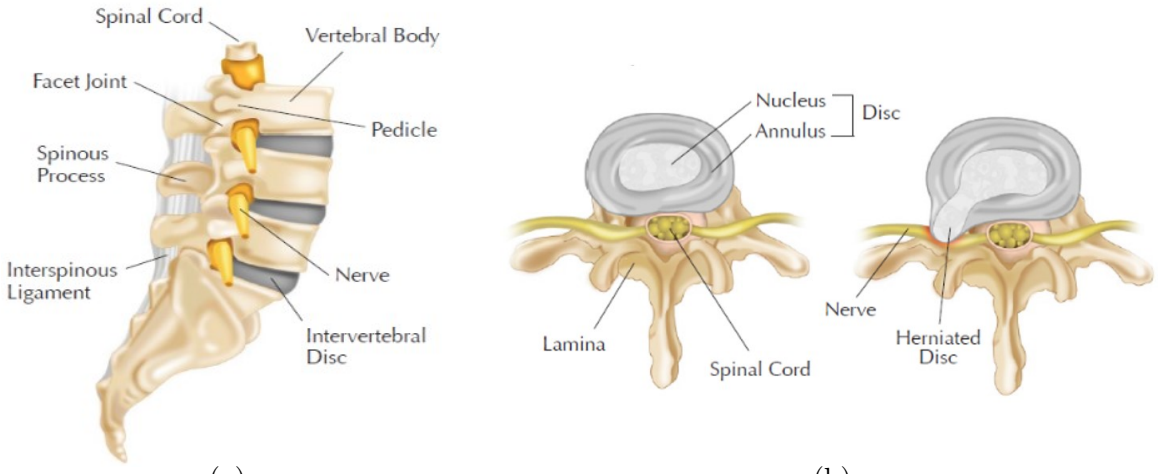

(a) (b)

Figure 1.1: (a) Lumbar spine (lateral view) highlighting key bony (vertebral body, facet joint, spinous process), nervous (spinal cord, nerve) and ligamentous (interspinous ligament) elements and the intervertebral disc [3]. (b) Lumbar vertebra (superior view) with a healthy disc (left), specifying one additional vertebral element (lamina) and the disc nucleus and annulus, and with a herniated disc (right), compressing a nerve [3].

1.2 Possible causes of discopathy

A discopathy can be normal if the wear and tear respects the expectations according to the stimulus, or premature when the wear and tear evolves faster than expected [1]. The natural evolution of discopathy varies from one patient to another. The pain could stabilize or increase until limiting the personal or professional activities of the patient. Among others, a discopathy can be due to overweight, carrying heavy loads, working with vibrations or long charge transportation [2]. Physiologically, the discopathy is mainly due to the dehydration of the annulus, leading to microfracture(s), which will extend with shocks to finally lead to the annulus tearing.

1.3 Arthrodesis

Due to the potential or experienced pain of the patient suffering from (degenerative) discopathy, a chirurgical operation could be advised or is required. The most performed surgical operation is an arthrodesis, which consists of fusing vertebrae around a defected joint (Figure 1.2a). In case of a discopathy, the arthrodesis consists of removing the damaged vertebral disc, and blocking vertebrae around it by connecting them together. Doing so, the vertebrae will fuse and the pain caused by the damaged disc will disappear, hence the alternative names: intervertebral, interbody or spinal fusion (Figure 1.2b). Over 300 000 lumbar intervertebral fusions are conducted each year in the United States [4].

An arthrodesis uses pedicle screws and union bars placed behind the column, which leave a large front lever arm with a risk of non-consolidation and persistent pain. Nowadays, to address this issue, an arthrodesis is often completed by implanting one or two cage(s) filled with bone grafts between the vertebral bodies to help supporting stresses and restore the stability (Figure 1.2a). The cage can be used as stand-alone fusion device, i.e. without posterior stabilization via rods and screw, but this is rather uncommon for lumbar regions. However, the cages could be misplaced or can move over the years and, which leads to pain and even a second operation. Therefore, the current solution is neither perfect for the patient nor for the hospital. A better solution could be to use bone cages that would integrate into the growing bone structure, such that these cannot move after intervertebral fusion, avoiding any complication. This thesis aims to design a bone cage, and the insertion tool, for lumbar intervertebral fusion.

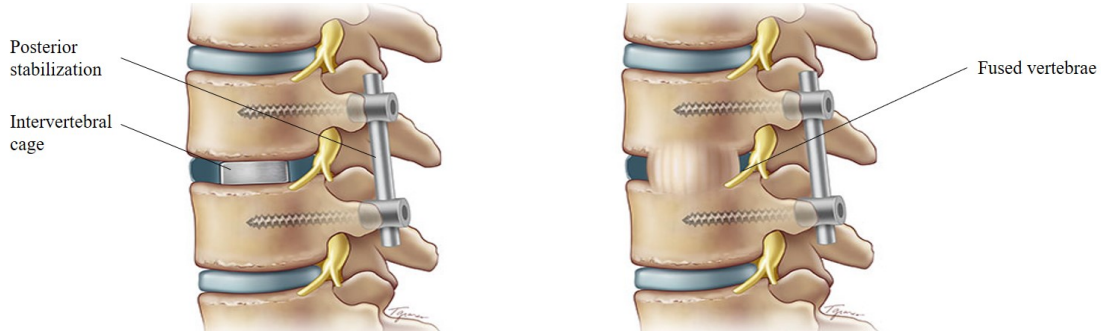

(a) (b)

Figure 1.2: (a) Lumbar arthrodesis (lateral view) using a metallic intervertebral cage and posterior stabilization [5].(b) Fused vertebrae (lateral view) [5].

Chapter 2

State-of-the-art

2.1 Possible causes of discopathy

2.1.1 Degenerative disc disease

The disc annulus is composed of concentric layers formed of collagen fibers [6]. This collagen is mostly type I collagen (stiff but brittle) in the outer portion, but gradually becomes a mixture of type I and type II collagen in the inner portion [6]. Disc degeneration could be described as a progressive replacement of the type II collagen by type I collagen, and the apparition of type III collagen [6]. Seemingly, a degenerated disc could be recognized by its decreased height, increased posterior and lateral bulging, anterior vertebral body osteophytes (or bone spurs, which is bone grown around the vertebral joint compressing the nerve [1] [8]) formation and disc dehydration (Figure 2.1) [7]. A main challenge is to differentiate these changes from age-related disc variations via medical imaging, such as radiography or magnetic resonance imaging (MRI) images. All these changes lead to a reduced ability to dissipate compressive forces.

Disc degeneration results in abnormal loading of the facet joints (Figure 2.1 and Figure 1.1, or subsection A.1.1), provoking its cartilage to break down and inflame, which triggers pain signals [9]. The phenomenon is referred as facets arthritis [7]. Other changes are due to disc degeneration, such as increased stress in adjacent ligaments and muscles and thickening of the ligament placed behind the nerve root, called the ligamentum flavum (described in subsection A.1.2 and represented in Figure A.2 and Figure B.1) [7]. This other phenomenon is referred as ligamentum thickening.

Disc degeneration is most often observed in the thoracolumbar spine, and this is due the increased supported weight by the intervertebral disc on the inferior spinal regions. Additionally, the junctions between the vertebral regions, i.e. the cervicothoracic, thoracolumbar, and lumbosacral junctions respectively for the junction between the cervical and thoracic regions, the thoracic and lumbar regions and the lumbar and sacral regions, are the most frequent site for degenerative disease (Figure A.1). This is due to the change of stiffness occurring in these junctions consequent to the change of the intervertebral disc size and composition and vertebral anatomy [6]. For example, at the cervicothoracic junction, since the thoracic vertebrae are mostly immobilized by the thoracic cage, during head motion, the cervical vertebrae act as a cantilever with a fixed

[1] The osteophyte formation is a side effect of disc degeneration since it aims to better distribute the load, which changes as a consequence of the change of the intervertebral biomechanical properties [7].

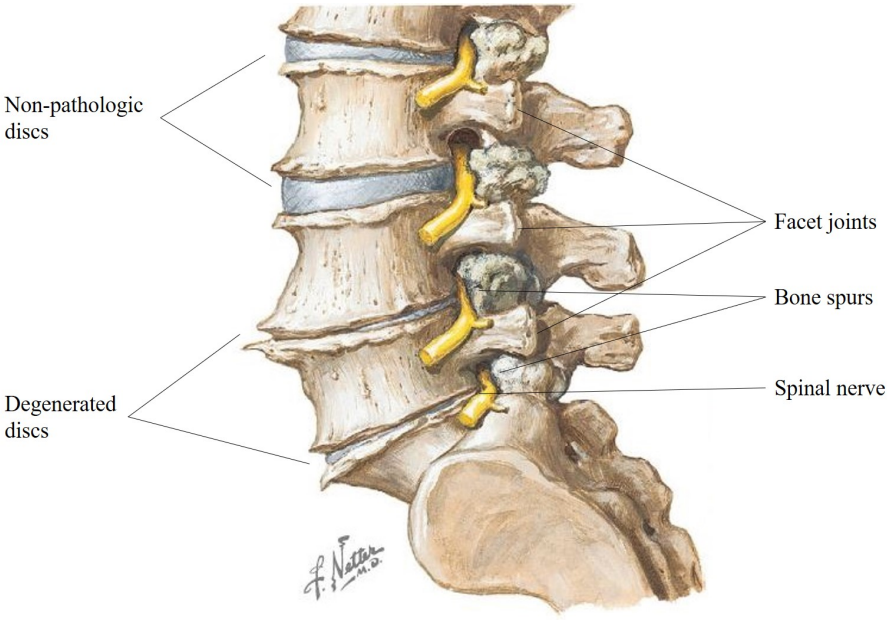

Figure 2.1: Degeneration of lumbar intervertebral discs degeneration in the lumbar spine leading to osteophytes formation that compress the spinal nerves (adapted from [7]).

end on the cervicothoracic junction, so maximising the stresses at this location [6]. Also, progressive endplate calcification changes its vascular network reducing supply to the intervertebral disc, which could lead to a progressive disc degeneration [6].

Lumbar disc degeneration does not systematically require a spinal fusion. Indeed, disc degeneration can lead to lumbar disc herniation, which is usually healed via a discectomy, since discectomy has a 85% to 90% success rate [7]. Also, disc degeneration can lead to a spinal stenosis (compression of spinal nerve(s) without annulus crack) that can be treated via decompressing the nerve alone (without intervertebral fusion). However, disc degradation requires a spinal fusion if it is accompanied by spondylolisthesis (vertebral slippage, described in subsection 2.1.3) or spondylosis (spinal bone degeneration, described in subsection 2.1.2) [7].

2.1.2 Myelopathy and spondylosis

A myelopathy is a degenerative pathology of the spinal cord, due to severe spinal cord compression [7]. Myelopathy may considerably affect the quality of life of the patient due to pain and motor disruption. On top of that, myelopathy increases the patient's predisposition to severe spinal cord injury after minor trauma [7].

The most common cause of myolopathy is spondylosis, referring to abnormal modification or degradation of vertebral bone. Spondylosis starts with the degeneration of the intervertebral disc, which can lead to disc inability to maintain its water content. In this case, disc dehydration and other disc component changes lead to a decrease of the disc height, and hence a change of its biomechanical properties since the annulus fibrosis has to sustain more weight than it is composed for [7]. This biomechanical modification can lead to several complications, such as disc herniation due to a cleft of the disc annulus, which can no longer retain the nucleus that will narrow the canal for the spinal nerves (called intervertebral foramen), and so compress the adjacent nerve (Figure 2.2). Also, spondylosis

can lead to a deformation of the vertebral bodies, the formation of bone spurs, a reduced lordosis and sometimes kyphotic deformity (spinal disorder consisting of an abnormal rounding of the upper back [10]). If spondylosis leads to a vertebral inflammation, the pathology is called a spondylitis, more specifically ankylosing spondylitis if it refers to the spine [11]. An example given in Figure 2.2.

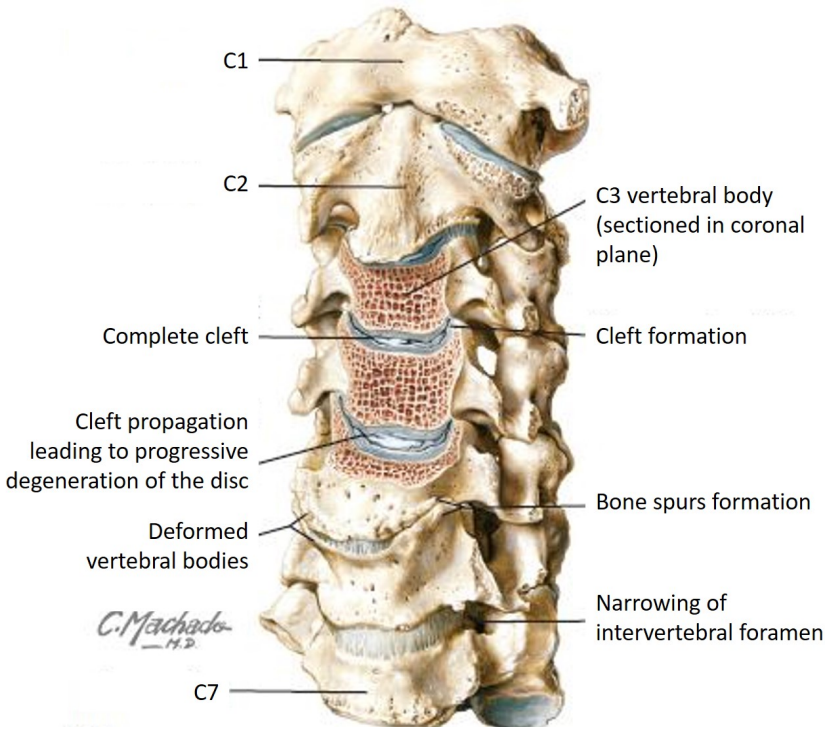

Figure 2.2: Degenerative changes in the cervical spine due to spondylosis: cleft formation, propagation and complete cleft, deformed vertebral bodies, bone spurs formation and narrowing of the intervertebral canal (adapted from [7]).

2.1.3 Degenerative lumbar spondylolisthesis

Spondylolisthesis consists of the slippage of a vertebra relative to an adjacent segment, and this as a consequence of displastic (congenital) or isthmic (due to defect or fracture of a bone connecting two facet joints) spondylosis (Figure 2.3). Typically, a superior vertebra slips forward (anterior direction) its inferior one, even if a posterior slippage can occasionally occur in the upper lumbar levels [7]. This slippage leads to disc erosion and narrowing since the disc is extended anteriorly. This decreases its height, hence leading to disc instability. The usual solution, after nerve decompression if necessary, is spinal fusion to decrease the vertebral slippage and restore most of the spinal stability (Figure 2.3). Degenerative spondylosis most commonly occurs at L4-L5 level, but has also been reported at other levels.

2.1.4 Scoliosis and sagittal plane deformity in adults

Scoliosis is a three-dimensional (3D) deformation of the vertebral column due to lateral curvature or vertebral rotation or both. Sagittal plane deformity refers to an abnormal

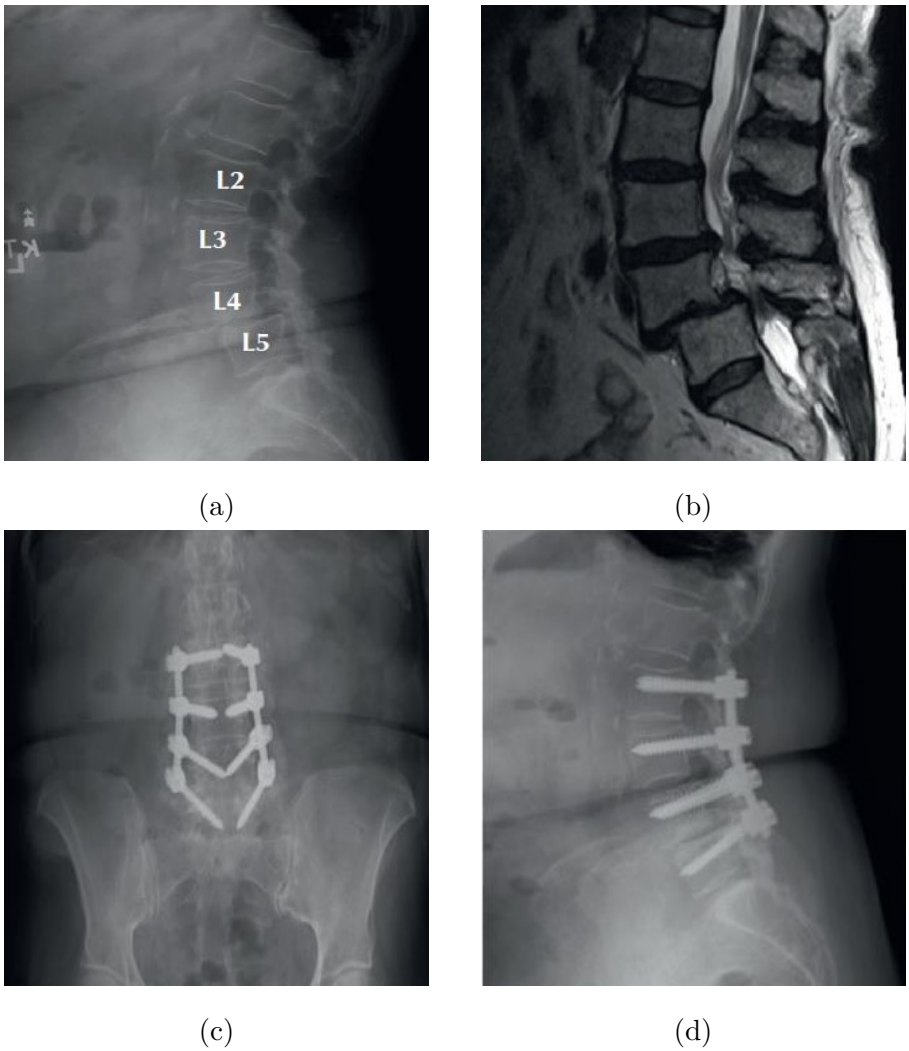

Figure 2.3: (a) Degenerative lumbar spondylolisthesis lateral radiographs showing mild slippage at L2-L3 and L3-4 in addition to severe slippage at L4-L5. (b) Degenerative lumbar spondylolisthesis lateral radiographs showing slight slippage at L2-L3 in addition to severe slippage at L3-L4 and L4-L5 [7]. Postoperative frontal (c) and lateral (d) lumbar radiographs showing instrumented fusion which considerably decrease vertebral slippage [7].

sagittal alignment of the spine [7]. Such vertebral column abnormality is often observed in children (mainly kyphosis, a exaggerated curvature of the thoracic spine [10]). If it is detected early enough during the childhood, a treatment to arrest the progression of the deformation is generally strongly recommended. Only if the deformation is untreated, it could become severe and require a surgical intervention: spinal fusion via an arthrodesis. Arthrodesis is used to restore coronal and sagittal balance to ensure a correct head positioning and to arrest curve progression. An example of spinal fusion used to correct scoliosis is shown on Figure 2.4.

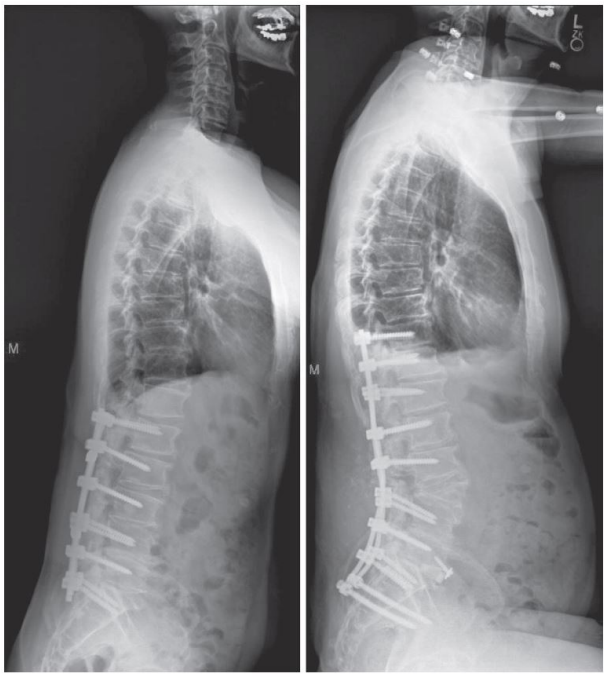

Figure 2.4: 67-year-old man with spinal deformity after lumbar fusion exhibiting a kyphotic posture (left) and the same patient after restoration of normal lumbar lordosis via an arthrodesis on more levels (right) [7].

2.1.5 Radiculopathy

A cervical radiculopathy consists of an inflammation of a nerve root (not the spinal cord, which is referred to as myolopathy) that can be acute or chronic. This frequently occurs as a consequence of disc degeneration (and its consequent facet arthritis or ligamentum thickening), spondylosis, spondylolisthesis or a combination of these factors [12]. Nerve compression can lead to pain, weakness and sensory defect corresponding to nerve dermatome and myotome, respectively an area of skin and group of muscles innervated by a single nerve [7]. An important difference with the myelopathy is that radiculopathy is a non-operative pathology, since more than 90% of patients with cervical radiculopathy improve with non-operative care consisting of maneuvers to decompress the nerve root or to relieve tension on it [7]. Therefore, even if the patient could be healed via an arthrodesis, non-operative care has to be firstly considered.

2.2 Arthrodesis: common medical procedures

An arthrodesis is a surgical operation consisting of provoking the fusion of two vertebrae over a joint space [13]. To do so, a wide spectrum of techniques exist[2]. The aim of this thesis is to focus on techniques based on a cage insertion between the lumbar vertebrae that are supposed to merge, with or without posterior stabilization.

[2]Described and compared by Lykissas and Aichmair [14].

2.2.1 Types of arthrodesis

To conduct a vertebral fusion using an intervertebral cage, several ways exist to access the spine and provoke the fusion [15]. The interbody fusion is named according to the spinal approach, which can be:

- posterior: Posterior Lumbar/Cervical Interbody Fusion (PLIF/PCIF)
- anterior: Anterior Lumbar/Cervical Interbody Fusion (ALIF/ACIF)
- lateral: Lateral Lumbar/Cervical Interbody Fusion (LLIF/LCIF)
- oblique lateral: Oblique Lateral Interbody Fusion (OLIF)
- transforaminal: Lumbar/Cervical Interbody Fusion (TLIF/TCIF)

All these approaches are represented on Figure 2.5 for a lumbar vertebra. The posterior, transforaminal and anterior approaches are the most commonly preferred by surgeons and hence, this thesis will focus on these, i.e. ACIF, TCIF, ALIF and TLIF.

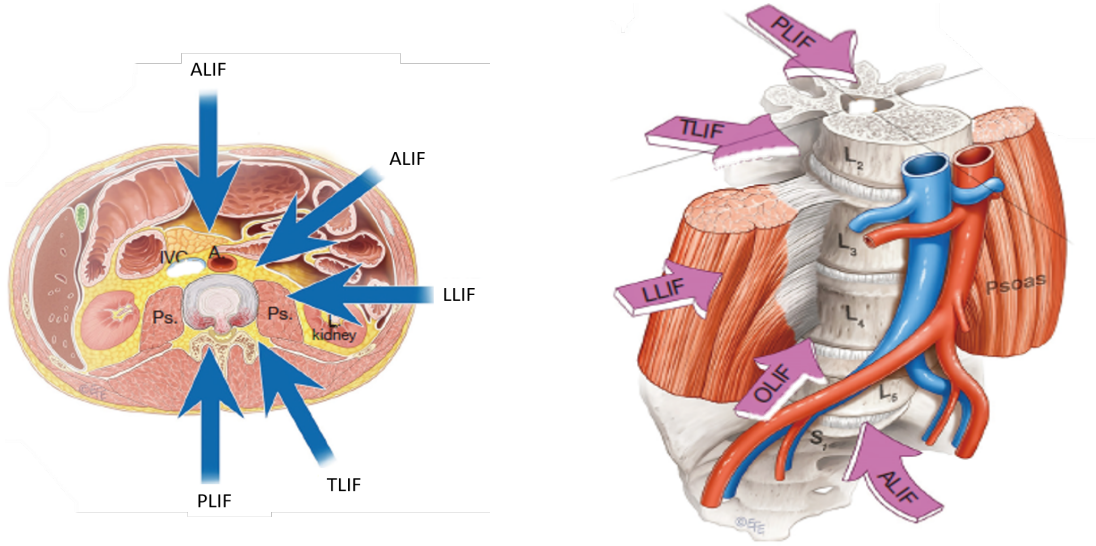

(a) (b)

Figure 2.5: Lumbar spine surgical approaches for interbody fusion on a spine section. (a) Superior view (IVC = inferior vena cava) (adapted from [15]). (b) Isometric view (A = aorta, Ps = psoas) [15].

2.2.2 Description of a generic arthrodesis procedure

Some steps are common to all approaches, i.e. ACIF, ALIF, TCIF and TLIF, and are visualized in Figure 2.6[3]). Table 2.1 presents few key features particular to each step of this generic approach.

Briefly, before operating, pre-surgical evaluations are performed to check for any contraindication to the arthrodesis or chosen approach. Afterwards, the patient is placed secured in a position depending on the approach and surgical level, i.e. which intervertebral disc to operate, on a standard radiolucent (allowing radiation to pass through) operating room (OR) table [18]. Once the patient installed, a general anesthesia is conducted with

[3]The generic procedure is illustrated for an ALIF, but the content is generic for ALIF and TLIF.

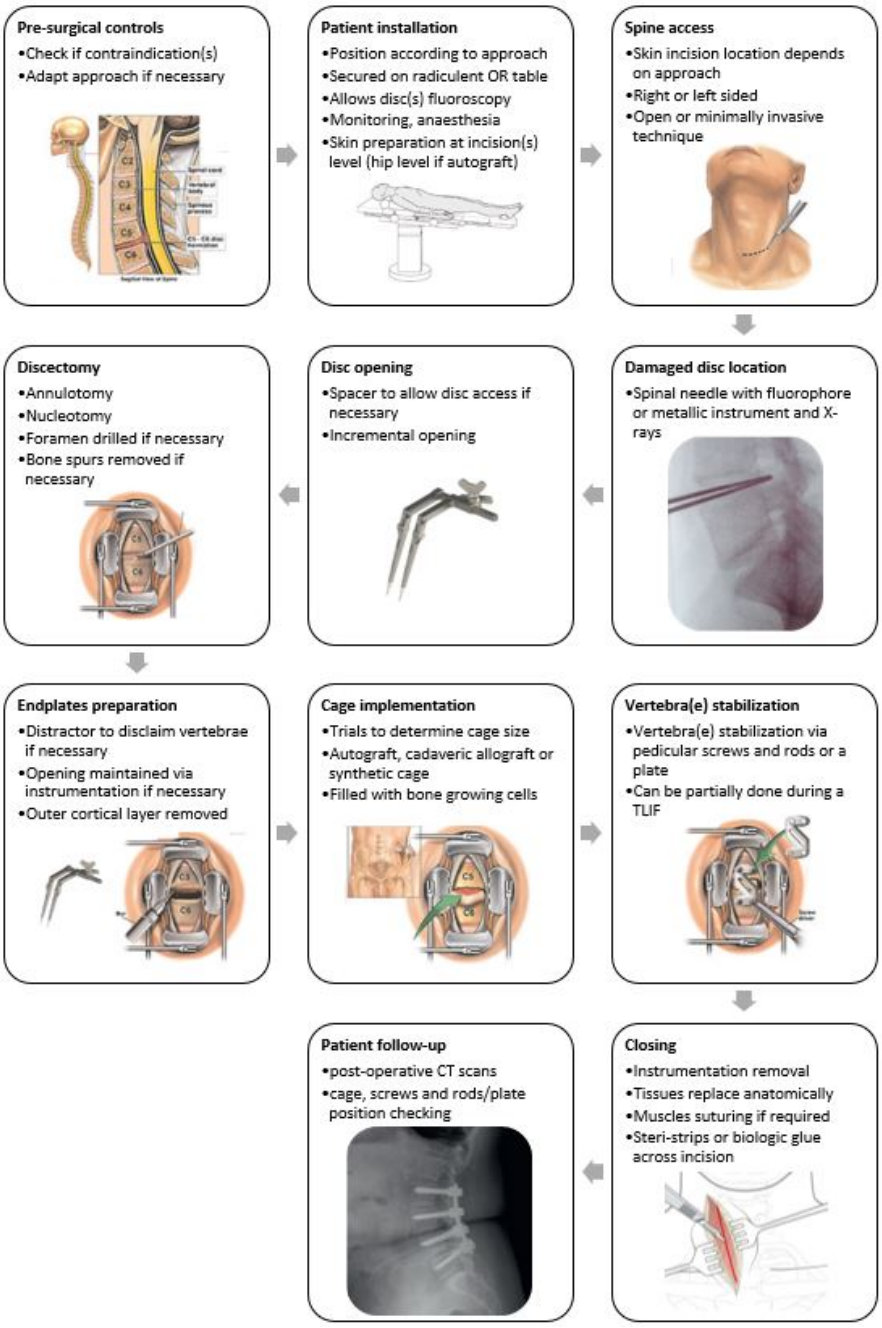

Figure 2.6: Generic procedure for an ACIF with the following illustrations. Pre-surgical controls: situation before the arthrodesis [16]. Patient installation: patient position [17]. Spine access: incision for a C5-C6 access [16]. Damaged disc location: how to check the surgical level via a metallic instrument and X-rays image [18]. Disc opening: one example of a post-pin distractor [19]. Discectomy: disc removal [16]. Cage implementation illustrates the bone removal from the iliac crest and its impaction (no cage is used for this illustration, but a cage is filled with the autograft in practice) [16], vertebra(e) stabilization illustrates how the vertebrae that has to merge are stabilized via rods and a plate [16], closing illustrates how the incision is closed [20] and the patient follow-up shows the arthrodesis result [7].

appropriate monitoring (details in Appendix D). When all the monitoring devices are placed, the patient is anesthetized and when falling asleep, the patient's skin located at the incision level is prepared as well as the hip if a fusion using allografts is planned [21].

The spinal lumbar approach starts with an incision depending on the surgical level. Even if the location of the incision and its size depend on the approach, both TLIF and ALIF can be right or left sided, respectively if the surgeon uses an incision on the left or right side of the midline [22, 23]. After the incision, the spine can be accessed via minimally invasive technique (minimal access spine technologies, MAST). Generally, this approach uses retractors: manual retractors such as Harrington and Balfour retractors (Figure D.7) or table-held retractors (Figure D.8). In case of MAST, laparoscopic retractors can be used for particular structures, but the global retraction is made through a barrel inserted and forming a tunnel to the spine. The next step is to locate the damaged disc to confirm the surgery level via the preferred technique of the surgeon (details in Appendix D) [18].

Next, the intervertebral nucleus has to be removed. In case of advanced disc degradation, the nucleus may be impossible to access. In that case, a small disc opener is inserted and progressively opened to provide access to the disc [24]. Then, the surface of the disc annulus is incised and removed (annulotomy) to allow access to the nucleus that is wide enough for the future instruments and cage insertion. This access is used to decompress the nerve, which is done by removing the osteophytes and the disc nucleus (nucleotomy). Usually, about 2/3 of the disc nucleus is removed using a small grasping tool, such as elevate curettes, while the remaining third is removing using surgical microscope or another precise tool [22]. For the discectomy, the transforaminal approach can be distinguished from the anterior approach. Since the ALIF and ACIF is used to insert two cages, the nucleus is totally removed. For TLIF, since only one cage is inserted, the disc is partially removed or totally removed and then can be refilled with bone autograft, to fill the free space before cage insertion [23]. The surgeon must pay attention to the central and opposite side of the disc, since these are easily missed with TLIF due to their difficult access. However, these are necessary to provide optimal area for interbody fusion [25]. Also, the foramen can be enlarged with a drill but only if necessary for a sufficient nerve decompression [21]. Please note that some bone spurs can be encountered between these steps and these have to be removed each time [26].

Now that the spinal nerve has the necessary space, the intervertebral space must be prepared for the interbody fusion. However, if the intervertebral space is not wide enough for endplate preparation or cage insertion, a distractor is used to disclaim the vertebrae via an incremental opening (the distractor is discussed in details in Appendix C). If necessary, the distractor stays in place to maintain the disc space or another device is placed for the same purpose. To prepare the endplates, each outer cortical layer is removed to expose the blood rich cancellous bone [21, 25]. This is used as a bed to hold the intervertebral graft, which can be an autograft, a cadaveric allograft or a synthetic cage containing either bone graft, β-tricalcium phosphate, stem cells, demineralized bone matrix or bone morphogenetic proteins (BMP) to facilitate the vertebral fusion [14, 7]. If the content of the cage (or the whole implant, which is uncommon nowadays) is obtained via autograft, the bone is extracted from the iliac crest. This additional surgical operation is done at the same time [18]. Prior to the cage insertion, a trial instrument is used to determine the cage size to be inserted. Then, the cage is filled and inserted using the appropriate instrumentation. More than facilitating the fusion, the inserted cage also restores some intervertebral space height and increases the opening of the neural foramina [22].

The above steps can be repeated as many times as the number of cage that must be placed. If necessary, the vertebrae that need to be fused are stabilized together via pedicular screws and rods or a plate. Please note that stabilization can also be done partially during a transforaminal approach [23].

The next step is to close the incision by removing the retractor(s) or the laparoscopic material, allow the tissues to replace anatomically and to suture the muscles (if some were cut) and the incised skin while the surgeon checks for any sign of thrombosis [18]. Usually, the position of the graft and of the stabilization material is checked via a anteroposterior and lateral radiograph before closing the incision [22]. Additionally, steri-strips or biologic glue is placed across the incision [21].

Lastly, a postoperative control can be performed via a computed tomography (CT) scan to check the position of the cage, screws and rods or plate [27].

2.2.3 Comparison of the anterior, posterior and transforaminal approaches

The anterior approach offers the advantage to not require to section the back muscles. On top of this, an anterior access allow to fully access to the anterior facet of the disc, so creating a wide access for discectomy, endplates preparation and cage insertion. However, this does not allow to use rods with screws to stabilize the joint if necessary. For this reason, this approach can be followed or (regularly) replaced by a posterior approach. Also, an ALIF allows access to the L4-L5 and L5-S1 intervertebral discs, but not to the ones above due to the aorta and vena cava (Figure 2.5). Since most of the disc degenerations take place in these discs, ALIF has been widely used.

Focusing on the posterior access, the TLIF is preferred to the historical PLIF since it passes between the muscles planes and then uses the natural opening of the intervertebral foramen to access the disc between the existing nerves [28]. Also, for TLIF, only one laminectomy is performed, allowing to access the disc only by one side, while PLIF requires a bilateral laminectomy. Therefore, TLIF requires less muscle, bone or ligament resection, hence reducing the length of the hospital stay and facilitating patient rehabilitation. In counterpart, only one cage can be inserted, while PLIF allows to insert two cages. Nevertheless, one cage is often enough [29, 23]. Due to the one-sided access, a TLIF requires specific tools for the nerve decompression by removing the disc and the bone spurs [23]. Also, a PLIF requires the surgeon to put forces on the nerves to retract them on the side, which is not the case for a TLIF. This increases the risk of both root irritation and the nerve penetration for a PLIF [30]. Please note that TLIF is a relatively new technique that has been popularized by the transforaminal lumbar approach. Therefore, few literature is currently available about this approach, but the scientific interest in this approach is raising. Table 2.2 summarizes pros and cons of each approach.

2.3 Clinically used cages and filling

Since the late 1980s, spinal interbody cages have evolved, both in terms of material and design [31]. The cage material and design have been adapted to restore intervertebral height, enable bone graft containment and restore the spinal stability such that intervertebral cage implementation becomes a highly successful means of achieving fusion [31]. Whatever the

Table 2.1: ALIF, ACIF, TLIF and TCIF features on top of the ones of the generic procedure. No noticeable feature appear regarding the disc localization, discectomy, endplates preparation, incision closing and patient follow-up.

Feature	ACIF	TCIF	ALIF	TLIF
Pre-surgery	/	/	Consume only liquid the day before [18]	/
Positioning	Supine position (on the back, Figure D.4) [22]	Prone position (on the stomach, Figure D.9)	Da Vinci (Figure D.4) or supine position [22]	Prone position (on the stomach, Figure D.9)
Spine access	2-inch incision lateral to the neck midline on the left or right side [22]	Midline incision and overlaying dissection of the muscles (Figure D.2). The surgeon can drill some vertebral bone to make the access more wide [7]	5-6cm incision depending on surgical level(s) (Figure D.5). Then, transperitoneal (peritoneum divided in the midline, exposure through it) or retroperitoneal (peritoneal content retracted, exposure sideways) approach [33, 34]	3-6inch midline incision (from the superior spinous process to the lowest spinous process). Ligamentum flavum resected and facets removed, nervous and muscular structure can be retracted if necessary (Figure D.10) [25]
Distraction	Generic or distraction pins above and below surgical level [22]	Generic or via screws and rod stabilization on the opposite side to the access [35]	/	Generic or via screws and rod stabilization on the opposite side to the access [35]
Cage insertion	One or two cages via medial access [21]	one cage via oblique access [35]	one or two cages via medial access [36]	one cage via oblique access [25]
Vertebral stabilization	Require additional posterior operation [21]	Generic or only the remaining stabilization if already done on opposite side to the access [35]	Require additional posterior operation [21]	Generic (could be done before on the opposite side to the access, in order to maintain disc distraction (Figure D.3)) [35]

Table 2.2: ACIF/ALIF, PCIF/PLIF, TCIF/TLIF: summary of pros and cons.

Approach	Pros	Cons
ACIF/ALIF	No resection of back muscles Wide access	No posterior stabilization Lumbar: only L4-L5 and L5-S1
PCIF/PLIF	Posterior stabilization Bilateral access	Resection of back muscles Nerve retraction
TCIF/TLIF	Posterior stabilization No resection of back muscles No nerve retraction	Unilateral access

surgical level or approach, several cage options are available [32]. These can be classified into metallic, composite and biological devices.

For whichever cage type, several cage size are always proposed to the surgeon and tested during the operation. This is because the cage size must be carefully chosen. Indeed, undersizing may result in loss of lordosis and inadequate stability for fusion, while oversizing may lead to insertion difficulty and disruption of the vertebral endplate, which may contribute to a long-term loss of intervertebral height (called graft subsidence) [25]. In what follows, different current or previously used cages are discussed.

2.3.1 Metallic devices

For all metallic implants, the advantages are the long shelf life, high and well-known mechanical properties and the lack of donor issue and immune response [32]. However, the metallic implants require a laborious shaping process and produce extensible artefacts on CT and MRI images [32, 37]. Also, metallic implants are subject to corrosion. Titanium (Ti), however, is highly resistant to corrosion, thanks to its TiO_2 formation [38]. The stiffness of metallic implants may promote long-term complication. One one hand, the implant can penetrate inside the cancellous bone of the adjacent vertebrae since this is softer, resulting in cage subsidence. On the other hand, the implant sustains most of the stresses. This results in a decreased loading of the surrounded bone [39]. This phenomenon is called stress shielding [39]. Stress shielding significantly decreases bone remodelling, and thus the bone density. As the bone properties are dependent on the bone density, the mechanical properties of the bone around the implant, i.e. the bone linking vertebrae that have to fuse, are significantly different [39]. This can lead to cage subsidence and bone-cage interface fracture [38]. Once the fusion matures, most metallic implants are left in place [40]. This can lead to long-term benefit, such as improved stabilisation or mechanical properties, but also to negative perspectives, such as toxicity or unwanted biomechanical consequences [40].

Bagby and Kuslich (BAK) cage

The BAK cage (Figure 2.7A) is a titanium cage originally designed to treat horses subject to cervical stenosis. Later, it has been certified for human interbody fusion [32]. In 1992,

it was the first successfully inserted cage for intervertebral fusion [38]. With its cylindrical design, it can be inserted through PLIF or ALIF. The holes allow to fill the cage with bone graft (or a substitute) to improve the arthrodesis efficacy. Thanks to its threaded surface, it can be screwed onto the endplates of each adjacent vertebrae, so promoting fusion and stability [38].

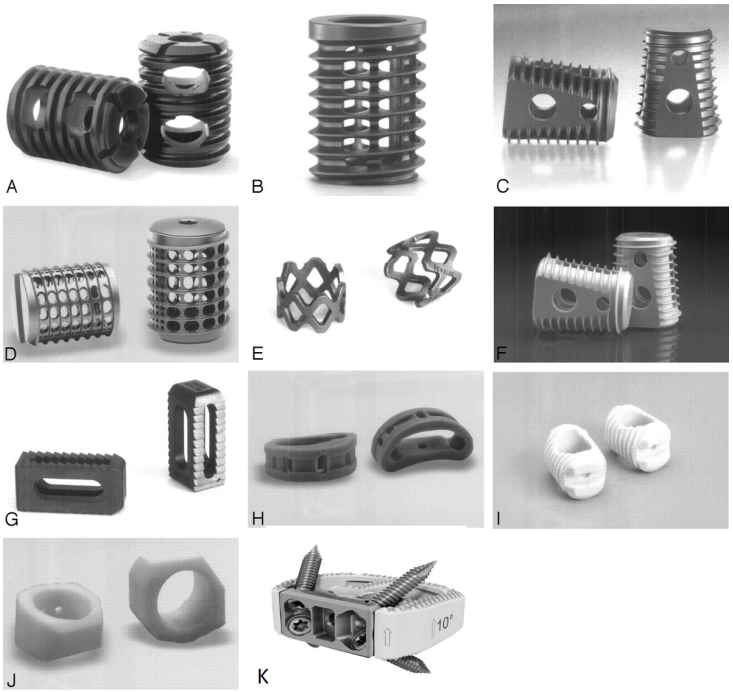

Figure 2.7: Cages design and materials advances [32]. Zimmer Spine: BAK cage (A), Stryker Spine: Ray Threaded Fusion Cage (B), LT-CAGE (C), Medtronic Sofamor Danek: INTER FIX device (D), Depuy Spine: Harms cage (E). Medtronic Sofamor Danek: PEEK cage (F). Brantigan Device; DePuy Spine: BOOMERANG (H), Bone Jowels (I), femoral Ring (J), Integral fixation cage (K) [41].

Ray threaded fusion cage

Ray has developed a second generation cage (Figure 2.7B) that is similar to the BAK cage, but with less titanium, so reducing the artefacts during CT and MRI imaging [32]. Also, the thread is deeper, facilitating tapping and stabilization even more [38]. As for the BAK cage, it can be filled with bone graft (or a substitute) and inserted via an ALIF or PLIF thanks to its cylindrical shape [38, 32].

Lumbar Tapered Fusion Device (LT cage)

The LT cage (Figure 2.7C) developed by Medtronics Sofamor Danek, was the most used cage for lumbar implants in the United States in 2005 [32]. This is thanks to its tapered (or wedge-shaped) design allowing to partially restore the patient's lordosis and increasing surface area for bone growth [32]. This surface also improves the stability and provides higher axial strength [38]. Also, the thin truncated side walls facilitate the imaging of bone formation inside and outside even when the implant is metallic [32].

INTER FIX and INTER FIX RP threaded fusion cage

The INTER FIX and INTER FIX RP cages (Figure 2.7D) were developed by Medtronics Sofamor Danek to reduce the imaging artefacts thanks to thinner walls comparing to the BAK or Ray cage [32]. This cage can also be filled if desired and inserted via both ALIF or TLIF.

Harms cage

The Harms cage, or cylindric mesh cage, was developed by DePuy Spine(Figure 2.7E). A titanium mesh is produced and rolled in a cylinder with reinforced ends [38]. The cage aims to maximize its bone growth thanks to an open diamond configuration [32]. The axial strength is ensured thanks to its 1mm wall thickness and the cage can be placed both via ALIF and PLIF [32].

2.3.2 Ceramic devices

Most of ceramic cages are made of silicon nitride (SN). SN is assumed to be easily visualized via MRI or CT, biocompatible and osteoconductive material with anti-infective properties and high mechanical and wear properties[42, 43]. Even if this implant is already widely used, only limited literature is available that assess its performance. Some estimate that SN cages offer similar fusion rate than PEEK implants [44, 45]. Yet, SN nitride is stiffer than bone, leading to potential cage subsidence and stress shielding, as for Ti cages [42, 43].

2.3.3 Polymeric devices

PEEK cage

The polyetheretherketone (PEEK) cage (Figure2.7F), developed by Medtronics Sofamor Danek, offers similar properties to the ones of cancellous bone [32], such as a similar elastic modulus [31], which leads to a good sharing and distribution of the stress [38]. This may decrease the cage subsidence and promote a faster and stronger fusion [38]. Also, PEEK is biocompatible and resistant to microbial adhesion, hence reducing inflammatory risk [38]. Usually, small metallic markers are placed on the cage to check the cage position after its insertion via CT imaging, as PEEK is radiolucent [32]. The cage design, which can be any shape or size, depends on the approach with which the cage is going to be implemented and on the patient.

2.3.4 Composite devices

A composite material is a material made of two or more materials that exhibit different properties than one of its material alone [46]. The main advantages of composite device is the radiculent behaviour on CT and MRI images and the large range of properties that could be obtained thanks to the materials mix [32]. As for any composite device, composite cages offer a highly flexible design, lower cost, improved productivity and corrosion resistance among many other advantages [47]. However, the drawbacks are the expensive manufacturing process and and the relatively unknown mechanical and biochemical properties.

JAGUAR I/F CAGE (Brantigan Device)

This cage (Figure2.7G), developed by DePuy Spine, is made of a carbon fiber–reinforced polymer [32]. Its typical rectangular shape makes it particularly adapted for a PLIF, and the superior and inferior facets can be slightly inclined to restore the patient's lordosis.

BOOMERANG II Device

The BOOMERANG II (Figure 2.7H) is a typical composite cage used for a TLIF. Thanks to its convex shape it can be inserted obliquely and then turned to align its convex facet with the anterior convex facet of the intervertebral disc [32]. The large hole allows bone filling for a faster vertebral fusion [32].

Magnesium-polymer cages: bioabsorbable

Bioabsorbable cages are a currently studied alternative to permanent cages [31]. However, based on bovine tests, magnesium-polymer is inferior to other implant's material due to its low osteointegration and its elastic modulus significantly different from the one of bone [48].

2.3.5 Devices made of biological tissue

Bone dowel and ring

Cages made of biological tissue, and more specifically bone, are typically shaped using cortical bone autograft or allograft. An autograft is when the transplanted bone comes directly from the body of the patient [49]. Autografts are often considered as the gold standard, as it does not provoke any immune response, decreases the risk of disease transmission and already contains patient's cells, proteins and calcified matrix that promote bone remodelling and osteointegration [49]. The drawback is the additional surgical operation required to harvest the bone, leading to additional risk of post-operative complications [49]. Autografts, mostly harvested from the iliac crest, are also highly dependent on the patient's bone quality [49]. Sometimes, to avoid the post-operative complications, the surgeon may choose to use the bone obtained during the nerve decompression and the access, mostly consisting of bone spurs or facets bone [49]. Allograft is obtained from a donor, usually provided by the tissue bank [49]. The bone is prepared via freezing or freeze drying with or without irradiating, to limit the immune response. As cells are removed via the irradiation, autografts does not stimulate bone remodelling as much as an autograft [49].

The bone can be shaped to form a dowel (Figure 2.7I) or a ring (Figure 2.7J), which both can be filled by bone graft or a substitute [32, 38]. The bone is shaped according to the chosen approach, surgical level and patient's lordosis. As the cage is made of cortical bone, the material Young modulus is higher than the one of cancellous bone, but significantly closer than the one of Ti or SN. Hence, the implant design needs to be optimized to obtain a structure stiffness similar to cancellous bone. If it is the case, bone cages promote a better load shearing, so enhancing fusion rate and bone remodelling and reducing stress shielding [38]. The main advantage is the bioabsorbtion after the vertebral fusion, oppositely to other implants that stay in place and can move, which potentially leads to post-surgery pain for the patient and would require a second operation. Also,

biological implants does not lead to imaging artefacts on CT or MRI [32]. Ergo, it can be very difficult to distinguish the implant from the new bone on CT or MRI images, except if markers are placed on the implant. However, the risk of disease transmission is higher and there is a significant risk of fracture during insertion [32]. Also, bone properties vary considerably according to the patient, extraction site and treatment. This makes it difficult to quantify precisely bone properties, causing randomness of the cage stiffness.

2.3.6 Integral fixation cages

Stand-alone ALIF cages, i.e. cages with an integrated stabilization system (Figure 2.7K), have been popularized over the past few years. These cages have the advantage to provide improved stability, which avoids to require an additional posterior stabilization [38]. This would avoid any complication associated with a combined anterior and posterior instrumentation, while still providing the advantages of an ALIF (Table 2.2) [38]. Theoretically, these cage can be made of any material, but the first one was made of PEEK material [38]. Recent studies demonstrated promising fusion rate, but long-term follow-ups are required to draw a conclusion [38].

2.3.7 Cage filling

Bone graft: demineralized bone matrix

The cage can be filled with bone graft, either from an autograft or an allograft. The bone is demineralized to remove the mineral content and expose bone-growing proteins (collagen and growth factors) [49]. Demineralized bone can be found in many forms, such as powder, gel, granule, chip or powder, but powder or granule are mostly used to fill the cage [49]. Once inserted in the cage, these will promote bone remodelling and consequently accelerate the spinal fusion and the cage osteointegration [49].

Recombinant Human Bone Morphogenetic Protein (rhBMP-2)

The Recombinant human bone morphogenetic protein (rhBMP-2) bone graft, commercially called INFUSE bone graft, is a combination of bone graft and BMP2. rhBPM-2 is a certified bone substitute for iliac crest graft that can be used with any cage type [32]. Using this substitute, it avoids the additional operation (usually done in parallel) for an autograft. BMP-2 is obtained by isolating them amount human bone and then replicated them using genetic engineering [49]. The rhBMP-2 attracts mesenchymal stem cells and bind to its receptors to cause a cell differentiation into osteoblasts and ergo initiate bone formation [32]. On top of its radiculent behaviour, the rhBMP-2 bone graft is proven to offer a faster vertebral fusion than iliac crest graft [32].

Mesenchymal stem cells (MSCs)

Mesenchymal stem cells (MSCs) are cells that have the ability to develop into several cell types, such as the ones responsible for bone remodelling. In addition to the MSCs cells, an osteoconductive matrix is required [50]. MSCs have the advantage to not provoke immune response [51]. Therefore, some trials were conducted and it appears that MSCs provide

promising results, but these are not yet confirmed via several studies with long-term follow-up [50].

Other potential substitutes for bone grafts exit, such as β-tricalcium phosphate (β-TCM). However, the ones mentioned above are the most widely spread [38].

To sum up, nowadays, Ti cages are widely used as they are historically the first successful intervertebral cages and because their mechanical and biochemical properties are well-known. However, among other complications, Ti cage subsidence and stress shielding remain problematic. Consequently, PEEK cages seem to be increasingly developed and used thanks to its Young modulus close to the vertebral one. However, cage bioabsorbtion remains a very attractive feature of a bone cage. Also, the natural porosity of bone might promote the fusion. Therefore, this thesis aims to optimize a bone cage design to avoid cage subsidence and stress shielding.

2.4 The implementation tool

To implement a cage, a dedicated instrumentation is required. The instrumentation allows to determine the dimensions of the cage, to distract the vertebrae and insert the cage (details in chapter 3). Ergo, the instrumentation can be distinguished between the trial tool(s), the distraction tool(s) and the insertion tool(s). Below, the instruments to implement a cage via a TLIF from three key suppliers is discussed (instrumentation for other approaches and more details can be found in Appendix C).

2.4.1 Medtronic

Medtronic developed a PEEK cage (Figure 2.8a) and its implementation instruments compatible for PLIF and TLIF that can be used via an open or MAST spine access [27]. Firstly, the vertebrae are distracted via a tool of 8mm height that is inserted between the vertebrae and then is opened until 16mm (Figure 2.8b) [27]. To maintain the distraction, it is advised to place screws and a rod on the side opposite to the access [27].

Then, a trial implant is inserted to define the implant size (the implant size is the size of the largest cage fitting the available space) [27]. Before inserting the implant, autograft is placed anteriorly and contralaterally, in the cage or both. Then, the implant is linearly inserted and stays obliquely in the inetervertebral disc (Figure 2.9) [27].

(a) (b)

Figure 2.8: Medtronic cage and distractor. (a) PEEK cage for PLIF or TLIF [27]. (b) Distractor when close (8mm) and open (16mm) [27].

(a) (b)

Figure 2.9: Medtronic cage insertion. (a) Cage insertion via a MAST with posterior stabilization on the side opposite to the access [27]. (b) Result after insertion and bilateral posterior stabilization [27].

2.4.2 Stryker

Stryker developed a cage and its instrumentation for TLIF, that can be used both with an open or minimaly invasive access [25]. The provided distractor is a T-shaped distractor that can increase intervertebral height from 7mm to 16mm, which can be read directly on the handle (Figure 2.10) [25]. A slaphammer is provided to insert the distractor if necessary [25]. It is specified that the distractor has to be lubricated and has to be in contact with the vertebral rim (composed of cortical bone) [25]. No procedure for keeping vertebrae distracted is provided.

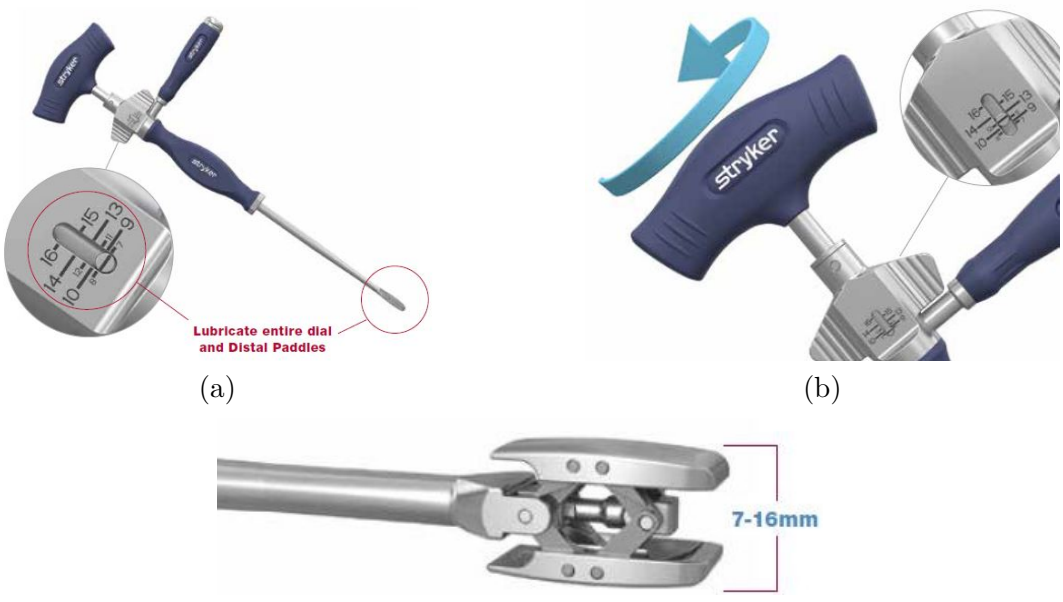

(a) (b)

(c)

Figure 2.10: Stryker distractor. (a) Distractor with its extension handle representation and a zoom on the lubricated zone [25]. (b) Distractor rotation for paddle discard [25]. (c) paddle discard range (c) [25].

Then, a navigation tool helps the surgeon to chose which implant size is the most appropriate (Figure 2.11) [25]. The implant height is defined by the height of the navigation tool that can fit [25]. The implant length is chosen by reading on the navigation tool the maximal length fitting via the access [25].

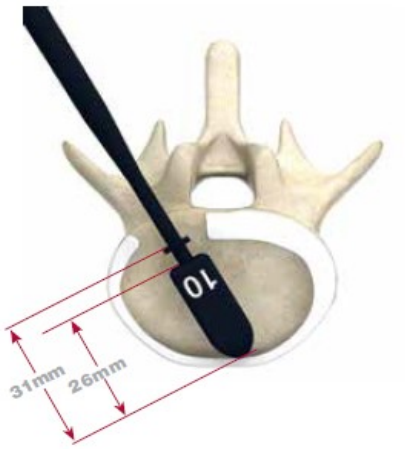

Figure 2.11: Stryker navigator trial that is 10mm wide, 26mm long with a ring for 31mm and 6 to 15mm high (since the cage are 26mm or 31mm long, 6 to 15mm high) [25].

The insertion of the cage is performed thanks to a combination of a linear insertion followed by an axial rotation, allowing the surgeon to place the rounded face of the implant on the anterior facet of the annulus (Figure 2.12) [25]. Again, a hammer might be used for implant insertion. The cage might be filled by any material promoting fusion if desired [25].

2.4.3 Zimmer Biomet

Zimmer Biomet provides an instrumentation for TLIF with a distraction tool similar to the one proposed by Stryker and an insertion tool very similar to the one proposed by Medtronic [52]. However, a small variation can be noticed. Indeed, the cage has an integrated fixation system (Figure 2.13a), which has to be set up once the cage is inserted thanks to the instrumentation (Figure 2.13b).

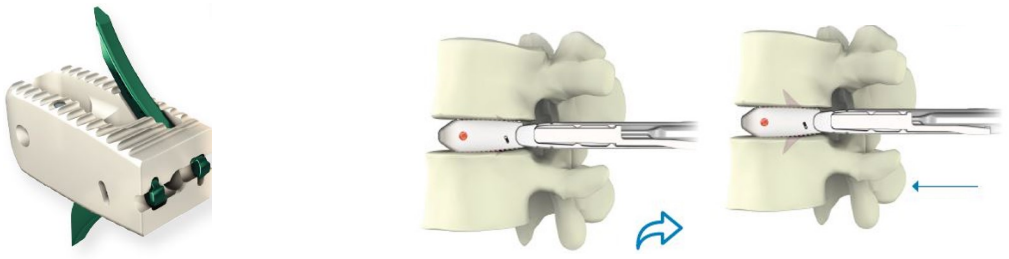

(a) (b)

Figure 2.13: Zimmer Biomet TLIF: cage and cage set up. (a) Cage with its fixation system deployed [52]. (B) Cage fixation set up [52].

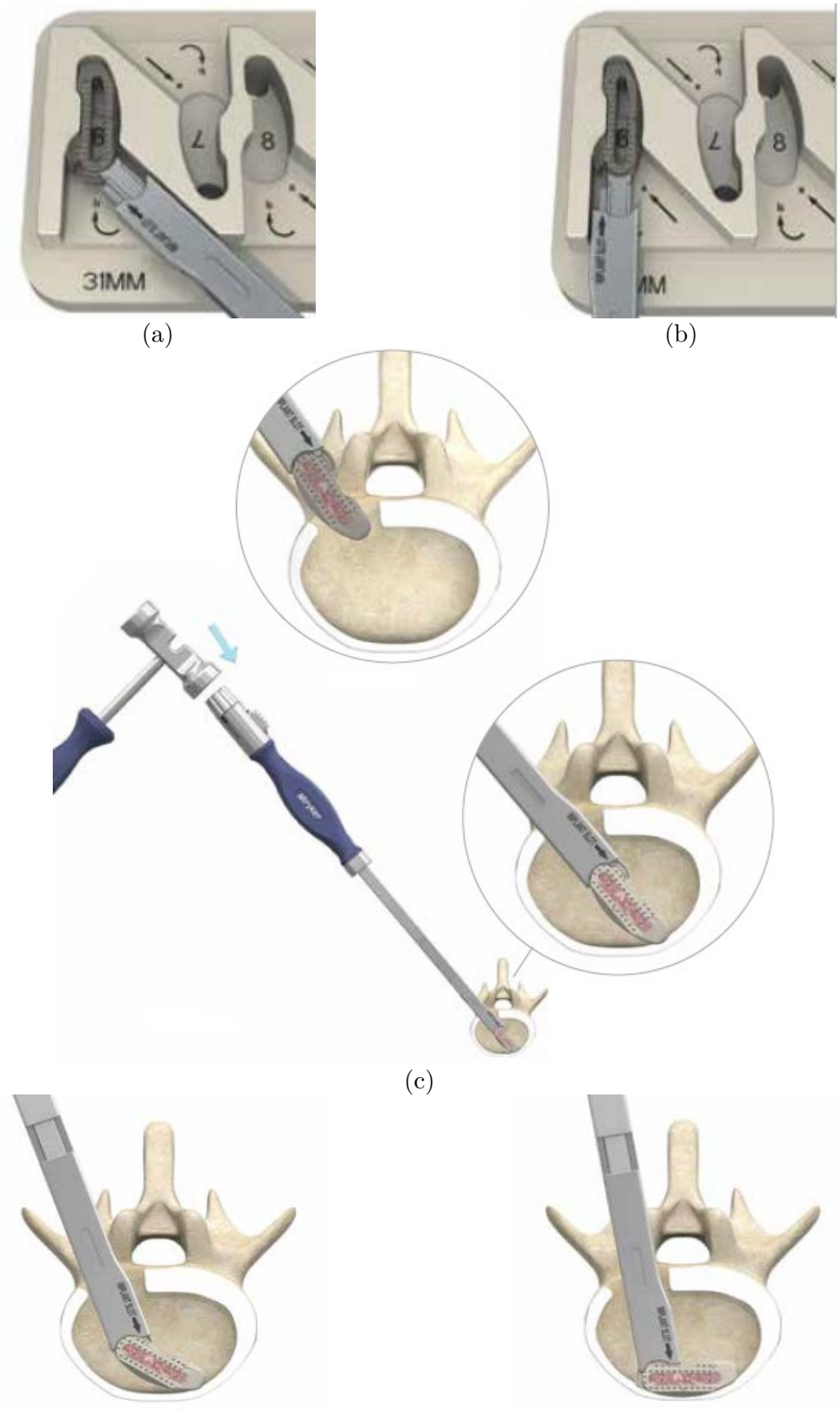

(a) (b)

(c)

(d) (e)

Figure 2.12: Stryker TLIF: Inserter cage fixation procedure (grabbing (a) and rotation (b)), primary impaction in the lock state (c) and final impaction in the rotation state (d) until desired position (e) [25].

Chapter 3

Problem statement and objectives

3.1 Problem statement

Even if PEEK and Ti cages are the two intervertebral cages that are the most frequently used, comparison studies show mixed results that could not define which one is superior [31]. PEEK cages might lead to a better disc height restoration thanks to a smaller subsidence and might decrease the stress shielding effect [53]. These thanks to a cage stiffness that is often closer to the one of cancellous bone than the one of a Ti cage. Silicon nitride implants may be superior to PEEK implants thanks to their lower migration and more optimal osteointegration, but the cage stiffness has to be carefully refined by the design as silicon nitride is stiffer than cancellous bone. Besides, no trustful results of its long-term efficacy are available [42]. Especially, none of them are bioabsorbable, leading to potential post-operative complications. This can lead to a second operation to remove the cage and implement a new fusion device, which is not to the advantage of either the patient nor the hospital.

A solution is to design a cage made of cortical bone. The design would allow to have adequate mechanical properties, i.e. a stiffness as close as possible to the one of cancellous bone, in order to minimize cage subsidence and stress shielding. Also, a bone cage should naturally be integrated into the bone which links the fusing vertebrae, reducing the risk of post-operative complications.

Additionally, the cage manufacturer often provides the instrumentation to distract the vertebrae and implement the cage, which is specific to the cage [1]. In the context of this thesis, the cage would be produced and used by the UCL St-Luc academic hospital (Belgium). More specifically, the cage would produced by the tissue bank and used by orthopaedic surgeons, who will be mentioned as the user in what follows. The St Luc hospital only owns the required tool to distract the vertebrae. Consequently, a dedicated instrumentation for the implementation of the cage is necessary.

3.2 Aim and objectives

This thesis aims to define a design of a cage made of cortical bone for a TLIF. The cage has to be shaped according to the approach. The mechanical properties of the cage should be

[1] Some manufacturers also provide the instrumentation to prepare the intervertebral space. However, this is not part of this thesis.

appropriate and cage anchorage should be present in order to avoid the cage to move after implementation. Also,a dedicated instrumentation should provide the tools to allow the surgeon to implement the cage in the distracted and prepared intervertebral space, taking into consideration that the cage is made of bone. It is important to remind that cage implementation groups three steps: choice of the cage size, cage insertion (or placement) and the removal of the insertion tool(s). The cage design might be adapted to the tool.

So, the objectives of this thesis are twofold. On one hand, a bone cage has to be designed such that:

- The cage shape is adapted to a TLIF
- The cage dimensions are adapted to a lumbar arthrodesis
- The design and mechanical properties of the cage minimize the risk of operative and post-operative complications
- The cage is made of cortical bone from the tissue bank

On the other, implementation tool(s) have to be provided, such that:

- The tool(s) allow the surgeon to choose a cage with dimensions appropriate to the anatomy of the patient without causing any damage
- The insertion tool is adapted to the cage (or cages if several provided)
- The insertion tool allows the surgeon to insert the cage as desired via an open or minimally invasive access
- The insertion tool can be retracted while leaving the cage in place

3.3 Impact of COVID-19

Initially, it was planned to define the dimensions of the cage, to produce it and evaluate its mechanical properties in the labs. This in order to optimize its design regarding its desired mechanical properties. In parallel, its dedicated tools had to be developed. Then, clinical tests had to be performed in order to test the optimized cage and its tools.

However, due to the COVID-19 situation, the methodology has to be adapted. Instead of producing the cage and testing it, a finite element model will be developed to simulate the load on the cage and optimize its design. In parallel, its dedicated tools will be designed. As this reorientation came late, the time was restricted. Also, developing a finite element model of bone is very complex. So, we decided to focus on the optimization of the design of the cage, and to propose tools without testing them. This choice was also motivated by the fact that no one knew if the labs would reopen before the end of the academic year, and so if the tools could be tested. Eventually, it turned out to be the right choice, as the labs did not open.

Chapter 4

Design of the bone cage

4.1 Design inputs

4.1.1 User inputs

4.1.1.1 Objectives

The goal is to design a cage made of cortical bone that can be inserted between L4 and L5 or L5 and S1 to restore the intervertebral space during the interbody fusion. The height and the lordosis angle of the intervertebral space have to be restored according to the anatomy of the patient, aiming to provide a maximal anterior stability. Furthermore, the cage has to allow (or promote) osteointegration as much as possible, such that the interbody fusion takes place as fast as possible. The cage will be shaped using the Charlyrobot 2U 4-axis machine (details on [54]). A dedicated instrumentation to determine the cage dimensions and insert the cage should be provided as well.

4.1.1.2 Dimensions

The access size to the intervertebral space can vary from one patient to another, and therefore cages with different sizes are typically provided. Since most of lumbar TLIF procedures concern the L4-L5 or L5-S1 discs, it is asked to focus on these both locations, assuming that it would be to the surgeon's choice to use the same device for another lumbar location. These locations generally allow to insert a cage of:

- 25 to 28mm long (Figure 4.1a)
- 11mm medio-lateral width (Figure 4.1a)
- 6 to 16mm height (Figure 4.1b)
- 0 to 8° lordosis angle (Figure 4.1b)

Indeed, as showed later, these values match both the anatomical dimensions and those of commercialized cage dimensions.

For the machining of the cage, the 4-axis machine has a 0.1mm precision using round burs with a minimal diameter of 2mm. Bone is a porous material, hence the machining precision might be decreased. Three-dimensional (3D) imaging datasets (CT) of the available cortical bone material will be provided to be able to define the cage volume. The machining requires a 1mm margin around the cage and a 10mm rod to clamp the cage between its centers within the Charlybot.

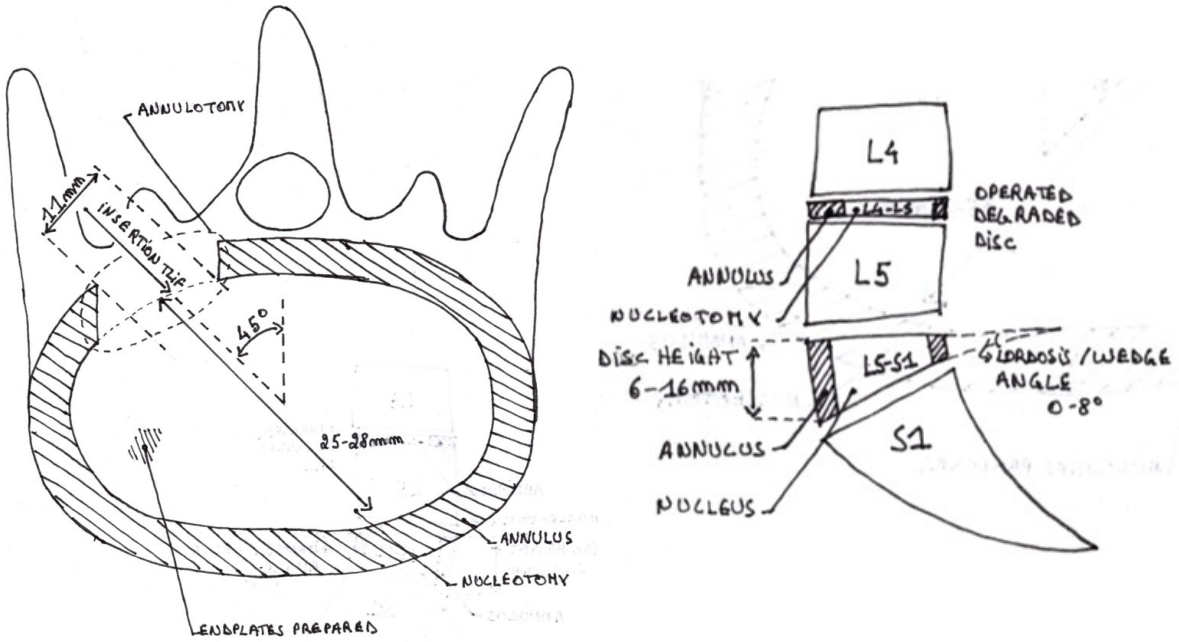

(a) (b)

Figure 4.1: Schematic representation of the cage requirements. (a) Top view. (b) lateral view [1]

4.1.1.3 Mechanical properties

Material properties The cortical bone is provided by the tissue bank of the UCL St-Luc academic hospital (Belgium). The cortical bone is harvested from tibial or femoral bone, using the standard from the the American Association of Tissues Banks [55]. First, the grafts are washed, the lipids are extracted and the proteins are inactivated. Then, the graft is freeze dried and sterilized by 2.5-Gy gamma irradiation [55].

Loads It should be avoided that the cage inserts into the vertebral body. However, some anchorage would be useful to avoid cage movement. Besides, the goal is not to reproduce the same properties as the one of an intervertebral disc, but rather to design a cage able to sustain the same stress, i.e. the intervertebral stress. As indication, it has been provided that, for someone of 50kg bending forward, the pressure can raise to $144 \frac{kg}{cm^2}$ due to the arm lever. The cage implementation is usually combined with a posterior stabilisation (Figure 1.2a) or with a posterior synthesis or both, according to the surgeon's choice. However, this should not be taken into consideration such that the cage can be implemented as a stand-alone fusion device.

In addition, it is not required to add any other material than cortical bone, but the intervertebral fusion has to take place as fast as possible, as the risk of fatigue fracture would decrease accordingly. To do so, there is no objection to add pores in the cage, with or without another material inside. During the operation, some material can be placed in the free space around the cage (if asked or needed). However, the choice of such material is not part of this thesis.

4.1.2 Literature inputs

On top of the inputs from the user, additional inputs from literature was needed.

4.1.2.1 Objectives

The cage should contain spaces to place imaging markers in order to perform post-operative verification, in order to distinguish it from the vertebral bone [25].

4.1.2.2 Dimensions

The disc nucleus geometry is used to define the cage length, height and slope, while its width is defined by the access width. For the cage length, since TLIF access is commonly at 45° to the medial axis, it has to be equal to or smaller than the length of a line at 45° to the medial axis inside the nucleus (Figure 4.1). Please note that the access can vary due to the anatomy of the patient, but 45° is a common assumption. Besides, literature often reports nucleus dimensions based on an elliptic approximated shape with a major and minor axis. Based on this geometry, the length of the access at 45° is computed via the polar elliptic equation:

$$r = \frac{ab}{\sqrt{r_1^2 sin(\varphi)^2 + r_2^2 cos(\varphi)^2}}$$

where
r_1 = The elliptic semi-major axis
r_2 = The elliptic semi-minor axis
φ = The angle
r = The radius with an angle φ

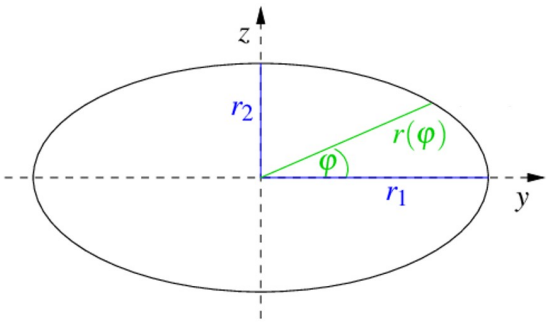

Figure 4.2: Polar ellipse frame [56].

So, for an access with an angle $\theta = 45°$ (or -45°), this leads to an access of a length equal to 2r. On top of evaluating the length, the disc height and lordosis angle are respectively used to determine the cage height and potential slope. Since the cage is intended to be used at L4-L5 or L5-S1 levels, both disc dimensions are studied. Additionally, dimensions of commercialized cages for TLIF are used as clinical standards (Table 4.1).

4.1.2.3 Mechanical properties

Material The cage will be made of cortical bone. This is a viscoelastic anisotropic material. However, it is supposed to be transversely isotropic, even if some small variations can be observed in the transverse directions (mostly due to experimental inaccuracies) [67, 39]. This means that its anisotropy leads to different longitudinal and transverse properties. On the other hand, the bone of the vertebral body, which is in contact with the cage, is mostly composed of cancellous bone. Some papers consider it as transversely isotropic as well [39], while others differentiate the lateral and antero-posterior direction [68]. To be as generic as possible, the cancellous bone is assumed to be anisotropic, but transversely isotropic, like cortical bone. The Hooke's law matrix, or stiffness matrix, of

Table 4.1: Cage design dimensions input from literature. Values from [66, 58] are taken as the mean for the superior and inferior diameters, for both genders, and some values are deduced from graphs since no table was provided. Disc height is the maximal disc height, usually in the middle. Discrete values are separated by ";", continuous ranges are given as "starting value-last value", discrete ranges are given as "starting value: step: last value". The anatomical values for the access width were asked to a surgeon. The anatomical values correspond to the disc or access (based on disc dimensions) values, while the clinical values correspond to cage dimensions.

Spinal region	**Context**	**Access or cage length [mm]**	**Disc or cage height [mm]**	**Access or cage width [mm]**	**Wedge or cage angle [°]**
L4-L5	Anatomical values	33.6 [57] 29.44±3.85 [58]	10 [59] 11.3±2.1 [60] 14.17±1.9 [61]	11	9.6±2.4 [62] 10.1±4.8 [63] 10.8±5.9 [64] 12.29±3.39 [65]
L5-S1	Anatomical values	18.3 [66] 32.11 [57] 28.82±4.4 [58]	10 [59] 10.7±2.1 [60] 13.36±2.6 [**discDimrealistic**]	11	15.2±5.1 [57] 12.6±2.4 [63] 15.1±6.1 [64] 15.58±5.43 [65]
L4-L5 and L5-S1	Clinical standards	26;31 [25] 22;26;32;36 [27] 30;34 [52]	6:1:12 [25] 8:2:16 [27] 8:1:14 [52]	12 [25] 10 [27] 10 [52]	0;4 [25] 0 (convex) [27] 0;5 [52]
L4-L5 and L5-S1	User needs	25-28	6-16	11	0-16

an anisotropic material is defined as [69]:

$$\begin{bmatrix} \epsilon_{xx} \\ \epsilon_{yy} \\ \epsilon_{zz} \\ \epsilon_{yz} \\ \epsilon_{zx} \\ \epsilon_{xy} \end{bmatrix} = \underbrace{\begin{bmatrix} \frac{1}{E_x} & -\frac{\nu_{yx}}{E_y} & -\frac{\nu_{zx}}{E_z} & 0 & 0 & 0 \\ -\frac{\nu_{xy}}{E_x} & \frac{1}{E_y} & -\frac{\nu_{zy}}{E_z} & 0 & 0 & 0 \\ -\frac{\nu_{xz}}{E_x} & -\frac{\nu_{yz}}{E_y} & \frac{1}{E_z} & 0 & 0 & 0 \\ 0 & 0 & 0 & \frac{1}{2G_{yz}} & 0 & 0 \\ 0 & 0 & 0 & 0 & \frac{1}{2G_{zx}} & 0 \\ 0 & 0 & 0 & 0 & 0 & \frac{1}{2G_{xy}} \end{bmatrix}}_{S} \begin{bmatrix} \sigma_{xx} \\ \sigma_{yy} \\ \sigma_{zz} \\ \sigma_{yz} \\ \sigma_{zx} \\ \sigma_{xy} \end{bmatrix}$$

Where:

E_i = Young modulus in direction i
ν_{ij} = Poisson's ratio for an extension applied in direction i and a consequent contraction in direction j
G_{ij} = shear modulus on the plane whose normal is in direction i with a force in the direction j

Defining a frame with the x, y and z axes aligned with the tangential, radial and longitudinal directions respectively (Figure 4.3), cortical bone is anisotropic in the transverse x-y plane. For such a material, the Hooke's law matrix S can be rewritten using five independent variables (Eq. 4.1)).

$$S = \begin{bmatrix} \frac{1}{E_T} & -\frac{\nu_T}{E_T} & -\frac{\nu_L}{E_L} & 0 & 0 & 0 \\ -\frac{\nu_T}{E_T} & \frac{1}{E_T} & -\frac{\nu_L}{E_L} & 0 & 0 & 0 \\ -\frac{\nu_L}{E_T} & -\frac{\nu_L}{E_T} & \frac{1}{E_z} & 0 & 0 & 0 \\ 0 & 0 & 0 & \frac{1}{2G_L} & 0 & 0 \\ 0 & 0 & 0 & 0 & \frac{1}{2G_L} & 0 \\ 0 & 0 & 0 & 0 & 0 & \frac{1}{G_T} = \frac{2*(1+\nu_T)}{E_T} \end{bmatrix} \quad (4.1)$$

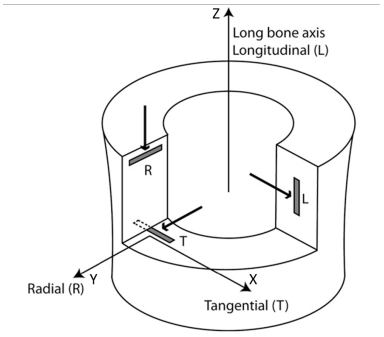

Figure 4.3: Defined frame for cortical bone [70].

Where

E_i = The Young modulus in direction i
ν_{ij} = The Poisson's ratio that corresponds to a contraction in direction j when an extension is applied in direction i
G_{ij} = The shear modulus on the plane whose normal is in direction i with a force in the direction j

Indeed, $E_X = E_Y$ such that $E_X = E_Y = E_T$ is the Young modulus in the transverse direction (TD) and $E_Z = E_L$ is the Young modulus in the longitudinal direction (LD). Also, the shear moduli are supposed to be symmetric, inducing that $G_{XY} = G_{YX}, G_{YZ} = G_{ZY}$ and $G_{ZX} = G_{XZ}$. Thanks to the transverse isotropy, for a force along the longitudinal (z) direction, the shearing behaviour is the same in the planes whose normal is in the tangential (x) or radial (y) direction. Therefore, $G_{XZ}(= G_{ZX}) = G_{YZ}(= G_{ZY}) = G_L$ is the shear modulus in the LD. $G_{XY} = G_{YX} = G_T$ is the shear modulus in the TD. Similarly, $\nu_{ZX} = \nu_{ZY} = \nu_L$ is the Poisson's ratio in the LD, $\nu_{XY} = \nu_{YX} = \nu_T$ is the Poisson's ratio in the TD and $\nu_{XZ} = \nu_{YZ}$, but the Poisson ratios are not symmetric. However, the transverse shear modulus is related to the transverse Poisson ratio and Young Modulus through $G_T = \frac{E_T}{1+\nu_T}$ and symmetry of the the Hooke's law matrix imposes $\frac{\nu_{XY}}{E_X} = \frac{\nu_{YX}}{E_Y}$ [69]. Consequently, the Hooke's law of a transversely isotropic material is fully defined via 5 parameters: $E_L, E_T, G_L, \nu_L, \nu_T$, even if G_T is often given.

So, the elastic behaviour of cortical and cancellous bone is defined by their transverse and longitudinal Young and shear moduli and Poisson ratio. Also, as viscoelastic material, their yield and ultimate stresses differ and depend on the stress type (compression, tension or shearing). Besides, their density and porosity are two interesting features when comparing cancellous and cortical one. Consequently, Table 4.2 presents mechanical properties of both vertebral cancellous bone and cortical bone.

Loads The lumbar spine kinematics is defined by six motions: flexion (forward bending), extension (backward bending), left and right lateral bending and left and right axial rotation (Figure 4.4) [84]. These result in 3 forces and 3 moments on the lumbar spine and sacral

Table 4.2: Vertebral cancellous and cortical bone properties. TD = Transverse direction (X, Y), LD = longitudinal direction (Z), AP = Antero-Posterior direction, LT Lateral direction, E = Elastic modulus ($E_Z = E_L$ in the LD and $E_Y = E_X = E_T$ in the TD), G = Shear modulus ($G_{XZ} = G_{ZX} = G_{YZ} = G_{ZY} = G_L$ in the LD and $G_{XY} = G_{YX} = G_T$ in the TD), ν = Poisson's ratio ($\nu_{ZX} = \nu_{ZY} = \nu_L$ in the LD and $\nu_{XY} = \nu_{YX} = \nu_T$ in the TD, $\nu_{XZ} = \nu_{YZ}$ is obtained via the stress and strain tensor symmetry: $\frac{\nu_{XZ}}{E_X} = \frac{\nu_{ZX}}{E_Z}$), YCS/UCS = yield/ultimate compressive stress, YTS/UTS = yield/ultimate tensile stress, YSS/USS = yield/ultimate shear stress, ρ = bone mineral density, p = bone porosity. For papers differentiating radial and circumferential direction in the transverse plane, the mean of both values are taken as transverse value.

Mechanical Properties	**Vertebral body (cancellous bone)**		**Cortical bone**	
	TD	**LD**	**TD**	**LD**
E [GPa]	0.04725±0.028[68] 0.14[71]	*3.78 [72]* 0.352±0.145[73] 0.2[71] 0.165±72.3[68] 0.176±0.103[74]	10.1±2.4[75] 6.15±2.6 [67] 9.55±1.36[76] 10.1±1.6[77] 11.3[71]	17.9±3.9[75] 18.16±1.88[78] 14.64 [72] 16.61±1.83[76] 19±1[77] 22[71]
G [GPa]	0.0483[71]	0.0483[71]	3.28±0.5[76] 3.8[71]	6.07±570[78] 4.74±0.65[76] 5.4[71]
$\boldsymbol{\nu}$	0.315[71]	0.203[71]	0.45±0.173[75] 0.484[71]	0.4±0.157[75] 0.37±0.03[76] 0.203[71]
YCS [MPa]		4.5±2.5 [74]	42.3±20.1[67]	115±16.36[78] 157[77]
UCS[MPa]		2.37±1.14[73] 5.3±2.4 [74]	131±20.7[75] 64.1±19.7[67]	205±17.3[75] 153.59±21.63[78] 136[77]
YTS[MPa]			52.5±6.3[79]	71.56±10.19[78] 114[77]
UTS [MPa]			53±10.7[75]	135±15.6[75] 92.95±10.07[78] 128 [77]
YSS [MPa]				40.95±5.16[67]
USS[MPa]				65±4.0[75] 46.31±5.82[78]
$\boldsymbol{\rho}[\frac{g}{cm^3}]$	0.162±0.035 (lumbar) [80]		0.907±0.047 (tibia) [80] 0.472±0.035 (femur) [80] 1±0.12 [81] 0.917±0.09 (tibia) [82]	
p [%]			6.8 [83] 9.3 (range: 2.4-40) [81]	

base [84]. The three forces are compression/decompression (or tension), posterior/anterior shear forces and left/right lateral shear forces (Figure 4.4). The three moments are: flexion/extension moment, left/right bending moment due to left/right lateral bending and left/right torsional moment due to left/right axial rotation (Figure 4.4). Different motions can lead to the same stress type in a same or different region, but with different amplitudes [71].

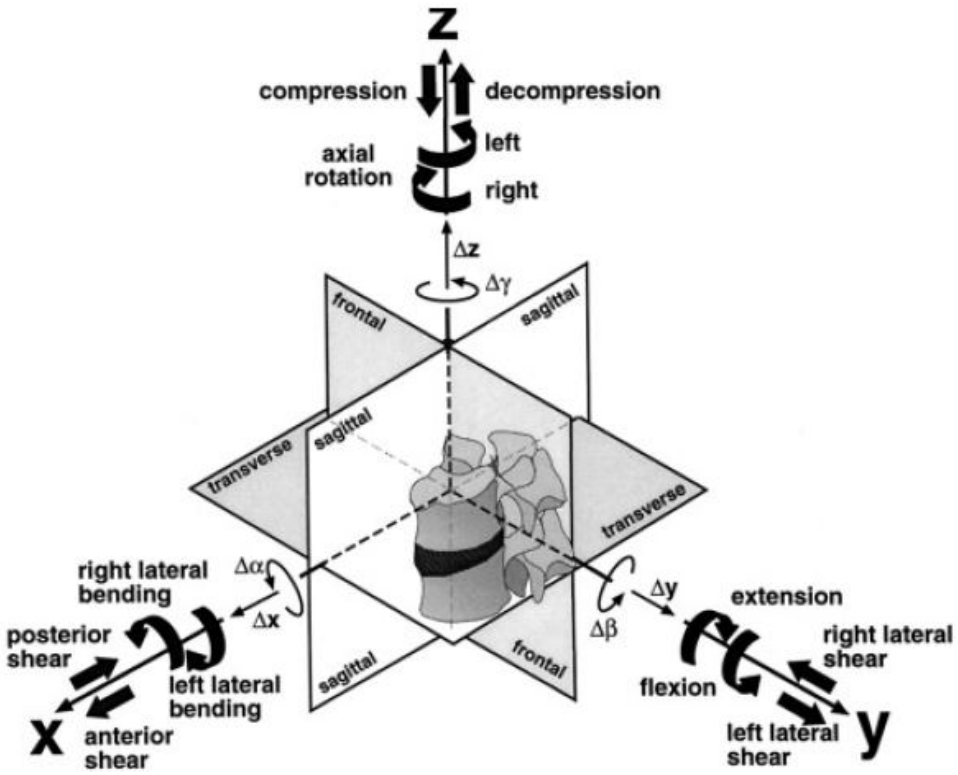

Figure 4.4: Intervertebral disc forces (compression and decompression (or tension) along O_z, posterior and anterior shear stress along O_x, right and left lateral shear stresses along O_y) and torques (left and right lateral rotation around O_z, left and right lateral bending around O_x and flexion and extension around O_y). The arrows of the motion components $\Delta\alpha, \Delta\beta, \Delta\gamma, \Delta x, \Delta y$ and Δz represent the positive directions [85].

As the vertebrae are stiffer than the discs, most stress is applied on the intervertebral disc [84]. However, due to the biological limits, the intervertebral forces and moments are not yet easily measured *in vivo* and even difficult to measure directly *in vitro* [86]. Therefore, respective consequent effects are measured instead. For instance:

- The compressive and tensile forces are usually evaluated via the axial force (compression or tension) or the intradiscal pressure (IDP) [71]. However, each one can be deduced from the other via:
$$IDP = \frac{Force}{Surface}$$
- The shear forces (antero-posterior and lateral) are usually evaluated via the postero-anterior (PA) or the resultant shear force (vector summation of the PA and lateral shear forces).

- The flexion/extension and bending moments are directly measured as moments or indirectly measured as a combination of compression and tension at key locations[87]
- The torsional moment is evaluated via the torsional moment or as shear forces at key locations [88]

However, due to the patient-specific cage and the uncertainty about the force(s) localization and magnitude, which depends on the patient's anatomy and activity, it may be safer to consider that the force is applied on the whole cage with its largest amplitude. Another reason is that the contact surface is neither ensured to cover the whole superior and inferior surfaces of the cage, nor to be continuous. So, by considering the maximal force over the entire contact faces, it is ensured that the cage can withstand this force wherever it is. As a result, Table 4.3 presents meaningful forces and moments applied on the intervertebral disc. Since lateral bending produces a combination of compression and tension, which are always inferior to the one produced by flexion or extension [71, 87, 89], these are not given.

It is commonly assumed and proven that the activity requiring the most compressive and tensile force and flexion moment is lifting a weight [86, 90, 91]. Therefore, only values corresponding to this activity and standing alone (as reference) are reported in Table 4.3. As for the mechanical properties, the values reported in the literature vary a lot, due to the same reasons on top of the subject activity and anatomy, sex and age.

Please note that, even if some are based on biological *in vivo* measures, models are always necessary to evaluate the force since these are rarely directly measured. For instance, if the muscle activity is recorded via an electromyography (EMG), a model is necessary to compute the developed force. Afterwards, to compute the total force or moment, the forces from different muscles cannot be simply summed. Indeed, this would assume that muscles are independent,i.e. that they independently work and that each work contributes to one moment only. This is anatomically unrealistic and could lead to a 22% error in regard to the evaluation of the compressive force [92]. To compute the total forces and moments, a three-dimensional model is usually required. However, such method differs from a three-dimensional FEM, which is not based on biological measure, but rather on tissues mechanical and geometrical properties with simulated loads [91, 93].

4.2 Design process

4.2.1 Design objectives

The design objectives, presented in the objective tree (Figure 4.5), are based on five questions:

- What device(s) must be produced?
- Who will use the device(s)?
- When will the device(s) be used ?
- How will the device(s) be used?
- Where will the device(s) be used?

The cortical bone is provided and shaped by the tissue bank. This shaping induces design and time constraints, i.e. the use of a 2mm diameter round bur and a production time of several hours. So, even if the dimensions can vary according to the patient anatomy,

Table 4.3: Intervertebral compressive and shear forces and flexion, bending and torsional moments. If several values are reported according to the patient's motion, only the largest value is reported. Since the torques are supposed to be symmetric for symmetric motions, the torque orientation is not specified. Data from [71] are based on a 7.5Nm moment for each motion. Data from [97] are obtained via few different models providing different values, but only the mean value for each activity according to each method is reported here [97]. IDP from [86] are converted to forces using the provided 18cm^2 disc surface.

Forces and moments	**Intervertebral disc**	
	L4-L5	**L5-S1**
Compression force [N]	194.44^{F}[71]* 984 [91]* 900 [94] 1980^{F} [94] 2385^{F} [95] 2160^{13} [94] 2020^{14} [96] 3770^{1} [91]* 4706.1^{3} [97]*	600 [86] 4140^{1} [86, 98] 3683^{1} [91]* 3778.6^{3} [97]*
Posterio-anterior shear force [N]	-44 [91]* -439^{1} [91]* 518^{4} [97]* 548.5^{5} [97]*	331 [91]* 1020^{1} [91]* 718.5^{5} [97]* 1478^{3} [97]*
Resultant shear force [N]	39.7 ^{B}[71]* 86 [99] 44.7^{B+E}[71]*	
Flexion moment [Nm]	-1.4 [91]* -3.25^{1} [91]* 217^{12}[92]	-1.2 [91]* -2.12^{1} [91]* 2.56^{2} [86] 197^{6}[93] 62.9^{6} [100] 360^{8}[101] 325^{9}[102] 139^{10}[103] 217^{11}[104]
Bending moment [Nm]	83^{6} [93] 114^{12}[92]	63.3^{6} [100] 240^{8}[101] 50^{9}[102] 54^{10}[103] 35^{11}[104]
Torsional moment [Nm]	36^{6} [93] 54^{12}[92]	9.1^{6} [100]* 70^{8}[101] 100^{9}[102] 37^{10}[103] 33^{11}[104]

^{F} pure forward symmetric flexion without load [71].
^{B} pure lateral bending without load [71].
$^{B+E}$ lateral flexion combined with extension without load [91].
^{1} maximal value for asymmetric lifting of a 19.8kg load at different distances from chest [91].
^{2} jumping on a trampoline [86].
^{3} 70° flexion and 20° rightward bending, holding 19.8kg at 38cm anterior and 47cm right to L5-S1 [97].
^{4} 70° symmetric flexion while holding a 19.8kg load at 32 cm anterior to L5-S1 [97].
^{5} 70° symmetric flexion while holding a 19.8kg load at 38 cm anterior and 47 cm right to L5-S1 [97].
^{6} when lifting a 4.54kg load from a table of 0.967m height [100].
^{7} asymmetric lifting of a 90N load [93].
^{8} symmetric lifting of a 292N load [101].
^{9} asymmetric lifting of a 392N load [101].
^{10} asymmetric lower lifting of a 114N load [102].
^{11} asymmetric lifting of a 114N load [104].
^{12} maximal values for various range of task with and without load [92].
^{13} climbing stairs, two stairs at a time [94].
^{13} Standing up [96].
Nothing precised means standing straight without load, as reference for comparison.
* data obtained via FEM.

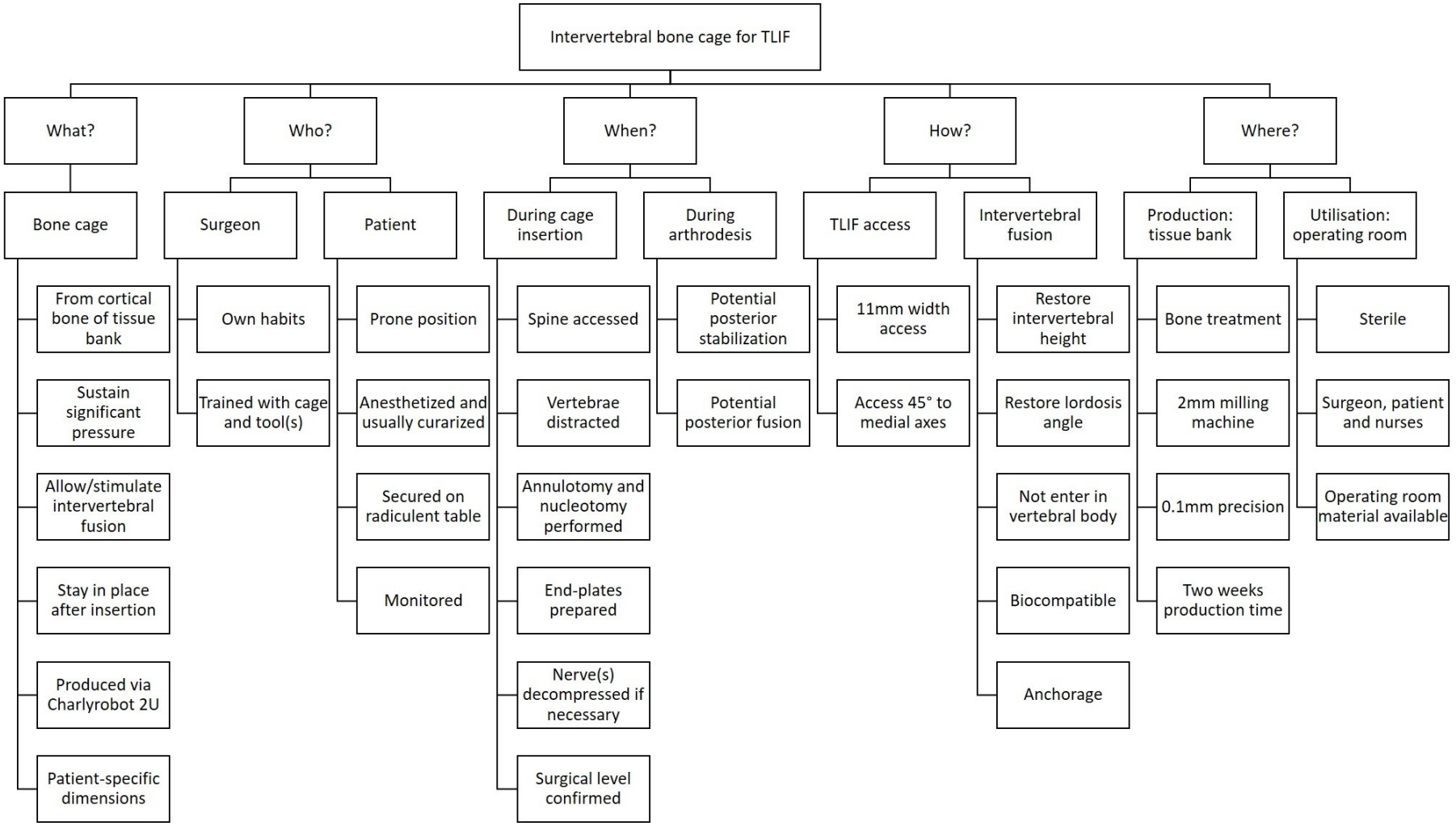

Figure 4.5: Objective tree for the cage (what?). The two main actors are the patient and the surgeon, even if other member of the medical staff can be present (who?). The cage is inserted during a TLIF, but one may distinguish the factors of the cage insertion itself and the factors of the arthrodesis independent from the approach (what?). The TLIF is characterized by its access and its result, i.e the intervertebral fusion (how?). The TLIF is used in an operating room but produced in the tissue bank of the hospital (where?).

it is impossible to produce the cage during the operation. Also, TLIF induces dimensional and mechanical requirements, such as a limited size and the ability to sustain significant pressure. On top to the limited tunnel access, the cage should not move once inserted. Also, the intervertebral fusion comprises two phenomena: the osteointegration of the cage and the bone remodelling around and through the cage. From the user point of view, the (trained) surgeon chooses the access side and might choose to add a posterior stabilization or fusion or both. From the patient's point of view, the intervertebral space and the patient are fully prepared for the implementation of the cage.

4.2.2 Design functions

The functions are classified as main functions (MF) or constraint functions (CF), which are respectively the actions and the environment adaptation of the cage. The functions of the cage are directly deduced from the defined objectives. Each function has its subsequent criteria to evaluate whether the function has been fulfilled (Table 4.4).

Regarding the dimensions, restoring of the intervertebral height and the lordosis angle define the cage height and potential slope (MF2), knowing that these can vary according to the patient anatomy (CF9). Then, the cage length and width are set by the TLIF access, which is 11mm wide and at 45° to the medial axis within the disc nucleus (CF6). The shape of the cage is determined by its final placement for a TLIF, i.e. in contact with the anterior facet of the annulus (CF6).

Regarding the design of the cage, it should avoid to damage surrounding tissues, so sharp edges should be avoided. However, an anchorage might be useful to avoid the cage to move once inserted (MF4). Also, the cage should be able to sustain the intervertebral stresses (MF1) while not penetrating the adjacent vertebrae (CF10). The design should consider the dimensional restriction due to the production (CF8).

As the cage is made of bone, the cage is naturally biocompatible (CF7) and allows osteointegration and bone remodelling but stimulating it can still be taken into consideration (MF3). Also, some markers are required to distinguish the cage from vertebral bone when checking the cage position thanks to medical imaging (MF5).

4.2.3 Design requirements

Based on both user and literature inputs, requirements regarding the cage dimensions and mechanical properties are defined.

4.2.3.1 Dimensions

Based on both user, literature and clinical inputs (Table 4.1), it has been chosen to provide cages of 10mm width to have 1mm margin, with three different lengths (24, 28 and 32mm), five different heights (7,8,9,10,11 and 12mm) and three different angles (0,5 and 10°) (Table 4.5). Consequently, $3 * 5 * 3 = 45$ different cage sizes are provided.

Also, in order to put the cage in contact with the anterior facet of the disc annulus (justification below), the anterior face of the cage should be rounded. To check the feasibility of this contact, the nucleus is assumed to be an ellipse with a semi-major axis a =17.8mm and semi-minor axis b = 17.8 (Figure 4.6) [58]. Consequently, with a width of 10mm, the other facet would be at $y = 17.8 - 10 = 7.8mm$. Based on the elliptic equation

Table 4.4: Cage main functions (MF) and constraint functions (CF) with their criteria to check if the function is fulfilled.

Function type	**Function**	**Function criteria**
Main	MF1: Sustain intervertebral stresses	1.1: No failure 1.2: No permanent deformation
	MF2: Restore disc height and lordosis angle	2.1: Maintain intervertebral vertical separation 2.2: Maintain the intervertebral lordosis angle
	MF3: Allow or facilitate intervertebral fusion	3.1: Allow or stimulate bone remodelling 3.2: Allow or stimulate osteointegration
	MF4: Stay in place after implementation	4.1: Minimal movement after implementation
	MF5: Post-operative check via CT	5.1: Position observable via CT
Constraint	CF6: Inserted via a TLIF access	6.1: 11mm wide access 6.2: access at 45° to the medial 6.3: paced in contact with teh anterior facet of the annulus
	CF7: Biocompatible	7.1: No immune reaction or rejection
	CF8: Produced by Charlyrobot 2U on bone graft	8.1: 0.1mm tolerance 8.2: 1mm outside margin for production 8.3: Produced from available bone grafts 8.4: Produced using a round bur of 1mm diameter
	CF9: Patient specific dimensions	9.1: Propose different dimensions for height, lordosis angle and length
	CF10: Does not penetrate vertebrae	10.1: Elastic properties close to cancellous bone

Table 4.5: Dimensions of the cages based on literature, user and clinical inputs (Table 4.1).

Cage length [mm]	**Cage height [mm]**	**Cage width [mm]**	**Cage (wedge) angle [°]**
24;28;32	7:1:12	10	0;5;10

$\frac{x^2}{a^2} + \frac{y^2}{b^2} = 1$, for $y = 7.8mm$, $x = \sqrt{[1 - \frac{7.8^2}{17.8^2}] * 25.7^2} = 23.1mm$. As the length of the cage has to be inferior or equal to $2x = 46.2$, the contact can always be achieved with cages up to 32mm long.

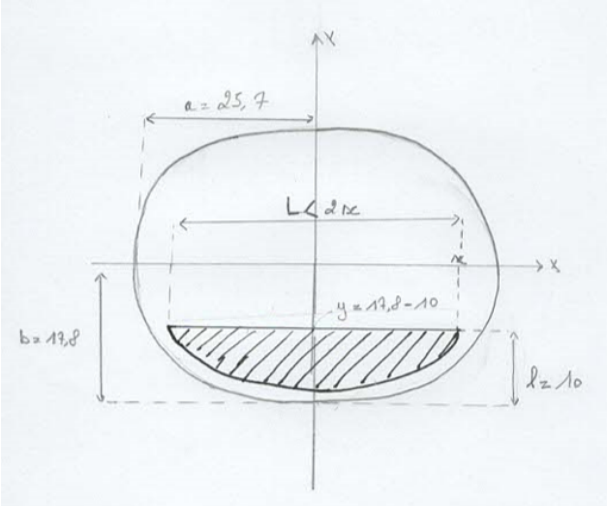

Figure 4.6: Elliptic approximation of the disc nucleus with a semi-major axis a=25.7mm and a semi-minor axis b=17.8mm and the cage inside contacting the anterior facet.

Also, the feasibility of each design is checked. Indeed, for the largest angle of 10°, which means a slope of 5° for the superior and inferior surfaces, the decrease of height is $10 * tan(5) \approx 0.87mm$ per surface, so a total decrease of 1.74mm between the anterior and posterior face. For the smallest cage height of 7mm, the means a posterior height of 5.26.

On top of that, the cage should have a grasping surface or anchorage system to avoid slipping (MF4) and markers (MF5) [25, 27, 52, 23]. Indeed, the annulus is mechanically weaker due to the annulotomy. So, its ability to constrain the cage without breaking, such that the cage would not move forward or laterally, is not fully reliable and an anchorage is required. To sum up, the dimensional requirements are:

- 24; 28; 32mm length
- 7; 8; 9; 10; 11; 12mm height
- 11mm width
- 0; 5; 10° wedge angle
- Rounded anterior face
- Grasping surface or anchorage system
- Space(s) for CT marker

4.2.3.2 Mechanical properties

According to the MF1, the cage must be able to sustain the same loads as the surrounded vertebrae. While sustaining these loads, the cage has to maintain an elastic behaviour, such that it goes back to its original shape after loading. Also, as specified by the CF10, the cage rigidity has to be close to the one of the adjacent elements, i.e. from the one of vertebral body (cancellous bone).

The material According to Table 4.2, the bone properties of the vertebral body and cortical bone vary considerably in the literature, most probably due to the difference in environment, measurement technique, boundary condition and stimulus intensity and rate. However, PEEK cage might be used as reference. PEEK has a Young modulus of 3.84MPa that is close to the one of cancellous bone [32, 72]. As a result, PEEK cage seems to have an appropriate stiffness such that it does not insert into the vertebral cancellous bone [32, 72]. Unfortunately, cortical bone is significantly stiffer than PEEK (Table 4.2). Intuitively, it means that, for a same design, a cage made of cortical bone will be stiffer than one made of PEEK.

However, cage stiffness is a result of both material properties and cage design. So, the cage stiffness has to be decreased. To do so, the cage porosity can be increased since porosity is the main factor affecting the Young modulus of bone [39], and therefore the stiffness of the cage. The goal would be to obtain a cage stiffness similar to the stiffness of the vertebral body. To compute to what extend the porosity has to be increased, the unit cell model can be used.

Loads The cage has to be able to sustain the same loads as the intervertebral disc. In practice, this is a highly safe criteria since the annulus, even if cut and consequently mechanically weaker, will partially sustain the intervertebral stress. Also, even if this should not be considered, an interbody fusion often uses a posterior stabilization.

Due to the numerous types of loads that are applied on an intervertebral lumbar disc, numerous tests could be simulated such as tensile, compressive, shear, flexion, bending or torsion tests. The flexion (and extension), bending and torsion moments can be approximated by their consequent compressive and shear forces, because of the cage position and dimensions. Since the cage is placed in the anterior part of the disc and its antero-posterior width is small (10mm), the moments lead to mostly homogeneous forces in the antero-posterior direction. This is not valid in the lateral direction except for the flexion (and extensions), which by definition lead to homogeneous forces laterally. Indeed, due to the cage length (24 to 32mm), the bending and torsion moments lead to considerably different forces on the cage surface according to the lateral location. Unfortunately, no measurement of the bending moment during daily static or dynamic activities were found. However, the bending moment and its corresponding lever can be compared to the flexion moment and its lever for other activities. Looking to activities 8,9,10 and 11 of Table 4.3, the ratios of the moments $\frac{M^{bending}}{M^{flexion}}$ can be computed as respectively $\frac{240}{360} = 0.6666$, $\frac{50}{325} = 0.1538$, $\frac{54}{139} = 0.3884$ and $\frac{35}{217} = 0.1619$. This provides an average of $0.2207 = 22.07\%$. Knowing that the data used to obtain the values in Table 4.1 give on average a lever ratio $\frac{d^{bending}}{d^{flexion}} = 1.69$, one can compute:

$$
\begin{aligned}
F^{bending} &= M^{bending} * d^{bending} \\
F^{bending} &= (0.2207 * M^{compression}) * (1.6296 * d^{compression}) \\
F^{bending} &= 0.3596 * \underbrace{M^{compression} * d^{compression}}_{F^{compression}} \\
F^{bending} &= 0.3596 * F^{compression}
\end{aligned}
$$

Consequently, the forces of the bending moment represent only about 35% of the forces from the flexion moment for similar activities. Of course, this would not be the case for pure bending activities. Anyhow, this is not common in daily life and forbidden before the

fusion is completed. As a result, neither the bending moment nor its consequent forces have to be simulated as the compression forces applied during flexion are superior and more common. So, it seems reasonable to only conduct shear and compressive forces tests based on flexion and torsion. However, the shear forces magnitude varies significantly into literature and according to the task (Table 4.1). The maximal shear force without weight is the postero-anterior shear force at the L5-S1 level of 331N. This is significantly smaller than compressive forces, confirming the intuition that compression would be the main force component on intervertebral disc, and that shear forces should not be used as design requirement.

Before osteointegration, the cage is not attached to the vertebrae and so can not be subject to tensile forces. Once the osteointegration started, the cage can be subject to some tensile forces. To test such a situation, it would require simulating the cage osteointegration or to perform mechanical tests with the cage between two vertebrae, all in a bioreactor. Since none of these options are the subject of this thesis, this will not be done. However, such simulations or tests may be useful to study the design effect on the cage behaviour under tension and its influence on the osteointegration (see section 7.2). So, only compression test will be considered in this thesis.

To sum up, the mechanical requirements are:

- The cage stiffness in the direction of the load has to be as close as possible to the one of cancellous bone in this same direction ($7.8\frac{kN}{mm}$ for compression).
- The maximal stress within the cage has to be inferior to its yield limit when sustaining an axial compression of 3.1kN.

4.2.4 Possible solutions

4.2.4.1 Individual solutions

Table 4.6 presents potential solutions for each function of Table 4.4. A solution is referred to as "Sol- Function Number.Solution Number". For example, solution 2 of MF1 is referred as Sol1.2.

The solutions for MF1 illustrate that the cage can be a polyhedron, for instance based on a circle or rectangle for Sol1.1 and Sol1.2 respectively. This polyhedron can be solid or porous (Sol1.4). The porosity can be achieved using one big pore or few small pores, which can be in any direction. Also, the cage can be formed by two plates, bonded by beams with whichever shape (with cylindrical shape for Sol1.3). However, Sol1.3 is excluded since our production is a top-down approach. It starts from a piece of bone that will be shaped, making such a design difficult to produce. So, the cage is designed via an extrusion of an arbitrary base, with pore(s) or not depending on other functions.

The Sol2.1 and Sol2.2 show that the superior and inferior surfaces can be flat or convex, depending on whether the intervertebral space is assumed to be flat or convex. It is chosen to use flat surfaces because the convexity is not well-documented and can vary according to the patient. Also, Sol2.1 and Sol2.2 show that, theoretically, the cage can be as wide as the disc nucleus (see CF6 why it will not). Sol2.3 proposes to insert two cages, but this possibility is excluded because of the preferences of the surgeon and the consequently increase of the operation time. Sol2.4 and Sol2.5 propose to place the cage either in contact with the anterior facet of the annulus, or in another location. Sol2.4 is chosen, because

Table 4.6: Morphological chart of the cage presenting potential individual solutions for each cage function.

Functions	**Solutions** 1	2	3	4	5
MF1[1]		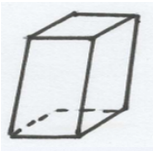	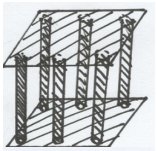	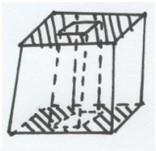	
MF2[2]	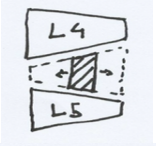		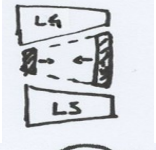	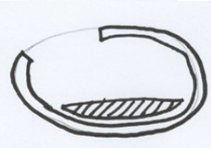	
MF3[3]	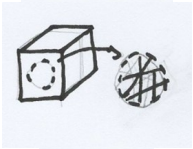	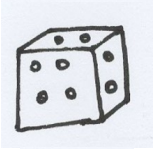	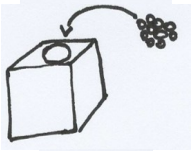		
MF4[4]	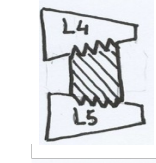	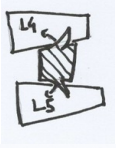	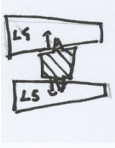		
MF5[5]	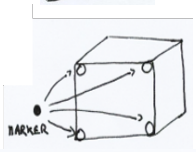	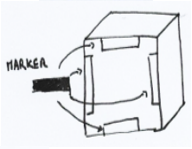	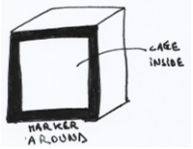		
CF6[6]	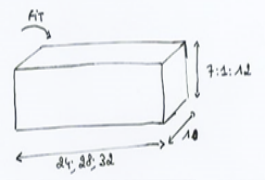				
CF7[7]	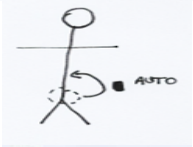				
CF8[8]	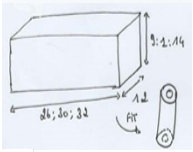	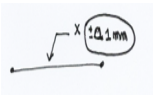			
CF9[9]	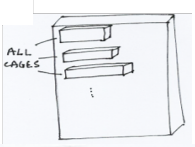	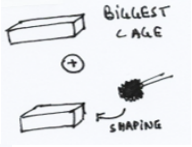			
CF10[10]	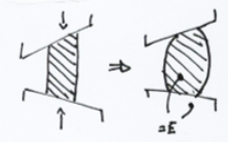				

[1] Sustain intervertebral forces
[2] Restore disc height and lordosis angle
[3] Allow or facilitate intervertebral fusion
[4] Stay in place after implementation
[5] Post-operative check via CT
[6] Respect required dimensions
[7] Biocompatible
[8] Produced by Charlyrobot 2U
[9] Patient specific dimensions
[10] Does not insert into the vertebrae

it is advised by the user, since the instability is mostly anterior (the posterior stability is ensured by the facets of the vertebrae) and because the larger compressive forces are applied anteriorly, as the lever of the moment (applied posteriorly) is longer.

MF3 is slightly promoted thanks to the cortical bone porosity, but this is very low (Sol2.1). Therefore, pores can be added to increase the cage porosity and so promote the fusion even more (Sol2.2). Also, Sol3.3 propose to add some bone graft or a substitute (details in subsection 2.3.7). It has been decided to study the possibility to add pores regarding its impact on the cage mechanics. If the cage is porous, the pores could be filled by any material, depending on the surgeon's choice.

MF4 can be fulfilled by adapting the cage surface (Sol4.1) or by adding an anchorage system, such as clips (Sol4.2) or screws (Sol4.3). Any anchorage system would require adding a mechanism, so another material than bone. As the cage is supposed to integrate into the fused vertebrae, Sol4.2 and Sol4.3 are rejected. So, the cage surfacing would be responsible of its fixture.

It is chosen to add discrete markers (Sol5.1) on the cage to be able to visualize it via CT or MRI. This because continuous markers (Sol5.2) and a full marker frame (Sol5.3) would lead to too much imaging artefacts and the addition of non-bioresorbable material. Also, most radioculent cage use discrete markers [25, 27, 52].

Sol6.1 provides the volume in which the cage should fit in regard to CF6 (there is no other solution). Indeed, the cage dimensions were already determined from the inputs (Table 4.5).

To use bone that would minimise the immune response, autograft (Sol7.1), allograft (Sol7.2) or heterograft (Sol7.3) can be used. Autograft is not preferred because it requires an additional operation. Heterograft is considered inferior to allograft, so autograft is chosen. Autograft can be based on fresh-frozen bone, freeze-dried bone or demineralized bone. Demineralized bone is like powder, so can not be used to form a cage. Freeze-dried bone is used as it is the one provided with the tissue bank (details in section 4.1).

Sol8.1 specifies that the implant should be extracted from cortical bone with 1mm margin around. for example, this means that for a cage of 24x10x8mm, a bloc of cortical bone of 26x12x10mm is required. Also, the cage has to be produced with a 1mm diameter round bur and be functional with 0.1mm tolerance on all its measures, as it is the production precision.

CF9 can be fulfilled by providing cages with all the possible dimensions (Sol9.1) or by providing a large cage that can be shaped during the operation according to the anatomy of the patient (Sol9.2). After discussing with the surgeon, it has been decided to use Sol9.1 as shaping the cage during the operation considerably increases the operation time. Also, most of clinically used cages are the same [25, 27, 52]. Sol10.1 shows that the cage stiffness has to be as close as possible to the cancellous bone young modulus, such that the cage deforms under stress and penetrates as less as possible its adjacent vertebrae. This will be done by adapting the porosity of the cage.

4.2.4.2 Combining solutions

The cage is designed as a polyhedron, potentially with pores (Sol1.4) to adjust its mechanical properties (Sol.10.1). These pores can be used to insert material promoting the fusion (Sol3.3) or not (Sol3.2). The base of the polyhedron is defined by Sol2.2 and Sol4.1, and the dimensions by Sol6.1 (Figure 4.7a). The cage is produced based on an allograft (Sol7.1)

with 1mm margin that should fit into the bone graft (Sol8.1) and will be produced with 0.1mm tolerance (Sol8.2). Some spaces will be available to add discrete marker at key locations (Sol5.1).

During patient flexion, the cage tends to move anteriorly. As the cage is placed in contact with the anterior facet, this would put too much pressure on the annulus. Therefore, the superior and inferior anchorages have to allow the cage to move posteriorly, but not anteriorly. On the other hand, the cage could move posteriorly during patient extension. This can happen as there is an empty space posteriorly. Also, the grasping surface has to be producible by the Charlybot 2U. It has been decided to use right-angled triangular grooves, such that the slope blocks anterior motion. The surfacing is 1mm deep and each triangle has a slope of 60°, such that 6 patterns can be repeating among the 10mm wide surface according to the limits of the machining (Figure 4.7b).

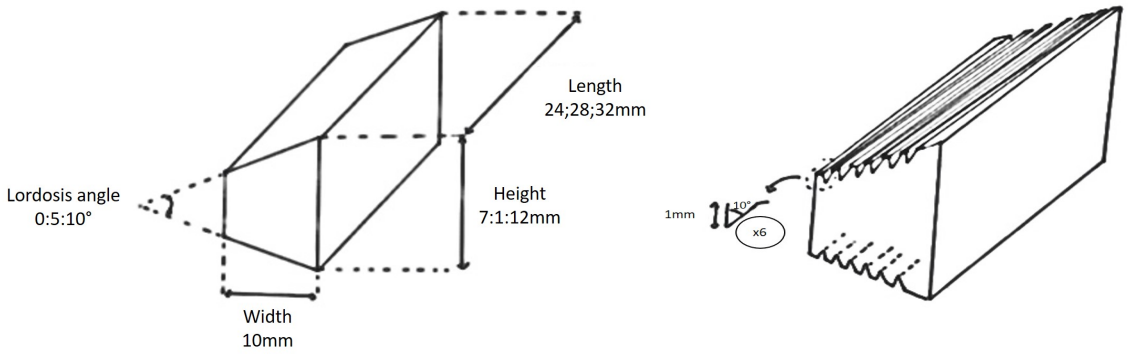

Figure 4.7: Cage primary design design without surfacing but with dimensions (a) and with surfacing (b). The cage can be 24, 28 or 32mm long, 7,8,9,10,11 or 12mm height with a lordosis angle of 0;5 or 10°.

Afterwards, a "coma-shape" is given to the cage such that the cage would have a continuous contact with the anterior face of the disc. The rounding could be achieved using the elliptic approximation of the disc (Figure 4.6). However, this would not be fully reliable regarding the anatomical variability. So, it is arbitrary chosen to round the anterior face using an ellipse centered at the center of the cage and adjacent to its anterior and lateral faces. Eventually, edges that are not part of the surfacing are filleted with a 1mm radius. Also, one lateral face is rounded on 2mm to facilitate the insertion. This is achieved using a tangent arc from the middle of the lateral face to a point on the posterior face which is at 2mm from the lateral face (Figure 4.8). Many values are arbitrary defined here, which is further discussed in section 7.2.

4.2.4.3 Production verification

Unfortunately, the desired surfacing is impossible to produce. The Charlybot 2U only has round burs, the smallest with a diameter of 2mm. Therefore, making triangular grooves on the cage surface is impossible.

Ideally, several surfacings should be studied in term of cage slippage, insertion inside the adjacent vertebrae leading to potential microcracks with their propagation induced in the adjacent vertebrae and the compression of the trabecular bone in the adjacent

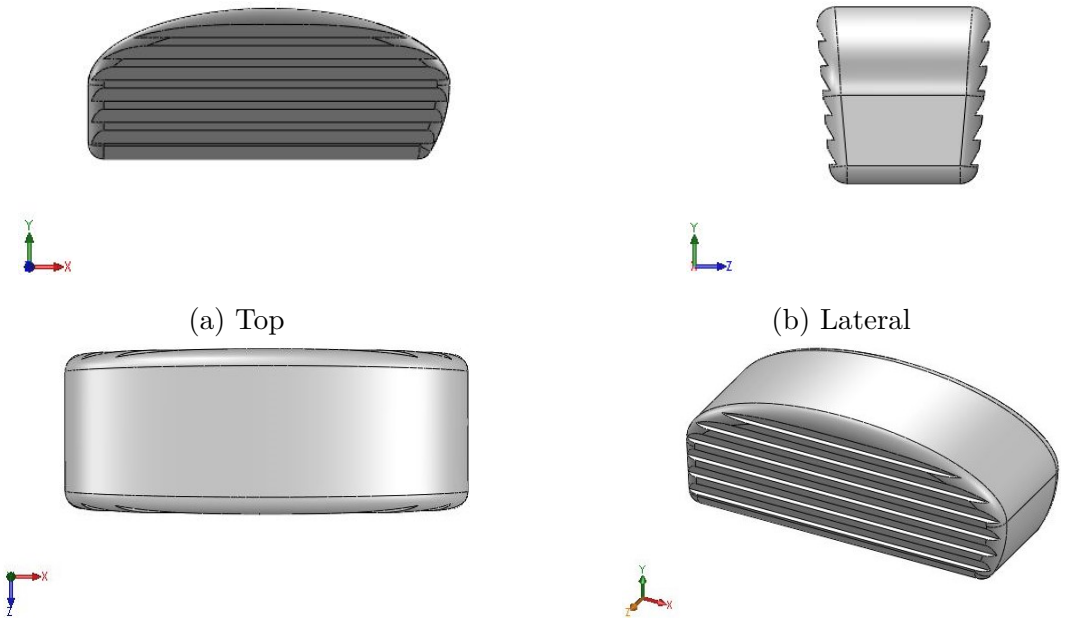

(a) Top (b) Lateral

(c) Frontal (d) Trimetric

Figure 4.8: Cage design without pores after combining solutions. (a) Top view. (b) Lateral view. (c) Frontal view. (d) Trimetric view.

vertebrae and other relevant factors. However, due to restricted time and the lack of access to the labs[2], this could not be done. Consequently, the surfacing is arbitrary defined in this thesis. We selected horizontal and vertical circular grooves on both top and bottom surfaces. These grooves are set to a diameter of 1mm, 0.5mm depth and repeated each 1.5mm. They are made by producing one groove in the middle of the surface in the x and y direction, and then linearly repeated six times in +x and -x direction, and 3 times in the +y and -y direction respectively (Figure 4.9). For the cages of 28mm and 32mm long, the grooves are repeated seven seven and height times respectively.

4.3 Design outputs

The first design output is obtained (Figure 4.10). As mentioned this design might be porous in order to obtain the desired mechanical properties. To facilitate the reading, three directions are defined:

- The longitudinal direction, which corresponds to the axis aligned with the length of the cage (Figure 4.7a), i.e. the bilateral axis
- The frontal direction, which correspond to the axis aligned with the width of the cage (Figure 4.7a), i.e. the antero-posterior axis
- The axial axis, which corresponds to the axis aligned with the height of the cage (Figure 4.7a); i.e; the craniocaudal axis

[2]Due to the lockdown

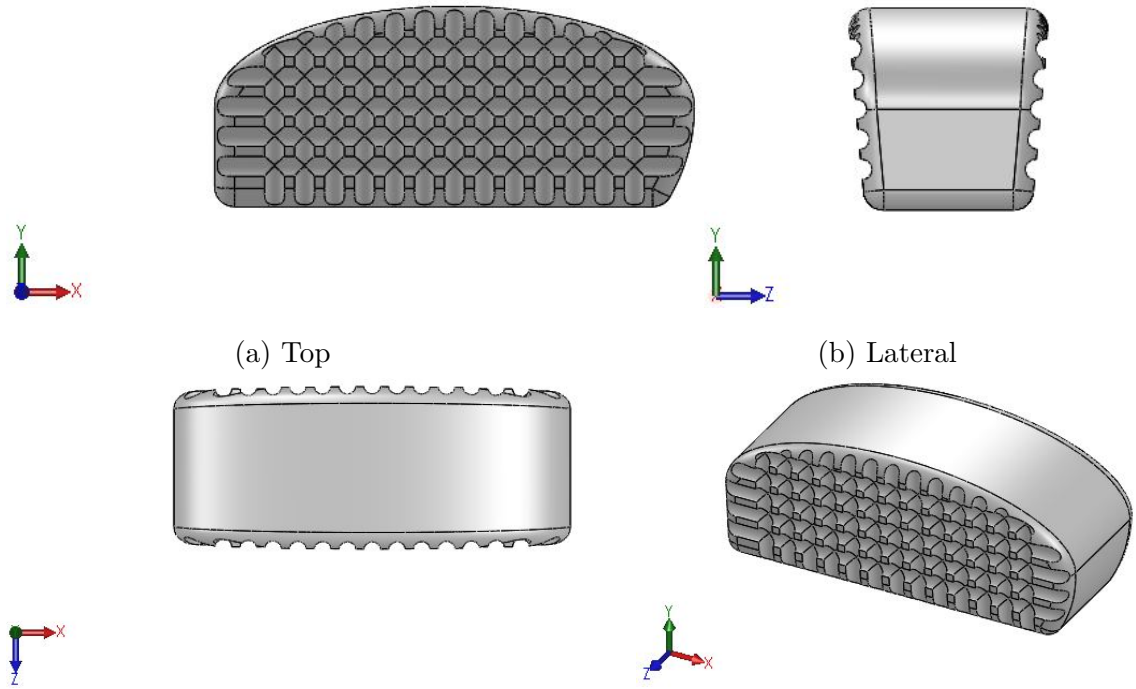

(a) Top (b) Lateral

(c) Frontal (d) Trimetric

Figure 4.9: Cage final design with the corrected surfacing according to production restrictions. (a) Top view. (b) Lateral view. (c) Frontal view. (d) Trimetric view.

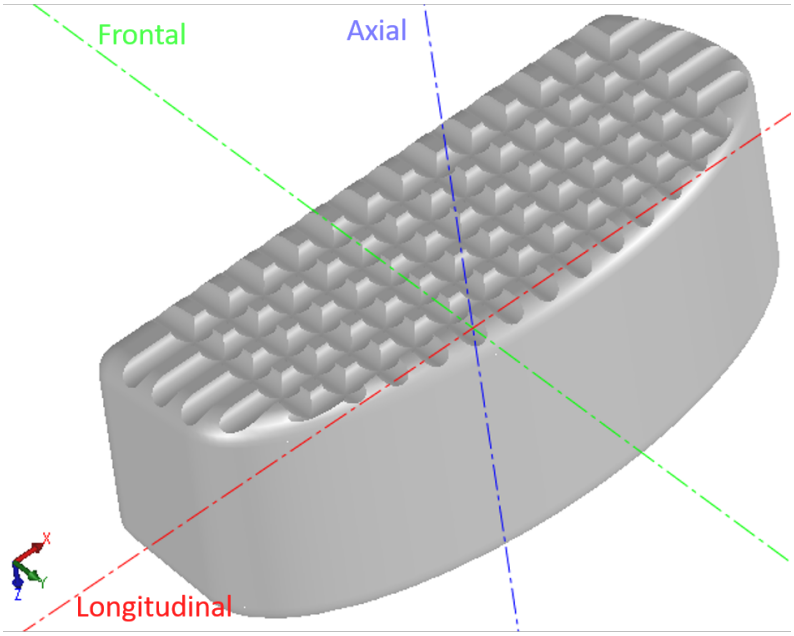

Figure 4.10: Design output: full designs with the axial, frontal and longitudinal direction in order to make pore(s), which can be one big or few small pores.

Chapter 5

Design optimization and validation

5.1 Goals and method

The design should be optimized in order to achieve three goals:

- Avoid permanent deformation of the cage, i.e. the cage has to be only elastically deformed during functioning.
- Avoid stress shielding and cage subsidence, i.e. obtain a cage stiffness as close as possible to the one of the vertebral body

Solidworks (SW) is used to design the models and to simulate the compression.

5.2 Description of the simulations

5.2.1 The cages

5.2.1.1 The designs

Based on the design output (Figure 4.10), an infinite number of different designs exists. Indeed, the direction, size and shape of the pores allow an infinite number of designs to be used in order to achive a desired porosity. So, it is chosen to only use elliptic or circular pore(s) (depending on the design), all in the same direction and, if few pores are used, they are all of the same size. Also, it is decided to use the cage of 24mm and 10mm high, with a lordosis angle of 10° for the simulations. The length of 24mm is chosen as it is the smallest, leading to the smallest inferior and superior surfaces and so to the highest pressure. The height of 10mm is chosen as it is the average one of all the proposed models, and the choice of a cage angle of 10° is justified in section 5.3.

Based on these assumptions, for each pore direction (axial, longitudinal or frontal), two options are possible: making few small pores or one large pore. When making one large pore, the pore is elliptic, and its axes ratio is equal to the ratio of the cage dimensions in its plane. For example, for a large frontal pore, its axis ratio = 2.4 as the cage dimensions in the frontal plane are 24x10mm, so with a ratio of 2.4 (Figure 5.1a). Please note that the large lateral pore is circular as the lateral dimensions are 10x10mm. For the large frontal hole, the extrusion is made in parallel to the superior and inferior facet, such that, in a lateral cut, the thickness between the pore and the superior and inferior surfaces is constant. When few pores are used, these are circular. First, one pore is put in the centre

of its plane. Then, this pore is symmetrically repeated laterally and perpendicularly. The repetitions are linear except for the perpendicular repetition of the frontal and lateral pore, which is a circular repetition around the intersection of the superior and inferior face (Figure 5.1b).

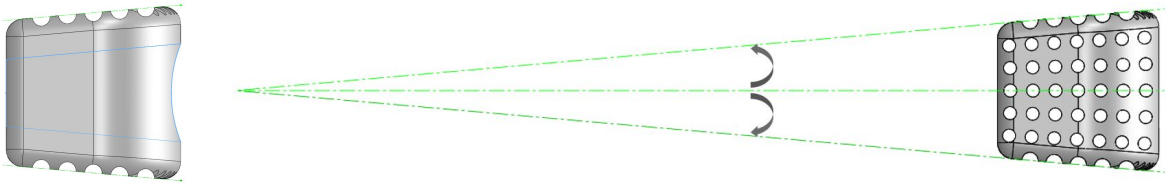

(a) (b)

Figure 5.1: (a): For one large frontal hole, the extrusion (blue) is parallel to the tangent of the superior and inferior faces (green). (b) For few lateral pore , the pore are repeated above and below the central ones using a circular repetition around the intersection of the planes tangent to the superior and inferior faces.

Consequently, seven designs are obtained (Figure 5.2). One corresponding to the full design and six for the porous designs:

- The full design: non-porous design
- The one frontal pore (OFP) design: one large pore in the frontal direction
- The few frontal pore (FFP) design: few pores in the frontal direction
- The one lateral pore (OLP) design: one large pore in the lateral direction
- The few lateral pore (FLP) design: few pores in the lateral direction
- The one axial pore (OAP) design: one large pore in the axial direction
- The few axial pore (FAP) design: few pores in the axial direction

All these designs will be studied for two porosities, a high one and a low one, such that designs can be compared for an equal porosity (or volume fraction) and the same design can be compared with high or low porosity. To determine these porosities, the unit-cell model has been used.

Unit cell model (UCM) Unit cell modelling allows to approximate a solid as a three-dimensional infinite periodic repetition of a single unit, called unit cell. The unit cell can vary and be adapted according to the material, structure, context and studied properties [39]. When using a UCM, it is important to differentiate the network and the material, i.e. the whole porous network and the material of which the porous network is made. If the single unit contains enough relevant features, even if simplifying subsequently the material complexity, the UCM provides useful insight into the mechanical behaviour of porous material [39]. Based on a cubic open-cell structure (Figure 5.3), the UCM provides (demonstration in Appendix E):

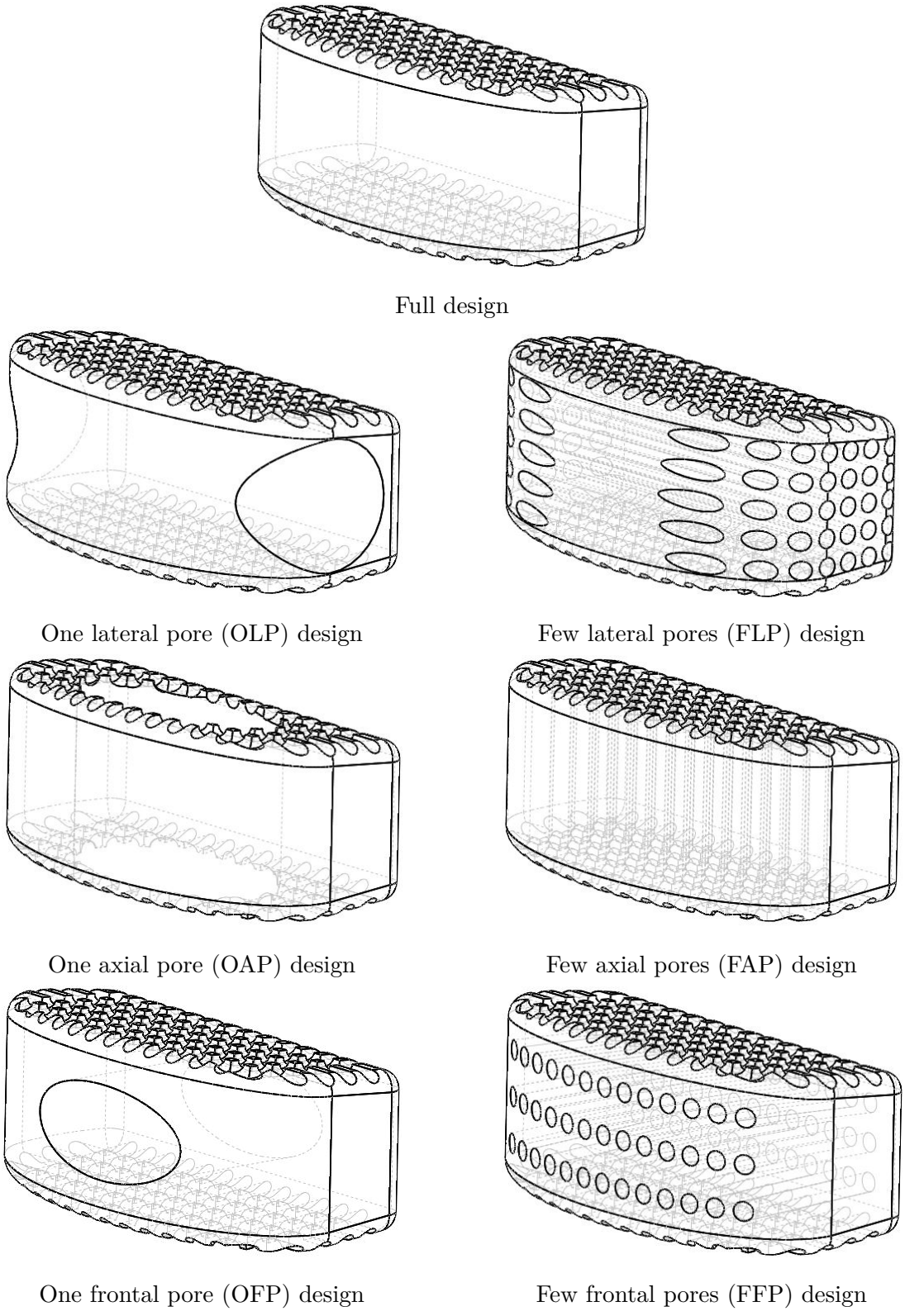

Full design

One lateral pore (OLP) design

Few lateral pores (FLP) design

One axial pore (OAP) design

Few axial pores (FAP) design

One frontal pore (OFP) design

Few frontal pores (FFP) design

Figure 5.2: Cage designs for simulations. Pore(s) can be lateral (medial), axial (supero-inferior) or frontal (postero-anterior). The desired porosity can be obtained via one large hole (one pore) or few small holes (few pores).

$$\frac{E_s}{E^*} = C_1 * (\frac{\rho_s}{\rho^*})^2 \qquad (5.1)$$
$$\frac{\sigma^*}{\sigma_s} = C_2 * (\frac{\rho^*}{\rho_s})^2$$

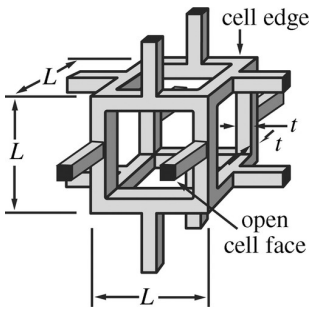

Figure 5.3: cubic open-cell structure [105].

Where

C_1, C_2 = constants (determined experimentally)
E_s = the Young modulus of the material
E^* = the Young modulus of the porous network
ρ_s = the density of the material
ρ^* = the density of the porous network
σ_s = the strength of the material
σ^* = the strength of the porous network

Such that:

$$\frac{\rho^*}{\rho_s} = V_f$$

Where V_f if the volume fraction, i.e. the ratio of solid volume on empty volume. V_f can be used to compute the porosity via:

$$p = 1 - V_f$$

For porous bone, as it is expected that $E^* = E_s$ and $\sigma^* = \sigma_s$ when $\rho^* = \rho_s$, $C_1, C_2 \approx 1$ [105]. This speculation is confirmed both by experiments and numerical simulations [105]. As the goal is to adapt the cage stiffness rather than the Young modulus of a material, Eq. 5.1 is adapted to relate the relative stiffness $\frac{k^*}{k_s}$ of the cage and its volume fraction $\frac{\rho^*}{\rho_s}$ via:

$$\frac{k^*}{k_s} = C_1 * (\frac{\rho^*}{\rho_s})^2 \qquad (5.2)$$

Due to this adaptation of Eq. 5.1, the constant C_1 will be numerically computed. Then, Eq. 5.2 will be used to define the porosity of the cage(s) using both viscoelastic and anisotropic linear models, but only with forces on the whole superior surface (the force localization is justified below).

5.2.1.2 The mesh

The mesh consists of standard equilateral triangle element of 0.6mm side length with a 0.03mm tolerance, as it is the most refined mesh allowed by SolidWorks. The mesh is produced using the automatic transition, which consists of a refining of the mesh for small features, details, holes, and fillets (example for full design: Figure 5.4) [106]. Please note that, for the FLH design, the triangles of the mesh ware increased to triangles of 0.8mm side length with a 0.04mm tolerance, as SolidWorks did not allow to use smaller triangles for this specific design.

5.2.2 The models of the material

To simulate the cage behaviour, the cortical bone material has to be implemented. Bone is an anisotropic viscoelastic material. It exhibits both elastic and viscous behaviour when

Figure 5.4: Mesh for the full design, using equilateral triangle element of 0.6mm side length with a 0.03mm tolerance, and the automatic transition.

undergoing deformation. Indeed, on top of its well-known elastic behaviour, it has the ability to dissipate mechanical energy due to viscous effects, meaning that the stress is strain-dependent [107, 108]. However, the simulation add-in integrated in SolidWorks (SW) allows to implement a material that can be anisotropic linear (elastic) or isotropic viscoelastic (non-linear), but not anisotropic viscoelastic. Therefore, it has been chosen to implement both anisotropic linear and isotropic viscoelastic material.

5.2.2.1 The viscoelastic models

The viscoelastic model uses the viscoelastic properties of bone, with either the properties in the fibers direction or the ones in the transverse direction. A viscoelastic behaviour can be seen as a combination of both elastic and viscous behaviour, respectively modelled as a spring and a dashpot in viscoelastic models. To describe viscoelastic deformations, they are two functions of the material. The creep function, which is defined as the strain variation under constant stress (creep behaviour, Figure 5.5a) and the relaxation function, which is defined as the stress relaxation of the material under constant strain (called relaxation behaviour, Figure 5.5b), both followed by their recovery phase once the stimulus removed (Figure 5.5). The creep behaviour is the tendency to move slowly when a force is applied or to deform permanently over time without the application of a force. The relaxation behaviour is due to an heterogeneous relaxation of fibers in the material [107].

The relaxation is modelled as stress relaxation over several segments under constant strain. To do so, it is commonly assumed that the generalized Maxwell model (Figure E.2), also called Maxwell–Wiechert model, is the most general model for linear viscoelasticity and the best compromise between accuracy and efficiency [110]. Regarding modelling of the creep behaviour, a generalized Kelvin model is suggested [77]. However, both relaxation and creep functions are linked by a well-known relationship. Indeed, one may focus on the generalized Maxwell model to obtain the relaxation functions and compute the creep function based on the generalized Kelvin model afterwards.

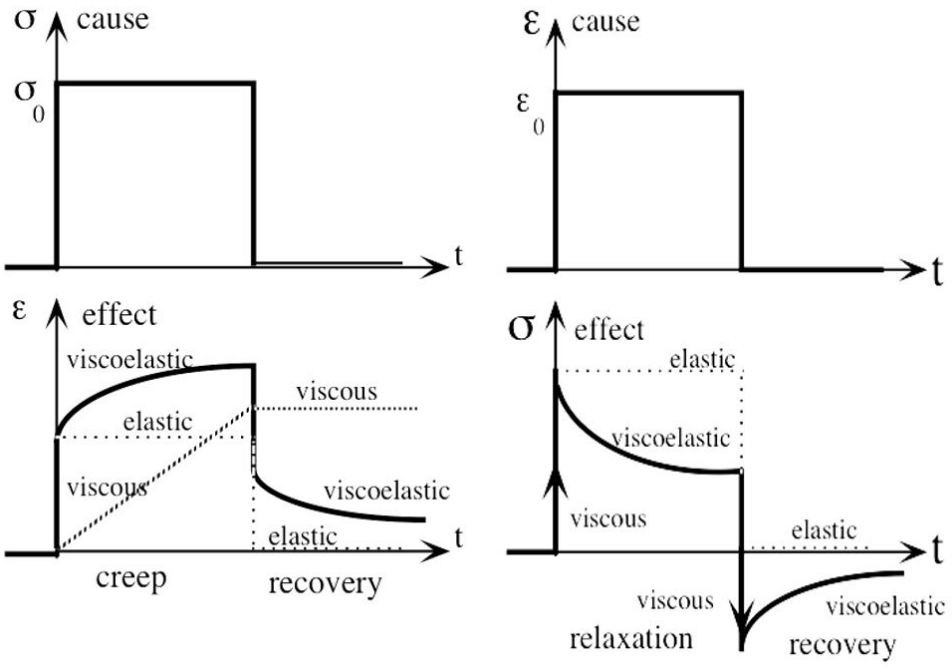

(a) (b)

Figure 5.5: (a) Creep function in response to a step of stress. (b) Relaxation function in response to a step of strain. Dotted lines represent the elastic and viscous (adapted from [109]).

Generalized Maxwell model for stress relaxation To model stress relaxation, the generalized Maxwell model uses as many spring-dashpot Maxwell elements as necessary in parallel to one spring such that the model behaves as the material under investigation [110]. Using a linear viscoelastic model to simulate bone viscoelasticity is a reasonable assumption, since linear elasticity is usually applied for small deformation, which is the case of bone deformation [107].

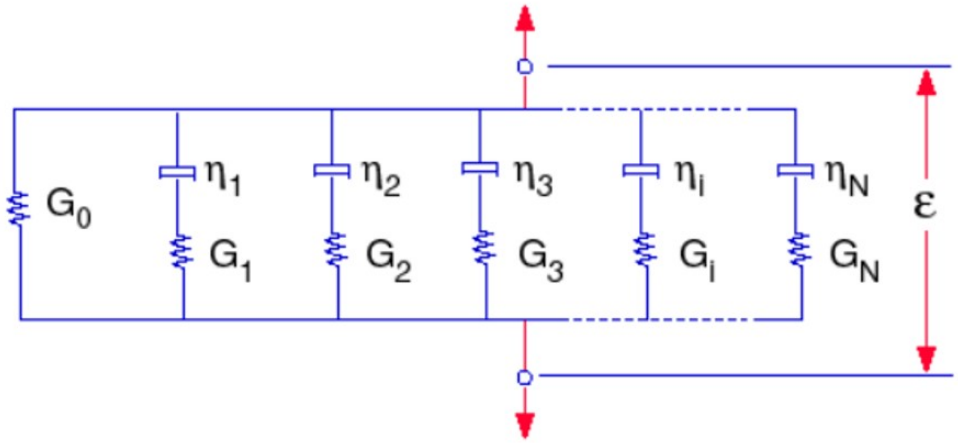

Figure 5.6: Generalized Maxwell model for material shear modulus G with one spring and N spring-dashpot Maxwell models in parallel and a global system strain ϵ [108].

Based on the model circuit (Figure E.2), the shear and bulk moduli of the material over time, i.e. the moduli relaxation, can be expressed via Prony series as (demonstration in Appendix E):

$$G(t) = G_0[1 - \sum_{i=1}^{n} g_i(1 - e^{\frac{-t}{\tau_i^g}})] \tag{5.3}$$

$$K(t) = K_0[1 - \sum_{i=1}^{n} k_i(1 - e^{\frac{-t}{\tau_i^k}})] \tag{5.4}$$

Where
- $G(t)$ = The shear relaxation function $[\frac{N}{m}]$
- G_0 = The initial shear modulus $[\frac{N}{m}]$
- G_i = The shear modulus of element i $[\frac{N}{m}]$
- $g_i = \frac{G_i}{G_0}$ = The ith shear relaxation modulus
- τ_i^g = The ith shear time constant [s]
- $K(t)$ = The bulk relaxation function $[\frac{N}{m}]$
- K_0 = The initial bulk modulus $[\frac{N}{m}]$
- K_i = The bulk modulus of element i $[\frac{N}{m}]$
- $k_i = \frac{K_i}{K_0}$ = The ith bulk relaxation modulus $[\frac{N}{m}]$
- τ_i^k = The ith bulk time constant [s]

The, using both relaxation functions, the (multi-axial) stress at each node is computed via the constitutive relation (vectors in bold) [108]:

$$\boldsymbol{\sigma(t)} = \int_0^t 2G(t-\tau)\frac{\partial \boldsymbol{e}}{\partial \tau}\partial\tau + \boldsymbol{I}\int_0^t K(t-\tau)\frac{\partial \phi}{\partial \tau}\partial\tau$$

Where:
- $\boldsymbol{e}$ = deviatoric strain [-]
- $\boldsymbol{I}$ = idendity vector [1] [-]
- ϕ = volumetric strain [-]

Generalized Kelvin model for creep compliance The generalized Voigt model (Figure E.3), also called generalized Kelvin-Voight model, can be used to model the compliance of viscoelastic material(demonstrated in Appendix E). Based on the definition of the compliance function, under constant stress σ, the strain relaxation $\epsilon(t)$ can be computed via $\epsilon(t) = \frac{\sigma}{J(t)}$. However, two well-known relationships exist between the stress relaxation and creep behaviour functions of a viscoelastic material, which allows to compute the compliance function based on the creep function [111]:

$$\int_0^t G(\tau)J(t-\tau)d\tau = t \tag{5.5}$$

$$\int_0^t J(\tau)G(t-\tau)d\tau = t \tag{5.6}$$

To sum up, even if understanding how the creep behaviour is modelled is essential, one may only have the Generalized Maxwell parameters and use Eq. 5.5 or Eq. 5.6 to numerically compute the creep compliance and model the creep behaviour. Consequently, only the stress relaxation parameters are required for viscoelastic simulations. It has

been demonstrated that, even if cortical bone is strongly anisotropic, no significant difference (p=0.02) is observed between the stress relaxation function along the transverse or longitudinal direction [112]. Therefore, the relaxation moduli, e_i, and their corresponding time constant, τ_i, can be assumed to be equal for both directions. Only the initial values of the shear and bulk moduli differ. So, their relaxation function (Eq. 5.3 and Eq. 5.4) can be written for both longitudinal and transverse directions as:

$$G(t) = G_0[1 - \sum_{i=1}^{n} g_i(1 - e^{\frac{-t}{\tau_i}})] \tag{5.7}$$

$$K(t) = K_0[1 - \sum_{i=1}^{n} k_i(1 - e^{\frac{-t}{\tau_i}})] \tag{5.8}$$

Shear and bulk relaxation tests are not common on cortical bone, and even less info is available on Prony series fitting to obtain such moduli. Therefore, to obtain these Prony series, one may assume that the Poisson ratio is constant. Accordingly, and using the definition of the shear and bulk moduli with regards to the Young modulus and Poisson ratio, one may assume:

$$G(t) = \frac{E(t)}{2 * (1 + \nu)} \tag{5.9}$$

$$K(t) = \frac{E(t)}{3 * (1 - 2\nu)} \tag{5.10}$$

Assuming that the Poisson ratio is constant is a strong assumption, since it has been proven that, for viscoelastic materials under constant strain, the Poisson ratio tends to increase with time and temperature [113]. On top of that, while some confirm that the Poisson is strain dependent [113], others confirm the opposite [114]. However, since the cage will stay in the same environment once implemented, the temperature can be assumed constant. If one thinks about the strain rate and time dependency, one could use the observation that, for viscoelastic materials, the Poisson ratio is supposed to be constant within elastic limits [115, 116, 117]. Hence, since the cage design aims to define its yield limits such that the maximal stress is inferior, this consolidates the assumption of a constant Poisson ratio during the simulations. Also, a constant Poisson ratio induces that the shear and bulk modulus are proportional to the young modulus, which implicates that the shear and bulk relaxation moduli (Eq. 5.7 and Eq. 5.8) are equal to the relaxation moduli of the Young modulus e_i. Consequently, using Eq. 5.9 and Eq. 5.10 in Eq. E.2 and $g_i = k_i = e_i$, we get:

$$G(t) = \underbrace{\frac{1}{2 * (1 + \nu)} * E_0}_{G_0}[1 - \sum_{i=1}^{n} e_i(1 - e^{\frac{-t}{\tau_i}})]$$

$$K(t) = \underbrace{\frac{1}{3 * (1 - 2\nu)} * E_0}_{K_0}[1 - \sum_{i=1}^{n} e_i(1 - e^{\frac{-t}{\tau_i}})]$$

Theoretically, G_0 and K_0 could be defined using only on E_0 and ν. So, for a 3D FEM analysis (using Prony functions), only the initial elastic modulus, the Poisson ratio and the shear and bulk relaxation moduli (presented in Eq. 5.7 and Eq. 5.8 respectively) would

be required [108, 118]. However, since the shear modulus is defined through the literature, this one is used to be more precise. This was not possible for the bulk modulus, which was then computed based on Eq. 5.10.

Based on Table 4.2, Table 5.1 presents the parameters of the viscoelastic models. Please note that data come from few papers as no paper providing yield and ultimate strength of bone in its longitudinal and transverse direction has been found, which can lead to consequent variability (briefly discussed in section 7.2).

Table 5.1: Parameters of viscoelastic material with transverse or longitudinal properties. The values of E_0, ν, G_0, YCS, YTS and ρ are defined as the average of the values presented in Table 4.2. Directions: T = transverse properties, L = longitudinal properties. E_0 = initial Young modulus $[GPa]$, ν = Poisson's ratio [], G_0 = initial shear modulus $[GPa]$, YTS/YCS= Yield tensile/compressive strength $[MPa]$, ρ = bone mineral density $[\frac{gr}{cm^3}]$, τ_i = relaxation time constant $[s]$, e_i = stress relaxation moduli [-].

	E_0	ν	G_0	YCS	YTS	ρ	e_i, τ_i
T	9.44	0.467	3.54	42.3	52.5	0.765	e_1, τ_1 = 0.11768,7.6998 e_2, τ_2 = 0.0351218, 1061.7 [112]
L	18.052	0.324	5.4	136	92.78		

One may notice that only one reference is used to obtain the moduli and time constants in Table 5.1. This is due to the high variation of Prony parameters in literature, since the number of terms of the Prony series differ according to the author choice. Consequently, the moduli and time constant highly diverge and cannot be averaged. It has been chosen to select the reference using a two-terms Prony series, since this is usually assumed to be sufficient to model the stress relaxation function [112].

Comparing bone YCS to YTS in both transverse and longitudinal directions (Table 5.1), the YTS force is superior in the transverse direction, but inferior in the longitudinal direction. Because the difference is larger in the longitudinal direction and because the YTS is commonly used as yield limit using the Von Mises stress criterion, the YTS is used as yield strength. Also, the difference between the compressive and tensile limits is relatively small in the transverse direction comparing to variations within literature, so choosing the smaller transverse limit remains realistic (Table 4.2).

5.2.2.2 The anisotropic models

Cortical bone is anisotropic, but transversely isotropic. Therefore, the material properties in each direction only depend on the fibers direction. So, the anisotropic linear model uses the elastic properties of cortical bone according to the fiber direction in the cage. Such an anisotropic linear model is fully defined using five independent variables (Eq. 4.1, which are E_L, E_T, G_L, ν_L and ν_T. However, G_T is also used to avoid potential error due to the utilization of its expression based on E_T and ν_T ($G_T = \frac{E_T}{1+\nu_T}$).

Due to the restriction in the production, the fibers can only be oriented axially (z) or longitudinal (x) (see frame in Figure 4.10). This was checked thanks to the CT scans of the available grafts, using the defined dimensions (Table 4.5). So, two anisotropic models are used: one with longitudinal fibers and one with axial fibers. Depending on the fiber orientation, each element of the stiffness matrix is assigned to the longitudinal or

transverse property. Eq. 4.1 was computed with longitudinal (x) fibers. Using a similar development for axial (z) fibers, and using properties of Table 5.1, Table 5.2 provides the parameters of both longitudinal and axial anisotropic models (the YTS is used as yield strength, as for the viscoelastic model).

Table 5.2: Parameters of anisotropic material with axial or longitudinal fibers. E = Young modulus $[GPa]$, ν = Poisson's ratio [], G_0 = shear modulus $[GPa]$, YTS= Yield tensile strength $[MPa]$, ρ = bone mineral density $[\frac{gr}{cm^3}]$, τ_i = relaxation time constant $[s]$, e_i = stress relaxation moduli [-].

	$E[GPa]$	ν	$G[GPa]$	$YTS[MPa]$	$\rho[\frac{g}{cm^3}]$
Longitudinal (x) fibers	$E_y = E_z = 9.44$ $E_x = 18.052$	$\nu_{xy} = \nu_{xz} = 0.467$ $\nu_{yz} = 0.324$	$G_{xy} = G_{xz} = 3.54$ $G_{yz} = 5.4$	$YTS_y = YTS_z = 52.5$ $YTS_x = 92.78$	0.765
Axial (z) fibers	$E_x = E_y = 9.44$ $E_z = 18.052$	$\nu_{yz} = \nu_{xz} = 0.467$ $\nu_{xy} = 0.324$	$G_{yz} = G_{xz} = 3.54$ $G_{xy} = 5.4$	$YTS_x = YTS_y = 52.5$ $YTS_z = 92.78$	

So, four models are obtained. In what follows, these are mentioned as:

- Viscoelastic transverse: the isotropic viscoelastic model of the material using the transverse properties (Table 5.1)
- Viscoelastic longitudinal: the isotropic viscoelastic model of the material using the longitudinal properties (Table 5.1)
- Anisotropic axial: the linear anisotropic model of the material with axial fibers (Table 5.2)
- Anisotropic longitudinal: the linear anisotropic model of the material with longitudinal fibers (Table 5.2)

One needs to note that the Young and shear moduli are larger than the average one for fresh bone, respectively 14.7GPa and 3.28GPa [119]. This can be explained by the freeze-drying process, which considerably decreases the material elasticity [112, 120]. Indeed, the mechanical properties of bone highly depend on its water content [121]. The water is mostly contained between the collagen fibers, which are responsible of the bone viscoelasticity. Consequently, the freeze-drying process seems to decrease the Young modulus by $\approx 50\%$, matching roughly the average 55% decrease found in literature for fresh bone [119]. For the same reason, the tensile strength is lower than the one for fresh bone (150MPa [119]), most probably due to the reduced elasticity. Eventually, most likely for the same reason, the density is a lot smaller than the one of fresh bone (typically between 1.5 and 2.5 $\frac{gr}{cm^3}$) [119]. Also, the bone treatment aims to increase the bone brittleness and decrease its work to failure [120].

5.2.3 Testing mode

It was decided to focus on compression only in this thesis (justification in section 4.2.3). The patient has to wait 14 to 48h after the arthrodesis before standing up. Once standing, the patient may alternate between standing, sitting or lying in static position. The patient may also conduct daily-life dynamic activities such as walking, running or climbing stairs, but without any loads. All this until a radiography had been conducted and confirming the intervertebral fusion.

In this context, the larger static and dynamic compressive forces are respectively $2385N$ when the patient stands up flexing forward and $2160N$ when the patient climbs stairs two stairs at a time respectively (Table 4.3). Even if the maximum of both is chosen, taking a 30% secure margin ensures that the actual interdiscal compressive force will never exceed the tested value, leading to $2385 * 1.3 = 3100.5 \approx 3100N$. This also takes into account the anatomical variability between patients. It is supposed here that the cage has to withstand all the forces, while a posterior stabilization can be implemented and the annulus will help to sustain some stress.

Regarding the force direction, some papers report forces normal to the endplate surface, i.e. normal to the surface of the cage, while other report the axial force, i.e. along the axial axis. However, for a surface with a maximal slope of 5°, their ratio can maximally reach $\frac{F_{axial}}{F_{normal}} = sin(5) = 8.7\%$. Therefore, it has been chosen to use axial force for the compression test in order to simulate pure compression. However, the difference between the results obtained with a force which is normal to the surface or axial will be discussed.

So, an axial force of 3.1kN is applied (the localization depends on the study, as explained below). Using the anisotropic linear model, simulations can only be static. However, simulations using the viscoelastic model can be static or dynamic. As the load is applied slowly, the relative acceleration and velocity of the cage compared to the vertebrae is very small, so the situation can be assumed quasi-static. This means that, at an instant of time, the situation can be assumed static. As the simulation works by solving the problem at each time step, each problem can be considered static. As a result, the inertia is neglected. Other studies modelling intervertebral forces also assume the loadings to be static [99]. Nevertheless, dynamic analysis might provide insights about the cage behaviour while walking, climbing stairs or other dynamic activities, thus for fatigue testing. This is not studied in this thesis, but briefly discussed in section 7.2. To check the static assumption, both static and dynamic simulations will be conducted and compared.

For both static and dynamic simulations, SolidWorks asks to provide the load variation over time. However, for a static analysis, the time is a pseudo variable that indicates the load level at each time step. As the maximal stress over the whole simulation period is considered, load variation does not influence the results for a static analysis. The difference between the static and dynamic results will be studied.

5.2.4 Boundary conditions

The inferior surface is fixed while the load is applied on the superior surface. The surfacing of the design implies that each surface has top facets, i.e. facets on the edge (or top) of the surfacing, which would be the only facets in contact with the vertebrae instantaneously after cage insertion. However, one may assume that the surfacing will penetrate its adjacent vertebrae, so providing anchorage, such that the fixation and forces will be applied on the

entire inferior and superior surfaces respectively. Therefore, two situations are studied: one with the fixation and load on top of the surface, and one on the entire surfaces.

5.2.5 The criteria of optimization

5.2.5.1 Elastic deformation

To study the yielding of the cage, the simulation tool allows to use four failure criterions: Von Mises stress, Maximal normal stress, Tresca criterion and Mohr-Coulomb. Regarding the viscoelastic model, even if the (linear) Tresca criterion is more conservative than the (non-linear) Von Mises criterion, hence the Tresca criterion can lead to take unnecessary measure [122]. Besides, the Mohr-coulomb criterion is often used for brittle materials, rather than for viscoelastic materials. The Von Mises criterion is verified for viscoelastic materials in case of elastic deformations. Even if it is a strong hypothesis, as it is intended that the maximal stress within the cage remains below its yield limit, the Von Mises criterion is applicable (discussed in section 7.2). Also, the Von Mises criterion is applicable when the properties of the material are defined as $\frac{YSS}{YTS} = \frac{1}{\sqrt{3}}$. Even if this was never properly verified, we selected the Von Mises criterion [123]. So, the Von Mises criterion, i.e. that the material yields when the Von Mises stress equals or exceeds the yield limit, is used for the viscoelastic model.

Regarding the anisotropic linear model, the Von Mises, Tresca or Mohr coulomb criterion cannot be used, as the yield limit depends on the stress direction. An ideal model would consider the principal stress direction, compute the yield limit of the material in its direction and compare them accordingly. However, such an advanced model would require advanced analytic modelling that cannot be performed due to the time constraint [2]. A solution is to analyze the normal stress in each direction. As the yield limit of the cage is known in each of these directions (depending on the fiber orientation), the material is assumed to yield if one of those normal stresses equals or exceeds the yield limit of the material in its own direction. However, this does not take into account shear stresses, like when using principal stresses, which, by definition, cancels shear stresses (discussed in section 7.2).

Hence, the first objective of the simulations was to compare the viscoelastic and anisotropic linear models, with their respective criterion. Then, the most relevant model was selected and used to optimize the design, such that the cage undergoes only elastic deformations. To evaluate how safe the design is, the maximal stress should be compared to the yield limit. This yield limit depends on the model. For the viscoelastic model, it depends if the properties are the transverse or longitudinal ones. For the anisotropic linear model, it depends on the force orientation (aligned or transverse to the fibers). To quantify such a comparison, the factor of safety of the maximal stress (FoS_{stress}) is defined as:

$$FoS_{stress} = \frac{\text{Yield strength}}{\text{Maximal Von Mises or normal stress}} \tag{5.11}$$

This factor should be at least ≥ 1. Please note that a security margin is often applied on this factor. However, the safety margin will be applied on the load (see below). Also, in order to compute the maximal load that the cage can withstand, the unit stress factor

[2] Consequently to the thesis reorientation from experiment to modelling, due to the COVID-19 situation

(USF) is computed, i.e. the maximal stress for a unitary load [124]. Then, the maximal load before yielding, F_{yield}, is computed via [124]:

$$F_{yield} = \frac{USF}{\text{Yield strength}} \tag{5.12}$$

5.2.5.2 Cage subsidence and stress shielding

Cage subsidence and stress shielding are explained by two situations imposed to the cage and its adjacent vertebrae: one where the force is imposed and one where the displacement is imposed. For an applied force by the vertebrae on the cage, this will lead to surface stress on the cancellous bone of the vertebral body. Intuitively, not taking into account changes in bone properties due to the pathology, this would lead to the same stress. However, the contact surface between the cage and the vertebrae is significantly smaller comparing to the contact of the vertebrae with an healthy disc. This means that, for an equal load, the stress would increase, which can lead to the insertion of the cage into the vertebrae. Studying this phenomenon would require to implement porous material, the interaction between cortical and cancellous bones and the effect of cage insertion on the cage and on the properties of the vertebrae. As this is out of the scope of this thesis [3], the contact surface of current TLIF cage can be used as reference, which can range from 133mm^2 to 180mm [125], or from 170 to 220mm^2 [27], so typically between 170 and 180mm^2.

The second situation is when the displacement is imposed. Then, if the cage is too stiff, most stress will be sustained by the cage [39], i.e. the load are not proximally transferred from the cage to the bone [126]. In this case, due to Wolff's law (bone remodel according to applied load direction and amplitude), the bone density around the cage will decrease [39]. Hence, the bone joining adjacent vertebrae will be mechanically weaker than native bone, resulting in potential post-operative complications. This is referred to as stress shielding. Nevertheless, the exact mechanical signal triggering bone remodelling remains uncertain between stress, strain or strain energy density [126]. However, stress is often taken as a reliable indicator. Experimental findings support the mechanical prediction that less stiff implant lead to more proximal transfer of the load [126]. Therefore, the cage stiffness has to be as close as possible to the vertebral body stiffness, which is $\approx 7.8 \pm 4.2 \frac{kN}{mm}$ [74]. However, one must be careful as reducing stress shielding induces increasing stresses at the cage-bone interface, so risking reducing osteointegration [126]. To find such a trade-off, FEM simulating osteointegration and bone remodelling is necessary, which is not part of this thesis.

To evaluate how close the cage stiffness is comparing to the vertebral stiffness, the ratio between between the cage stiffness and the vertebral body stiffness is computed, called the stiffness factor of safety ($FoS_{stiffness}$i, which is defined as:

$$FoS_{stiffness} = \frac{\text{cage stiffness}}{\text{vertebral body stiffness}} \tag{5.13}$$

This ratio should be as close as possible from 1.

[3] Because the thesis had to be reoriented due to COVID-19 situation, the time restriction did not allow to develop such a complex model

5.3 Results

Based on the description of the simulations, seven studies are necessary:

- Study 1: Application of the force. this study aims to define if the force (and fixations) should be applied on the top or on the entire surfaces.
- Study 2: Static versus dynamic. This study aims to choose between the static or dynamic simulation using the viscoelastic models
- Study 3: Porosity (UCM). this study aims to define the low and high porosity of the cages, using the UCM model.
- Study 4: Viscoelastic isotropic versus linear anisotropic: this study aims to choose between the viscoelastic models or the linear anisotropic ones
- Study 5: Cage angle. This study aims to define the cage angle that will be used for the simulations.
- Study 6: the USF hypothesis. This study aims to check if the USF hypothesis is verified.
- Study 7: Design optimization. This study aims to define which design(s) would be the most appropriate.

For all results, the hypothesis of the USF is cross-checked, i.e. if $\sigma_{max} = 3100 * USF$.

5.3.1 Study 1: Application of the force

To define the force localization, the Von Mises stress and cage deformation are compared using the full design when the force and fixtures are applied on the top of the surface (edge of the surfacing) or on the whole superior surface. As Von Mises stress are used, the comparison is done using the viscoelastic models.

The maximal Von Mises stress is always larger when the force is only applied on the top of the surface (Table F.3, crosses in Figure 5.11a) than when applied on the entire surface. This is confirmed on the stress heatmaps for the full design using the viscoelastic longitudinal model (Figure 5.7).

When the force is applied on the top of the superior surface, high stress concentrations are observed on the faces where the force is applied (Figure 5.7b). Hence, the surfacing is likely to penetrate the vertebrae and to collapse (scaled up deformed results in Figure 5.7d). Therefore, we assume that the force should be applied on the entire surface for all designs (similar results are observed with other designs).

5.3.2 Study 2: Static versus dynamic

For the viscoelastic model, one may choose between conducting static or dynamic studies. Intuitively, a dynamic study would be necessary for fatigue testing, but not for a one load step. However, the difference between the results using a static or dynamic study is analyzed in order to confirm this hypothesis.

Probing few nodes on the viscoelastic model after running a non-linear dynamic simulation shows that the stresses and displacements are mostly linear to the force. Also, no differences were observed regarding the nodes displacement over time depending on load variation over time. Indeed, for three different loadings variations (linear increase, a charge-uncharged, and a linear increase then rest), mostly no difference was observed

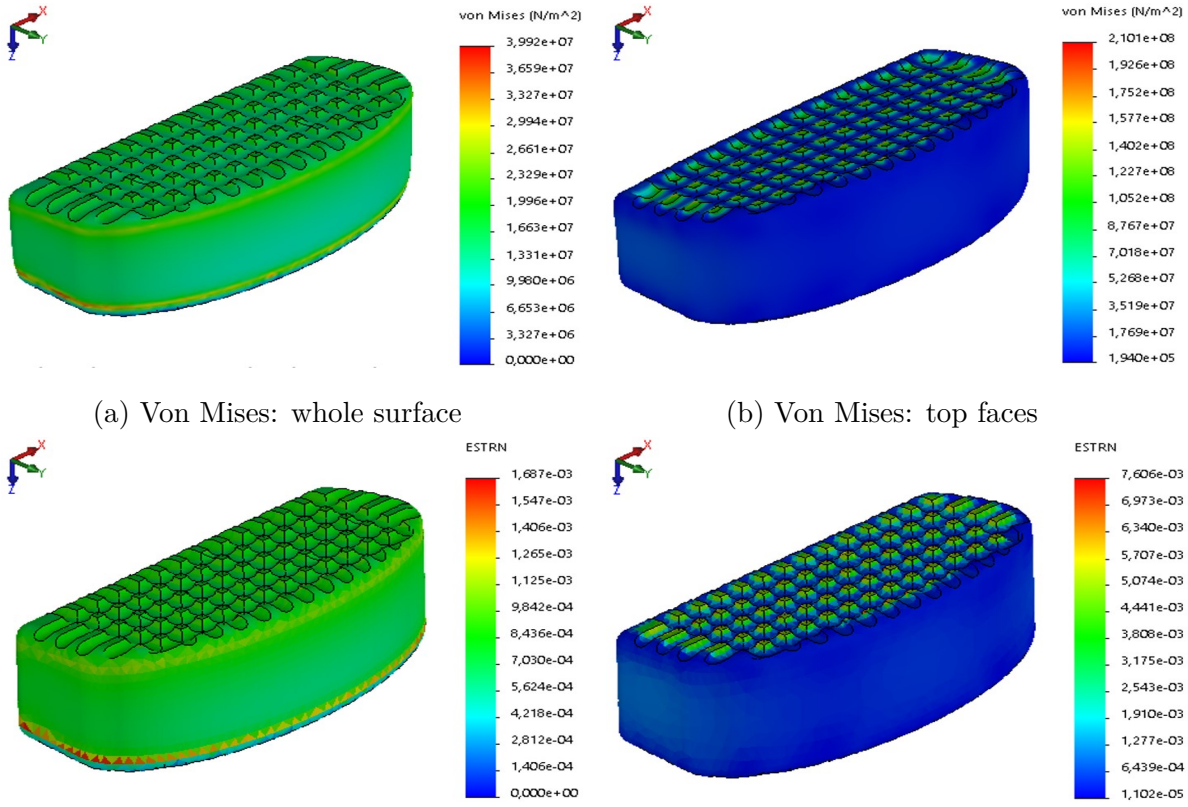

(a) Von Mises: whole surface

(b) Von Mises: top faces

(c) Resultant displacement: whole surface

(d) Resultant strain: top faces

Figure 5.7: Comparison of Von Mises stress and resultant strain when force applied on the whole superior surface (whole surface) or on the top of the surface (top faces), using the full design with the longitudinal viscoelastic model. (a) Von Mises stress when forces applied on the whole superior surface (deformed results, scale = 120). (b) Von Mises stress when forces applied on the top faces of the superior surface (deformed results, scale = 120). (c) Resultant displacement when forces applied on the whole superior surface. (d) resultant displacement when forces applied on the top faces of the superior surface.

(<1% for 3 critical nodes) using static simulations. Despite, as Solidworks requires to define the load variation over time, the force is linearly increased from 0 to 3.1kN over a 1s time step for the coming static analysis. [4]

5.3.3 Study 3: Porosity (UCM)

To obtain C_1 from Eq. 5.2, the full, OLP and FLP designs are used with the four models (Table 5.1 and Table 5.2) and with four different volume fractions: 0.49, 0.6,0.8 and 1 (Table F.1). 0.49 is chosen as the smallest volume fraction since it is the smallest one for which the pores of the FLP do not interfere with the surfacing. Then, Eq. 5.2 is fitted using *graphPad Prism*, via the least square method (Figure 5.8a) [127].

It is observed that, when the Young modulus differs, the stiffness differs proportionally (Table F.4). However, for the same cage porosity with different material properties, the

[4]SHOW DATA ON THIS: Add a nice figure with several types of stimulus and response here, if time as I don't know how to extract that on the same graph

(a)

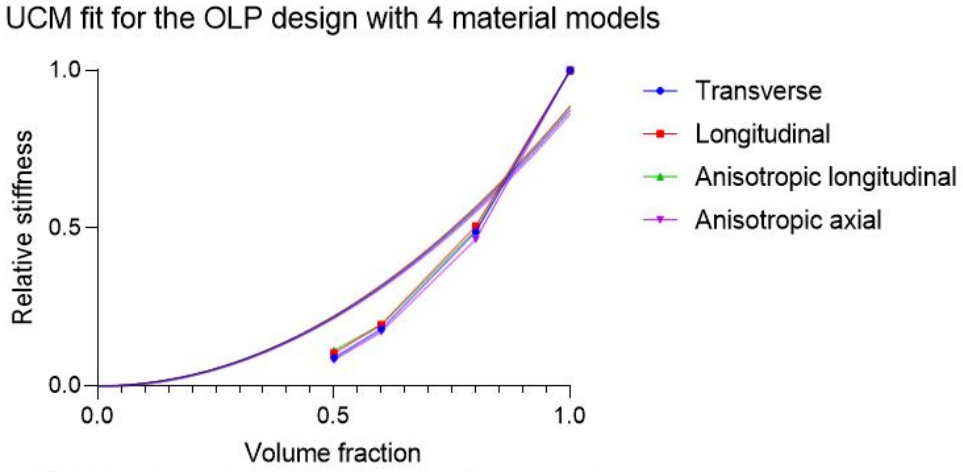

(b)

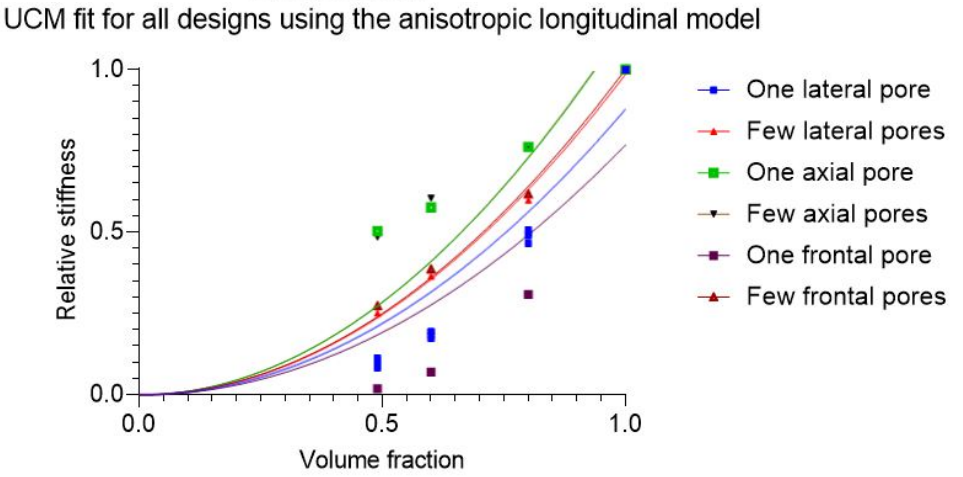

Figure 5.8: (a) Unit cell model fit for the one lateral pore (OLP) design with the viscoelastic model using transverse (transverse) or longitudinal (longitudinal) properties and with the anisotropic linear model using longitudinal (anisotropic longitudinal) or axial (anisotropic axial) fibers. (b) Unit cell model fit for the full, OLP and FLP designs using the anisotropic linear model with longitudinal fibers. Design can be with one (squares) and few (triangles) pore(s). Stripped dark line for Eq. 5.2 with $C_1 = 0.985$. All the data points from the OLH design with all material models (from (a)) are represented as blue squares.

relative stiffness remains roughly constant. This shows that, for the same cage design with the same porosity, the relative stiffness is equally affected independently by the Young modulus of the model. Indeed, the fit for different material properties of the OLP design provides similar values of C_1 (relative difference $< 3\%$), with a mean of $C_1 = 0.877$ (Figure 5.8a). Results with anisotropic properties does not differ from isotropic ones. So, it has been chosen to study the difference between designs for only one material. This material is arbitrary fixed to the anisotropic one with longitudinal fibers (justified thanks to later results) (Table F.2). Besides, a linear model is applicable as stiffness is computed with elastic deformation.

The fit for different designs using anisotropic properties with longitudinal fibers provides value from 0.7687 to 1.137 with a mean of 0.985 (dark stripped line in Figure 5.8b), so up to a relative variation of $\approx 48\%$. However, the relative stiffness seems still to increase exponentially with the volume fraction, so matching the UCM theory. Already,

some elements appear. Axial hole(s) decrease(s) the stiffness the less, so increasing the relative stiffness. The FLH and FFH seems to fit the best, probably thanks to their more homogeneous nature than designs using one large pore, so respecting more the homogeneously hypothesis of the UCM. Also, few pores designs lead to higher stiffness than their corresponding single pore designs.

The goal is to define the low and high porosity of the designs. As p=0.51 ($V_f = 0.49$) is the maximal porosity that can be achived with OLH design, this is fixed as the high porosity. Using a volume fraction of 0.5 and a constant $C_1 = 0.985$, Eq. 5.2 provides the low relative stiffness of 0.21985, so a cage stiffness of $65.955\frac{kN}{mm}$ ($k_s \approx 30\frac{kN}{mm}$. So, the initial goal of setting the minimal volume fraction such that the cage stiffness matches the vertebral body stiffness (7.8kN) is impossible, even with longitudinal fibers (axial fibers would increase the stiffness due to the higher axial Young modulus than longitudinal one). The high relative stiffness is set to the middle between the low relative stiffness and 1, so set to $\frac{1+0.21985}{2} \approx 0.6$. Consequently, Eq. 5.2 defines the high volume fraction as $\sqrt{\frac{0.6}{0.985}} = 0.787$, or a porosity p=0.213. As a result, two porosities are studied with the porous designs: p=0.51 as high porosity and p = 0.213 as low porosity.

5.3.4 Study 4: Viscoelastic isotropic versus linear anisotropic

Simulations are used in order to choose between the anisotropic linear, using the maximal normal stress criterion, or the isotropic viscoelastic model, using the Von Mises criterion. First, the criterions might be analyzed from a theoretical perspective. The Von Mises criterion is mostly applied for ductile materials. For brittle materials, a principal stress analysis is usually preferred [128]. Comparing the bone YTS to UTS and YCS to UCS (Table 4.2), the difference between the yield and ultimate limit of treated bone is very small. For instance, the largest difference is observed for the compressive properties in the transverse directions: $UCS - YCS = 97.65 - 42.3 = 55.35$ (97.75 is the average UCS, Table 5.1). Even if this more than the double of the UCS, similar variation is observed in literature. If only one paper is used as reference, this difference is about 20MPa [67]. Also, regarding the transverse direction only, the YTS is very close to the UTS ($\approx$ 25% difference, Table 5.1). Therefore, this intuitively tends to believe the cage bone to be brittle. On top of this, the bone treatment, more specifically the freeze-drying and irradiation, increases cancellous bone brittleness [120]. This can be expected for cortical bone as well. As a result, the cortical bone used for the cage can be assumed to be brittle and a principal stress analysis would be preferred. However, a normal stress analysis would be applicable, as it is commonly used for brittle material, even if it does not take the shear stresses into account.

Then, the Von Mises and the maximal normal stress criterions can be analyzed based on the results of simulations (Figure 5.9a). Comparing the anisotropic linear and isotropic viscoelastic models, for the full design, the maximal Von Mises stress leads to a larger or roughly equivalent FoS_{stress} than normal stresses (Figure 5.9b). The more the porosity increases, the closer the FoS_{stress} based on Von Mises stress is to the ones based on a normal stress. This could be explained by the fact that porosity might induce shear stresses, which are not considered with normal stresses. So, the Von Mises stress increases and its FoS_{stress} decreases. Indeed, at high porosity, the maximum relative difference reaches 76.16%. However, the FoS_{stress} is then below 100%, which is not the goal of the design. This means that the FoS_{stress} based on normal stress is the smallest FoS_{stress}

around the 100% limit. Also, at high porosity, the FoS_{stress} based on Von Mises stress is inferior to the other ones. So, this means that using the maximal normal stress is the worst scenario around 100% and, when it is not (for high porosity), using the Von Mises stress would provide a FoS_{stress} below 100% as well. So, using the anisotropic models with the maximal normal stress criterion is the safest option and will be used for further simulations.

(a) Maximal stress

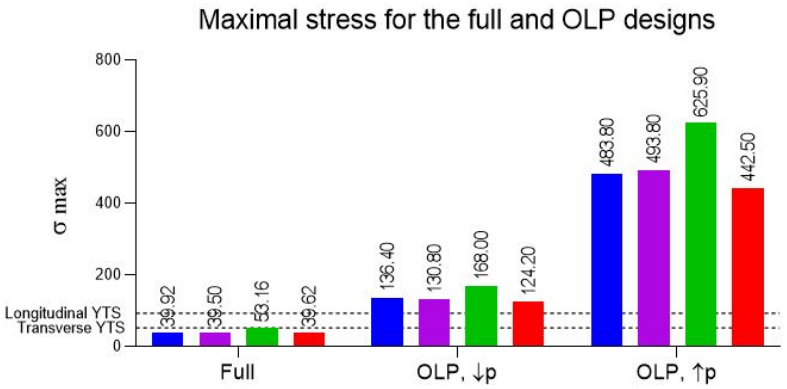

(b) FoS_{stress}

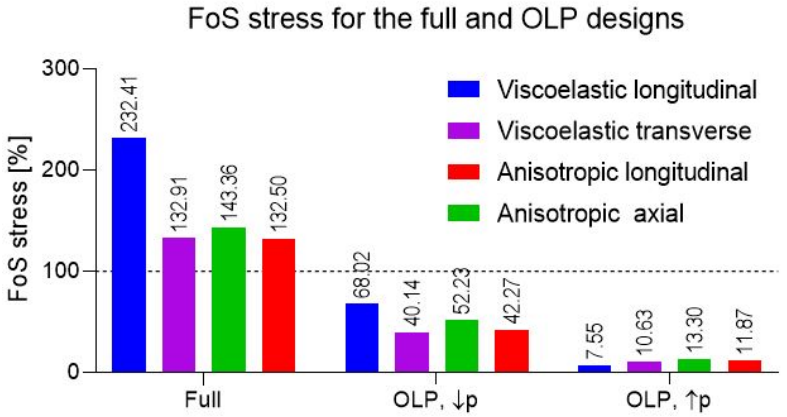

Figure 5.9: (a) Maximal stress (always in axial (z) direction) for the full and OLP (with low and high porosity) designs according to the material model. stripped line for the longitudinal and axial yield strength, i.e. the yield tensile strength (YTS).(b) and FoS_{stress} for the full and OLP (with low and high porosity) designs according to the material model, based on stress of (a). Stripped line for $FoS_{stress} = 100\%$.Same legend for both.

5.3.5 Study 5: Cage angle

Using the full design with anisotropic properties, arbitrary chosen to be with axial fibers, an angled cage can be compared to a flat cage. Similar stress distribution and magnitude according to cage slope is observed (Figure 5.10). However, all normal stresses are larger with the angled design (in absolute value), which are concentrated on the edge between the superior and inferior surfaces, and the anterior, posterior and lateral surfaces (Figure 5.10). So, in order to use the worst scenario, the angled design with the maximal angle is chosen, i.e. an angle of 10° (Figure 4.10). [5]

[5]TO CHECK IF TRUE FOR OTHER DESIGNS, IF YES/NO MENTION IT

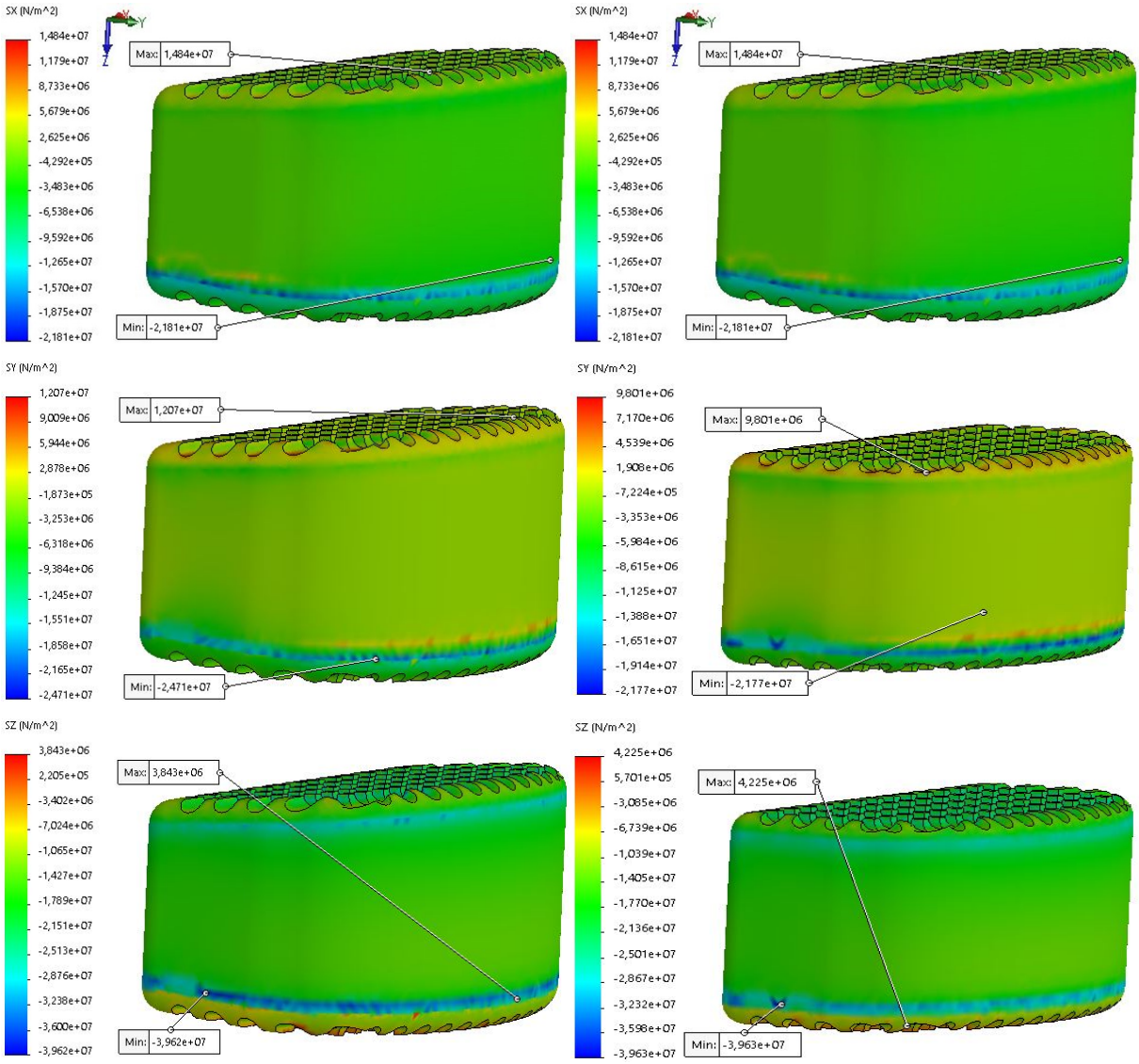

(a) Angled cage (10° angle) (b) Flat cage

Figure 5.10: Normal stress along the X, Y and Z directions (see frames above, same frame for all heatmaps) for an (a) angled cage with a 10° angle and (a) a flat cage. Both are based the isotropic axial model with forces and fixations on the entire surfaces. Similar results are observed using the longitudinal anisotropic model.

5.3.6 Study 6: the USF hypothesis

Before computing the maximal force that the cage can withstand without yielding, the stress should be checked to be linear to the load. To so so, using the maximal stress σ_{max} for a force of 3100N, one may check if:

$$\sigma_{max} = 3100 * USF$$

First, the USF hypothesis is verified for the full and OLP designs. It is observed that the maximal stress for 3100N is roughly equal to $3100 * USF$ for all models (Figure 5.11a) [6].

[6]Change the legend of the figure: OLH -> OLP

The large Von Mises stresses differs more from the line, which is likely caused by numerical approximation of large numbers. Results proves that forces on the top of the surfaces lead to larger maximal stress than forces on the whole surface (crosses in Figure 5.11a).

(a)

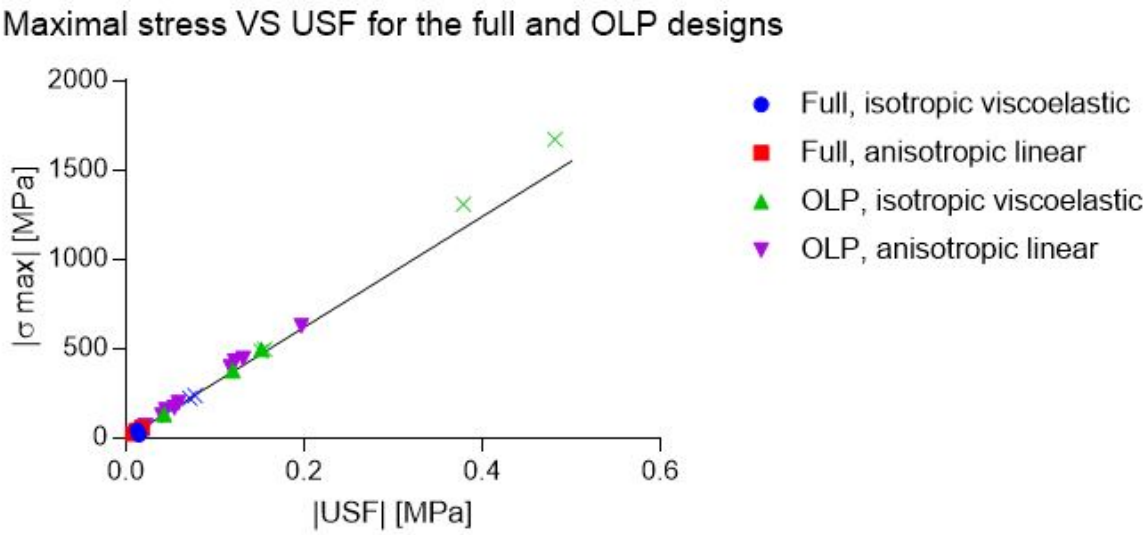

(b)

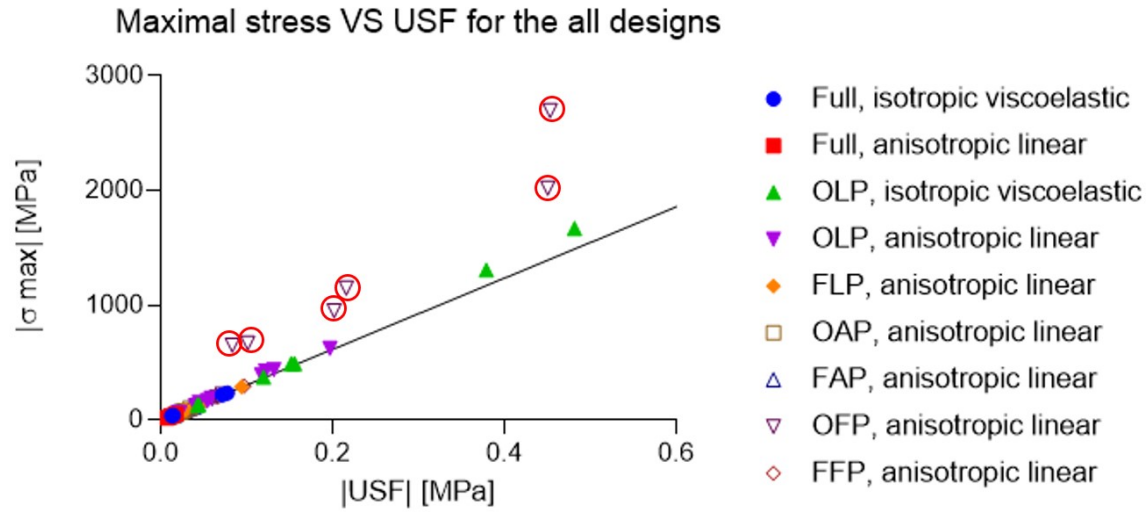

Figure 5.11: USF fit for Von Mises stress using the viscoelastic models and all normal stresses using the anisotropic models. For the viscoelastic models, the forces are applied on the top of the surfacing (crosses) or on the whole surface (default symbol). For the OLP design, results are obtained with both high and low porosity. (a) Fit for the full and OLP design. (b) Fit for all designs with low and high porosity, using only the anisotropic models for the additional designs. Dark line for $\sigma_{max} = 3100 * USF$.

Even if this hypothesis seems to be verified and would be reasonable for a linear model, it is decided to numerically compute the USF for each design and porosity using the isotropic model, instead of mathematically compute it via $USF = \frac{\sigma_{max}}{3100}$ (Figure 5.11b). The hypothesis is verified for all configurations expecting one, which is the OFP design with a high porosity (in bold in Table F.7, encircled in red in Figure 5.11b). This is

explained by the simulation using the large displacement solution for these designs. Indeed, when the computed displacement using the small displacement theory is too large, SW suggests using the large displacement method. In this case, the load is stepped and the geometry is updated between each step [129]. Consequently, the stress obtained with a unitary force is not proportional to the one obtained with 3.1kN, as the geometry has been changed consequently to the load (Figure 5.12).

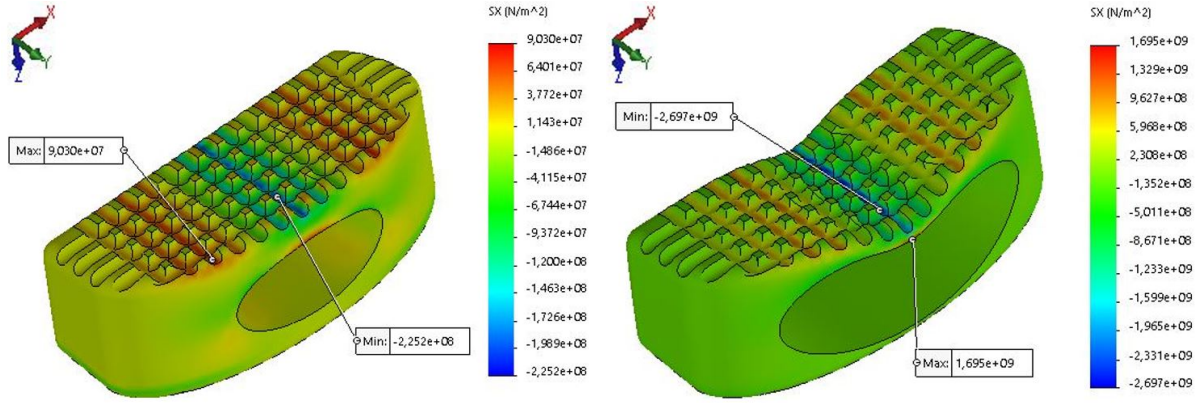

(a) (b)

Figure 5.12: OFP normal stress in x using the longitudinal anisotropic model. Comparison for low (a) and high (b) porosity. Similar stress distribution is observed for other elliptic proportions.

To sum up, six parameters of the simulations are deducted:

- The force is applied on the whole superior surface (and the fixation on the whole inferior one) rather than on the top of the surfacing, as the surfaces are likely to penetrate inside the adjacent vertebrae and to collapse
- The viscoelastic model is used with static simulations
- The low and high porosities are respectively equal to 0.2013 and 0.5
- The model is anisotropic linear and the maximal normal stress criterion is used as yield criterion
- The cage has the maximal angle because it maximizes the stress, i.e. an angle of 10°
- The USF is verified for small displacement, hence it will be still numerically computed in order to verify if the small displacement theory is applied

Eventually, a cage angle of 10° was computed to not lead to significantly different load (max. 8.7%). However, this hypothesis will be checked thanks to simulation via comparing results with a flat cage and an angled cage.

5.3.7 Study 7: Design optimization

Once the porosities, boundary condition, model of the material and cage slope determined, the cage optimization can be conducted. Two factors are studied: FoS_{stress} and $Fos_{stiffness}$. These both factors are studied independently and combined. Based on the analysis, the design(s) matching the most the requirement will be selected.

The maximal stress σ_{max} and the maximal USF always appear to be at the same localization, and the relation $\sigma_{max} = 3100 * USF$ is roughly verified for every simulation, which validates the small displacement and USF proportionality hypothesis.

5.3.7.1 Maximal normal stress analysis

Effect of the fibers orientation The FoS_{stress} shows that the fiber direction has an effect on the stress distribution, as the distribution differs accordingly (Figure 5.13). Indeed, aligning the fibers in the longitudinal direction increases the FoS_{stress} in the longitudinal (x) direction while decreasing the one in the axial (z) direction, because the maximum stress in the x direction decreases and the YTS in the longitudinal direction increases (Table F.3, Table F.4, Table F.5, Table F.6 and Table F.7). Longitudinal fibers also lead to an increased FoS_{stress} in the y direction compared to axial fibers. This can not be due to the YTS as it remains the transverse YTS for axial or longitudinal fibers. So, it means that the maximal normal stress in the y direction decreases with longitudinal fibers. The normal stress in the z direction generally decrease when fibers are longitudinal aligned (as seen in Figure 5.9a), expecting for the FAH design with a low porosity, which is explained by a high stress concentration due to the interaction of a small pore and the surfacing.

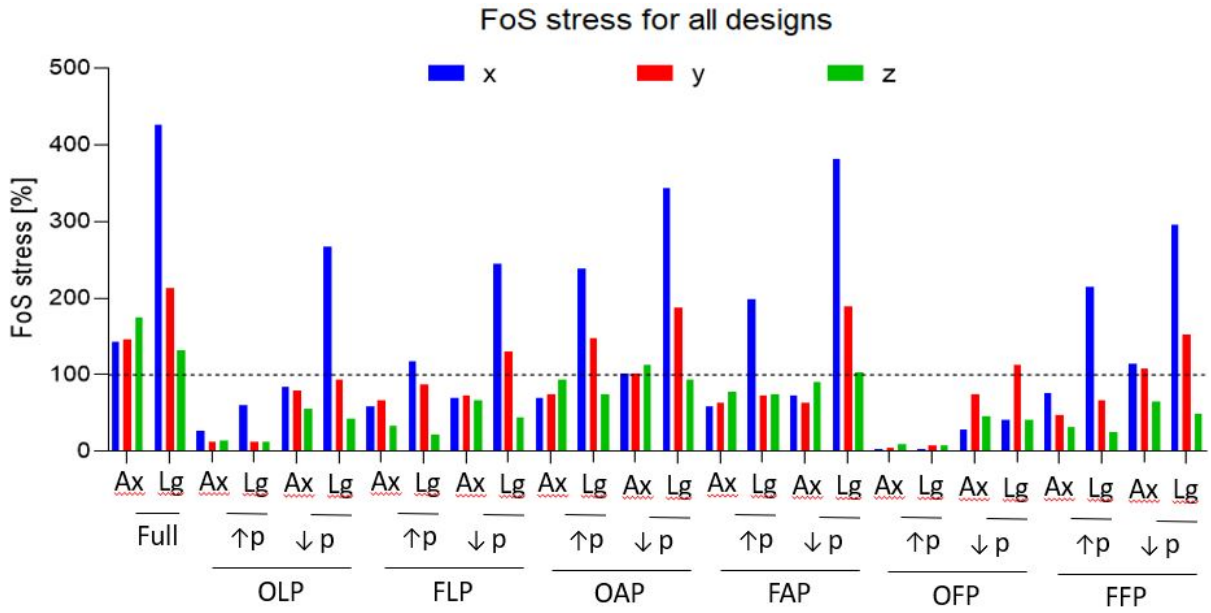

Figure 5.13: FoS_{stress} [%] for all designs with high and low porosity (for porous designs) and using the axial (Ax) and longitudinal (Lg) anisotropic model.

Effect of the porosity For a same design, the porosity affects how the FoS_{stress} ditribution varies according to the fiber direction (Figure 5.13). For example, for the OLP design with a small porosity, the difference of FoS_{stress} according to the fibers orientation is equal to 33.3, 1 and 2.95 in the x, y and z direction respectively. Differently, for the high porosity of the OLP design, these differences are 182.67, 13.65 and 12.96 respectively.

Effect of the design The design, for an equal porosity and the same fiber orientation, affects the FoS_{stress} along the x, y and z axis (Figure 5.13). Indeed, the variation of the FoS_{stress} distribution with the same porosity when switching the fiber direction differs according to the design (Figure 5.13). For example, the FoS_{stress} for the OLP design with high porosity and longitudinal fibers is not the same as for the FLP with same porosity and longitudinal fibers. This for all stress directions.

To sum up, switching from axial to longitudinal fibers decreases the x and z normal stresses while increasing the normal stress in the y direction. On the other hand, this switch decreases the axial YTS and increase the longitudinal one, so increasing the FoS_{stress} in the x direction but decreasing it in the z direction. Nevertheless, there is one exception. The FAP design with a low porosity exhibits a slight increase FoS_{stress} in the z direction (13.02% increase). However, this variation of stress distribution when switching fiber orientation depends on the design and porosity independently.

Design selection The designs leading to a minimal FoS_{stress} (among the three directions) under 100% should be excluded as it means that one normal stress is greater than the yield limit. [7] Based on this selection criteria, only the OAP with axial fibers and FAP with longitudinal fibers are selected, both with low porosity. However, the OAP with longitudinal fibers have a minimal FoS_{stress} of 93.2%, which is large compared to the remaining designs (closest FoS_{stress}: same design and fibers orientation but with high porosity: $FoS_{stress} = 74.57\%$).

5.3.7.2 Stiffness analysis

The $FoS_stiffness$ is also studied as selection criteria (Figure 5.14). Ideally, this factor should be as close as possible to 100%, such that the cage stiffness is as close as possible to the vertebral body stiffness.

Effect of the fibers orientation, design and porosity The cage axial stiffness is always higher with axial fibers, so leading to higher $Fos_{stiffness}$ (Figure 5.14). Besides, for all designs, the stiffness is always smaller with the high porosity for the same fibers direction, leading to smaller $FoS_{stiffness}$ (Figure 5.14). The $FoS_{stiffness}$ variation also depends on both design and porosity independently.

Design selection The OFP design has the $FoS_{stiffness}$ the closest to one. After, the OLP and FLP designs with a high porosity and longitudinal fibers have the $FoS_{stiffness}$ the closest to 1. Regarding the low porosity designs, the OFP and FFP designs, again with longitudinal fibers, would have the stiffness the closest to the one of a vertebral body.

5.4 Discussion

Based on the results of the FoS_{stress}, the OAP with axial fibers and FAP with longitudinal fibers are selected; Also, the OAP with longitudinal fibers is close to be accepted. Observing

[7] Please note that, in practice, FoS above 100% are often chosen as safety margin. However, in this context, this would require excluding all designs. One may consider here that the safety margin here is applied on the load.

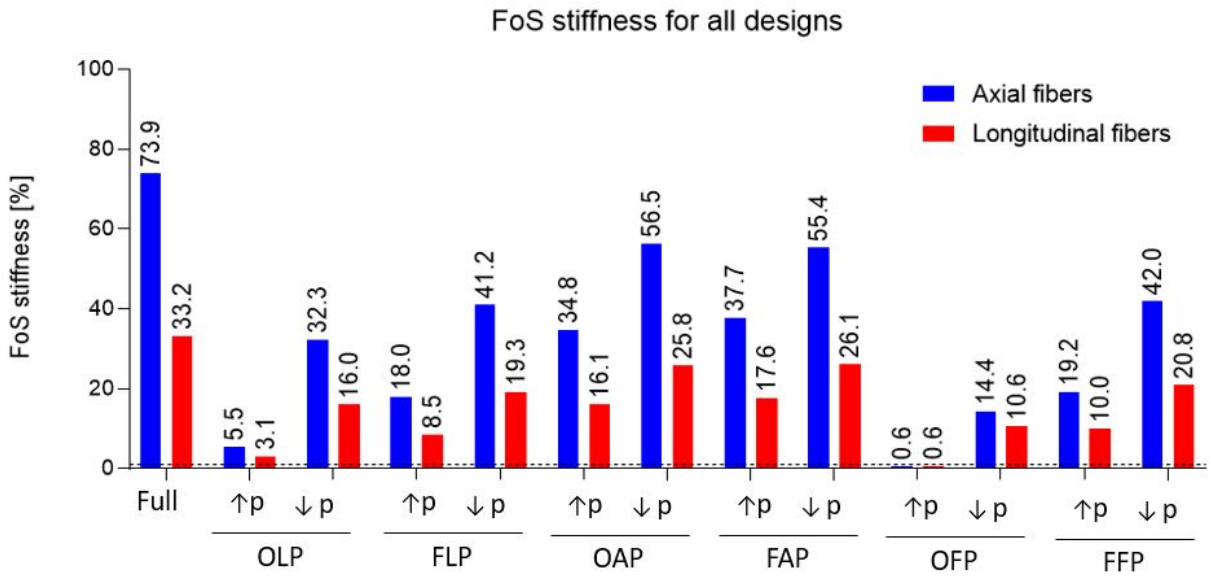

Figure 5.14: $FoS_{stiffness}$ [%] for all designs with high and low porosity (for porous designs) and using the axial (Ax) and longitudinal (Lg) anisotropic model.

the stress distribution, the absolute maximal stress is observed on the top of the surfacing for the OAP(Figure 5.15). So, this stress is likely to have the same consequences as when stresses were only applied on the top of the surfacing, i.e. instantaneously after the insertion of the cage, which were accepted when studying the force localization. So, this design is selected as well.

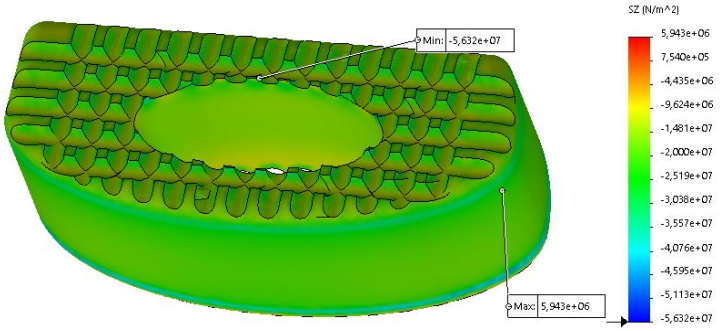

Figure 5.15: OAP design at low porosity with longitudinal fibers. Heatmap of the normal z stresses.

Regarding the higher $FoS_{stiffness}$ with axial fibers, this is explained by the higher axial Young modulus of cortical bone, leading to higher axial stiffness with axial fibers (Table 5.2). Also, the smaller stiffness with high porosity is consistent with the UCM defining the relative stiffness, i.e. the $FoS_stiffness$, exponentially proportional to the volume fraction, i.e $1 - porosity$.

The $FoS_{stiffness}$ results would suggest using the OFP design. However, as shown previously (Figure 5.12), this design leads to extensive displacement and stress. Hence, this design is excluded. Then, the OLP design with high porosity seems to best match the vertebral body stiffness. However, this design leads to large stresses, which generate a minimal FoS_{stress} far below 100% (Figure 5.13).

Here, a trade-off appears between decreasing the cage stiffness to match the vertebral body stiffness and keeping a sufficient FoS_{stress}. None of the designs selected based on FoS_{stress} (FAP with longitudinal fibers or OAP with axial or longitudinal fibers) provides an acceptable $FoS_{stiffness}$ (26.078, 59.46 and 25.807). So, two options appear. One option is to select one design with an appropriate FoS_{stress} and assume that its stiffness is decreased enough, assuming that the cage stiffness has to be close to the one of the vertebral body, but not equal [8]. A second option is to select few designs to combine them and try to decrease the stiffness more. In what follows, the designs providing the best trade-off between the FoS_{stress} and $FoS_{stiffness}$ are selected, and their potential combinations will be analyzed with the final design in subsection 7.1.1.

So, the goal is to to obtain a $FoS_{stiffness}$ as close as possible to 100%, and a FoS_{stress} as large as possible. To define which designs to combine, one may define the ratio of both FoS_{stress} and $FoS_{stiffness}$ as the FoS_{ratio}:

$$FoS_{ratio} = \frac{FoS_{stiffness}}{FoS_{stress}}$$

As the $FoS_{stiffness}$ of the remaining designs (OFP excluded) is always greater than 100%, the $FoS_{stiffness}$ has to be as small as possible. Oppositely, the FoS_{stress} has to be as large as possible. So, the FoS_{ratio} has to be as small as possible.

According the FoS_{ratio}, using longitudinal fibers seems to best minimize this ratio, thanks to the natural smaller stiffness of the bone in its transverse direction (Figure 5.16). Also, the results with a high porosity are excluded, as this lead to FoS_{stress} below 100%. In this context, the OAP and FAP appear to be the best trade-off between maximizing FoS_{stress} and minimizing $FoS_{stiffness}$, what confirms the selection made based on FoS_{stress}. However, if it is assumed that the cage will have a low porosity to avoid it to break, the FAP design might be the best one.

If axial pores have to be combined with another design, some biological consideration has to be taken into consideration. With longitudinal fibers, natural pores due to bone canals will appear in the lateral (x) direction. Also, as the cage is placed anteriorly to the disc, on top of the supero-anterior (axial) bone remodelling, the bone remodelling had mostly to take place in the antero-posterior (frontal) direction [9]. For both these reasons, adding frontal pores might be the more usefull. Therefore, the OAP or FAP design might be combined with the FFP design if the stiffness with axial pore(s) alone is not sufficient (as the OFP is excluded).

5.4.1 Final design(s)

As final designs, two possibilities arise. Their final porosity will be optimized with the unique design outputs, as this one also depends on the instrumentation (developed in chapter 6). However, it already appears that using axial pore(s) with longitudinal fibers is the best trade-off between avoiding yielding and decreasing the cage stiffness. If the achieved stiffness is not sufficient, frontal pores can be added for durther decreasing it. So, two designs are considered: one combining the OAP and FFP designs, called final design 1

[8] Ideally, the stiffness of an existing cage which do not provoke stress shield or cage subsidence, such as one made of PEEK, would be measured and used as reference.

[9] Note that these osteons would have been useful with axial fibers to stimulate supero-inferior bone remodelling, but this would increase the axial stiffness too much.

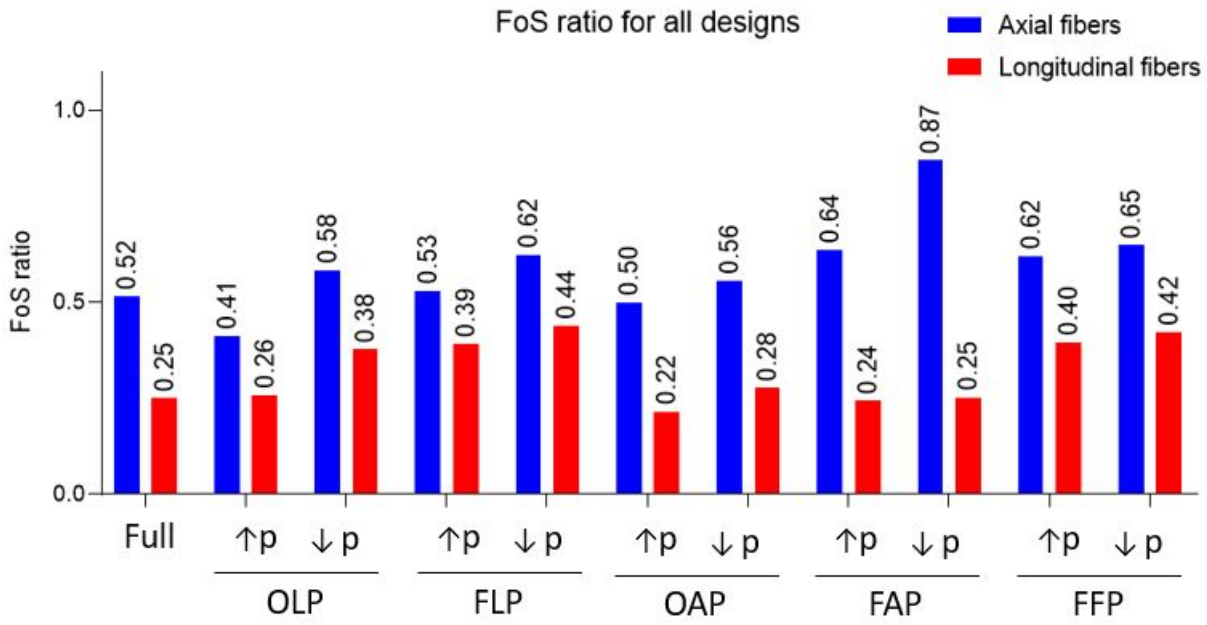

Figure 5.16: FoS_{ratio} ($= \frac{FoS_{stiffness}}{FoS_{stress}}$) for all designs expecting the OFP design, for low and high porosity and with axial and longitudinal fibers.

(FD1), and one combining FAP and FFP designs, called final design 2 (FD2). In both case, the frontal pores can be removed, which allows to work with only two final designs while taking into consideration the OAP and FAP designs alone and their combination with the FFP design.

Optimizing such designs is a very complex problem. This because the goal is to have a maximal normal stress as small as possible while having a cage stiffness as close as possible to $7.8\frac{kN}{mm}$. To do so, few factors can be adjusted:

- For the FD1:
  the shape and dimensions of the axial pore
  the number, distribution, shape and dimensions of the frontal pores
- For the FD2:
  the number, distribution, shape and dimensions of the axial pores
  the number, distribution, shape and dimensions of the frontal pores

Before doing the optimization, the instrumentation is designed. The reason for that is that the instrumentation might exclude one final design, or promote one more than the other.

Chapter 6

Design of the instrumentation

6.1 Design inputs

6.1.1 User needs

During a TLIF, the lumbar spine (L4-L5 or L5-S1) is approached by the left or right side, according to surgeon's preference. Using the tools that are available, the surgeon can distract the vertebrae and prepare the intervertebral space. So, the user needs an instrumentation that allows to choose the appropriate cage size and insert the cage in its desired position. All the instrumentation should be retracted while leaving the cage in place and without causing damage. To fulfil these functions, the instrumentation can consist of single or multiple tools.

6.1.2 Literature inputs

The functions of the instrumentation are, thus, to provide a measure for the dimensions of the cage and to allow the insertion of the cage. As the surgeon works through a tunnel to access the spine, the equipment has to be as less bulky as possible [52]. These functions are referred as the measurement and the insertion respectively. To make the instrumentation compatible with the cage, the cage is often adapted to the instrumentation, without compromising the cage properties [25, 27]. Also, the same instrumentation is often used to insert several cages, meaning that it should be durable [130]. The instrumentation will be used by one surgeon and has to be user-friendly [130].

For determining the dimensions of the cage, the surgeon can use few stand-alone tools or ghost cages, and visualize the results via a lateral imaging. The advantage of using ghost cages is that it only requires to use the tool(s) for the insertion of a cage, referred as insertion tool, but multiple times with different ghost cages. However, the insertion tool(s) should allow to remove the ghost cage. To avoid this potential issue, specific tool(s) to measure the dimensions of the appropriate cage, referred as measurement tool(s), can be designed. However, this means that additional tool(s) should be provided. In what follows, the tools referred to all provided tool(s), which can consist of insertion tool(s) and ghost cages or insertion tool(s) and measurement tool(s). Please note that some commercialized devices evaluate the appropriate cage size thanks to their provided tool to distract the vertebrae (details in Appendix C). However, such a tool does not have to be provided here.

6.2 Design process

6.2.1 Design objectives

The objective tree presents the main objectives of the tools (Figure 6.1). Two objectives can be distinguished: the evaluation of the appropriate cage size and the insertion of it (what?), which are achieved before and during the cage insertion respectively (when?). The approach is a TLIF (how?), which is performed by one surgeon (who?) in an operating room (where?).

Also, even if the user will be trained to use the tools, these have to be as user-friendly as possible. For the cage insertion, it is relevant to note that the cage is allowed to move inside the disc (as the nucleus is removed). The access is 11mm wide (while the cage is 10mm wide, providing 1mm margin laterally) and has the same height as the one of the cages (no margin axially). The tool(s) should be biocompatible, and its utilization should not damage the surrounding tissues.

6.2.2 Design functions

Three functions highlight the three steps for which the tools are used (Table 6.1), i.e. the choice of the cage dimensions (MF11), the cage insertion (MF12) and the removal of the tool(s) (CF13). The result should be that a cage with the appropriate dimensions is inserted in its desired position.

These three main functions should should a TLIF implementation (CF14). This means that the approach is unilateral and its side depends on surgeon's choice. The spine can be exposed with an open or minimally invasive access (no quantitative dimensions available regarding a minimally invasive access). Then, the intervertebral space is reached through an access of 11mm wide that is roughly as high as the cage. Also, the tool should be biocompatible, durable, user-friendly and used by one single surgeon, who would not have to follow an intensive training in order to use it (CF15 and CF16).

6.2.3 Design requirements

6.2.3.1 Functional requirements

The functional requirements specify what the tool(s) must do, i.e. what are the end-goals of the tools. These can be summarized by two main requirements based on MF11 and MF12 (Table 6.1):

A) Determine the appropriate cage dimensions
B) Insert the cage in its desired position

Also, all the tools should be biocompatible, durable, user-friendly and used by one surgeon without requiring too much training.

A) To choose between the available dimensions of the cage, one may use ghost cages or measurement tool(s). However, the insertion tool(s) will be firstly designed to know if ghost cages can be used in this context.

Figure 6.1: Objective tree of the tool(s), which have to determine the cage size and insert it (what?). The only user is the surgeon (who?). The tool(s) is used before the TLIF to choose the cage size and during it to insert the cage and retract the tool (what?). The TLIF is characterized by its access and its conditions on the tool(s), i.e. their biocompatibility and that they should not damage surrounding tissues (how?). The tool(s) is/are used in an operating room (where?).

Table 6.1: Main functions (MF) and constrain functions (CF) of the tool(s) (numbering starting from the last function of the cage).

Function type	**Function**	**Function criteria**
Main	MF11: Able to define the appropriate cage dimensions	11.1: Surgeon can choose the cage height, length and angle among the ones available 11.2: Done during the operation (as quick as possible)
	MF12: Desired cage insertion	12.1: Tool(s) compatible with the cage 12.2: The cage is placed in its desired position
Constrain	CF13: Removal while leaving cage in place	13.1: Remove tool(s) without moving cage
	CF14: Used during TLIF access	14.1: All functions can be fulfilled using an open or minimally invasive access to the spine 14.2: Insertion of the cage via a "11x*cage high*" access to the intervertebral space 14.3: Only one unilateral access, side up to surgeon 14.4: Sterilizability and biocompatible 14.5: Not damage surrounding tissue
	CF15: Handled by one surgeon	15.1: Tool(s) user-friendly 15.2: The utilization of the tool(s) should not require too much training
	CF16: Tool(s) can be reused for multiple TLIF	16.1: Durable

B) The cage insertion can be decomposed of three steps: linear insertion, axial rotation and forward motion (Figure 6.2). During the cage insertion, the axial rotation and the linear motion could be repeated in an arbitrary order. So, the linear and rotational motions should be independent. Many existing tools rely on the annulus to induce the cage rotation [25]. The cage is pushed on the annulus by the tool and, thanks to the cage convexity and the annulus convexity, the cage rotation is induced. However, this will not be considered as sufficient, as the cage is made of bone and its rough surface may damage the annulus in case of high friction.

6.2.3.2 Dimensional requirements

Looking to currently existing tools, a working length (length of the tool without the grip) of 191mm seems sufficient [131]. Hence, we selected a working length of 200mm. Then, the

(a) (b) (c)

Figure 6.2: Steps of the cage insertion. (a) Linear insertion via an access at 45° to the medial access until the cage has entered inside the (rest of) annulus. (b) axial rotation inside the annulus. (c) linear forward motion until the cage is in contact with the anterior facet of the annulus.

tools, or part of the tools, which should enter the intervertebral space for either evaluate the cage dimensions or insert the cage, should be at most 11mm wide and as high as the cage. Thus, the tools are set to be maximum 11mm wide and 12mm high. This is a safe dimensional choice. On top of that, a grip should be is added at the tool extremity (on the surgeon's side), which can have any dimensions.

To summarize, the dimensional requirements can be summarized as:

- A 200x11x12mm working part
- A grip with any dimensions at the extremity (on the surgeon's side)

6.2.4 Generating and evaluating solutions

6.2.4.1 Individual solution

Solutions fulfilling the functions of Table 6.1 are presented in Table 6.2.

A) Regarding MF11, one or few tool(s) can be used in order to determine the cage dimensions. Sol11.1 shows that the cage length can be chosen by reading on the measurement tools the maximal length fitting within the intervertebral space. Sol11.2 shows that this can be done by adding markers on the tool and perform a lateral medical image of it (this is done for some existing cage [52]). However, bone is not radiolucent and the cage might not be contrasted enough towards vertebral bone. However, using markers requires additional material and precautions. Therefore, marker should be added only if clinical trials show their necessity. Then, to evaluate the cage height and angle, Sol11.3 proposes to use 15 measurement tools or ghost cages for the 5 different height and 3 different angles. Sol11.4 proposes to use 3 trial tools or ghost cages for the three different angles and, on each one, add a plate on which a scale would allow the surgeon to define the height of the cage. The plate would be slipped until it is in contact with the vertebra or the annulus or both (as the access is at least as high as the maximum height of the cage, the plate fits into the access). However, Sol11.4 is not feasible as the surgeon needs to insert a tool or a

Table 6.2: Morphological chart of the tool(s) presenting solutions for main function and constraint function of the cage (corresponding numbers).

Functions	**Alternatives**			
	1	2	3	4
Sol11[11]	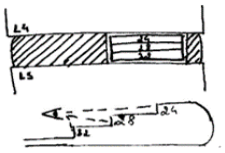		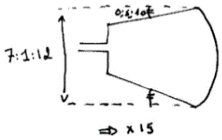	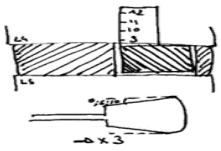
Sol12[12]	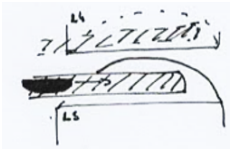	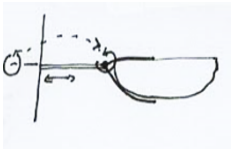	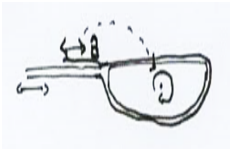	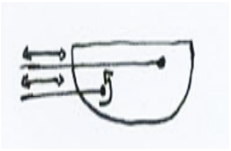
Sol13[13]	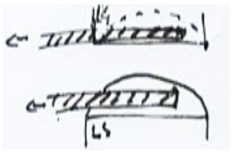	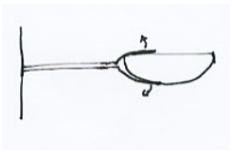	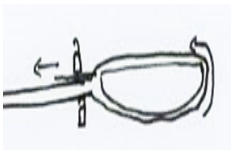	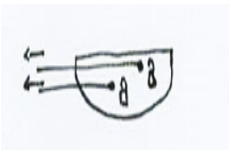
Sol14[14]	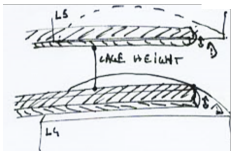	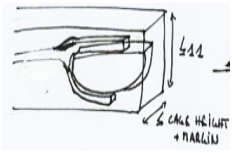	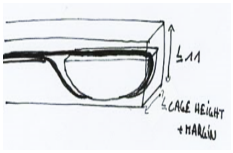	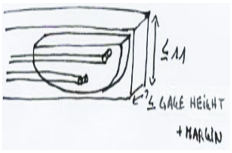
Sol15[15]	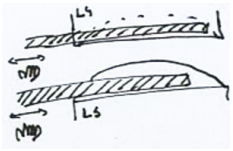	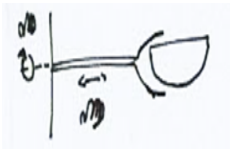	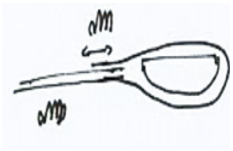	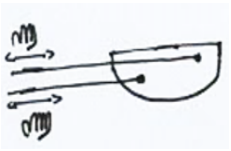
Sol16[16]	Ti			

[11] Able to define the appropriate cage dimensions
[12] Desired cage placement
[13] Removal while letting cage in place
[14] Used during TLIF access
[15] Handled by one surgeon
[16] Tool(s) can be reused for multiple TLIF

cage with a specific height in order to decide the height of the cage but can not decide with a plate external to the intervertebral space.

So, a measurement tool or ghost cage, would be provided for each cage height (Sol 11.3). Regarding the cage slope, the surgeon can choose it even with a flat trial tool, but it would be more reliable with an angled trial tool. Each trial should allow the surgeon to determine the cage dimensions by looking via the access if possible (Sol11.1) or using lateral imaging (Sol11.2), with markers in the cage only if necessary.

B) Sol12.1 proposes to add plates adjacent to the superior and inferior vertebrae before the insertion of the cage, this in order to minimize friction. To fix the cage on the insertion tool, a plier can be used (Sol12.2). The tool would move linearly, and the plier would rotate to rotate the cage. To remove the tool, the clamp would move away from the cage

and be carefully retracted (Sol13.2). Sol 12.3 and 12.4 allow the same motion, but via using a wire around the cage or two rods attached on the superior or inferior surface of the cage respectively. The tools would be retracted via unlocking the wire and pulling on one side (Sol13.3) and via unlocking the rods from the cage and pulling on it (Sol13.4). Adding plates to insert the cage will not be considered as it could damage surrounding tissues (CF14.5). Also, Sol12.3 requires making a small groove around the cage, which would require high precision that cannot be achieved with the production restrictions and it would weaken the cage. Sol13.3 argues why this solution is rejected, as removing the wire which is around the cage would lead to high friction, which would risk moving the cage after insertion (contradictory to MF13.1). Also, Sol13.4 is rejected as it requires two rods, but the access is too small axially (no margin). Therefore, Sol13.2 is only considered for the cage insertion, so one insertion tool will be provided.

The Sol14 precises that the tools should fit within the available space. This brings an additional argument to reject Sol12.1 and Sol12.4, which would put additional material between the superior and inferior surface of the cage and the vertebrae, while this space is highly restricted (mostly no margin). The solutions 15 shows how the tools would be handled by one surgeon.

Eventually, Sol16 proposes Ti as only potential material for the tools. Ti is the material used for most of the existing TLIF tool(s) [130, 25, 27, 24, 52]. This can be explained by its appropriate properties such as its lightweight with a high tensile strength, durability (CF16.1), sterilizability (CF14.3) and biocompatibility (CF14.3). The insertion tool is designed first, to know if using ghost cages would be feasible.

6.2.4.2 The insertion tool

Combining solutions

The insertion tool is based on Sol13.2. This tool allows to grab the cage using a plier specific to the cage, which can be loosened via doing a manipulation on the grip, such as via tightening the handle (Figure 6.16, red). Once grabbed, the cage can be linearly inserted (Figure 6.16, blue) and rotated (Figure 6.16, green). Then, the cage is loosened and the inverse rotation and linear motion can be achieved in order to remove the insertion without moving the cage. Hence, the cage design has to be adapted in order to fix the cage on the insertion tool via the plier.

The anchorage

In order to grab the cage with the insertion tool, an anchorage should be provided in the cage. This anchorage should be within the cage. As the anchorage should allow the plier to rotate around it, the contact between the anchorage and the insertion tool should be circular.

A grabbing beam The anchorage is usually done thanks to a cylindrical axial "beam" within an empty space of the cage (hereafter referred to as grabbing beam). Already, a design constraint due the insertion tool appears. As an anchorage should be provided, no pore can be done across the space where there is the anchorage. To define the dimensions of the anchorage, the grabbing beam radius (r), the plier width (x) and the space between

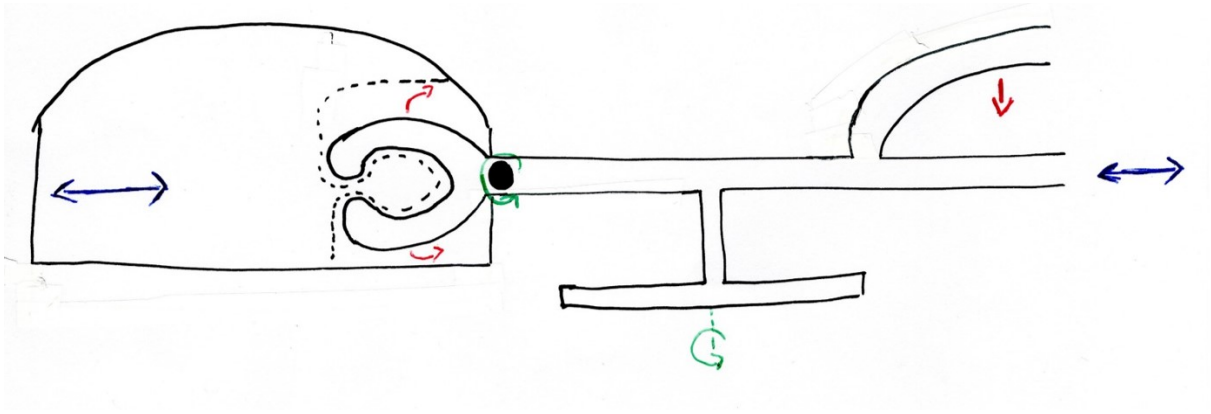

Figure 6.3: Schematic representation of the insertion tool. The arrows of the same color show the associated motions. Tightening the handles spreads the braces of the clamp (red). Moving linearly the tool moves linearly the cage (blue). Rotating the side handle rotates the cage (green).

the plier and the beam, i.e. the necessary space such that the plier can rotate without moving the cage, have to be defined (Figure 6.4).

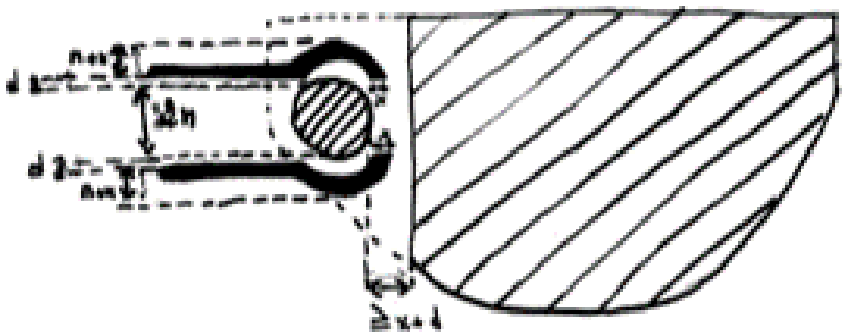

Figure 6.4: Cage anchorage: dimensions. r = radius of the cylindrical grabbing beam = inner radius of the plier. x = width of the pliers. d = necessary release distance.

Arbitrary, the width of the pliers (x) is fixed to 0.8mm and the release distance (d) to 0.2mm [1]. So, in order to allow the plier to rotate around the cylindrical beam without rotating the cage, an empty space of 0.8+0.2=1mm wide around the grabbing beam is necessary. In order to evaluate the feasibility of the anchorage, a beam radius of 2mm is used (Figure 6.5a), and the same simulations as for the cage designs are conducted on the OAP design with a low porosity using the longitudinal anisotropic model.

Simulations show that this design leads to a maximal z normal stress larger than the yield limit (52.5MPa in z direction for longitudinal fibers, Figure 6.5b). This was observed for other grabbing beam radius and beam localization. This is explained by the fact that the grabbing beam should sustain more stress than the nodes at the same localization without the anchorage system.

Among many other (simulated) solutions, the grabbing beam can be reduced to a radius of 1mm (as it decreases the absolute maximal stress, assuming this provides enough

[1] In case of this tool would be clinically tested, these distances would be adjusted id the tests reveal them not sufficient.

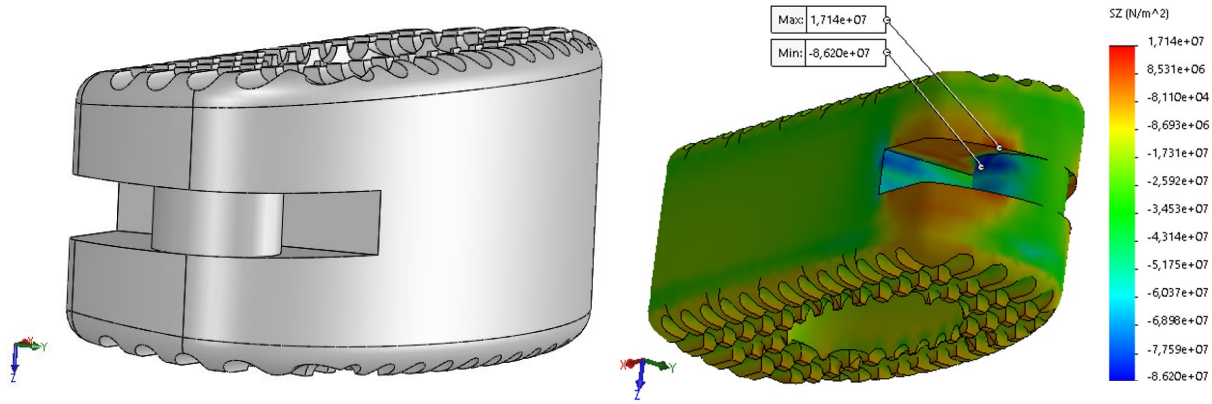

(a) (b)

Figure 6.5: Case usual anchorage design with an anchorage of 2mm height and cylindrical beam with its axis in the middle of the frontal length and its edge adjacent to the the lateral surface of the cage. (a) Anchorage within the OAP design. (b) Normal z stress heatmap using the longitudinal anisotropic model (normal z stress is the maximal normal stress).

stability when inserting the cage) and the grabbing beam can be moved to the cage corner (the plier would protrude by 1mm, which would give a total width of 11mm and therefore allow to enter through the 11mm access, Figure 6.6a). Also, a cavity can be created in the posterior part of the cage (as the lateral surface is flat there, avoiding stress concentration on the anterior surface when porous) (Figure 6.6b). However, none of these options are producible. Indeed, a round bur of 2mm diameter should be able to produce it. So, a 2mm wide access should be provided all around the beam. So, for a design with a centered beam (like Figure 6.5a), a full 2mm wide empty space behind the beam can be created (Figure 6.6c). For a beam on the corner of the cage, a 2mm wide access can be provided (Figure 6.6d). However, both lead to a maximal stress above the yield limit (Figure 6.6c and Figure 6.6d).

It appears that two constraints, i.e. the material and production constraints, would require an advanced optimization in order to find the most appropriate anchorage (discussed further in section 7.2). Figure 6.6 shows that the structure would break due to concentrated stresses within the grabbing beam.

A straight slot To decrease the stresses, one may use a straight slot (two half circles bonded by two straight line) instead of a cylindrical beam to grab the cage with the insertion tool, in order to increase the cross surface of the anchorage system and so decrease the maximal stress, while keeping circular surfaces between the insertion tool and the anchorage (Figure 6.7a). This solution alone did not solve the stress issue even if the stresses were reduced (Figure 6.7b). Additionally, the global shape of the cage can be changed to minimize the surface above the empty space (Figure 6.7c). This did not solve the issue either, even if the maximal stress was close to the yield limit (Figure 6.7). It was considered to fill the space behind the straight slot which is not necessary for the rotation of the plier around it. However, due to production constraints, only a very small part could be filled, and this influenced only slightly the results.

Based on these analyses, grabbing the cage laterally was excluded. Indeed, due

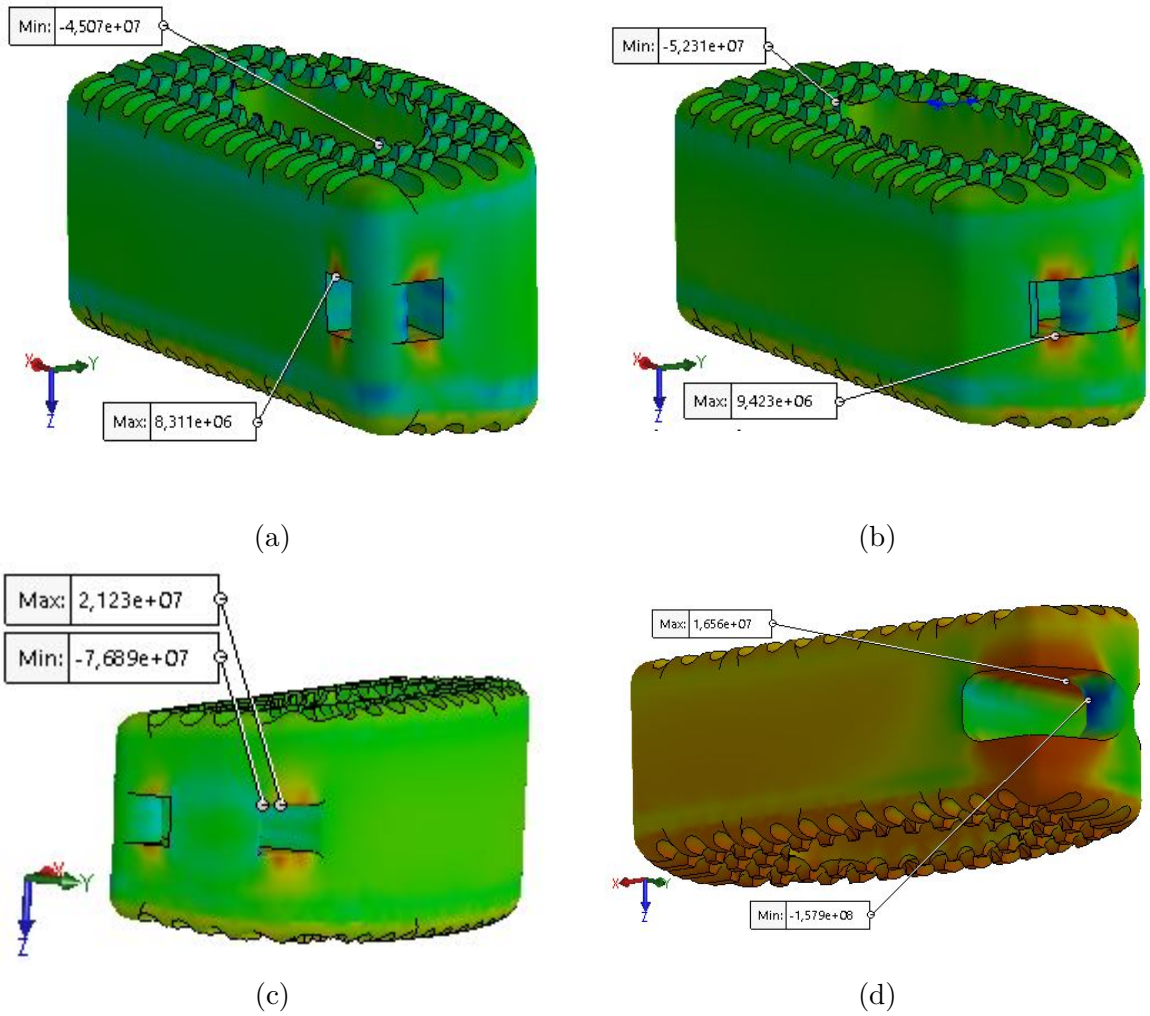

Figure 6.6: Potential anchorage system with a grabbing beam radius of 1mm. (a) Grabbing beam on the corner. (b) Grabbing beam in a cavity. (c) Anchorage system with frontal hole to allow the machinning machine acceding the whole beam surface, which lead to yield (yield limit: 52.5MPa). (d) Grabbing beam with its axis in the middle of the frontal length and its edge adjacent to the the lateral surface of the cage, with a 2mm wide access to the beam.

to the production constraints, this requires making a large frontal hole all around the anchorage, which lead to a maximal stress above the yield limit. Intuitively, this was already highlighted when examining the stress for the OFP and FFP (Figure 5.13).

Axial anchorage So, it is decided to grab the cage axially. To this end, a circular hole is done on the superior and inferior surfaces, in which the plier would be inserted to attach the cage. Once the cage grabbed, the cage can be move linearly (Figure 6.8a) and rotate (Figure 6.8b), which can be done multiple times in an arbitrary order in order to place the cage (Figure 6.8c). When the cage placed, it might be loosened, and the tool is able the make the inverse rotation (Figure 6.8d) and to be linearly retracted (Figure 6.8e). As the access is 45° or less to the medial axis, the cage should at most rotate of 45° (the access is generally less angled, 45° is taken as safety margin). Figure 6.8d illustrates that the tool

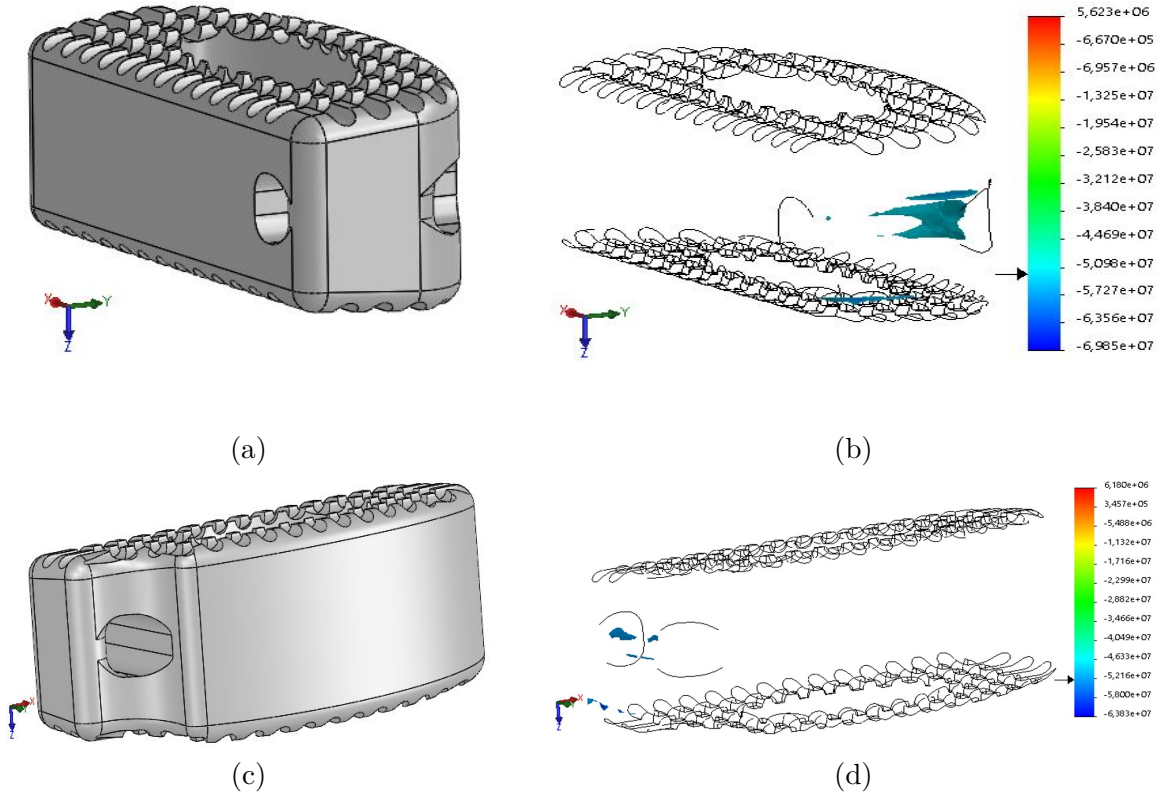

Figure 6.7: Potential anchorage system with a grabbing straight slot of length of 5mm, width of 1mm. (a) Anchorage system using a straight slot. (b) Normal z stress for design (a). (c)Adaptation of (a) adjusting the cage design to minimize the amount of surface above the empty space (d) ISO clipping of z normal stress for 52.5MPa using (c), showing stress above the yield limit within the grabbing system.

can be in contact with the annulus (red). However, most existing tool grab the cage and perform the same motion, and the tool fits inside the available place after cage placement. Nevertheless, this should be checked when testing the tool.

The insertion path defines the design of the anchorage system on the cage. First, a flat surface should be created such that the tool can slide and tight the cage to attach it, and a maximal rotation of 45° of the tool around the hole should be allowed once the cage unattached by loosening the cage (Figure 6.9a). For the maximal slope, taking the surfacing into account, this means that the surface is at $\approx 1.8mm$ from the most superior part of the cage (Figure 6.9b). Then, a hole is made on the created flat surface because the friction is not supposed to be sufficient to ensure enough stability (Figure 6.9b). When the plier is outside of the hole, the tool should be removed. So, the anchorage should be defined such that, once the tool is loosened, it can be removed within the available space. As there is 1.8mm free above the surface, the hole is arbitrary set to be 1.5mm deep (Figure 6.9b and Figure 6.9. Please note that the dimensions are arbitrary chosen and should be checked, especially if 0.3mm margin would be enough for the plate of the plier and if an additional margin should be provided to remove the tool (see section 7.2). In order to have one tool for all design, the hole is set to be 1.5mm deep for every design. This means that, for whichever design, the flat surface should always be at 1.8mm deep. The radius of the hole is arbitrary fixed to 2mm, which can also be adapted based on

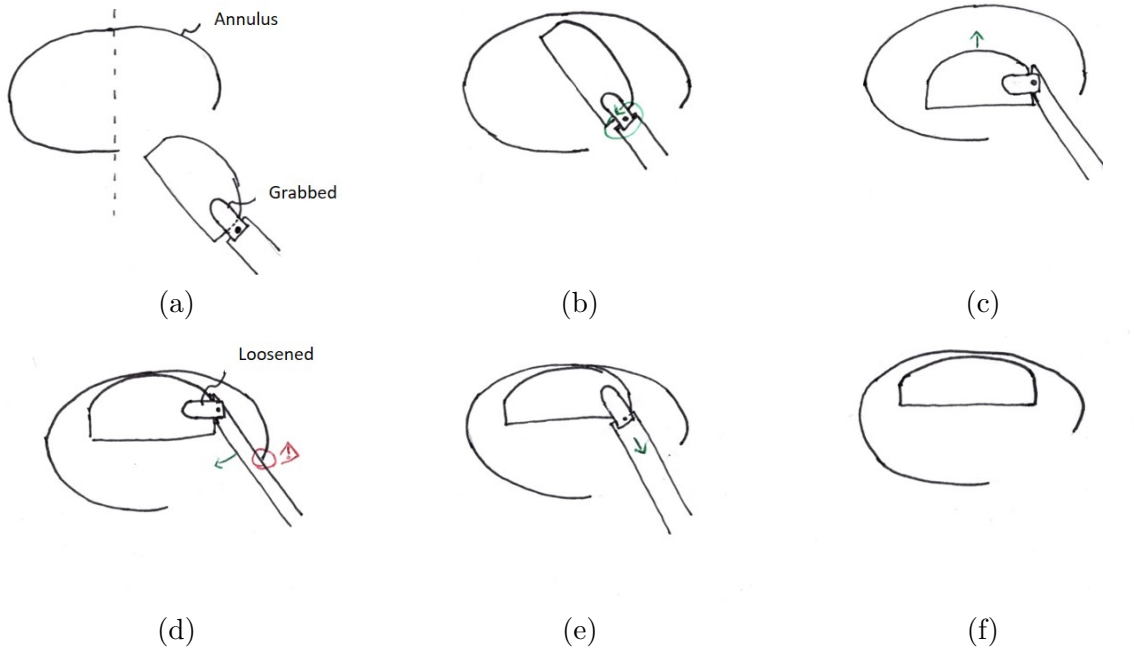

Figure 6.8: Steps of the insertion of the cage using the insertion tool. (a) Cage fixation on the tool and linear insertion. (b) Cage rotation. (c) Cage linear forward motion until in contact with the anterior facet of the annulus. (d) Loosen of the cage and reverse rotation of the tool. (e) Tool linear removal. (f) Final result when cage placed.

clinical testing.

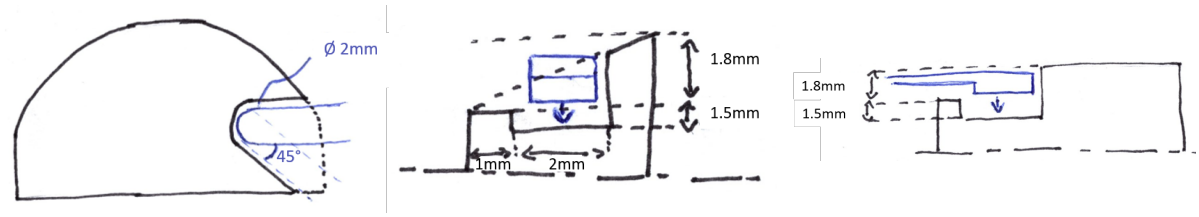

Figure 6.9: Cage anchorage for the insertion tool (blue) from a top (a), lateral (b) and frontal (c) view.

Based on all these specifications, the anchorage is added on the OAP cage design. To take the production constraint into account, all edged are rounded with a circular fillet of 1mm radius (Figure 6.10).

Even if this anchorage leads to stresses above the yield limit, even above the failure limit, this is only around the anchorage system (Figure 6.11). So, yielding occurs within the surfacing, which is acceptable. Nevertheless, this is due to high stress concentration on the intersection of the anchorage and surfacing. Therefore, some design optimization with the final design might potentially eliminate these regions and so avoid yielding.

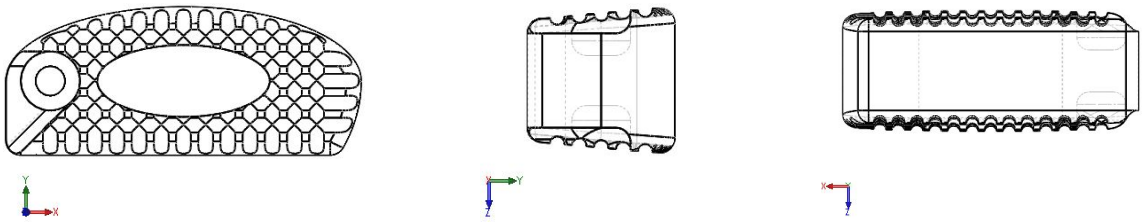

(a) (b) (c)

Figure 6.10: OAP design of the cage with anchorage for the insertion tool from a top (a), lateral (b) and posterior (c) view.

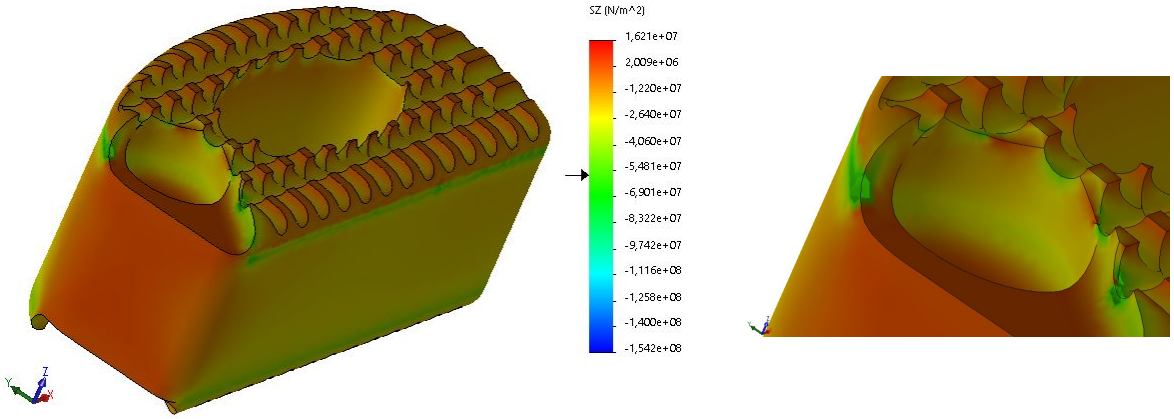

(a) (b)

Figure 6.11: Normal z stress for the final design with the anchorage. (a) normal Z stress ISO clipping within the range [-52.5;52.5]Mpa. (b) Zoom on the region of interest, highlighting yielding volumes (regions outside the range are removed).

6.2.4.3 The measurement tools

Based on the insertion tool, using ghost cages is rejected because removing the cage would require making a perfect inverse rotation which can be very challenging and would increase the operation time. Indeed, ghost cages are never used for TLIF in the literature, but rather for PLIF of ALIF, which uses a straight access. So, measurement tools will be provided.

Usually, the height of measurement tools is 1 to 1.5mm smaller than the one of the inserted cage, in order to avoid losing the pressfit (the pressure on the cage which would keep it in place once inserted). So, it is chosen to use measurement tools 1mm less high. The height and length of the cage can be determined with a straight insertion, while the cage slope can be only determined if the measurement tools can be placed like the cage, i.e. if the surgeon can make a 45° rotation of the tools. Here, two situations appear. The first situation if when the access is a tunnel, in which case a rotation of the measurement tools is impossible, and the tool can only be inserted linearly (Figure 6.12a). These measurement tools are referred as straight measurement tools. The second situation is with a two-sided open access, which is like a tunnel access, but the lateral faces can be spaced (like a speculum, resulting access on Figure 6.12b). In this case, the measurement tools can be rotated to be placed like the cage (Figure 6.12b). However, this would not be

representative of the cage length that can be inserted as the motion is different. These trial tools are referred as angled measurement tools. Please note that straight measurement tools might be sufficient to define the cage slope, as some manufacturer only provide straight measurement tools [25].

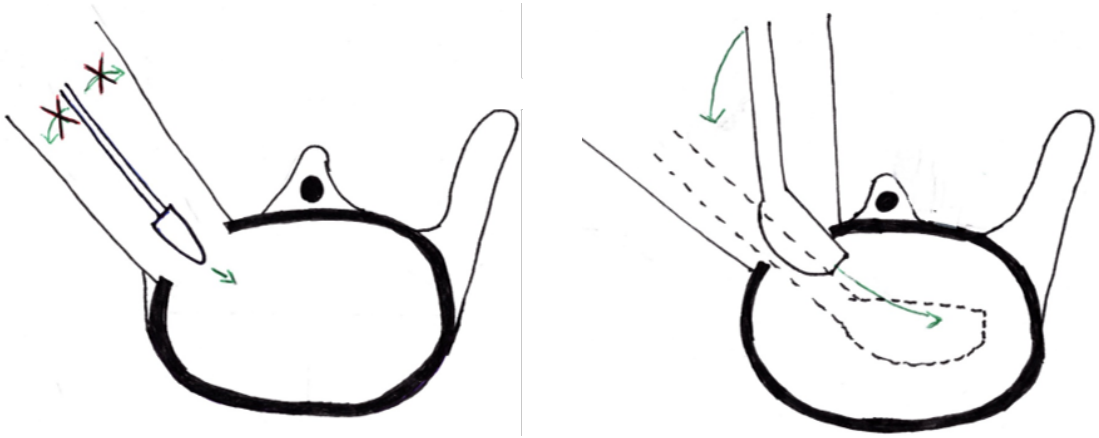

(a) (b)

Figure 6.12: Cage trial tools. (a) Straight trial tool for a tunnel access. (b) Angled trial tool for a two-sided open access (like a speculum).

Therefore, a linearly inserted straight measurement tool will be used to define the cage length and height (Figure 6.17). To this end, the design delimits the three lengths, which can be seen via looking through the access if this is wide enough or using a lateral imaging. Please note that the access is oblique, but the lateral imaging can be adapted to be orthogonal to the tool axis, such that the imaging is at 90° to the tool and the length can be easily visualized. Once the cage length and height determined, and if possible, one or few angled measurement tool(s) are inserted in order to define the cage angle (Figure 6.18). The angle measurement tools should not help to determine the length, but still be representative of the cage height. So, these will have the minimal length to facilitate their insertion but all available heights and angles. These tool have not been evaluated due to the lack of access to the labs [2].

6.3 Design output

6.3.1 The cage

Due to the anchorage, one lateral portion of the cage cannot be porous. In practice, even if the anchorage is not directly in contact with the vertebrae, bone will fill the gap thanks to bone remodelling. Therefore, the load will be applied on the anchorage through the formed bone, but only after some bone remodelling. For this reason, it would be unrealistic to simulate load on it without taking bone remodelling into consideration. However, after bone remodelling has filled the cage between the vertebrae and the anchorage, the reestablishment of the anterior stability should remain symmetric. Therefore, the pores can only be symmetric.

[2]Consequent to COVID-19 situation

6.3.1.1 OAP versus FAP

For the OAP design, the axial pore remain centered on the middle of the cage, with an elliptic shape (Figure 6.10). For the FAP design, some changes have to be done. First, the pores which would go through the anchorage are removed, as well as the corresponding pores on the other lateral side, in order to keep the symmetry. Then, the pores must be at least 2mm in diameter, due to the production restrictions. The pores should be at least at 1mm from the anchorage. Then, these are symmetrically distributed (Figure 6.13).

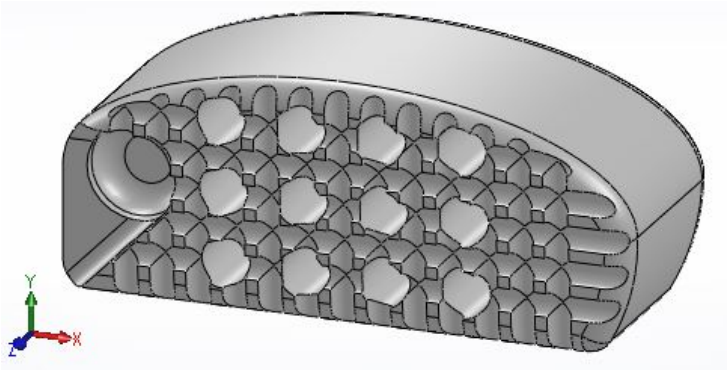

Figure 6.13: Final design of the FAP design, with an anchorage for the insertion, low porosity and taking the symmetric and production restrictions into account.

The FAP design provides roughly the same axial stiffness as the OAP design for the same porosity (was observed on Figure 5.14 and confirmed by simulation with the adapted design of Figure 6.13). However, the FAP design exhibits very thin walls, between each other pore and between the pores and the cage walls. Hence, one may assume that, in case of non-axial load such as torsion, these walls would break easier than the ones of the OAP design. So, the FAP design is rejected and the OAP design is selected. Therefore only the FD1, using one large axial pore with few frontal pores, is considered for the optimization of the cage porosity.

6.3.1.2 Optimization of the cage porosity

Analysis of the parameters of FD1 Based on FD1, three possibilities appear:

- All pores dimensions are set to zero, such that the design becomes the full design (Figure 6.14a)
- Only the dimensions of the frontal pores are set to zero, such that the design becomes the OAP design (Figure 6.14b)
- the OAP is combined with frontal pores of 1mm radius, with centers space of 3mm (Figure 6.14c)

The frontal pores are set to 1mm radius, due to the production restriction. As already mentioned, the full design does only lead to small fracture at the intersection of the surfacing and the anchorage (Figure 6.14a). Regarding the OAP design, some exceeding stress appear just above the fixed (down) surface, on the opposite side of the anchorage (Figure 6.14b). This is explained by the reduced surface of on which the force is applied, due to the anchorage, leading to more stress concentration in this region. This shows that, in case of using the OAP design, the porosity should be adapted due to the anchorage.

Regarding the OAP combined with the FFP, a large portion of the cage volume exceeds the yield limit (Figure 6.14c). This shows that frontal pores would not be indicated, as this leads to high stress concentration around it. This might perhaps be reduced with smaller pores, but this is not feasible due to the production constraint, and so not tested. Similar results are observed for other pores localization and numbers. So, combining frontal pores with an axial pore is excluded. Therefore, the FD1 is reduced to the OAP deisgn.

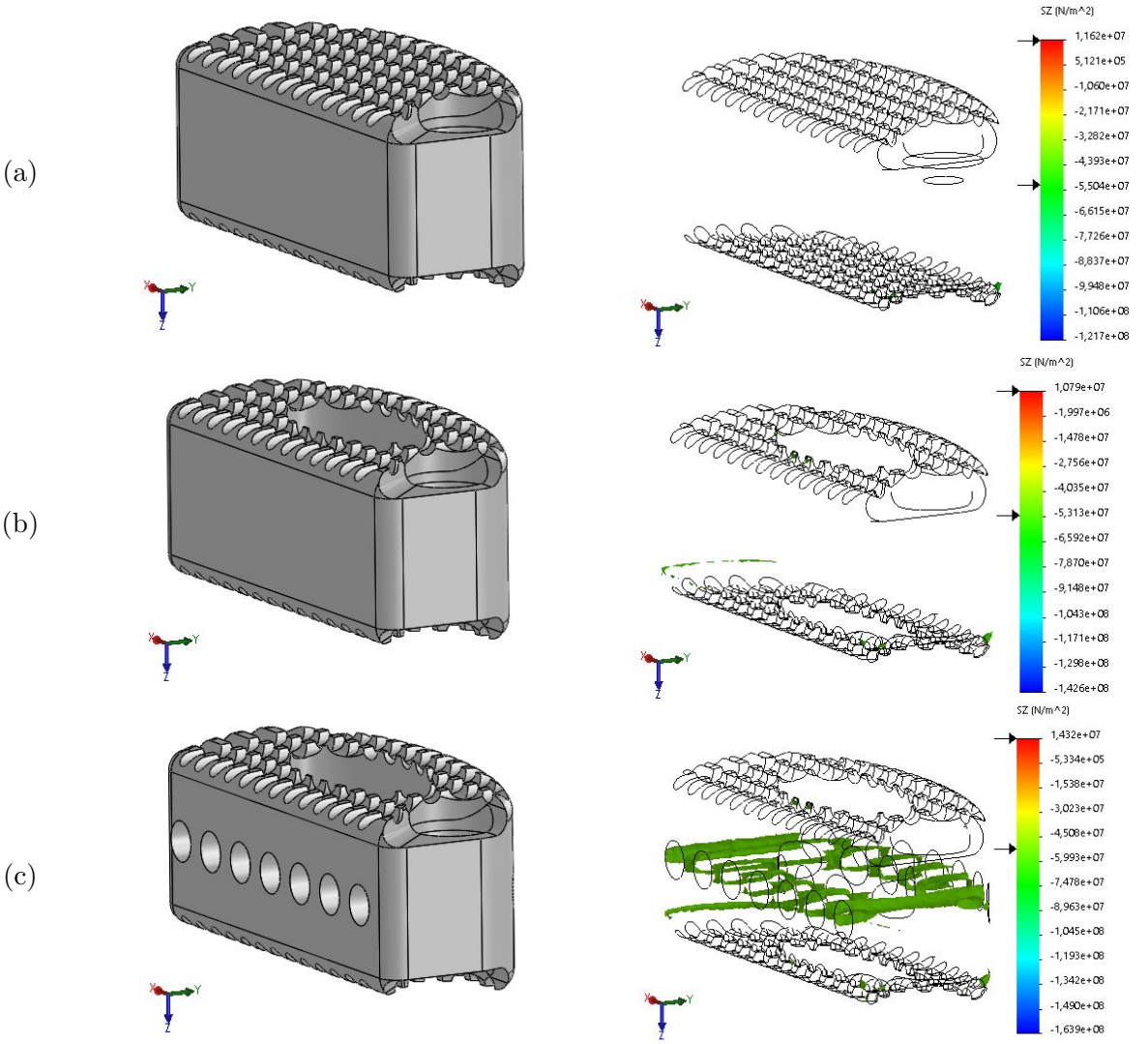

Figure 6.14: Final designs of the cage with anchorage for the insertion tool (left) and an iso clipping for the range [-52.5;52.5]Mpa of normal z stress (right). (a) All pores dimensions are set to zero, such that the design becomes the full design. (b) Only the dimensions of the frontal pores are set to zero, such that the design becomes the OAP. (c) OAP with low porosity is combined with frontal pores of 1mm radius, with centers space of 3mm.

Optimization of the OAP design Regarding the OAP design, the optimization study integrated in SolidWorks is used. The variables are lengths of the major (x axis) and minor (y axis) axis of the ellipse forming the pores. The major axis is tested within the range [1:6]mm, as 1mm is the minimal axis length due to the production constraint and

6mm is the maximal length which does not interfere (with the anchorage with an arbitrary margin of 1mm). The minor axis is tested within the range [1:4]mm for the same reason, but regarding the outer wall for the maximal value. As constraints, the absolute normal x, y and z stresses should be below 92.78,52.5 and 52.5MPa respectively (these are the yield limits in each direction). Only the region of interest, i.e. the region outside the surfacing and the anchorage, are used for the optimization, as microcracks in the surfacing and anchorage are accepted. The region of interest is manually delimited. The goal is to maximize the average displacement of the top surface, i.e. the surface where the force is applied.

Using the cage of 24mm and 10mm high with a lordosis angle of 10°, a first optimization suggested a major axis of 6mm and a minor axis of 1mm. This shows that the major axis can be increased until reaching its maximal value without leading to excessive stresses. However, this is not the case of the minor axis, which leads to excessive stress on the intersection of the anterior facet and the fixed surface if the minor axis is too large (similar to the stress distribution shown on Figure 5.10). Based on this, a new optimization was launched using a major axis of 6mm and the same range for the minor axis, but with smaller steps, in order to obtain more precision on the optimal minor axis. A minor axis of 2.2mm is chosen as it maximises the axial deformation ($z = 0.01824mm$), so minimizing the cage stiffness ($k = 169.96\frac{kN}{mm}$). This same optimization should be apply to each cage, in order to define the pore dimensions (see section 7.1). One may wonder if a rectangular hole (with rounded corners for manufacturing) would not be better, but an optimization with a rectangular pore provides a smaller axial deformation (0.015mm) when respecting the same stress limits. So, the pore is elliptic with a major axis of 6mm and a minor axis of 2.2mm (Figure 7.1).

Please note that this design of the cage exhibits microcracks within the surfacing, but this is supposed acceptable and could maybe be corrected thanks to design optimization. Also, the contact surface projected on the plane tangent to the surfacing, i.e. the contact surface without surfacing or the surface orthogonal to the compressive force, is equal to 173.38mm^2. This surface is the minimal one (larger surface for cage of 28 or 32mm long), and this is within the range of commercially available cages (170 to 180mm^2). Hence, assuming that the required surface is independent from the cage properties, the cage would provide enough contact surface.

With the final design, simulations reveal that the design of 7mm does break, even without pore (full design), for any lordosis angle. The cages with all the other dimensions (Table 4.5) does not break, even with an axial pore of 2mm diameter (minimal pore size). Therefore, all the other designs are accepted, and the pore dimensions will be optimized for each design independently.

6.3.2 The insertion tool

The insertion tool allows to lock or unlock the cage, thanks to sliding forward the slide lock (this is preferred to the initial idea of pressing the grip, to avoid interfere with the grip and provide a user-friendly grip), which move the plier in order to tight the cage in the plier (Figure 6.16, green). Also, the plier can rotate via rotating the rotating knob (Figure 6.16, yellow). The linear motion is achieved via moving the tool using the grip (Figure 6.16, blue). The cage design presents an anchorage adapted to the plier of the insertion tool (Figure 6.10)

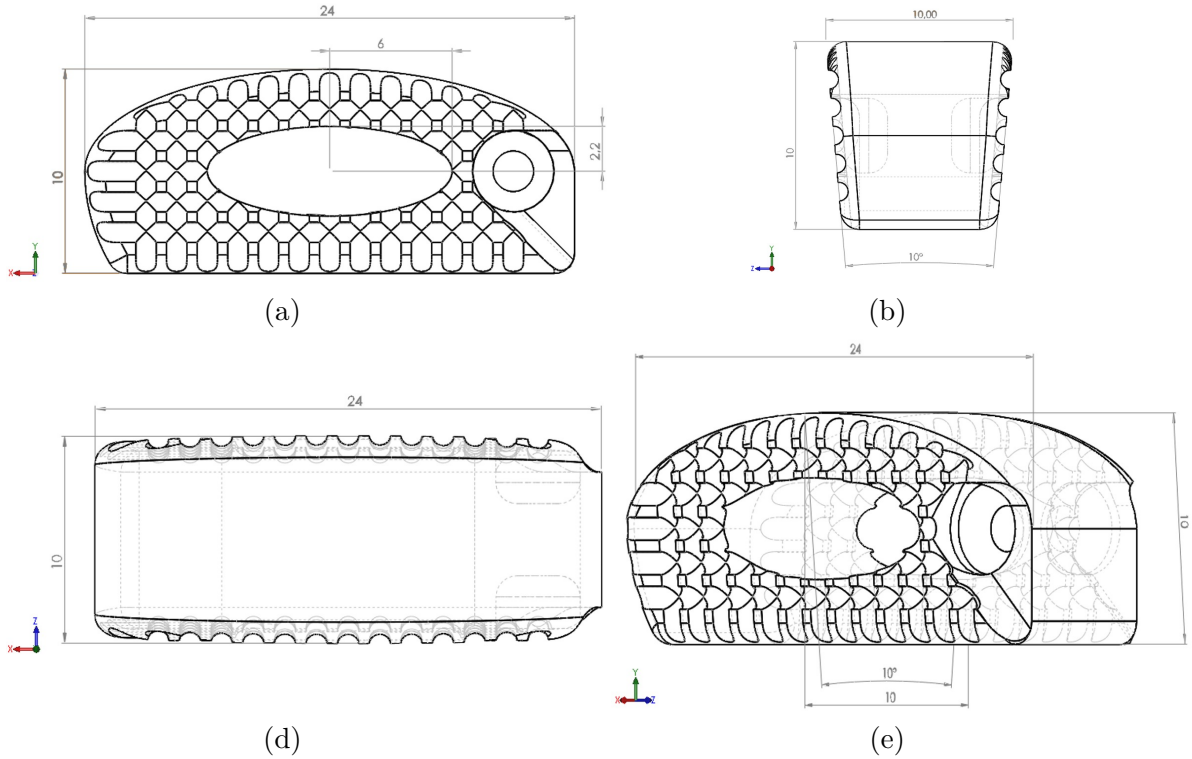

Figure 6.15: Cage final design (length: 24mm, width:10mm, height=10mm, angle=10°) with one elliptic (major axis: 6mm, minor axis: 2.2mm) large pore and an anchorage for the insertion tool from a top (a), lateral (b), posterior (c) and three-dimensional (d) view.

6.3.3 The measurement tools

The straight measurement tools is composed of one bulky part of a length of 24mm, followed by a decreased section and by an increased section, creating a ring that corresponds to a 28mm length. Then, the section is decreased and increased again until reaching the start of working part of the tool, corresponding to a 32mm length. This design allows the surgeon to define the length of the cage entering the available space via:

- The tool does fit including the ring: use 24mm length cage
- Ring fits but not the start of the working part of the tool: use a 28mm length cage
- Start of the working part of the tool fits: use a 32mm length

This can be visualized via directly looking through the access of via lateral imaging. This tool is provided for all cage height minus 1mm, i.e. with heights of 6, 7,8,9,10 and 11mm height (Figure 6.17).

After the cage length and height are defined, if the access is a two-sided open access, an angled measurement tool can be inserted to decide the cage angle. So, only one angles measurement tool would be used if possible. This tool should have the same height as the appropriate straight measurement tool. Once the angled measurement tool is inserted ((Figure 6.12b), a lateral imaging helps to decide the appropriate cage angle via visual inspection of the fit of the angled measurement tool with a 5° angle or 10° angle or both. Figure 6.18 shows the angled measurement tool for a 7mm height and 10° angle, but ten of them will be provided for the five heights of 7,8,9,10 and 11mm and the two angles of 5° and 10°.

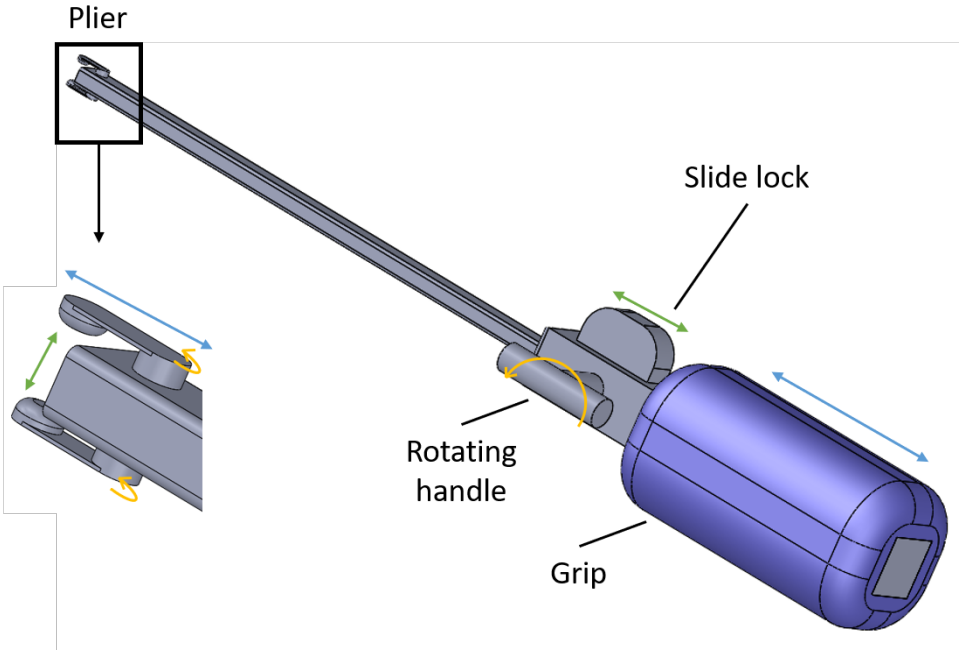

Figure 6.16: Insertion tool showing the linear motion thanks to linear motion of the grip (blue), rotational motion of the plier thanks to the rotation of the rotation button (yellow) and cage locking via tightening of the cage by the plier thanks to the sliding locking button (red).

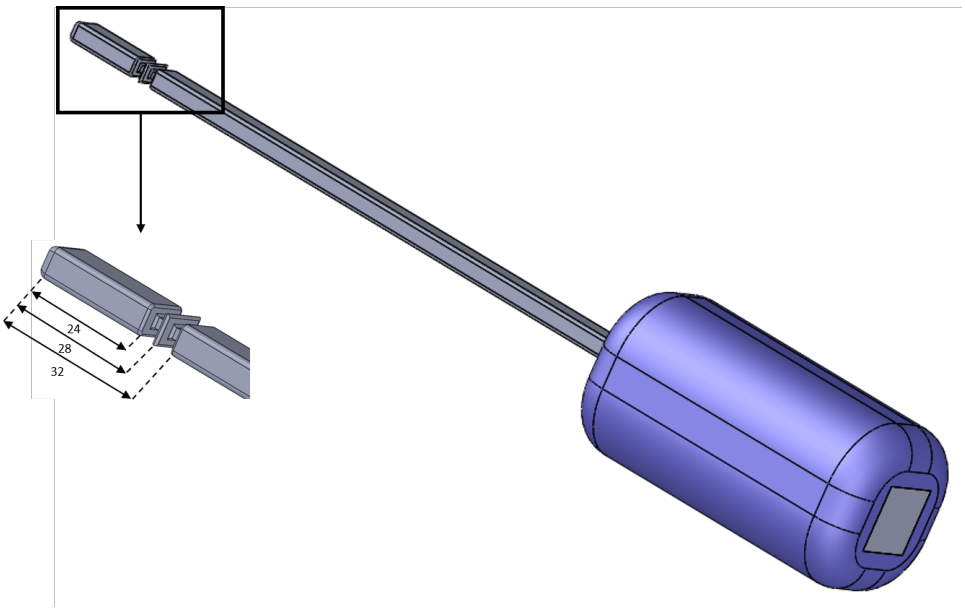

Figure 6.17: Straight measurement tool of 8mm height. Zoom on the extremity which allow to evaluate the appropriate cage length via a visual inspection through the access or using lateral imaging. Five straight measurement tools are provided for the five cage heights minus 1mm (7,8,9,10 and 11mm).

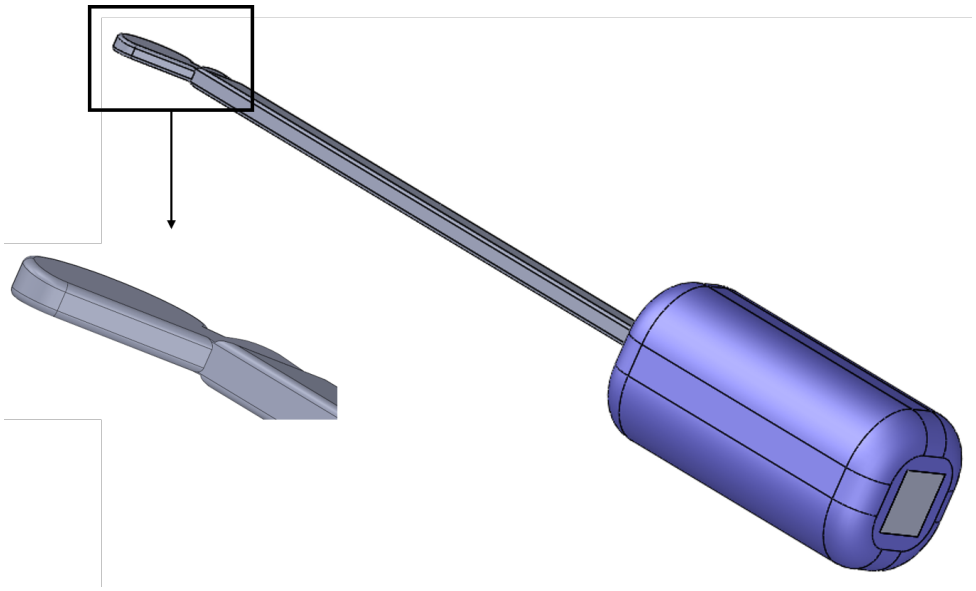

Figure 6.18: Angled measurement tool of 10mm height and 10° angle. Zoom on the extremity which allow to evaluate the appropriate cage angle via a visual inspection using lateral imaging. Ten angled measurement tools are provided for the five measurement height (6,7,8,9,10 and 11mm) and two different angles (5° and 10°).

6.3.4 Tools optimization

Based on a feedback from an expert, some features of the tools are changed before presenting the final design, as a small second design loop. First of all, the material is changed from titanium to inox 316L, as it exhibits the same advantageous material properties while being significantly cheaper. The grip is adjusted to be more user-friendly. The tool is made of concentric cylinders instead of rectangles, as cylinder is easier for the manufacturing of the tools and also cylinders present smoother insertion. Consequently, the forward part is flattened for the insertion, on a height corresponding to the measurement height, on a arbitrary distance of 40mm that is supposed to be enough to fully insert the tool. Indeed, the tool would be inserted of 32mm maximum inside the nucleus, and the annulus is 5mm on average (this distance might be corrected according to clinical trials if necessary) [61]. Also, the fillet of the forward face of the straight trial tool is corrected for a easier insertion. Regarding the insertion tool, the forward part of the working rod is rounded because the previous design did not allow to rotate the cage once fixed. So, it means the working part cannot, or only very slightly thanks to a linear contact, be used to push on the cage. this means that the linear and rotating motions of the cage are fully ensured by the plier alone. The plier dimensions are corrected in order to be able to fix any cage, even the smallest one. The corrected tools are presented in section 7.1.

Chapter 7

Final design and future perspectives

7.1 Final design

7.1.1 The cage

The final design of the cage is based on simulations performed with the one providing the minimal contact surface (24mm long), the average height (10mm high) and the maximal stress (10° angle). the desired porosity is achieved via one elliptic axial pore in the middle, and the optimization of the cage determined the lengths of the major (in the direction of the length) and minor (in the direction of the width) axes of this pore. This in order to obtain the appropriate stiffness and axial strength while not yielding. A surfacing is performed to ensure cage fixation once implemented, using circular grooves of 1mm radius and spaced of 1.5mm on both superior and inferior surfaces. An anchorage adapted to the insertion tool is added on one side, on both inferior and superior surfaces (Figure 7.1).

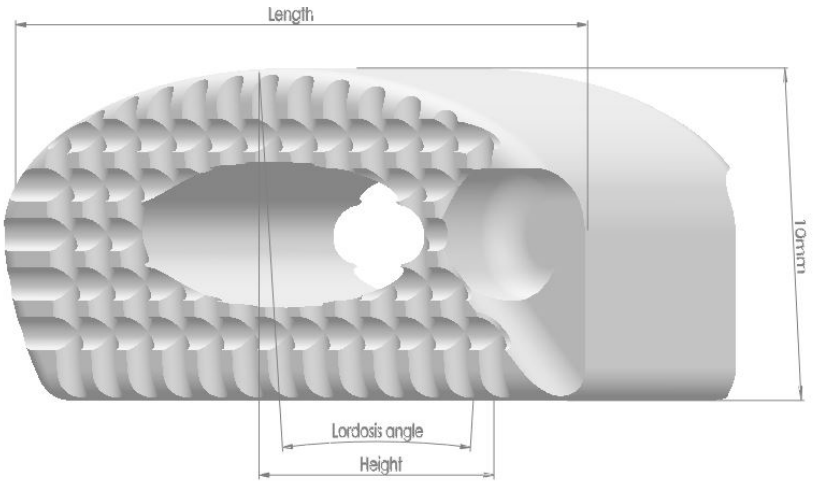

Figure 7.1: Optimized design of a cage made of cortical bone for a TLIF, using a large axial elliptic to adjust its mechanical properties and an anchorage to attach it to the insertion tool. The cages are all 10mm wide, but the length, height and lordosis angle vary. The dimensions of the axial pore vary according to the dimensions of the cage.

The provided cages have all possible dimensions that could be required based on clinical and anatomical values (Table 4.5), but the cages of 7mm high are excluded as these would

break, even without pore. All the cages are 10mm wide. So, 45 cages with different dimensions are provided for insertion (Table 7.1). The optimized dimensions of the axial pore is provided for the cages with the smallest, medium and largest volume (Table 7.1).

Table 7.1: Dimensions of all cages using the notation *length* x *height* x *lordosis angle*. The dimensions of the axial pore is given for the cages with the smallest (24mm x 8mm x 10°), medium (28mm x 10mm x 5°) and largest (32mm x 12mm x 0°) volume using the notation (*Length of major axis* x *Length of minor axis* below the cage dimensions.

24mm long	**28mm long**	**32mm long**
24mm x 8mm x 10° (*6mm* x *1.2mm*)	28mm x 8mm x 10°	32mm x 8mm x 10°
24mm x 9mm x 10°	28mm x 9mm x 10°	32mm x 9mm x 10°
24mm x 10mm x 10°	28mm x 10mm x 10°	32mm x 10mm x 10°
24mm x 11mm x 10°	28mm x 11mm x 10°	32mm x 11mm x 10°
24mm x 12mm x 10°	28mm x 12mm x 10°	32mm x 12mm x 10°
24mm x 8mm x 5°	28mm x 8mm x 5°	32mm x 8mm x 5°
24mm x 9mm x 5°	28mm x 9mm x 5°	32mm x 9mm x 5°
24mm x 10mm x 5°	28mm x 10mm x 5° (*7.9mm* x *1.7mm*)	32mm x 10mm x 5°
24mm x 11mm x 5°	28mm x 11mm x 5°	32mm x 11mm x 5°
24mm x 12mm x 5°	28mm x 12mm x 5°	32mm x 12mm x 5°
24mm x 8mm x 0°	28mm x 8mm x 0°	32mm x 8mm x 0°
24mm x 9mm x 0°	28mm x 9mm x 0°	32mm x 9mm x 0°
24mm x 10mm x 0°	28mm x 10mm x 0°	32mm x 10mm x 0°
24mm x 11mm x 0°	28mm x 11mm x 0°	32mm x 11mm x 0°
24mm x 12mm x 0°	28mm x 12mm x 0°	32mm x 12mm x 0° (*6.8mm* x *2.8mm*)

7.1.2 The tools

Five straight measurement tools of 7 to 11mm high are provided to evaluate the cage height and length (Figure 7.2a), and ten angled trial tools of 7 to 11mm high and with a 5° or 10° angle are provided to evaluate the cage slope (Figure 7.2b). The measurement tools are 1mm less hiss high than the cages, in order to avoid loosing the pressfit. One insertion tool is provided, which allow to attach any cage and insert it via a TLIF approach, i.e. allows linear motion and rotation (Figure 7.2c).

To implement the cage with the appropriate dimensions, its height and length are first determined using the straight measurement tools. Then, if the access allows it and if the cage should be angled, a angled measurement tool, with the same height as the

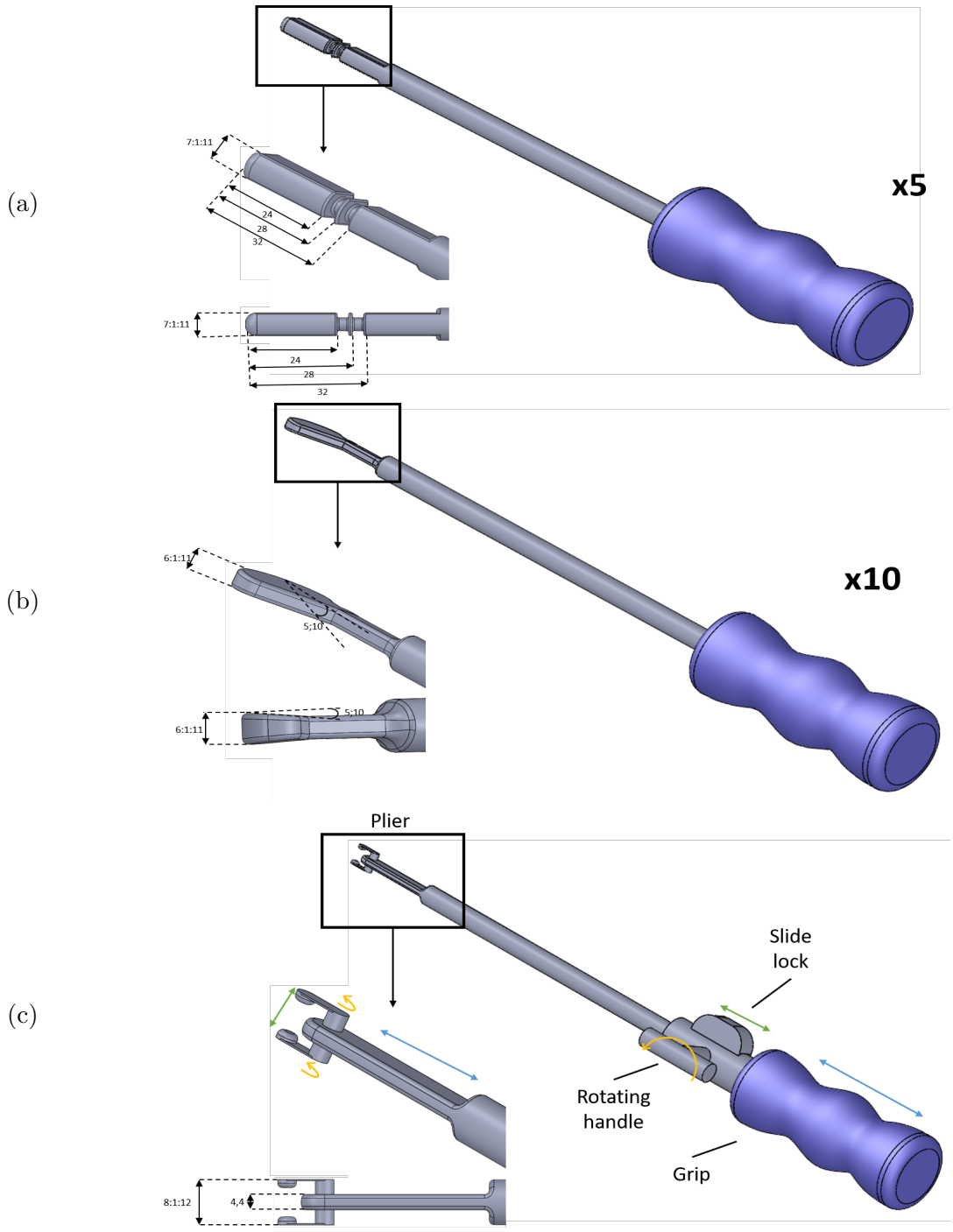

Figure 7.2: (a) Straight trial tool of 7mm height. Zoom on the extremity which allow to evaluate the appropriate cage length via a visual inspection through the access or using lateral imaging. 5 are provided for the 5 trial height (7,8,9,10 and 11mm). (b) Angled trial tool of 10mm height and 10° angle. Zoom on the extremity which allow to evaluate the appropriate cage angle via a visual inspection using lateral imaging. 10 are provided for the 5 trial height (7,8,9,10 and 11mm) and two different angle (5° and 10°). (c) Insertion tool showing the linear motion thanks to linear motion of the grip (blue), rotational motion of the plier thanks to the rotation of the rotation knob (yellow) and cage locking via tightening of the cage by the plier thanks to the sliding locking knob (red).

straight measurement tool, is used to determine the lordosis angle of the cage. If this is not possible, the straight measurement tool can be sufficient to define the appropriate cage slope. Then, the cage is inserted using the insertion tool and the insertion tool is retracted without moving the cage.

7.2 Future perspectives

7.2.1 The cage

7.2.1.1 The simulations

Experimental data of bone properties Simulations are a very powerful tool allowing to model the cage and simulate many different designs and anchorages, which allows to obtain many data a lot easier and faster than experimentally. Also, it allows to visualize and analyze elements that cannot be analyzed using experiments. However, the accuracy of the simulation might be discussed. The main factor affecting the model accuracy is the bone properties, which vary a lot. Indeed, these vary according to the donor and harvesting site, but also due to the bone treatment and testing method. Consequently, the properties of the models are not fully reliable. A solution would be to compute all these properties on random samples of femoral and tibial cortical bone from the tissue bank of St-Luc hospital, in the transverse and longitudinal direction, including computing the relaxation function.

Models The studied models are isotropic viscoelastic or anisotropic elastic. Therefore, even if the anisotropic linear was chosen because the bone treatment of the tissue bank increases the graft brittleness, none of them truly modelized bone material, which is anisotropic viscoelastic. Therefore, developing an anisotropic viscoelastic model would be more precise. This would be even more necessary in order to make fatigue simulations, for which a dynamic analysis is required.

Regarding this viscoelastic model, one may develop a more relevant criterion to determine if the cage is yielding. Indeed, it is here chosen to use the normal stress to consider the fiber direction and the yield limit accordingly. However, normal stresses do not take into account shear stresses. So, developing a criterion for anisotropic viscoelastic material, which would take into account shear and normal stresses and fiber direction, would be more reliable. Also, the difference between the compressive and the tensile yield strength, even if close, would be considered. For instance, a principal stress analysis would take the shear stresses into account, and then a model to compute the yield limit in the principal stress direction should be developed. Also, the Tsai-Wu criterion might be an appropriate start, as it is applicable for linear anisotropic material with different tensile and yield strength, but then the viscoelasticity should be taken into account [132].

Ideally, a model simulating bone remodelling and osteointegration would be ideal in order to design the cage providing minimizing stress-shielding and maximising osteointegration and bone remodelling [126]. However, such a model is very complex.

Boundary conditions The boundary conditions are directly applied on the cage, while the cage will be inserted between two vertebrae and the loads and fixture applied on the vertebrae. To simulate that, a full vertebral model should be developed, and the

interaction between the cage and the vertebrae should be implemented. Then, the forces of the muscles would serve as stimulus, such as the ones provided in Ode [99]. Regarding the load, only compression is tested. Even if it is the dominant load, *in vivo* motions would induce shearing as well. Ideally, a compressive pre-load should be applied, combined with flexion (or extension), lateral bending or axial rotation or a combination of them, but this would require the full model described above. Also, the applied force can be discussed as the one used for the simulation (3.1kN) is very high comparing to the one suggested to test intervertebral cages by other references [133], but similar to loads evaluated vie non-invasive measures and modelling [99] and to the only ones measured *in vivo* [86].

7.2.1.2 The designs

Dimensions Regarding the chosen designs (see section 7.1), no design is perfect. Many choices have been arbitrary, such as the surfacing, fillets, the global shape of the cage and the radius of the rounding of one lateral surface for insertion, even if the dimensions of the cages are based on anatomical and clinical dimensions. All these parameters should be studied, independently and combined, in order to optimize the design, and especially the surfacing. Indeed, it is supposed to provide anchorage. However, the high pressure on the part which would be first in contact with bone can lead to microcracks within the cage or the vertebrae or both. These can propagate and change the mechanical properties of the cage. To study that, a model of the failure phenomenon and propagation within bone should be used.

Porosity Also, the UCM could be adapted to cortical bone. Indeed, the UCM uses an isotropic model, mostly used for cancellous bone. So, another unit cell can be used in order to better model the cortical bone behaviour, and experiments can be performed to define the constants.

Also, the porosity is arbitrary achieved through few designs. Indeed, the porosity can be obtained using pores with other shape, other distribution and direction. This leads to an infinite number of possibilities, which require a well advanced optimizing algorithm. Eventually, some spaces can be provided in order to place markers for imaging, in case the cage is not contrasted enough towards vertebral bone.

Surfacing Also, the surfacing can be adapted to the axial hole and anchorage, to avoid having incomplete surfacing pattern which would lead to higher stress concentration than complete ones. Also, it seems unrealistic to have so sharp structure made of bone, as these would fall during production anyway. The surfacing can be corrected via adding or removing material. It is chosen to remove material, to minimize the volume of the surfacing entering the adjacent vertebrae and so minimizing the risk of fracture.It was checked that the correction of the surfacing did not increase stresses or influence the optimization of the pore dimensions (Figure 7.3). However, this leads to a strongly asymmetric surfacing. This means that the cage would not be symmetrically fixed within the vertebrae. So this surfacing correction is recommended only if the uncorrected surfacing causes cracks propagation within the cage or the vertebrae.

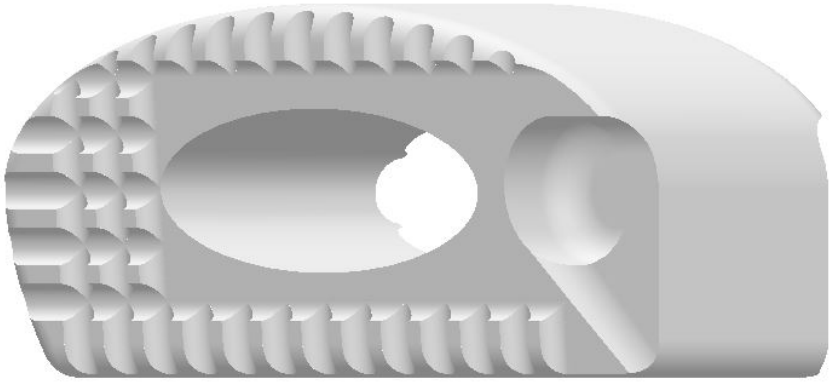

Figure 7.3: Potential correction of the surfacing via removing all incomplete patterns of the surfacing

7.2.2 The tools

Many shapes and dimensions of the tools are arbitrarily defined, such as the shape of the grip and its dimensions, the shape and dimensions of the working part between the grip and the functional part of the tool. The grip would require further studies to make it as user-friendly as possible, as well from a design as from a material perspective. To decide, one may investigate which shape provides the best trade-off between mechanical properties and visibility, even if the chosen shape is currently used for commercialized device, and therefore seems to be appropriate [25].

7.2.2.1 The insertion tool

Anchorage The anchorage system might be further investigated, even if this one seems appropriate regarding the production constraints. Also, the insertion tool is purely mechanical. Some electronic or imaging or both could be integrated. The mechanic of the tool is not yet defined. Even if this is a rotation and a tightening using a plier, one may study how to transfer and change the axis of the rotation of the rotating handle and the linear motion of the slide lock to the plier through the working part between them.

Alternatives The insertion tool exhibits one major weakness: the two thin plates of the plier. Indeed, these might be too weak regarding the torque to apply when rotation the cage (for the linear insertion, a a large contact area is provided thanks to the contact between the cage and the working rod of the tool). If these plates are mechanically too weak, their thickness might be increased and the deepness of the anchorage accordingly, such that the plier does not exceed 10mm high when the cage is fixed. However, this might not be sufficient. In this case, other solutions might be considered.

A first idea would be to use and anchor expansion system. To do so, a cylindrical hole would be made laterally on one side of the cage (alternative (a), Figure 7.4a). Then, a anchor expansion would be placed inside. So, by inserting a cylindrical element with an adapted diameter within this anchor expansion , such as a multi-strand cable, an expansion system would lead to high friction and anchorage, so fixing the screw to the cage. Then, by moving the cable as desired, the cage would move the same way. To move the cage, a concentric tube robot technology is indicated. However, the main challenge

would be to remove the tool so the screw and the anchor, while the cage would remain in place, as the screw would not be able to be removed linearly due to the annulus on the lateral side of the cage. Also, the axial pore can be used. For instance, a cable can go through the anchor fixation with an inverse cone at its end. Then, via pulling the cable, the anchorage would be deployed (alternative (b), Figure 7.4b). But again, removing the anchor remains challenging. Therefore, it may be envisaged to remove the anchor. To still provide a sufficient fixation, a locking system might be used within the axial pore. To do so, two options are possible: a inflated locking system (alternative (c), Figure 7.4c) or a rotating locking system (alternative (d), Figure 7.4d). However, both would lead to high stress concentration on the corner and it should be verified if this does not lead to cage failure. A last solution, which was already envisaged, is to use a wire all around the cage (alternative (e), Figure 7.4e). By pulling on both ends of the wire, the cage would be fixed. By pulling on one end of wire, the cage would rotate. By unlocking one wire and pulling on the other, the wire is retracted. This offers the advantage to do not require any hole, but should be tested to check is the applied torque for the rotation is sufficient but also if removing the wire would not damage the annulus. One may also argue that alternatives a) and d) would be preferred, as these are the only ones having a continuous stress zone (red in Figure 7.4).

These alternatives for the insertion tools can be briefly compared. Alternatives (a) only require a lateral hole, while alternatives (b), (c) and (d) require also an axial pore. So, in case of the clinical trials exclude the axial pore, these would not be envisaged. In this case, using the full design, simulations show that alternative (a) would lead to microcracks around the hole, which would contraindicate the alternative. On top of this, if the porous design is kept, simulations show that alternatives (b), (c) and (d), would lead to cage failure, similarly as with frontal pores (Figure 6.14c). So, to use these alternatives, the hole should be refill once the cage placed, which would complicate the operation. Eventually, Alternative (e) does not require any hole. However, alternative (e) is the one risking the most to damage surrounded tissue, due to the wire which would contact the annulus. However, if there is damage, it can be included in the operative damages and would be assumed to be naturally repaired. Also, this might be the one transmitting the less torque, as it only relies on friction between the wire and the cage cannot be squeezed too tight, which would risk damaging the cage.

7.2.2.2 The measurement tools

Many measurement tools are provided here; Therefore, one may think about having one tool on which the head will be changed with the wanted dimensions for measurement. This may increase the operational time and the tool complexity, but also reduce the cost and size of the box containing the tools, which is beneficial regarding the sterilization. So, this option would be considered.

Also, the intervertebral space is here supposed to be fully prepared. So, some tools to prepare the intervertebral space, i.e. for the annulotomy, nucleotomy, bone spurs removal, nerve decompression and endplates preparation could be necessary. Available tools from the hospital but also from the commercialized cages can be used to perform the first tests on the developed cage and tools. However, the tools from the hospital are not intended for a TLIF and so can be imprecise and using tools from another manufacturer is not acceptable on long-term. So, a dedicated instrumentation to prepare the intervertebral

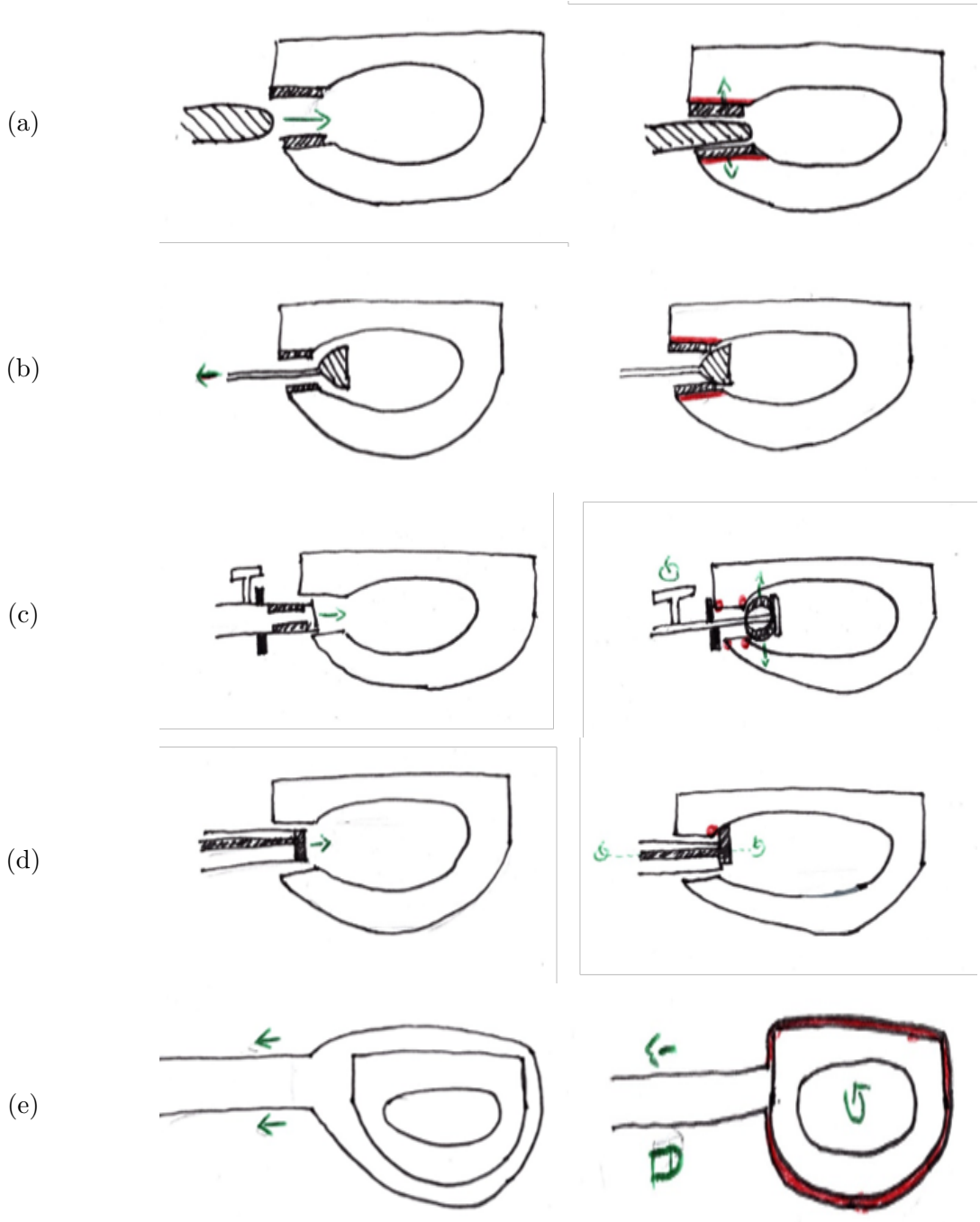

Figure 7.4: Alternatives to the insertion tool. (a) Anchor fixation with insertion of a multi-strand wire. (b) Anchor fixation with a reverse cone. (c) Inflating locking system. (d) rotating locking system. (e) Fixation and rotation using a wire. The motions are in green, and the zone of stress are in red.

space would be necessary. Anyhow, one may think to transform the trial tools into rapes, which would allow to prepare the endplates and evaluate the appropriate cage dimensions at the same time, so reducing the operation time and risk. Also, the distractor might be used to directly evaluate the appropriate cage height, such that only one straight measurement tool would be used to only determine the cage length (and prepare the

endplates if necessary).

7.2.3 Mechanical testing

7.2.3.1 The types of test

The main next steps would be to test the final designs cage *in vitro* and then *in vivo*. A testing method is proposed in Comer et al. [133]. *In vitro* testing would allow to test he mechanical properties of the cage as an inert device, while *in vivo* testing takes the biological interactions into account. For *in vitro* testing, if the goal is to test the bone remodelling on top of the mechanical properties, a bioreactor could stimulate bone remodelling. In both cases, mechanical testing is very important as fatigue failure is the main failure risk of intervertebral cages, even if revascularization and bone remodelling aim to prevent fatigue failure [55].

For each test, care must be taken to apply a preload beforehand and during it, as this would be the case once inserted and as this influences the properties. For instance, the torsional stiffness is strongly correlated with the axial stiffness [88].

7.2.3.2 Standards procedures

Some standards procedures are provided by few institutions regarding intervertebral implants. The ISO standard testing procedure for spinal implant is specified by the *ISO 12189 (2008): Implants for surgery — Mechanical testing of implantable spinal devices — Fatigue test method for spinal implant assemblies using an anterior support* [134]. This standard aims to provide basis assessment method for testing the intrinsic static and dynamic strength of spinal implants [134].

There are many standards for spinal implants testing provided by the American Society for Testing and Materials (ASTM) [135]. These are often recommended by the Food and Drug Administration (FDA) as golden standards for new implants testing. For a new bone implant for spinal interbody fusion, the most relevant standards are:

- *ASTM F1717-18: Standard Test Methods for Spinal Implant Constructs in a Vertebrectomy Model* [136].
- *ASTM F2077-18: Test Methods For Intervertebral Body Fusion Devices* [137].
- *ASTM F1798-13: Standard Test Method for Evaluating the Static and Fatigue Properties of Interconnection Mechanisms and Subassemblies Used in Spinal Arthrodesis Implants [138].*
- *ASTM F3292-19: Standard Practice for Inspection of Spinal Implants Undergoing Testing* [139].
- *ASTM F2267-04: Standard Test Method for Measuring Load Induced Subsidence of Intervertebral Body Fusion Device Under Static Axial Compression* [140].

The two ways to mechanically evaluate spinal implants alone are provided by ASTM F1717 and ASTM F2077. One main difference is the use of a vertebral model for the first one (*in vivo in vitro* usually via two polymers blocks linked by metallic rods) while the second one uses two simple testing block above and below the implant [135]. Another difference is that ASTM F1717 advises to apply loads for three different static tests (tension, compression, and torsion) and one fatigue test in compression although ASTM F2077

indicates to make static and fatigue test in three modes (pure compression, compression-shear, or torsion) [135]. Since both these standard procedures are defined for one-piece implants, ASTM F1798 is defined for arthrodesis devices composed of several pieces. Consequently, it is focused on the mechanism interaction such as it can be compared between different design [138]. During all these potentials tests, ASTM F3292 provides standards for failure inspection to reduce the bias as much as possible when reporting measures [139]. The ASTM F2267 is slightly different since it intends to indicate how to quantify the implant's subsidence characteristics as this is a potential clinical failure mode [140].

7.2.4 The material of the cage

Cortical bone offers the advantage to be bioresorbable and biocompatible. These advantages are very attractive regarding the risk of post-operative complications with non-bioresorbable cages. However, cortical bone has many drawbacks. As mentioned above, the mechanical properties of graft based on cortical bone vary a lot. Therefore, the properties of two cages will never be the same and some uncertainty is inevitable. Also, cortical bone is a lot stiffer thank PEEK (Young modulus of 3.84GPa and 9.4GPa for PEEK and cortical bone in their more elastic direction respectively), and yields for a smaller maximal stress stress (yield limit of 120MPa and 52.5MPa for PEEK and cortical bone in their more elastic direction respectively). So, it is more difficult to obtain a stiffness close to the one of the vertebral bodies while not yielding using cortical bone than PEEK. One may mention that Ti cage are widely used and work, despite its large Young modulus (110GPa). This is thanks to its large yield limit (880MPa), allowing to use very porous Ti cage, so reducing its stiffness significantly. However, none of them offers the bioabsorbable advantage. Anyway, new bioabsorbable material, such as ceramics or magnesium-alloys, would offer this advantage and propose mechanical properties that would be the same from one cage to another. Also, this would use an easier manufacturing which reduces the production constraints and so allow designs that can not be obtained with cortical bone. These can be used as stand-alone cage, but also as a part of an hybrid cage composed of cortical bone and another material, which would exhibit other mechanical properties and maybe allow other designs, for example for the anchorage.

Appendix A

Anatomy

A.1 Spinal anatomy

The vertebral column is formed of 33 vertebrae stacked vertically upon one another, each separated by fibrocartilaginus disc [141]. The spinal cord anatomy could be described via its skeleton and bones structures (osteology), via its joints and articulations (arthrology), via its nerves and the nervous system (neurology) and via its circulatory system (angiology), via the structure, arrangement and actions of its muscles (myology). Based on these features, some disease leading potentially to an arthrodesis are pointed and explained.

A.1.1 Osteology

The 33 vertebrae of the vertebral column are distinguishes according to five regions represented on Figure A.1. From superior to inferior region, these are the cervical (7 vertebrae from C1 to C7), the thoracic (12 vertebrae, from T1 to T12), the lumbar (5 vertebrae, from L1 to L5), the sacral (5 fused vertebrae, from S1 to S5) and the coccygeal (3 to 4 fused vertebrae, from Co1 to Co3) [141]. Since the aim of this thesis is to develop a surgical tool for arthrodesis, only the regions with unfused vertebrae are of interest. On top of that, arthrodesis is mostly performed on the cervical and lumbar vertebrae since the thoracic ones are not subject to a lot of motions thanks to the support provided by the thoracic cage.

All the vertebrae have a body surrounded by a cortical rim expecting the vertabrae C1 and C2 (respectively named atlas and axis) due to their particular set of articulations that provide the required mobility degree for head motion [143]. Since the mass supported by each vertebra increases for lower vertebrae, the vertebral body becomes larger for inferior vertebrae to provide more stability [141]. The vertebral body is lined with hyaline cartilage called the endplate, so avoiding direct contact with the intervertebral disc, and is surrounded by cortical bone within trabecular bone inside [144].

The vertebral arch, what is the the lateral and posterior part of each vertebra, form with the vertebral body the whole vertebra within a hole named foramen. All foramens linked together form the vertebral canal enclosing the spinal cord [144]. Briefly, the vertebral arch is composed of five majors bony prominences for muscles and ligaments attachment: the spinous and transverse process, the pedicle, the lamina and the articular process which are all indicated on Figure A.1 when appearing.

The vertebral, thoracic and lumbar vertebrae could be distinguished thanks to their

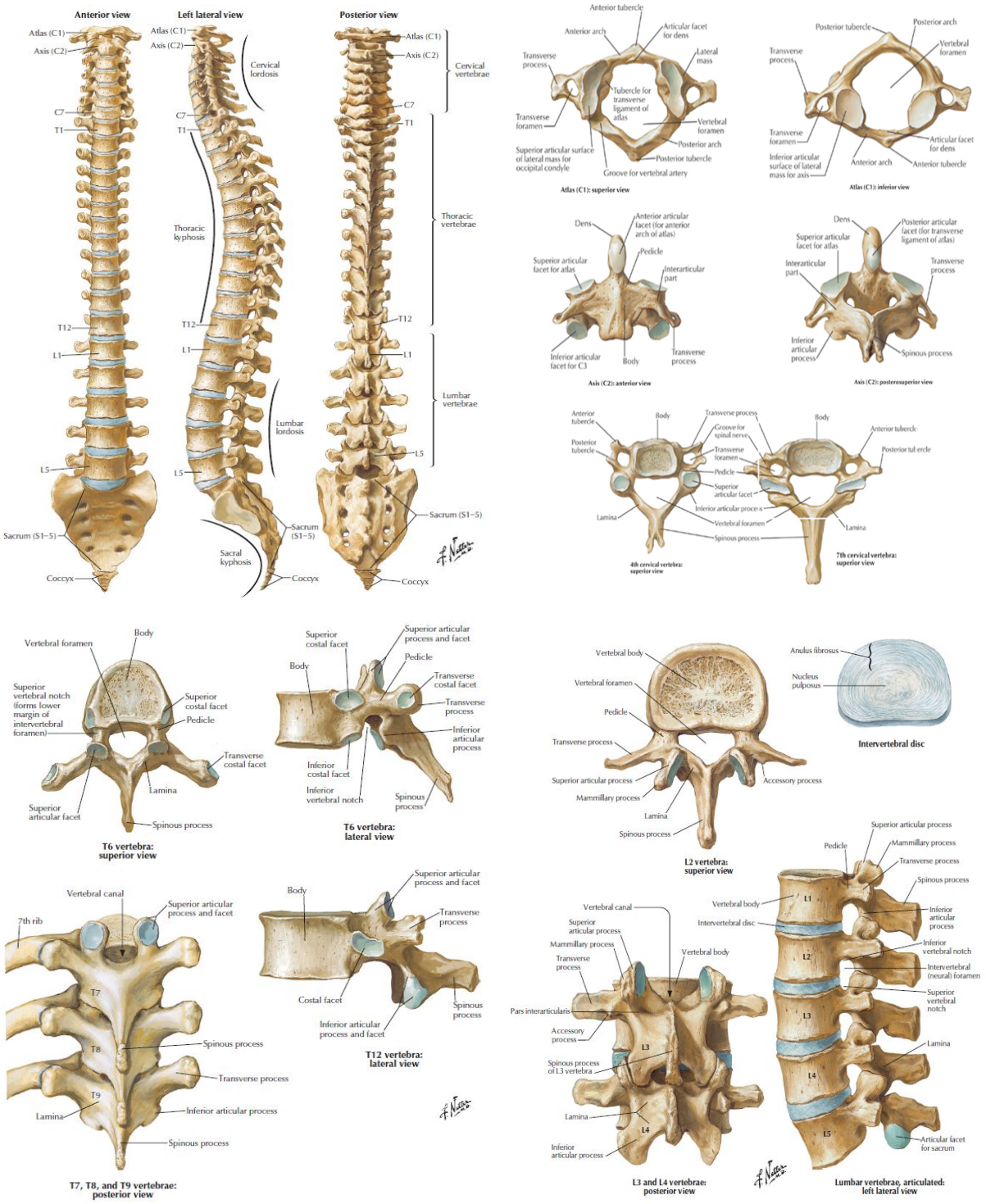

Figure A.1: Vertebral cord osteology. Spinal cord overview (top-left) from the anterior, left lateral and posterior view [142]. Cervical vertebrae osteology (top-right) from the superior, and inferior view for the vertebra C1, from the anterior and postsuperior view for the vertebra C2, with the superior view of the 4th and 7th cervical vertebra [142]. Thoracic vertebrae osteology (bottom-left) from the superior and lateral view for the vertebra T6, from the posterior view for the vertebrae T7 to T9, from the lateral view for the vertebra T12 [142]. Lumbar vertebrae osteology (bottom-right) from the superior view for the vertebra L2, from the posterior view for the vertebrae L3 to L4, from the left lateral view for the vertebrae L1 to L5 and with a representation of the intervertebral disc [142].

respective particular features. The cervical vertebrae have three distinguishing anatomical components: the spinous process for the vertebrae C2 to C6, the transverse foramen and the triangular shaped vertebral foramen. The thoracic vertebrae has two demi facets (the inferior and superior articular facets), one or two costal facet(s) on the transverse process and obliquely oriented spinous process. Lastly, the lumbar vertebrae are largest and lack some characteristics of others vertebrae such as the transverse foramina or the spinous processes from the cervical vertebrae or the costal facets from the thoracic ones.

A.1.2 Arthrology

As the spinal cord aims to provide stability and mobility to the human body, joints and ligaments have to be able to sustain the human mass while having the required degrees of freedom. Therefore, according to the spinal cord region, the ligaments arrangement differs since their respective mass sustainability and mobility roles differs. On top of that, the ligaments are used to protect the neural structures and to absorb energy during fast motions to avoid potential injuries via their viscoelastic non-linear responses [6].Figure A.2 presents the arthrology of the three regions of interest for arthrodesis as well as the lumbosacral region since the lumbar region is significantly linked to the sacral region.

Even if the spinal cord regions have different functions, some common features can be extracted. The left and right superior and anterior articular facets articulates respectively with vertebra above and below (if there is one) [144], therefore meaning that each vertebra has two superior and inferior articular joints (one left one right) [141]. On top of that, the vertebral bodies articulate via intervertebral discs, forming the intervertebral joint. Furthermore, the anterior and posterior longitudinal ligaments cover the full length of the vertebral column to prevent respectively hyperextension thanks to its substantial thickness and hyperflexion (this late is thinner). The anterior longitudinal ligament is link to each of its adjacent vertebra and intervertebral disc. Lastly, the ligamentum flavum link the lamina of adjacent vertebrae and the interspinous (or intertransverse) and supraspinous ligaments join respectively the spinous process to the adjacent spinous process and the adjacent tip [144], all to limit excessive flexion [141].

The cervical vertabrae joints and ligaments is particular due to the craniocervical junction, in which the sophisticated ligamentous network, composed of height ligaments, is key to maintain the head stability and protect the neurologic structure [7]. The thoracic vertebrae are connected to the ribs via several ligaments around joints, called the costovertebral joints. The bodies and the ribs heads are connected through the costocentral joints (joint of head with rib in Figure A.2), by use of the radiate ligament of head and rib. The costal heads two to ten are all connected to two vertebrae via several ligaments, forming the costocentral joints. The costotransverse joints link the facets on the transverse processes and on the tubercles is surrounded by an articular capsule (the facet capsular ligament) and reinforced via the costotransverse and lateral costotransverse ligaments. The articular processes of the thoracic vertebrae form the facets zygapophysial joints via their superior and inferior projections that is stabilised by the interspinous ligament [7]. The spinal ligaments are mostly composed of collagen expecting the ligmentum flavum that mostly contain elastin [6].

The intervertebral discs are strong fibrocartilagenous structures that interpose between adjacent vertebrae to provide a buffering bond. These discs, represented in Figure A.1, are composed of outer concentric layers named the annulus fibrosus with a central pulpy

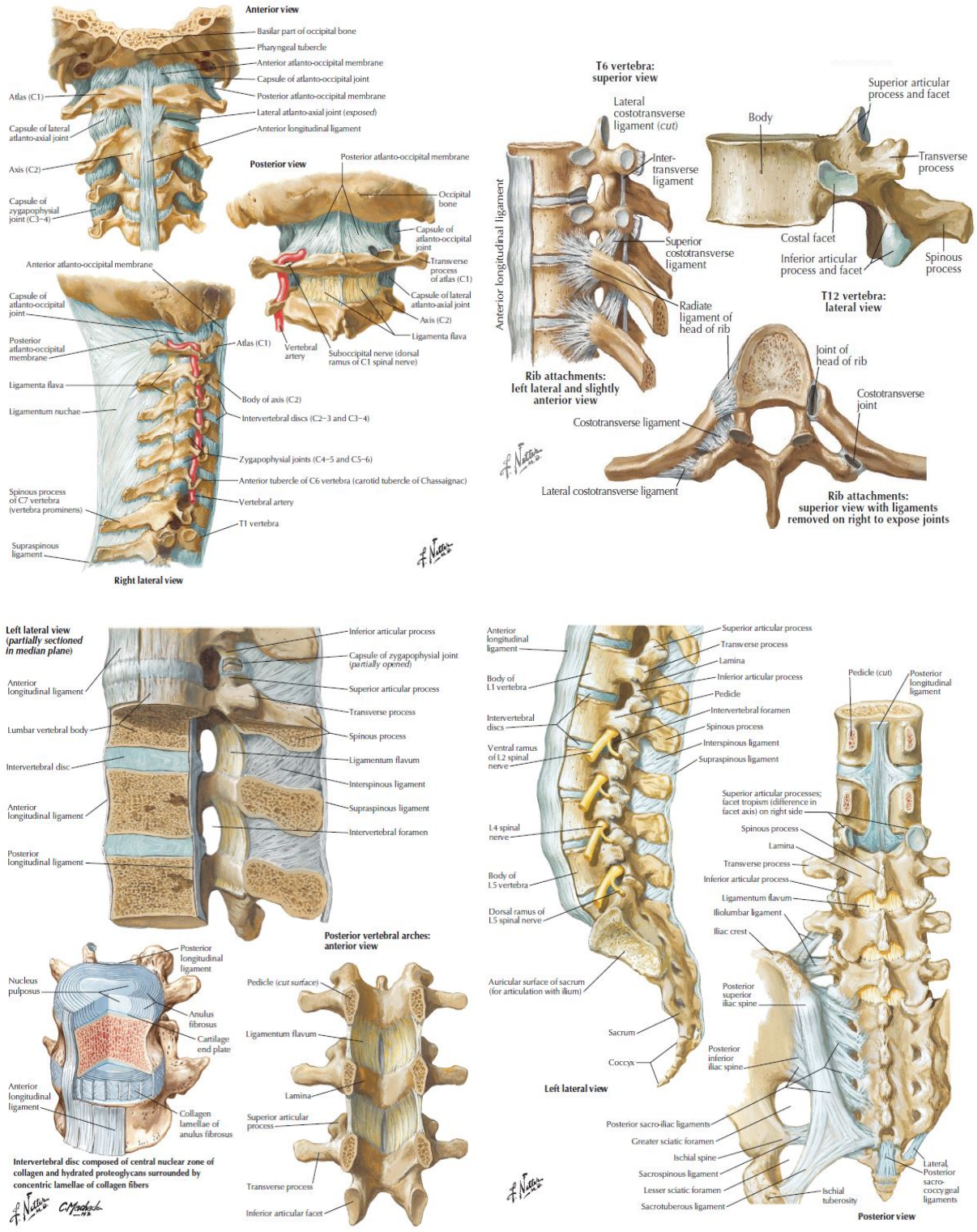

Figure A.2: Vertebral cord arthrology. Cervical vertebrae arthrology (top-left) from the anterior, posterior and right lateral view [142]. Thoracic vertebrae arthrology (top-right) with a superior view of the T6 vertebra, lateral view of the T12 vertebra and a superior view of the rib attachment [7]. Lumbar vertebrae arthrology (bottom-left) with a left lateral and a posterior anterior view and in addition the intervertebral disc composition [142]. Lumbosacral arthrology (bottom-right) with a left lateral and posterior view [142].

zone named the nucleus pulposus inside that contains mostly type II collagen fibers in an aqueous gel rich with proteoglycans that links to the collagen fibers end [6]. Intervertebral discs represent 25% of the vertebral cord heights, self filled from 30% to 50% by the nucleus, with discs thickening from the upper to the lower end [6]. Discs are mostly responsible for the convexity (lordosis) of the lumbar spine with a lower contribution from the vertebrae shape.

A.1.3 Neurology

The vertebral column neurology is constituted of the spinal cord and its peripherical nerves. This spinal cord is one of the most important body structure since it establishes a bidirectional nervous link between the brain and the body while performing some preliminary or total information processing respectively for the central or autonomous nervous system. The spinal cord extends continuously from the foramen magnum (a large oval opening in the occipital bone of the skull [145]) to extend until the vertebra L1 or L2 with 1cm to 1.5cm diameter [146]. The spinal nerve is divided into five regions with the same names as the ones of the vertebrae regions but that are generaly into 4 regions by grouping the sacral and coccygeal regions together, as in the Figure A.3. Since cross-sectional features are mostly common for all vertebral level, only 2 cross sectional sections with similar features are shown in Figure A.3.

As illustrated in the relation of spinal roots ti vertebrae of Figure A.3, from the spinal cords emerges two rows of nerves in the 31 gaps in-between the vertebrae (counting the space above C1 as a gap), forming 31 nerves pairs with a dorsal and ventral root among which 8 cervical, 12 thoracic, 5 lumbar, 5 sacral and 1 coccygeal all exiting below their corresponding vertebra excepting C1 to C7 nerves that emit from above their respective vertebrae [146]. Since the vertebra level is three segments above the cord level in the thoracic and upper-lumbar part of the spinal cord, the corresponding nerves travel a longer path before reaching the intervertebral foramen. The spinal cord exhibit two major enlargement: the cervical enlargement from vertebra C3 to vertebra T1 and the lumbar enlargement from vertebra L1 to S2.

As shown on the spinal nerves zoom of Figure A.3, the spinal cord is shielded by three meningues: the dura, archnoid and pia matters from the outer to inner level. The dura is attached to the spinal cord by the denticulate segments emanating from the pia matter [146].

The spinal cord internal structure is not of high interest since it should not be affected by a intervertebral disc herniation and therefore not be modified during and after the bone cage implementation. However, the cross sections of Figure A.3 shows the dorsal root and the sympathetic ganglions positions that are wider than their respective nerves and that could be affected by a disc herniation due to their proximity with the intervertebral disc.

A.1.4 Angiology

The blood vessels of the vertebral column are around the vertebrae and inside the vertebral canal. During a surgical operation, the blood supply to the vertebral canal has to be carefully considered since, in case of blood supply defect, the spinal cord will stop to make the nervous link between the brain to the body [148]. Figure A.4 presents the vertebral

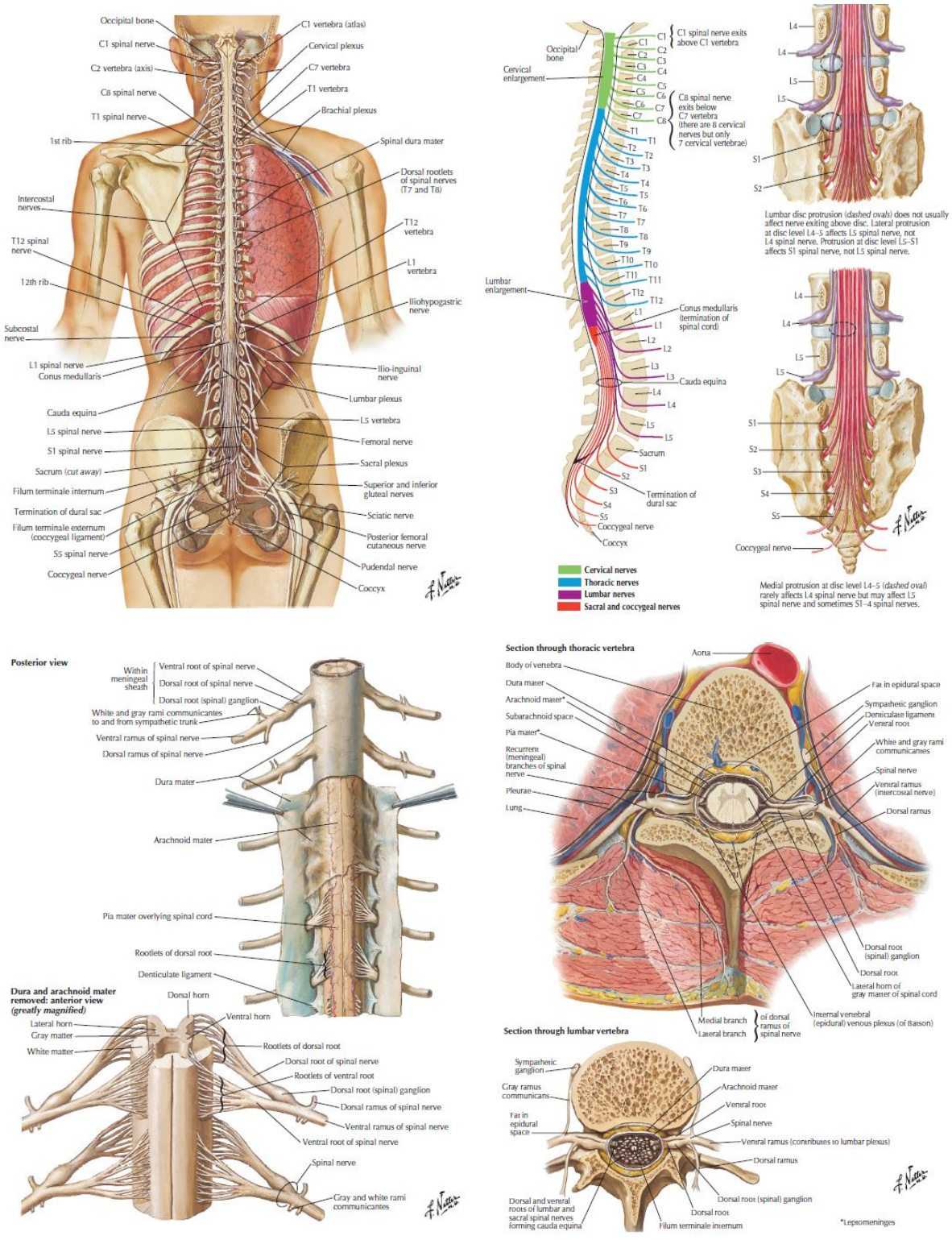

Figure A.3: Vertebral cord neurology. Spinal cord and ventral rami (anterior spinal nerve divisions [147]) in situ (top-left) [142]. Relation of spinal nerve roots to vertebrae (top-right) with a lateral cross section color-coded according to the spinal nerve regions and posterior cross sections highlighting potential disc protusions affecting nerves [142]. Spinal nerves zoom (bottom-left) with a posterior view and an anterior view without dura and arachnoïd matter [142].Spinal nerve origins cross sections (bottom-right) with one section through thoracic vertebra and one through lumbar vertebra [142].

cord blood arteries and veins. Thanks to the aorta along the vertebral column, the spinal cord has a close access to oxygenated blood.

Looking to the spinal cord irrigation on the intrinsic distribution of Figure A.4, the spinal cord is supplied by the anterior and both the left and right posterior spinal arteries. However, for the upper cervical regions, as shown on the cervical columns veins image of Figure A.4, they are two anterior arteries but these merge into one anterior artery afterward. To supply the spinal cord, the anterior spinal artery inserts into the spinal cord via the anterior median fissure. furthermore, the arterial vascorona form a plexus of small arteries all around the spinal cord that is used for blood supply of surface regions and so making the link between the irrigation from the anterior spinal artery (inside in the spinal cord) and from the posterior ones (outside the spinal cord) [148]. This disposition is repeated along the whole spinal cord to provide uninterrupted supply. The nerves from the spinal cord are supplied by the anterior and posterior spinal arteries that comes from the bifurcation of the segmental spinal arteries, self going through the intervertebral foramen from the anterior and posterior spinal arteries [148].

The desoxygenated blood is drained out of the spinal cord via the anterior and posterior spinal veins that join into the internal vertebral venous plexus which empty into the external vertebral venous plexus via the basivertebral veins [148], all shown on the intrinsic veins distribution of Figure A.4. The blood from the external vertebral venous plexus drains depending on the location.

These are some variants of the arterial organization according to the patient. Even if the artery insert into the dura at level T9 to T12 (75% of cases), it could happen at the level T5 to T8 (15% of cases) or at the level L1 to L2 (10% of case) [148]. Also, the anterior spinal artery diameter could vary between on patient to another.

The intervertebral disc is fed via a vascular network with the vertebral body going trough the hyaline endplate between the vertebra and the disc to provide the predominant nutrient source via staying at the annulus periphery [6].

A.1.5 Myology

The muscles associated to the vertebral column are on the back since the thorax and abdomen contain the organs, with respectively abdominal and pectoral muscles. The muscles of the back can be divided into 3 categories: the superficial that are used for shoulder movements, the intermediate associated to thoracic cage motion and the deep that are responsible of the vertebral column movements. all these muscles and their nerves are represented in Figure A.5

The high muscle density of the back illustrate why the arthrodesis can be performed by the anterior way: to avoid having to section so many muscles and so decrease the rehabilitation difficulty and time of the patient. However, when spinal cord stabilization is required, a posterior approach is necessary.

A.2 Abdominal anatomy

The abdominal anatomy has to be shortly described to explain the anterior approach to lumbar spine since this approach access the spinal cord via the abdomen. However, only the elements key to understand and explain the approach are of interest here, all

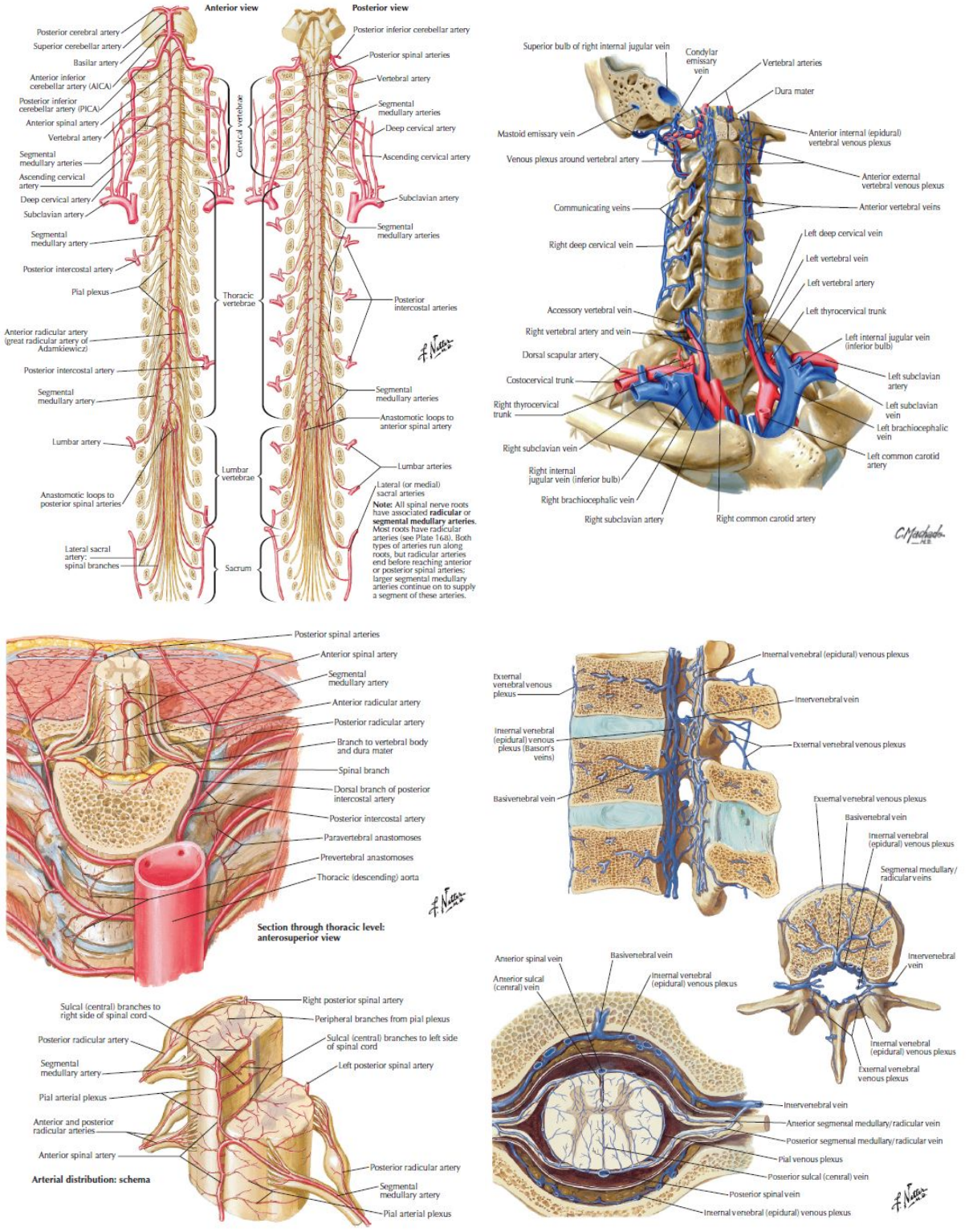

Figure A.4: Vertebral cord angiology. Arterial overview (top-left) from the anterior and posterior view [142]. Veins of cervical column (top-left) from a postlateral view with a cross section of the lower skull part [142]. Intrinsic distribution of the arteries in the spinal cord (bottom-left) with a anteriorsuperior view of a section through thoracic vertebra and the arterial distribution around the spinal cord [142].Intrinsic distribution of the veins in the spinal cord (bottom-right) with lateral view of a section through thoracic vertebrae, a superior view of a isolated vertebra and of a cross section through the spinal cord [142].

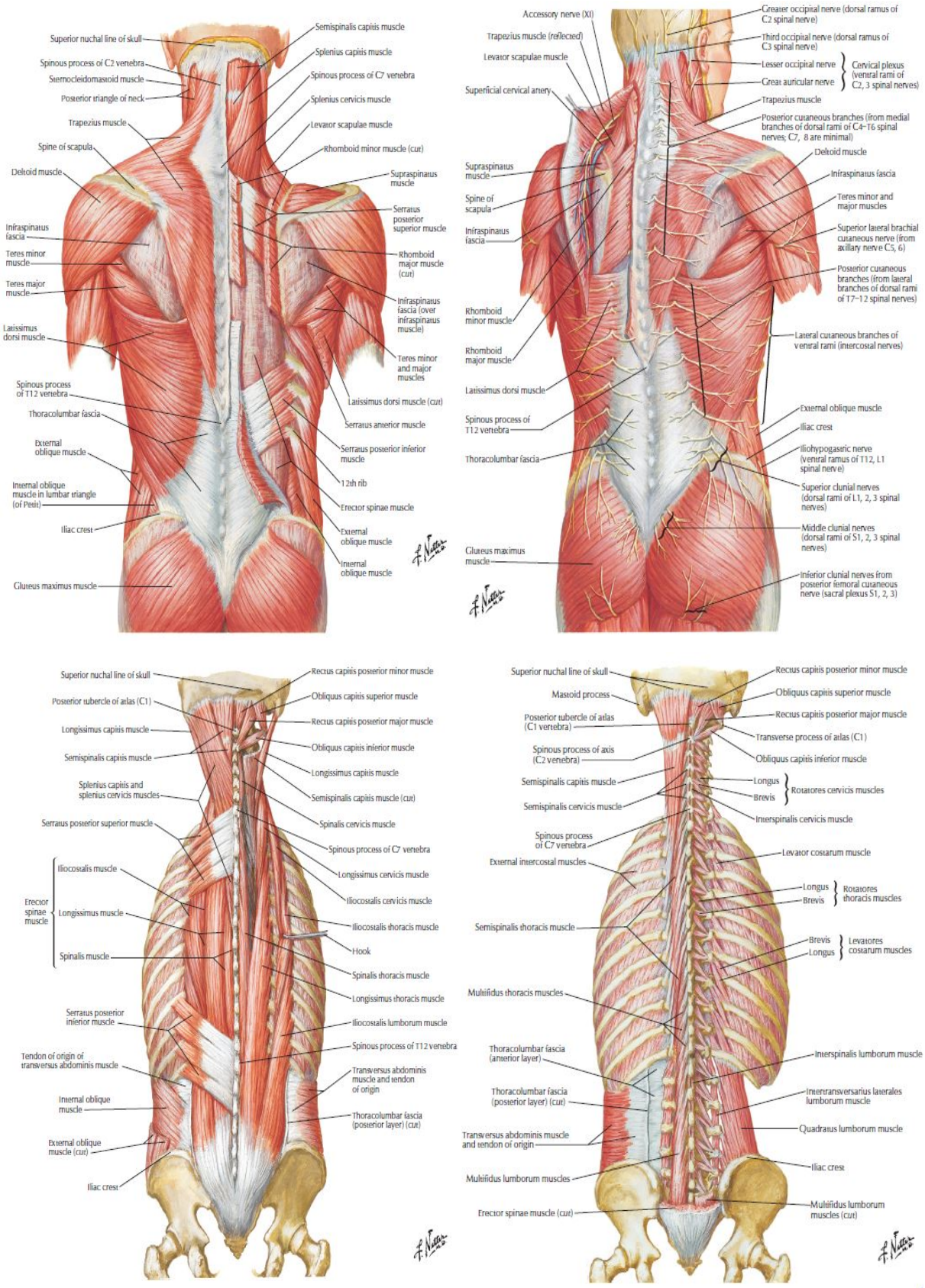

Figure A.5: Vertebral cord myology. Muscle of back on the superficial layer (top-left), intermediate layer (bottom-left) and deep layer (bottom-right) from the posterior view [142]. Nerves of the muscles of the back (top-left) from a lateralposterior view [142].

represented on Figure A.6.

First focusing on the abdominal membrane, the layers above the arcuate line are (superiorly convex line approximately positioned half way between the umbilicus and the pubic crest [149]) are consecutively the skin, subcutaneous tissue, anterior layer of rectus sheath (dividing into the aponeurosis of the external and internal oblique muscles), rectus abdominis muscle, posterior layer of rectus sheath (dividing into the aponeurosis of the internal oblique and transversus abdominis muscles), transversalis fascia, extraperitonal fascia and peritoneum [34]. Slightly differently, below the arcuate line, posterior layer of the rectus sheet is not present resulting in a rectus muscles directly onto the transversalis fascia [34].

From the vascular point of view, the key elements are the aorta and it bifurcation into the left and right iliac arteries, typically at the L4-L5 level, the inferior vena cave rightsided positioned to the aorta, the middle sacral artery and vein from the left common iliac artery and vein and the iliolumbar vein (not on Figure A.6, represented later on Figure D.6) from the left internal iliac vein self from the left common iliac vein [34].

Focusing on the organs, after most of the abdominal content is retracted, only the left kidney is still present but it is rarely visualized due to the surrounding perinephric fat.

Looking to the muscles represented on Figure A.6, the most important one is the major and minor psoas muscles that are paraspinal to the L1-L5 level [34].

The abdominal neurology is mostly composed of lumbar segment of the sympathetic chain on the paraspinal, anterior and medial facet of the psoas, the presacral nerves grouping all nerves over the sacrum, the lumbosacral nerves and the genitofemoral nerves of the Figure A.6 [34].

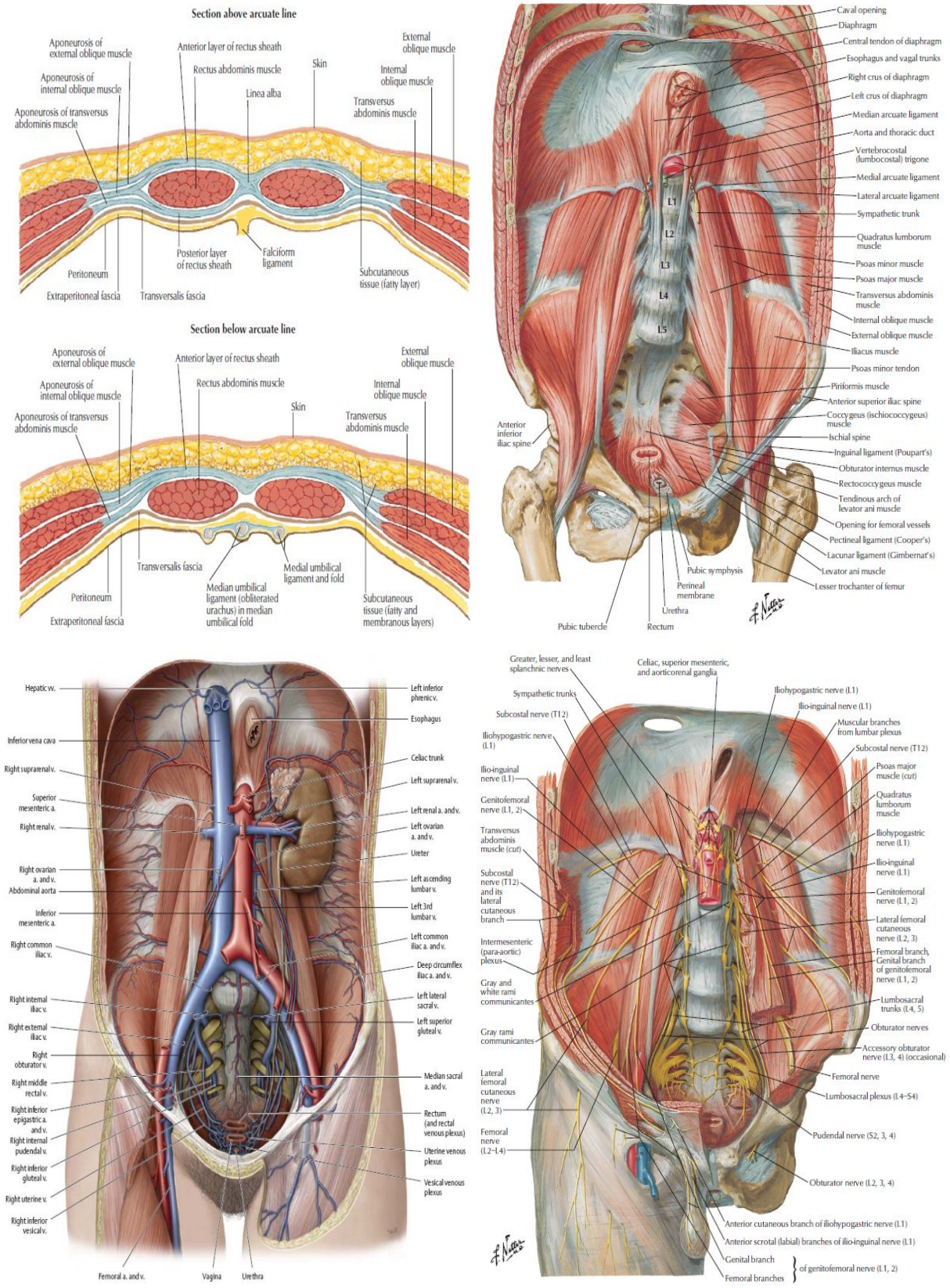

Figure A.6: Abdominal wall anatomy (top-left) above and below the arcuate line [142], muscles of the posterior abdominal wall (top-right) [142], anterior view of a female abdomen with all organs removed excepting the left kidney and suprarenal gland (bottom-left) [150], nerves of posterior abdominal wall (bottom-right) [142].

Appendix B

Biomechanics

B.1 Spinal biomechanics

Since an arthrodesis aims to fix vertebrae together, understanding the vertebrae motions, limitations and forces is important to ensure that the fixation does fix the desired degrees of freedom and that the used system could sustain the applied force while keeping an appropriate force distribution on the vertebral column.

B.1.1 Kinematics

The spine has six degrees of freedom (DOF) thanks to its axial, sagittal (or flexion-extension) and lateral rotations and its axial (or compression extension), lateral (or medial-lateral) and anteroposterior translations [6] that all are represented on Figure B.1. A functional spinal unit (FSU), represented on Figure B.1, of the vertebral column is comprised of two vertebrae, the inferior and superior vertebra, one intervertebral disc in-between and 10 linked ligaments (excepting for the upper cervical spine due to the craniocervical junction using 8 ligaments per vertebra, as specified in subsection A.1.2: Arthrology), all represented on Figure A.2 [6]. Among these ligaments are ligamentum flavum (LF), intertransverse, posterior and anterior longitudinal ligaments (ITL, PLL and ALL), facet capsular ligament (CL), interspinous and supraspinous ligament (ISL and SSL) are the most relevant for an anterior or postlateral arthrodesis since their are on the anterior and lateral facets of the FSU. One FSU has 6 DOF and, since the motion of one vertebra is reported relative to another one, the reported vertebra motion is the same as the one of the FSU.

Even if Figure B.1 only represent the lumbar FSU, the displacement and load names are the same for the vertebral and thoracic vertebrae. Therefore, based on Figure B.1 and for all vertebrae, flexion and extension refer to bending respectively forward and backward an axis orthogonal to the sagittal plane, together referring to sagittal bending. Lateral bending refers to bending leftward or right the axial vertebral axis, hence being left or right lateral bending. Axial torsion refers to rotating around the axial vertebral axis, for example when turning the head [6].

Some other terms must be explained to fully define the spinal cord kinematic. The motion pattern refers to vertebral body displacement when under load and is especially complex for the spinal cord. Since, according to the load direction and amplitude, standard motion patterns are known, when the motion pattern does differ from the standard one

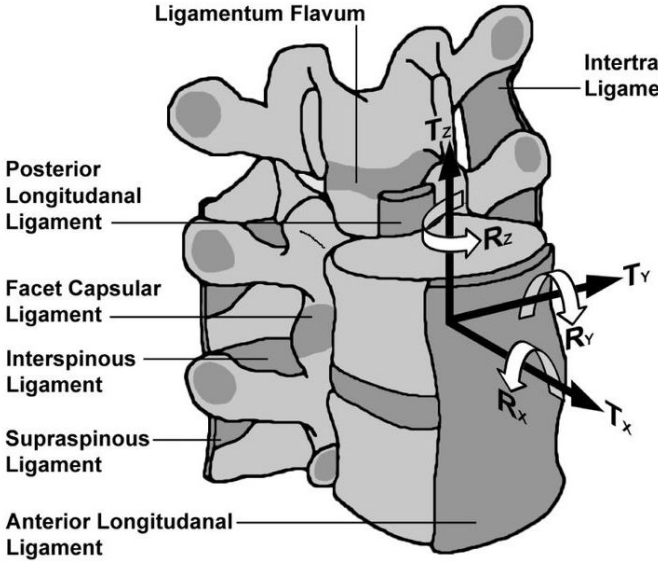

Degrees of Freedom

Axis	Displacement	Load
Anterior-posterior	T_x	F_x
Medial-lateral	T_y	F_y
Compression-extension	T_z	F_z
Lateral bending	R_x	M_x
Flexion-extension	R_y	M_y
Axial rotation	R_z	M_z

Figure B.1: Lumbar spinal cord functional spinal unit representation specifying key ligaments names and spinal cord degrees of freedoms representation with both rotations and translations displacements and loads names with their corresponding symbols [151].

in the same conditions, then this could indicate an abnormality [6]. The second term is coupling, that refers to motion along axes secondary to the one of the load. Coupling can change due to abnormality. Hence, coupling could be combine with the motion pattern to indicate clinical instability [6]. The instantaneous axe of rotation (IAR) is the axis of each of the three possible rotations, visualized on Figure B.1. The IAR location can change due to vertebral anatomical variations, such as disc degeneration [6].

B.1.2 Loads

The ligaments mechanical responses had been mainly characterized via *ex vitro* testing, hence their mechanical behavior *ex vivo* is not clearly known. However, it is assumed that the ligaments can work under a load closer to their failure strengths than bone [6]. The ligaments typically assumed features are given in Table B.1.

The loads could be studied according to the free body diagram to analyze the forces applied on a FSU of interest, and so on a joint of interest [6]. Another method is to use surface electrode to measure with mathematical model to compute the force performed by the spinal muscles [6]. Another way to obtain the spinal muscles forces is to measure the pressure in the intervertebral disc via a needle pressure transducer, so a more invasive measure device, and combine it with a model computing the force according to the pressure [6]. A last method to study loads effect on the spine is to analyze the IAR location region. All these methods methods allow to detect a potential abnormality, such as a disc degeneration decease. Figure B.2 shows the IAR region with a normal and degenerated intervertebral disc for extension and left lateral bending.

Table B.1: Failure load, strength and stain and the maximum *in vivo* strain for the anterior and posterior ligaments (ALL and PLL), the ligamentum flavum (LF), the facet capsular ligament (CL) and the interspinous and supraspinous ligament (ISL and SSL) [6].

Ligament	**Failure load [N]**	**Failure strength [Mpa]**	**Failure stain [%]**	**Maximum in vivo strain [%]**
ALL	450	11.6	37	13 (flexion)
PLL	324	11.5	26	13 (extension)
LF	285	8.7	26	15 (flecion)
CL	222	7.6	12	17 (torsion)
ISL	125	3.2	13	28 (flexion)
SSL	150	5.4	33	31 (flexion)

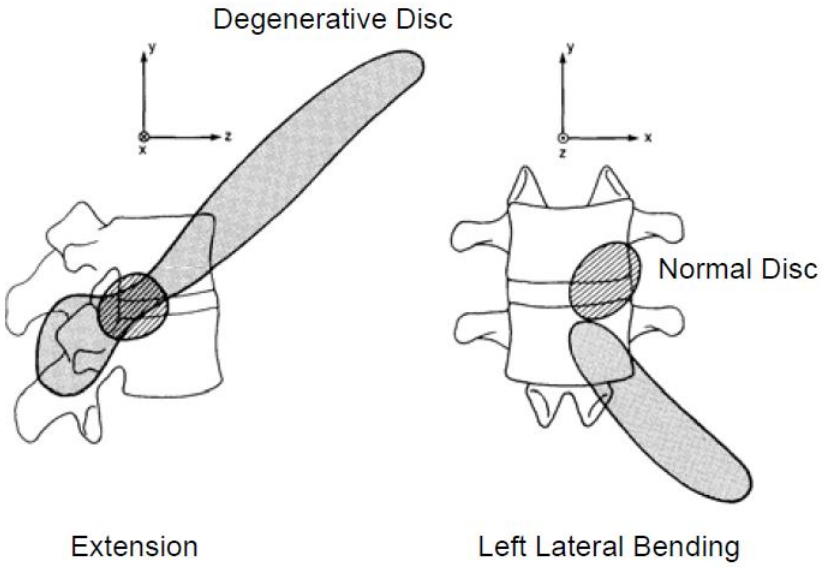

Figure B.2: Intentaneous axe of rotation (IAR) region with a normal (full grey) and degenerated (hatched grey) intervertebral disc for extension (left) and left lateral bending (right) [152].

B.1.3 Vertebral bones mechanical properties

All vertebrae are composed of cancellous bone in the inner part (the vertebral body in Figure A.1) and cortical bone on the outer shell (all the remaining parts). However, most of the compressive loads is applied on the cancellous bone since the compressive load is transmitted through the intervertebral body that directly lies on the vertebral body. Cancellous bone is an anisotropic viscolelastic material that behave elastically for a wide range of non injurious strain with a elastic modulus proportional to the bone density to the second power [6]. Table B.2 presents the compressive strength of vertebrae.

The increase of compressive strength from the cervical to the lumbar vertebrae is

Table B.2: Compression strength of vertebral bodies from C3 to L5 grouping vertebrae with similar compressive strength for normal adult [6].

Spinal region	**C3-C7**	**T1-T6**	**T7-T8**	**T9-T12**	**L1-L5**
Compressive strength [N]	1.6	2.0	2.3	3.6	5.6

explained by the vertebrae volume increase since the compressive strength normalized by the vertebrae surface is approximately 8 MPa for all vertebrae of a normal adult. On top of that, the vertebral yield stress of 2.5 MPa and the elastic modulus of 40 MPa are fairly constant over all vertebrae. Furthermore, in general, a vertebra is weaker in posterolateral regions than in the center and an increase of 25% porosity, typically because of patient aging, lead to 50%decrease of strength.

B.1.4 Intervertebral discs mechanical properties

The intervertebral discs mechanical properties are explained by the annulus fibrosus properties. The annulus fibrosus is formed by concentric layers of collagen fibers wounded in in a helecoïdal manner. The inner third of the annulus, composed of type I collagen, is connected to the endplate while the remaining ones, composed of a 40% type I and 60% type II mixture, are connected to the vertebral body [6]. As shown on Figure B.3, The annulus fibers are orient by +30° and -30° consecutively, so leading to 120° for one layer with respect to each adjacent one. In practice, the number of layers is not constant over the whole disc. The number of distinct layers varies from 25-30 in the anterior annulus, 20 in the posterolateral annulus and less than 20 in the posterior annulus [6]. On top of that, the layers does mostly not remain intact and the maximum number of incomplete layer is found in the posterolateral annulus [6].

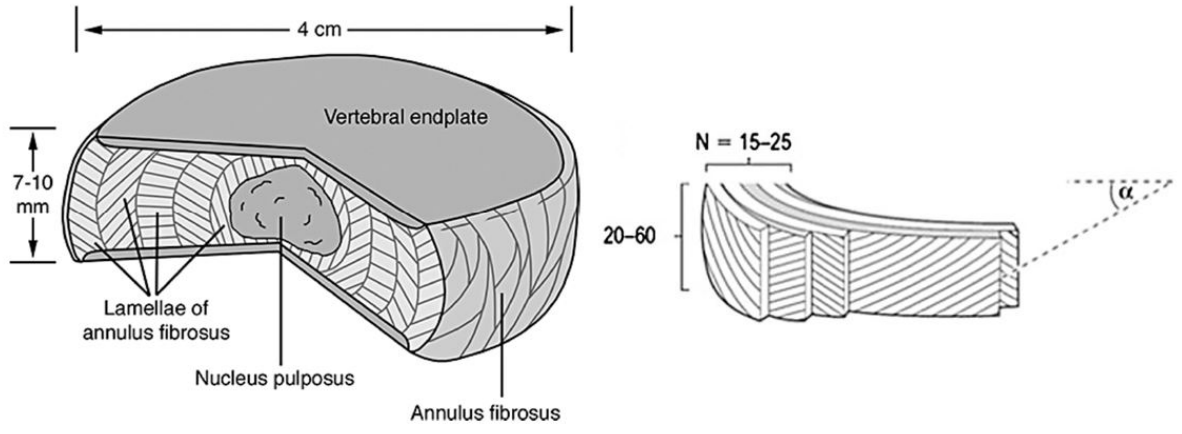

Figure B.3: Intervertebral disc structure. Disc overview with a vertebral endplate (left) and lamalae quantified structure (right), $\alpha = 30°$ [62].

To test the intervertebral disc properties, the general procedure is to test a FSU response in several conditions and then to test a isolated disc behaviour to avoid any confound. Based on Figure B.4, the FSU rotation is affected when removing the annulus,

meaning that the annulus plays a role in the FSU rotation pattern. Furthermore, the isolated disc behaviour shows that only severely degraded disc does exhibit unusual creep behaviour.

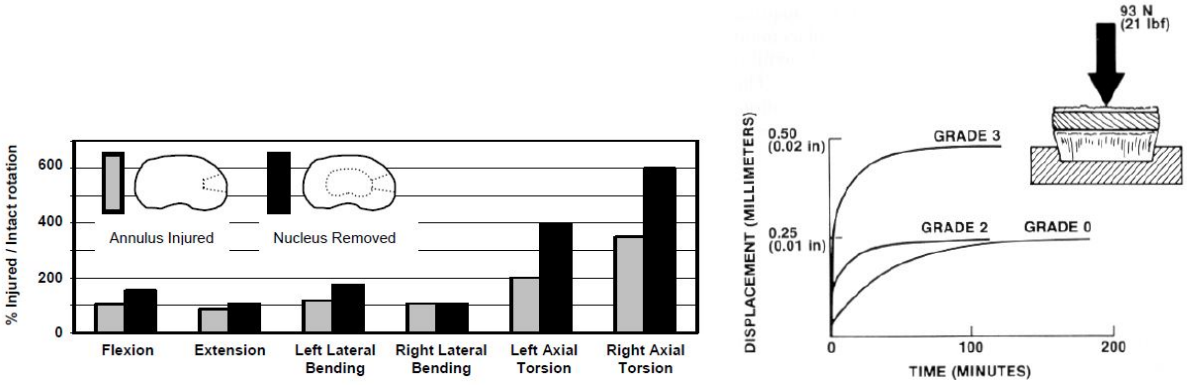

Figure B.4: Functional spinal unit rotation effect for several motions with annulus injured and disc removed intervertebral disc (left). Creep behavior of isolated intervertebral disc for normal (Grade 0) and severely degenerated (Grade 3) discs (right) [152].

Appendix C

Commercialized arthrodesis cage and implementation tool(s)

C.1 For XLIF and LLIF

DePuy Spine Inc: lateral approach

This device is intended for a interbody fusion via a lateral approach and fully documented in [153]. Even if this device is used for lateral approach, some features are relevant for one based on posterior or transforaminal approach.

One noticeable feature of the use of a dilator that will be inserted after skin and fat incision but does not require any pre-insertion muscle incision. The surgeon has to access the muscle just before the spine, confirm the surgical level via fluroscopy and then insert this dilator through the incision and the muscle until the intervertebral disc, like on the Figure C.1. Once the small dilator inserted, a wider dilator is inserted all around.

Figure C.1: DePuy Spine Inc: Mis lateral plateform dilator insertion on a sectional sueprior view (a) and a global overview (b), both highlighting the muscle penetration [153].

Afterward, a retractor is assembled and deployed according to the measured depth on the dilator. Once inserted, it is connected to a rigid arm and the dilator is removed, as shown on Figure C.2. Then, the retractor can be expanded by 1mm increment and the blades toeing is performed via a blade driver into the drive gears, see Figure C.2. When

the retractor placed, a fixation pin is used to stabilize it and the blade length can be manually adjusted. Also, the a light source can be added.

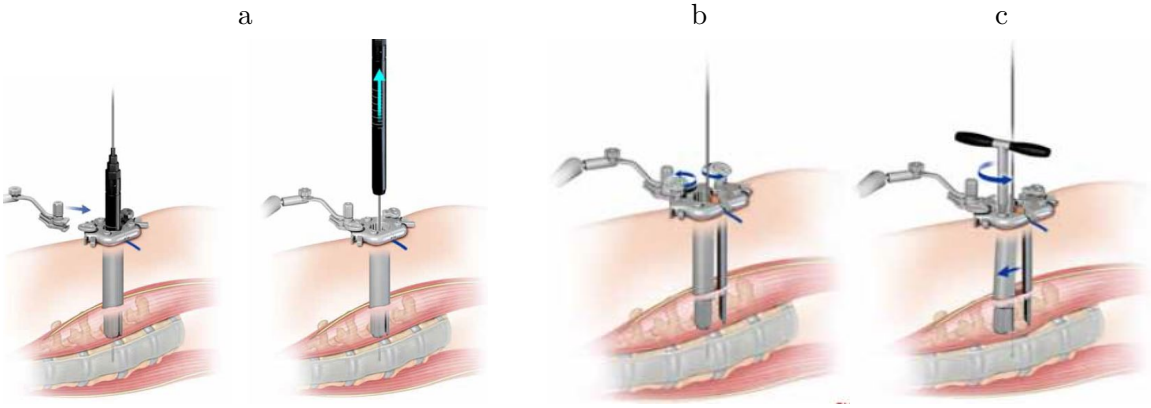

Figure C.2: DePuy Spine Inc: Mis lateral platform retractor (provided in 3 pieces, here represented after assembled) in place (a) and being attached to a fixed arm (left) and dilator removal (removal), retractor expansion (b) and toeing (c) [153].

After the annulotomy and disc preparation via the surgeon preferred endoscopic tools, a distractor is used to increase and gauge the intervertebral space.

Before putting the implant, several trial are impacted until having a satisfying placement and fit via specific device. Once obtained, the corresponding implant is filled with bone graft and impacted while monitoring placement under fluoroscopy. If necessary, insertion blades with a use guide, summarized on Figure C.3, are provided to facilitate the cage placement. On top of that, a graft retention device is provided if necessary, also represented on Figure C.3.

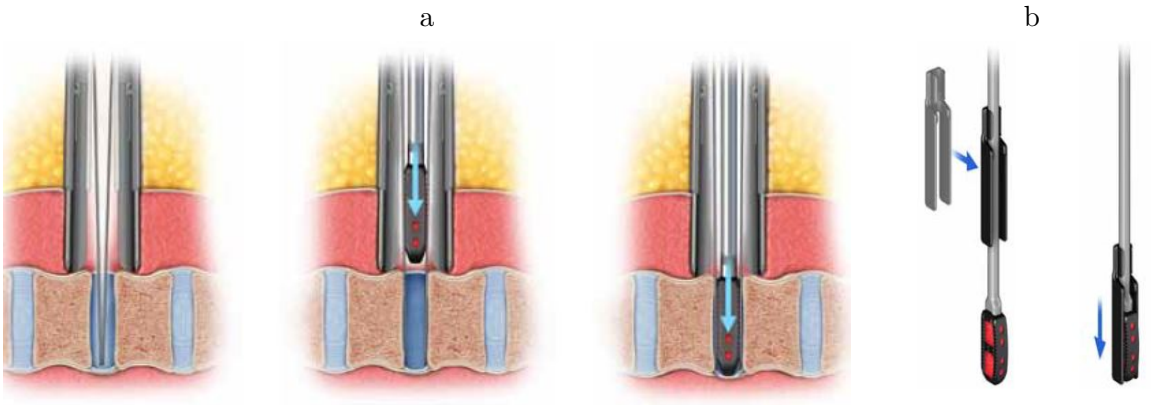

Figure C.3: DePuy Spine Inc: Mis lateral plateform insertion blade procedure (a) and graft retention tool (b) [153].

C.2 For ALIF

Medtronic: ALIF

Medtronic has been developed instruments and technique for all the approach of interbody fusion. One for ALIF using lumbar tempered cage use a procedure with some particular features [154].

Since all the technique is based on a perfectly central placement of the surgical too, the diskectomy has to be performed precisely in the disc center with a precise shape. To do so, the center of the disc has to marked with both AP and lateral fluoroscopy, a centering pin is placed in the center and marks are placed at the midline, as on Figure C.4. This marks are used to place the appropriate template used to mark the lateral margins by incising the disc annulus sharply, also represented on Figure C.4.

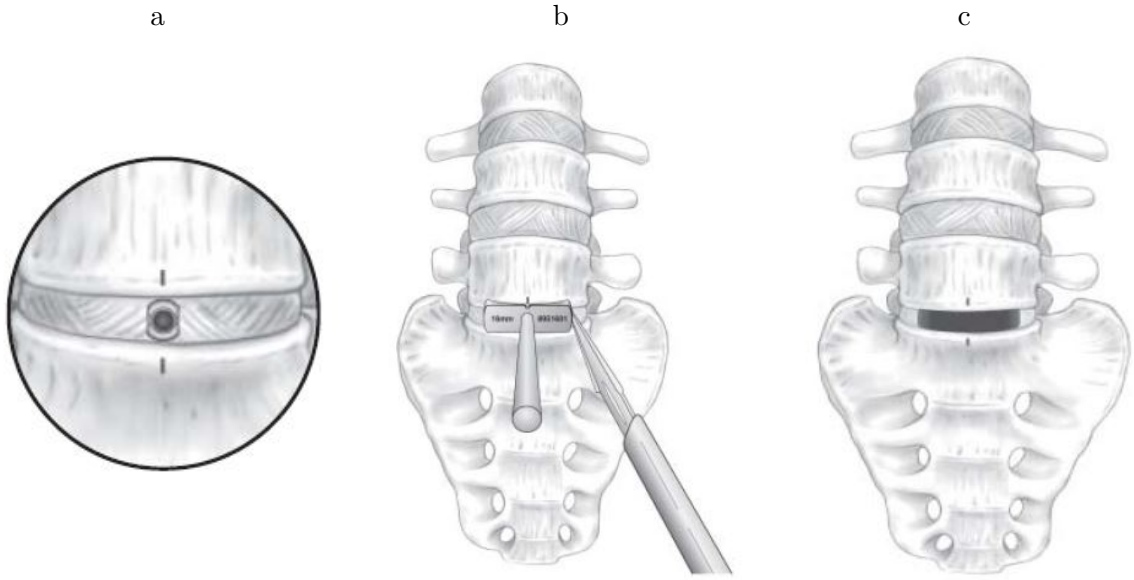

Figure C.4: Medtronic ALIF: pin placement and marks at the midline (a), use of appropriate template to incise diskectomy limits (b) and diskectomy result (c) [24].

Also, the surgical tool contains two barrels, so allowing to insert two distractors after the tool insertion on Figure C.5: one circular and one c-shaped. This is handful to remove only one distractor after disc spacing, for instance the cylindrical one, such that the cylindrical barrel can be used for the next steps while the c-shaped one maintain the intervertebral space, as represented on Figure C.5.

This cylindrical free barrel is used to measure the fix a desired depth and a specific tool function is used to prepare the endplate for this desired depth, as shown on Figure C.6, differing to other tools with which the surgeon is up to prepare the endplate with unprovided tools according to the usual procedure. Lastly, the free barrel is used for cage insertion with 3mm steps.

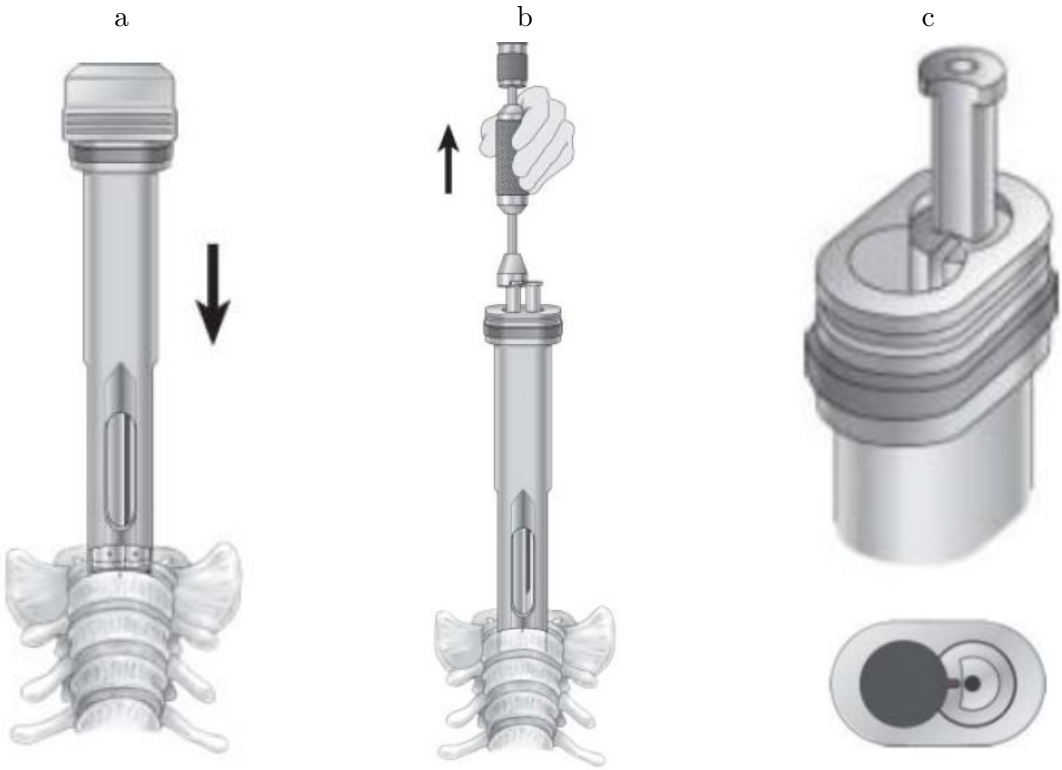

Figure C.5: Medtronic ALIF: tool placements (a), instrument and procedure to remove the instrument from one barrel (b) and tool with removed cylindrical barrel (c) three-dimensional view and superior view [24].

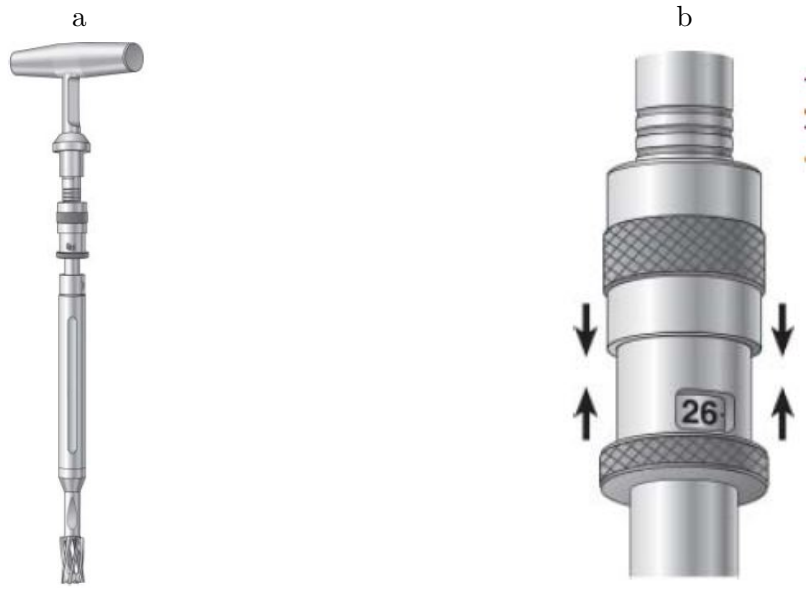

Figure C.6: Medtronic ALIF: endplate preparation tool (a) and zoom on the depth regulator feature (b) [24].

C.3 For PLIF and TLIF

DePuy Spine Inc: PLIF

DePuy synthes has been developed several PLIF instrumentation and technique, among which one for titanium cage [24]. One first notice is that a instruments and technique is provided to remove the cage. However, since this paper aims to implant bone cages that should merge with the growing bone in the intervertebral space, this is not relevant here.

This technique bring to the first light one relevant step. Using the posterior approach, the vertebrae could be too narrow to insert a vertebrae spacer. Therefore, a small disc opener can be use firstly to enlarge the access for the disc spacer. Also, is the intervertebral space is really narrow, using consecutively wider disc spacer allow to increase the intervertebral space progressively. Figure C.7 shows the difference between the disc opener and the intervertebral disc space.

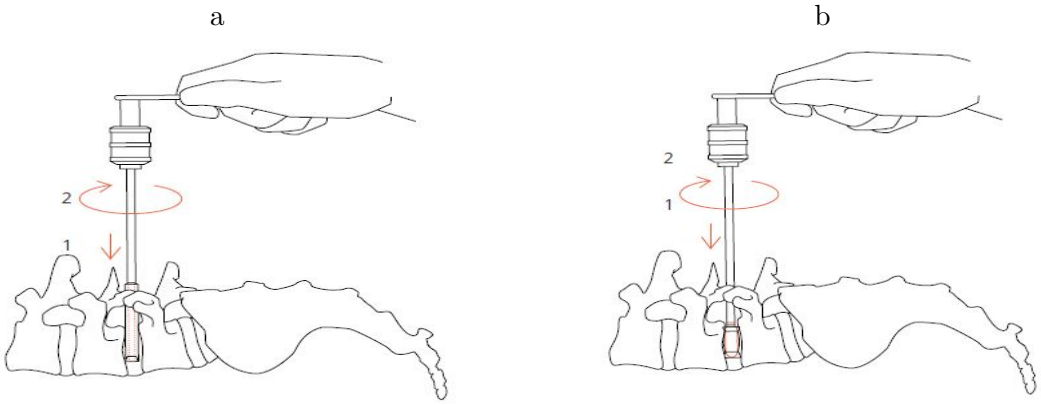

Figure C.7: Synthes: disc opener (a) and spacer (b) for PLIF, both worjing via insertion (1) and 90° clockwise turn (2) [24].

A last notice is that, since the cage has two flat side and two perforated sides, the cage is inserted with its flat sides in contact with the end-plates and then turned by 90° to have the perforated sides in contact with it.

Medtronic: TLIF and PLIF

Medtronic also developed instruments and surgical technique for PLIF and TLIF [27]. A first notice is that Medtronic specify the x-ray marker location at the beginning of the surgical guide. One could so wonder if it could be useful to add space for x-ray marker during cage sculpting and add markers at these locations afterward.

Moreover, their developed tools are compatible with both open TLIF and MAST TLIF, as shown on Figure C.8. Figure C.8 shows at the same time that a cutter is used to access the disc nucleus while a rotated cutter and/or a shaver is used to remover the the nucleus (no detail about their mechanical functioning is provided).

To maintain the disc space after disc retractor (Figure 2.8b), working as shown on Figure C.8, it is suggested to use screws and one rod on the opposite side of the TLIF approach side to maintain the intervertebral disc space.

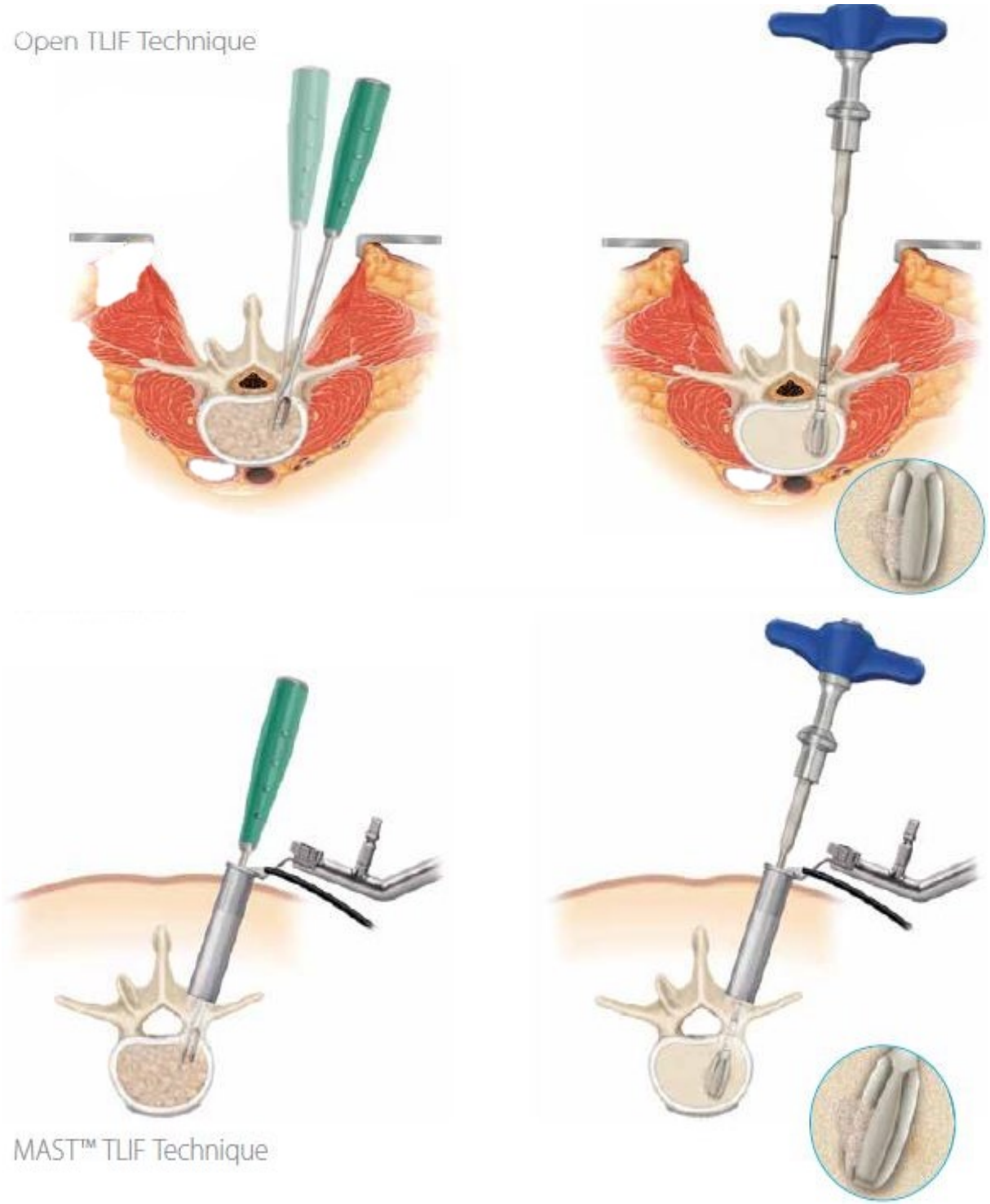

Figure C.8: Medtronic TLIF: tool for disc space preparation is both compatible for open sugery (top) and MAST (bottom) access [27].

The used tools for end-plate preparation are angled, what can be visualized on Figure C.9. The described technique also use trials to choose the appropriate cage and a cage insertion tool is provided, specific to the cage shape. The technique place autograft in the cleaned and prepared intervertebral space before placing the cage.

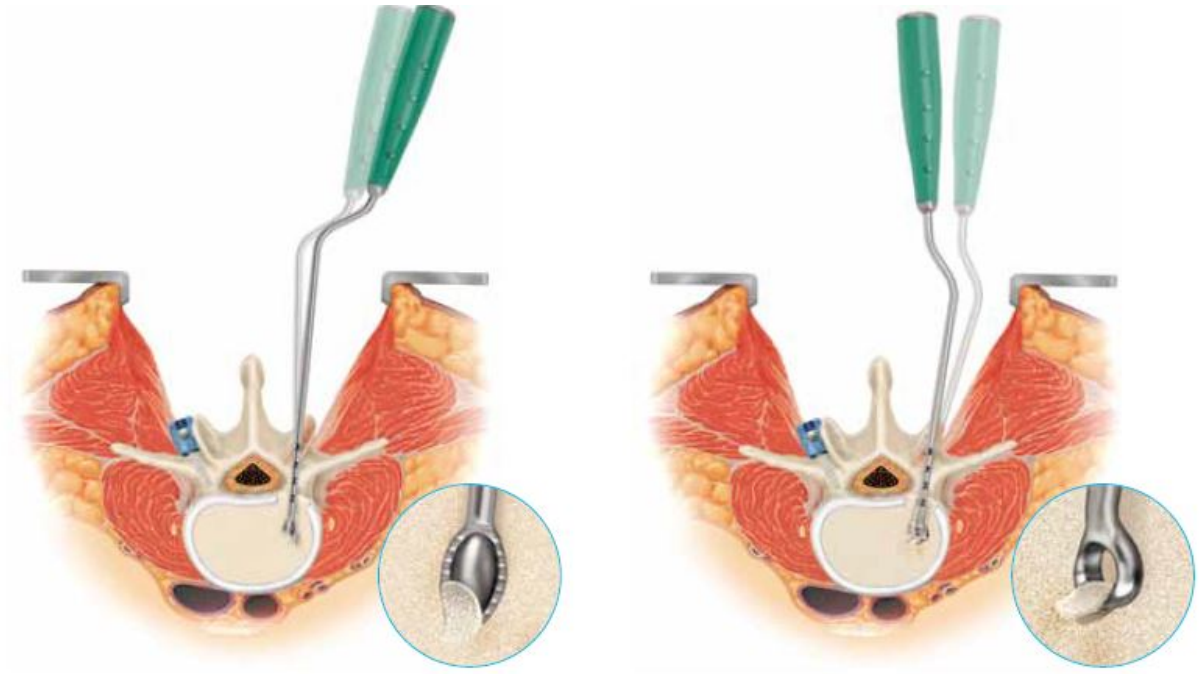

Figure C.9: [Medtronic TLIF: angled instrument for endplate preparation [27].

After placing the screws and rod on the approach side and closing, the cage placement is controlled via X-rays thanks to the cage markers. Medtronic also provide a pedicle navigation and neuromonitoring device.

All the remarks about the PLIF are also true for the TLIF instruments and procedure, expecting the angles instruments that are specific for TLIF procedure.

Orthopaedic implant company (Stryker): PLIF

The cage implementation technique for PLIF provided by the orthopaedic implant company provides some other useful features that could be relevant for TLIF as well [155].

First of all, two techniques for disc distraction and endplate preparation are proposed. One uses one unique instrument with two smooth faces and two sharps ones. The smooth are used to distract the disc by impacting wider and wider distractors. To do so, the distractors are inserted with its widest part facing laterally and then turned such that this widest part distract the disc with its smooth faces. The sharp faces is used once the final distractor inserted since, by rotating the distractor, the sharp edges will prepare the endplate for cage implementation. The second technique use first distractor with four smooth edges and then another instrument with four sharp edges is inserted for endplate preparation. This both technique are proposed since, depending on surgeon preference, one would prefer the first or second one. However, the second does reduce the injury risk since no sharp edge is on the distractor. The surgeon can evaluate if the endplate is ready by looking to the removed material after removing the endplates preparation tool.

Also, the technique provide instrumentation for the cage preparation, for instance the bone graft placement. As shown on Figure C.10, it allows to fix the cage to the instrument and to place bone graft inside the cage. On top of that, a final impactor is provided in addition to the primary impactor to tamp the cage to its final position after removal of

the primary cage impactor, following the procedure of Figure C.10. A last small notice about the x-ray markers is that they are one horizontal and one vertical marker.

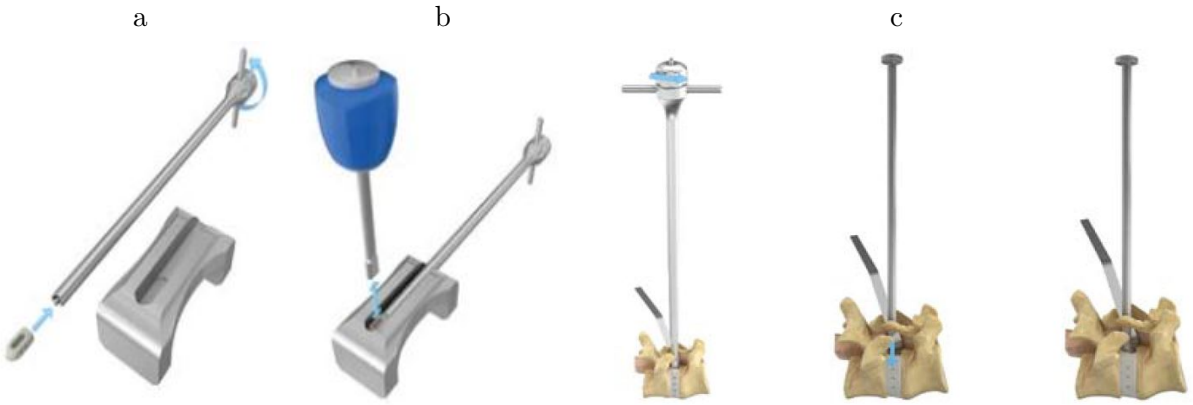

Figure C.10: Orthopaedic implant company (Stryker) PLIF instrumentation and technique: cage fixation (a), filling with bone graft (b) and insertion (c) with impaction using primary (left) and final (right) impactors [155].

Stryker: TLIF

Stryker developed a very well documented instrumentation and technique for TLIF [25]. All the surgical guide is explaining and illustrating an open approach but it is specified that a minimally invasive approach is very similar and is typically conducted via the same instruments following the same steps.

Even if the surgical guide shortly explains how to access the intervertebral disc space and perform the discectomy and endplate preparation, Stryker provide instrumentation for distraction and cage implementation only. But it uses the annulotomy explanation to insist on the required access area to insert the cage, for instance 12mm wide incision since the cage is 12mm wide.

The first provided instrument is a paddle dynamic distractor with its extension handle, represented on Figure 2.10. The extension handle is mandatory to prevent excessive torque on the instrument's distal end. Also, prior to use it, the distractor must be fully closed (7mm) and the indicator and paddles are lubricated. For distractor insertion, a slaphammer is provided if necessary. Also, the guide specifies that the distractor paddle must contact the cortical rim and that it could be confirmed via fluroscopy. The distraction is made via rotating the T-shaped distractor handle while over distracting the disc space and over torquing the paddles is carefully considered, as shown on Figure 2.10. Once distraction performed, the distraction is stabilized according to one of the previously described technique and the distractor is closed and removed.

The second provided tool is a navigator trial that aims to try different implant size by attaching the chosen trial, attach it to the navigator trial and insert it into the disc space, as shown on Figure 2.11.

Once the implant size chosen, the surgeon can implant the filed cage via a straight or bayoneted inserter, both on Figure 2.12. This inserter can be in a lock or rotate state. The rotate state is used to grab the implant by the procedure shown on Figure 2.12 (this

can also be done manually). Afterward, thee lock state is used to primary impact the implant and the rotate state is then used to to rotate the implant, such as on Figure 2.12. During the impaction, a slaphammer can be fixed to the inserter if required.

Zimmer Biomet: TLIF

Zimmer Biomet provides an instrumentation for TLIF with a distraction close to the one proposed by Stryker and an insertion very similar to the one proposed by Medtronics [52]. However, some small variation can be noticed because of the cage (Figure 2.13a). The cage have integrated an fixation system, which have to be set up once the cage implemented (Figure 2.13b).

First of all, Zimmer Biomet does not provide any tool for disc removal. Also, the provided distractor is a very similar T-shaped paddle distractor of Stryker.

For the endplates preparation Zimmer Biomet does provide angle curette as the one on Figure C.11. This is provided to ensure a sufficient preparation in the regions difficult to access, what was noticed by the Stryker guide by no specific instrument were provided for these zones [52].

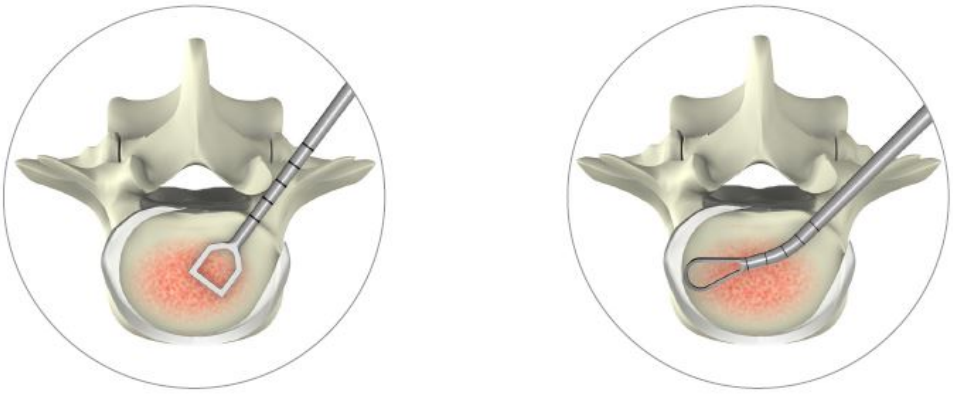

Figure C.11: Zimmer Biomet TLIF: straight curette (left) and angles curette (right) for endplate preparation, the angled one for easily missed zone during endplate preparation [52].

Afterward, trials are used to determine the cage dimensions and an instrument to put bone graft into the cage is also provided, but this one provide a knocking system to lock the cage during cage filling [52].

The cage impaction use the particular cage design that has fixation to the endplate to ensure the cage to be maintained in place, but this is not relevant for bone cage impaction that will not have this kind of mechanism. However, a last notice is that an instrumentation and technique for implant removal for revision is provided [52].

Appendix D

Detailed approaches

Based on the generic arthrodesis procedure and ACIF, ALIF, TCIF and ALIF specifications presented in section 2.2: Arthrodesis: common medical procedures, some clarifications and illustrations for all these approaches are provided.

D.1 Pre-surgical steps

Before operating, some pre-surgical controls are performed to check for any contraindication to the arthrodesis or chosen approach. Afterward, the patient is placed in a position depending on the approach and secured via security belts or straps on a standard radiculent (allowing radiation to pass through) operating room (OR) table with special padding and supports to adjust patient's position that is carefully placed such that a fluoroscopy of the affected discs can be performed [18]. Once the patient installed, a general anesthesia is conducted with intraoperative monitoring, including blood flow and pressure monitoring via a central venous pressure and a arterial line respectively, a Foley catheter and a pulse oxiometry to measure blood oxygen level [18]. Electrodes can be placed and secured in case of neuromonitoring and sequential compression devices can be used to decrease the risk of deep venous thrombosis [22]. If necessary, the patient can be incubated by a breathing tube such that the patient breathes via a ventilator during the operation [23] When all the monitoring devices are placed, the patient is anesthetized and when falling asleep, the patient's skin located at the incision level is prepared as well as the hip if a fusion using allograft is planned [21]. Obviously, the patient's surgical area is cleaned, special sterile drapes are placed and the operating team wear sterile surgical attire [23].

About the access side choice, even if there could be anatomical reasons to choose, the chosen side mostly depends on surgeon's preference [7]. Generally, right-handed surgeons tends to use a right-sided approach, and inversely for left-handed surgeons [22]. According to the access side, the assistant is usually across the table and the scrub nurse place next to the instrument table on the patient foot (Figure D.4) [18].

To confirm the surgical level, several techniques exist. Some surgeons can use a spinal needle and insert it into the disc to inject a fluorophore while other surgeons just place a metallic instrument beneath the affected disc. Then, a X-ray image is obtained to check if the instrument or fluorophore is at the same level as the damaged disc [18].

D.2 Anterior cervical spine approach: ACIF

Firstly, about the patient positioning, the patient is lied on an operative table on the back (supine position). On top of that, a soft pillow can be placed under the patient knees to flex the hips and knees and so prevent stretch injuries. To facilitate the cervical spine visualization during the fluoroscopy, especially for lower cervical surgery, patient's shoulder can be tapped down to slightly tract the shoulder but avoiding excessive traction that can lead to plexus stretch injuries. Lastly, a folded towel is placed under the patient's neck to help the neck to support the chocks due to the graft and potentially rod and screws placement [22]. Once the patient installed, the patient is anesthetized and when falling asleep, the patient's neck is prepared as well as the hip if use of allograft [21].

Afterward, the surgeon make a 2-inch incision lateral the neck midline on the left or right side. In case of more than a two-level operation, an additional carotid longitudinal incision must be considered [22]. The incision is used to make a tunnel to the spine by moving aside muscles, retracting the trachea, aspophagus and arteries (the carotid must be protected) medially and incising the prevertebral fascia to expose the intervertebral disc [21], what result in the situation represented on Figure D.1.

To distract the discs before discectomy, distraction-post pins can be placed above and below the disc after the anterior longitudinal ligament is incised [22]. Thereafter, the disc outer wall is cut allowing to remove the nucleus.

Thereafter, if the nerve is compressed, the surgeon decompress it as described in the generic procedure [21]. Some surgeons choose to cut the posterior lateral ligament to ensure adequate cord decompression and to avoid missing a disc fragment but this is subject to a lot of controversy due to the potential worsen spinal instability. Decompression is considered completed when a small probe can pass easily through each foramina, what mean that the neural foramina is open bilaterally [22].

Once the discectomy finished, the intervertebral space is further distracted if necessary (again via the distraction pins, or another device depending on available instrumentation and surgeon preference) and prepared for the interbody fusion, what is done during the sixth surgical step represented on Figure D.1. If required, the vertebrae are stabilized thereafter using a metallic plate centered on the cage impaction level(s) and fixed via pedicles screws [21].

The seventh and last step is to close the incision and check the graft and plate position as explained in the generic procedure.

Figure 2.6 illustrates some of the key steps since the generic example was illustrated for an ALIF procedure.

D.3 Transforaminal cervical spine approach: TCIF

The advantage of a TLIF is the facilitated access since it is based on a posterior access, hence requiring the patient to lie face down on the OR table. The access consists only of a midline incision and overlaying muscles dissection to expose the spinous process and the laminae, as represented on Figure D.2 [7]. Afterward, to have access to the intervertebral disc space, the surgeon can perform a laminectomy (laminae and spinous process removed) or a laminoplasty (laminae and spinous process altered) depending on the required access and the vertebral anatomy [7]. For example, the roof of the foraminal can be drilled with a 3 mm cutting high-speed burr until reaching the anterior cortex of the superior articular

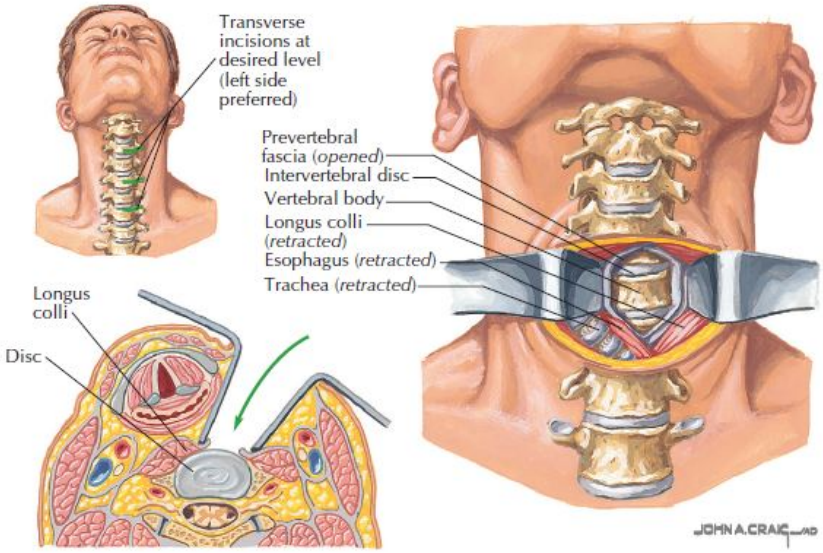

Figure D.1: Anterior open approach to the cervical spine with named anatomical structures [7].

facet [35], resulting in a transforaminal access to the intervertebral space represented on Figure D.2. Once the laminectomy or laminoplasty performed, the dorsal nerve root (see Figure A.3) is cranialy retracted to access the ucinate process (that is a hook shaped structure found bilaterally in the superolateral margins of the vertebral body in vertebrae C3-C7 [156]) and expose the disc space [35]. Then, the ucinate process is drilled radially to conserve its lateral wall intact, that is used as a constrain to retract the root cranialy if necessary. Now that the access to the intervertebral disc is available, the surgical level can be confirmed using one of the generic techniques.

The available transforaminal approach allows a more-steeper medial angulation access just above the superior pedicle wall, as shown on Figure D.3. Thereafter, the surgeons performs the annulotomy, nucleotomy and nerve decompression successively. Then, this access is used to insert a curette to prepare the endplates [35]. Once the end plates prepared, the filled graft can be placed in the intervertebral space.

The vertebrae stabilization using pedicle screws and rod can be placed before or after cage placement. As seen on Figure D.3, some surgeons prefer to place the screws and one rod on the opposite side of the transforaminal approach before placing the graft and set the second rod afterward, so maintaining disc space space during the cage impaction what allows to remove the distractors even if it should stays without stabilization, while others place the screws and both rods after placing the cage.

Lastly, the opening is closed via a dural patch and the incision is closed as usual D.3.

D.4 Anterior lumbar spine approach: ALIF

Since the operation requires to immobilize the abdominal content, the patient has to consume only liquid the day before the operation [18]. Also, evaluate sign of calcification in the iliac vessels and aorta as well as the presence of bone spurs from the spine is essential since these increase the surgery risk [18]. On top of that, for males over 40, postmenoposal

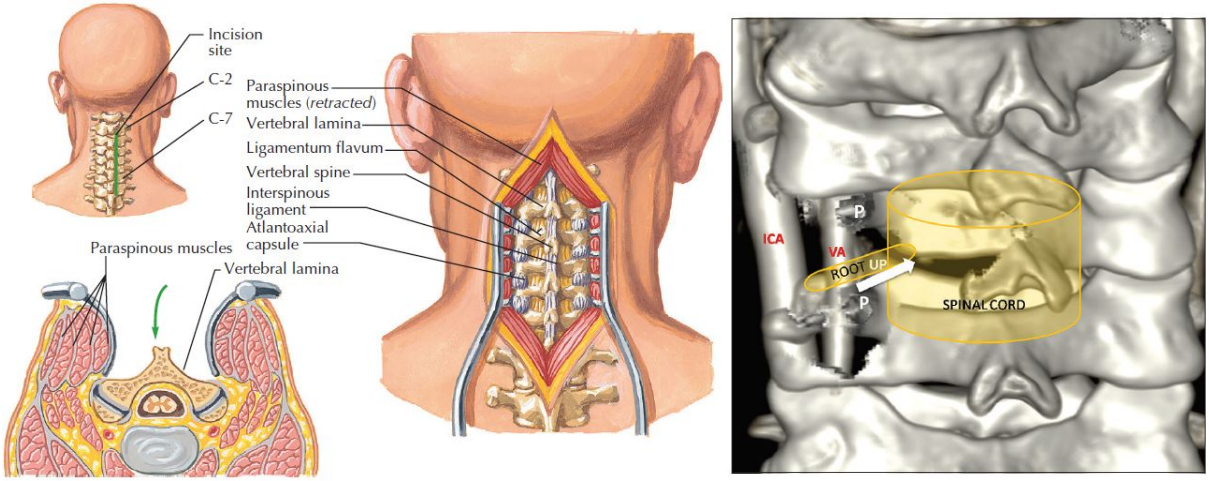

Figure D.2: Posterior open approach to the cervical spine (left) [7]. Transforaminal approach for cervical interbody fusion with allograft (right) three-dimensional surface reconstruction of cervical computed tomography scan image with angiography where the lamina and lateral mass are digitally subtracted and the encountered nervous structure (spinal cord and root) are highlighted [35]. The UP arrow shows the used trajectory to the intervertebral disc space. ICA: Internal carotid artery, VA: Vertebral artery, P: Pedicle in cross-section, UP: Uncinate process.

women and patients with history of claudification, palpate pedal pulses must be performed and if any deficit is noted, this has to be further investigated via non-invasive technique [18]. This avoid to confound post-operational complications and pre-existing abnormality [18]. Some contradiction of an anterior approach to the lumbar spine could be a previous abdominal surgery or exposure to the lumbar spine and obesity, what may involve to change the approach [34].

If this approach is used, the patient has to be placed in a neutral supine position (legs together, arms abducted by 90° that could be extended or folded and secured on the chest). The table should be adjusted to allow abdominalperineral (AP) and lateral fluoroscopy at the level of the affected disc(s) [18]. The patients arms has to be immobilized without causing hyperflexion and no bolster should be used since it would lead to iliac vessels hypertension and lumbar spine overload, what may hind an necessary discectomy and cause posterior disc space distraction [18]. Please note that the "Da Vinci" position shown on Figure D.4 is an alternative position with an appropriate OR table [18].

To approach the lumbar spine anteriorly, two major approach exist, both could be right or left sided. Firstly, an incision of 5 to 6 cm is made depending on the operated lumbar level(s), as shown on Figure **??**, from the cranial to the caudal end, what highlights the importance to localize correctly the surgical level(s). Once the rectus fascia exposed, it is incised 1 to 2 cm from the midline in same direction than the skin incision to see the right rectus muscle [36, 18]. Afterward, the muscles fibers are detached from the linea alba via a circumferential dissection (paying attention to avoid the inferior epigastric vessel) and the rectus muscle is detached and retracted toward the midline [18]. Then, the transversalis and extraperitoneal fascia are carefully incised until reaching the peritoneum.

From here, if the surgeon decide to use a transperitoneal approach, the peritoneum is divided in the midline and the disc exposure is obtained through the peritoneum. However,

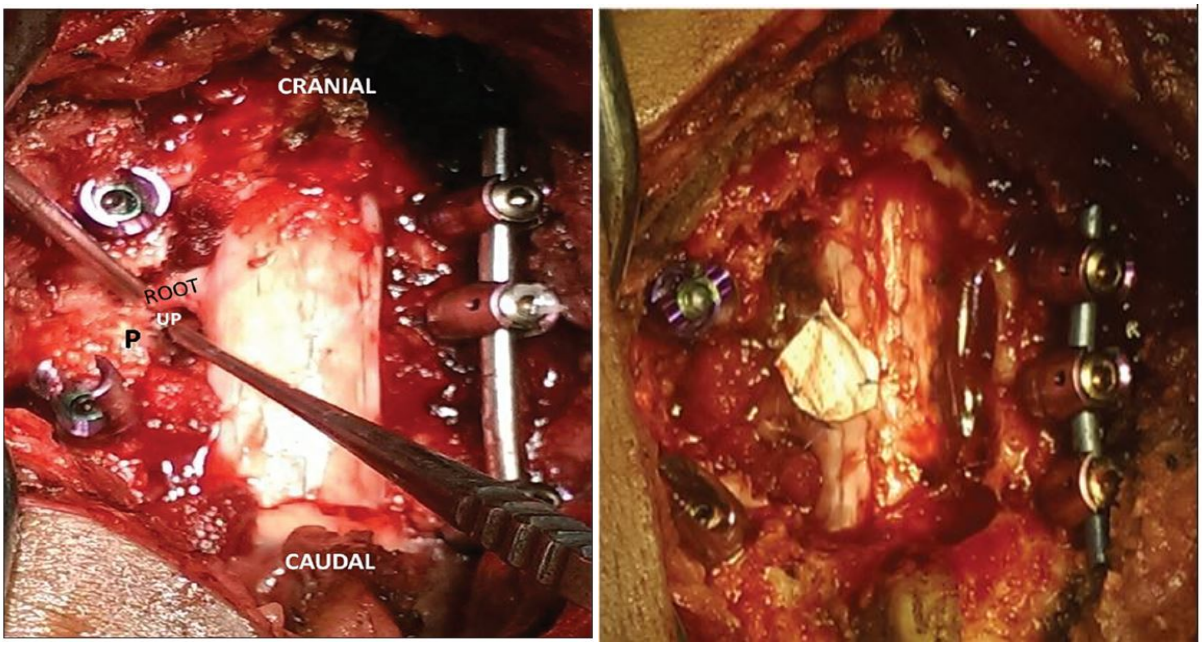

Figure D.3: Intraoperative picture of a patient showing the access to the C4-C5 interbody region under the retracted root, just above the superior wall of lower pedicle (left). P: Pedicle not instrumented, UP: Uncinate process [35]. Intraoperative images of a patient 3 (Group-I) showing C5-C6 facetectomy with transforaminal approach closure with dural patch [35].

this technique lead to longer hospital stay, more respiratory complications and higher perioperative complication and morbidity rate than the followed retroperitoneal approach [33]. Therefore, the retroperitoneal approach is usually preferred.

So, the more usual retroperitoneal approach consists of progressing laterally along the peritoneum until the fascia ends at the arcuate line to retract to peritoneal content and expose the lumbar spine [34]. To do so, the edges of the incision reaching the peritoneum are grasped and detached as far as possible from the peritoneum via careful incisions [18]. Next, a finger dissection detach and push posteriorly the peritoneum from the posterior rectus fascia, leading to the retroperitoneal space shown by the hand position on Figure D.5. Then, the peritoneum is pushed posteriorly medially until reaching the psoas and then medially while continuing dissection, paying to the genitofemoral nerve and ureter, where the the disc, vertebral body and iliac arteries can be palpate medially [18]. At this point, the peritoneum can be retracted via retrators and the fat can be taken off using sponges, such that the desired level is accessed [18].

Some access has specific properties that has to be specified. For instance, the access to the L5-S1 disc has to be done below the aorta and vena cava vein bifurcation while the access to the L4-L5 disk is done above, as represented on Figure D.6. Also, for operation on L4-L5 alone or combine with L5-S1 or L3-L4, the iliolumbar vein(s) must be ligated and cut by placing a right angle clamp around it and tying with a ligature close to the junction with the common iliac vein, as shown on on Figure D.6. Now, the left iliac vein and artery has to be separated from the spine using finger dissection (ensuring at least one finger space between the vessels and the spinal cord) and a pusher to maintain them on the patient's right [34]. The remaining running vessels can be transected and swept to

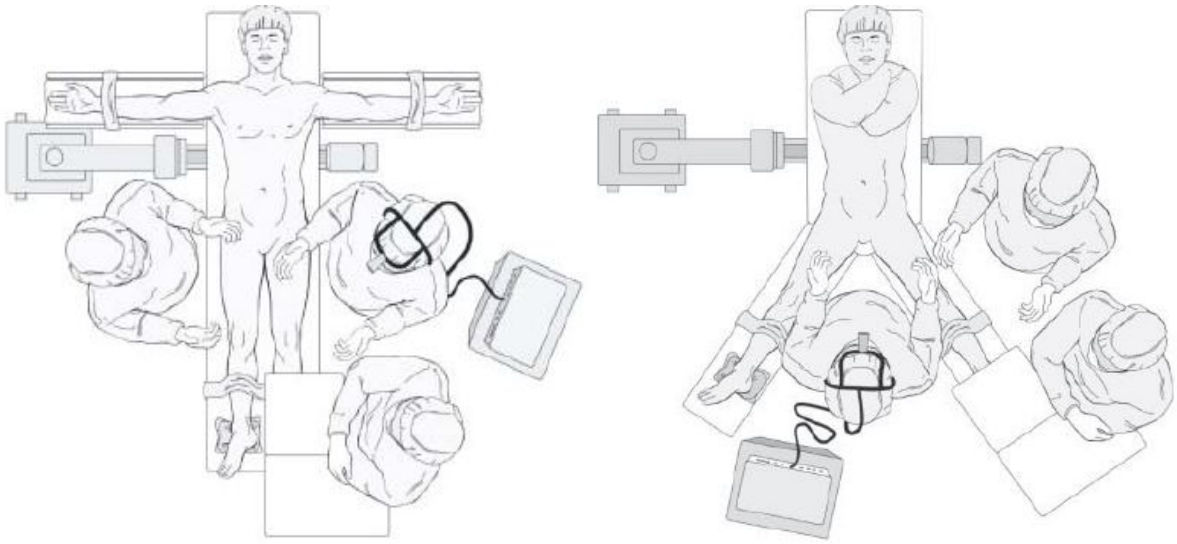

Figure D.4: Patient's supine position (left) and "Da Vinci" position (right) with the surgeon, assistant, nurse and instrument table location for a left side access.

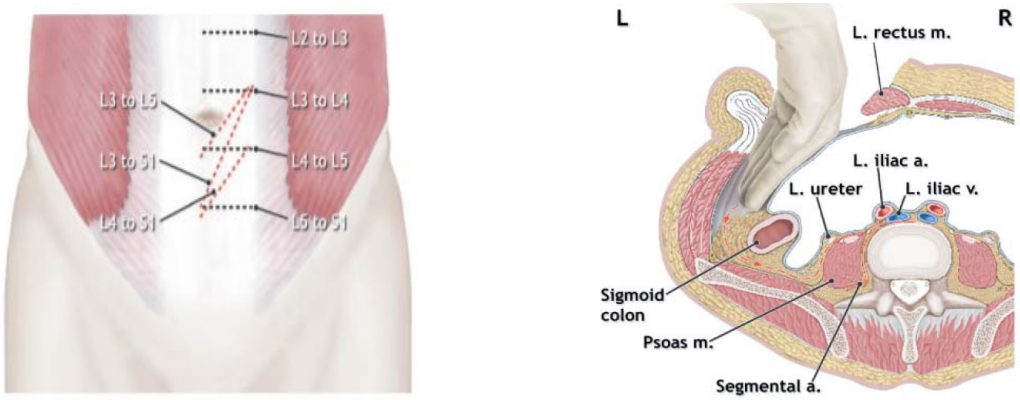

Figure D.5: ALIF incision depending on the operated lumbar level (left) [18]. Please note that the incision location can vary depending on patient anatomy. Retroperitoneal approach with the surgeon hand in the retroperitoneal cavity (right) [18].

their closest side [34]. Figure D.6 represents the final access.

Once the access to the lumbar spine obtained, several methods exist for the disk exposure. The first is to simply maintain the current situation, for instance keeping sweeping the vessels via manual retractors. Figure D.7 depict the exposure for a L4-L5 and L5-S1 exposure. The main difference is that, for L5-S1 level, the exposure is obtained below the bifurcation, so between the iliac vessels and that the middle sacral vessels might be taken between clips, ligatures or cautery (avoided in male due to risk of injury to the superior hypogastric plexus fiber) [18]. Also, the left vessels can be held to the right using a peanut sponge. For the L2-L3 and L3-L4, the access and exposure is the same as for L4-L5 but the iliac vessels are usually not mobilized, so avoiding to transect the iliolumbar vein, making these access easier (except for obese patient that make anterior access to L2-L3 very challenging) [18].

The second option for lumbar spine exposure is to use table-held retractors [18]. Briefly,

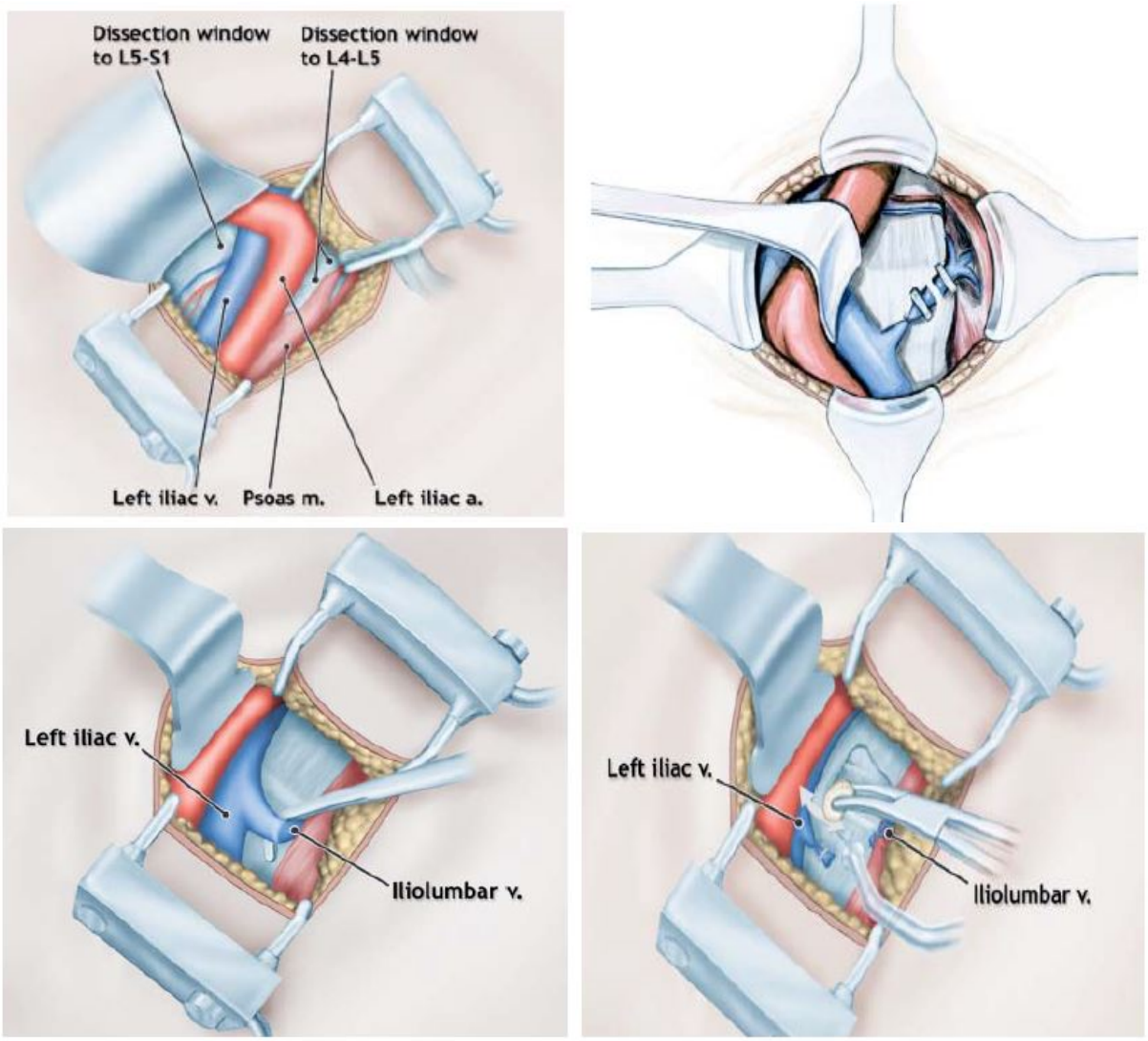

Figure D.6: Access to the retroperitoneal space for surgical levels L4-L5 and L5-S1 with major neurovascular structures (top-left) [18]. Mobilization of the left iliac vein and ligation of the iliolumbar vein for L4-L5 approach (top-right) [18]. iliolumbar vein ligation via a right-angle clamp (represented in position) (bottom-left) [18]. Final L4-L5 access after mobilization of the left common iliac vein and artery and other vessels with sectioned iliolumbar vein (bottom-right) [18].

the previous retractors has to be removed, the table-held retractors blades are assembles (as many as necessary depending on surgical level(s), incision length and surgeon's preference) and fixed to the table [18]. Afterward, the first blade is used to expose the anterior surface of the spinal cord by elevating the vascular structure after anchoring the reverse lip of the blade to the spine's edge, as depicted on Figure D.8 [18]. Then, a second blade is placed on the patient's left side following the same procedure, resulting in the rightward situation of Figure D.8 [18]. Lastly, fluoroscope is used to determine the midline position and supplementary blades are placed consequently if necessary [18].

Now the exposure is ensured and stabilized, the anterior longitudinal ligament is opened to access the inetervertebral disc(s) and the next steps are the same as for any

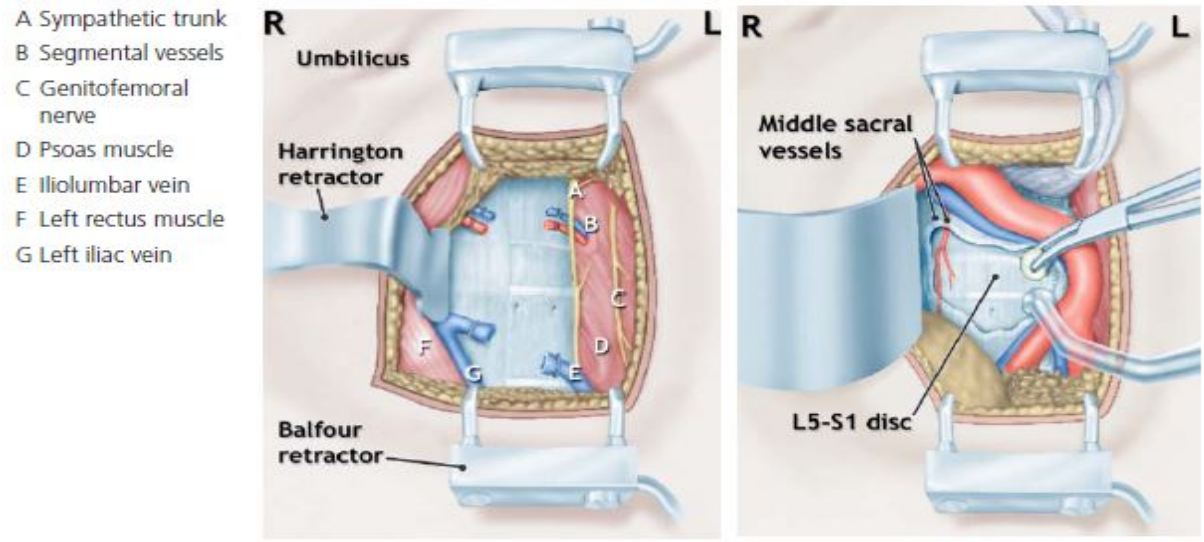

Figure D.7: ALIF exposure using retractor at the L4-L5 level (left) and L5-S1 level (right) [18].

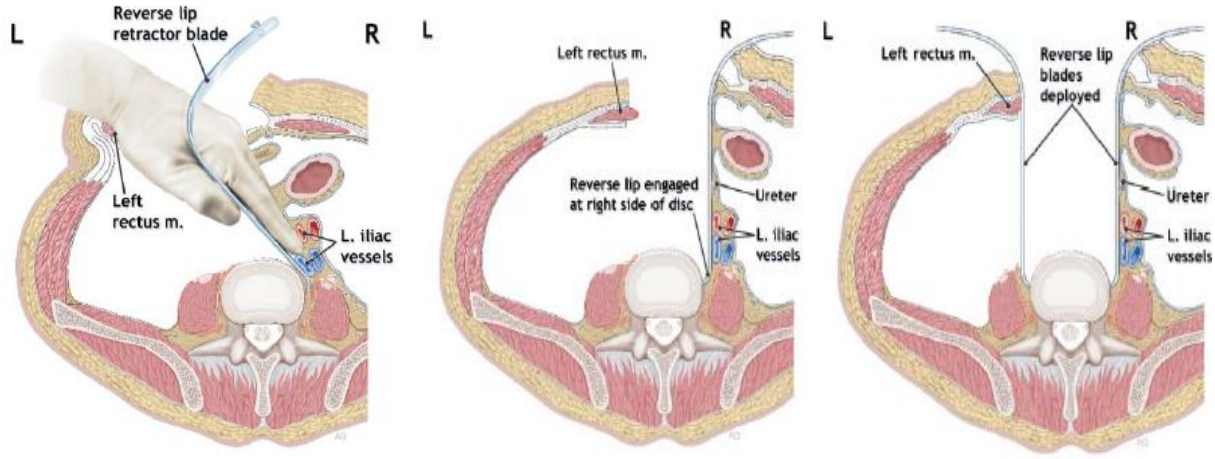

Figure D.8: ALIF exposure to L4-L5 using table-held retractors main steps [18].

interbody fusion [33]. The disc is excised, required nerve decompression is performed, the intervertebral space is prepared for interbody fusion, and a filled cage is placed in the intervertebral space. Lastly, the retractors are removed and the access is closed [18].

On top of that, if vertebral stabilization is needed, a posterior approach can be used to stabilize the vertebra(e) with rods and screws.

D.5 Transforaminal lumbar spine approach: TLIF

For a transforaminal approach, as for a posterior approach, the patient is placed and secured in the prone position represented on Figure D.9 (please note some particular case(s) could require lateral position) [23]. Then, the patient is generally anesthetized and required monitoring is set.

To access the lumbar spine, a 3 to 6 inch incision (depending on the number of involved

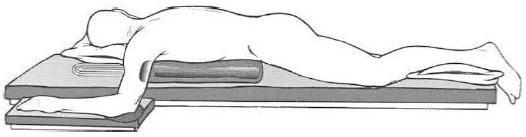

Figure D.9: Patient positioned prone on chest roll [157].

level(s)) is made at the surgical level(s) in the midline. Typically, the incision start from the superior spinous process to the lowest spinous process, so from L3 to L5 for a L4-L5 level [25]. After the skin, the thoracolumbar fascia (see Figure A.5) and paravertebral (also called erector spinal) muscles (spinalis, longissimus and iliocostalis muscle of Figure A.5) are incised and retracted using manual or table-head retractors to maintain the access. Laterally, the goal is to expose the facets, what fix the lateral incision limit [25]. Then, the inferior articular process of the superior vertebra (left or right process for left or right sided approach respectively) is removed with two cuts: one medial to the facet until its superior border and one horizontal towards the foramen [25]. After both cuts, the inferior articular process is removed and the ligamentum flavum is visualized [25]. At this stage, x-rays is performed to confirm the surgical level [23]. Once the surgical level confirmed, the disc must be accessed. After the laminectomy, the ligamentum flavum is released using a curette (ligamentum flavum releasing is preferred to resection even if resection can be necessary for patients with neurologic compression [25]) to perform a facetectomy and so access to the intervertebral disc, exhibiting at the same time the spinal root shown on Figure D.10. The nerve roots and neurologic structures can be carefully protected and retracted if the access is not wide enough, but this is whatever strongly recommended to minimize nervous injury risk [23].

If necessary, at this stage, a distractor is used to restore and measure the intervertebral space and the distraction is maintained via pedicles screw and one rod on the opposite side to access or external distraction can be used, bony element distraction (only for open surgery, via maintaining pressure on spinous process or laminae) or positioning device (for lordosis) [25]. Then, the disc nucleus is partially removed or totally removed and then refill with bone autograft [23]. The surgeon must pay attention to the central and opposite side of the disc since these ones are easily missed with TLIF due to their difficult access but these are necessary to provide optimal area for interbody fusion [25].

Ensuing cage impaction, if necessary, the vertebrae can be stabilized via rods and screws. As for the TCIF, one sided stabilization can also be done before the disc replacement since the rod will not obstruct the disc access. In that case, only one rod is placed after cage impaction.

Lastly, retractors are removed and the incision is closed by the usual procedure.

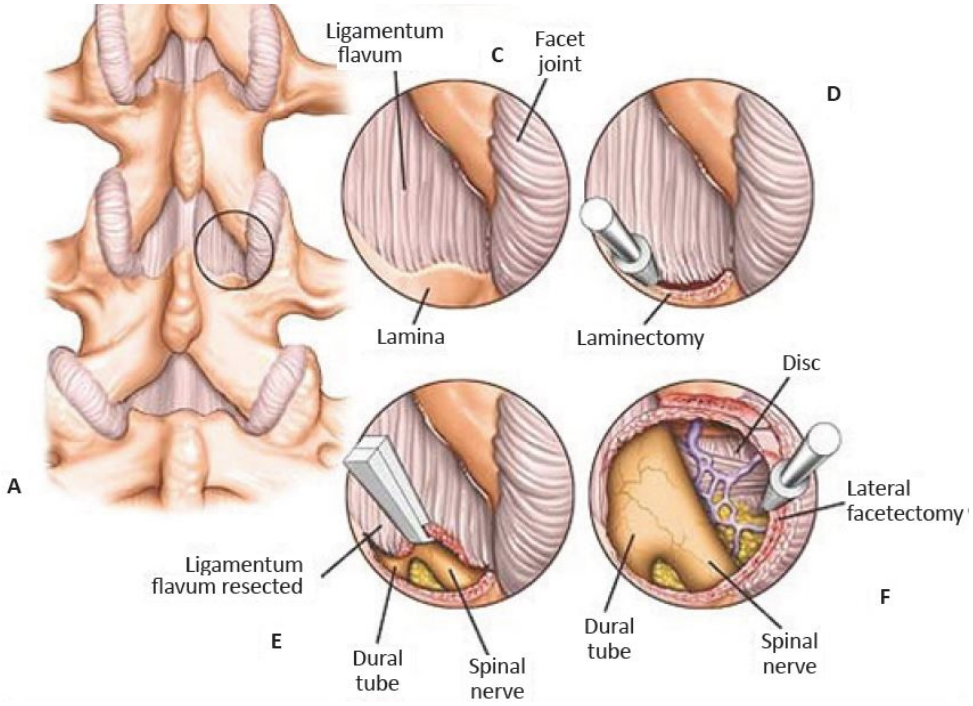

Figure D.10: TLIF: Intervertebral disc access via one-sided laminectomy with key structured. Confirmation of surgical level (A), the one-sided laminectomy is performed (C), the ligamentum flavum is sectioned and retracted (E) and facectomy can be performed laterally to the spinal nerve (F). [26]

Appendix E

Demonstrations

E.1 Uni cell model

Before starting developing unit cell model (UCM) hypothesis and equations, two well-known equations from beam theory must be explained. For a beam of length L fixed on its both extremities with an applied force F on its middle, the beam deflection if given by:

$$\delta = \frac{FL^3}{48E_sI} \text{ with, for a rectangular beam, } I = \frac{bh^3}{12}$$

where:

δ = beam deflection $[m]$
F = applied force $[N]$
L = initial beam length as described on Figure E.1 $[m]$
E_s = structure Young modulus $[\frac{N}{m^2}]$
I = beam inertia moment $[kgm^2]$
b = beam section width in the neutral axis direction $[m]$
h = beam section height $[m]$

When discussing an UCM, the whole unit cell properties has to be distinguished from the material properties:

- a_s: property a for the material of which the porous network is made, i.e. the **s**olid
- $a*$: property a for the porous network, i.e. the spatial arrangement of the solid

Focusing on bone, unit cell modelling is used to study bone properties by defining each cell as as a structure of bone material filaments, that can be considered as beams. For instance, Figure E.1 represents a potential unit cell in which each unit segment can be considered as a beam fixed on both extremities with an applied force in its middle. This structure can be repeated in 3D and linked together to model a porous network and fit to its shape.

The unit cell model can be used to link the relative young modulus $\frac{E^*}{E_s}$ to the relative density $\frac{\rho^*}{\rho_s}$. To obtain this link, lets start with the expression of the strain ϵ :

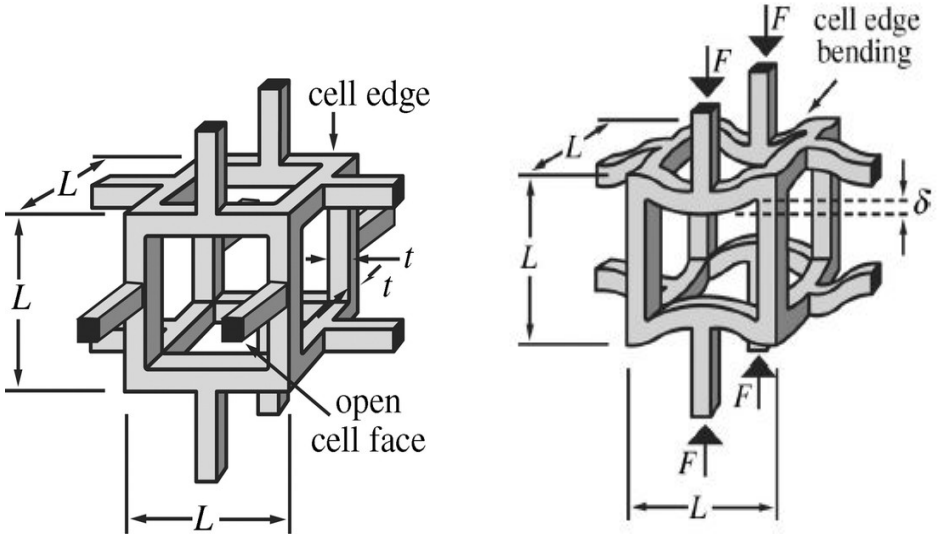

(a) (b)

Figure E.1: (a) An idealized open-cell structure. (b) Structure under pure bending due to an applied force F leading to a deflection δ [105].

$$\epsilon = \frac{\delta}{L}$$ With δ = deflection on L = width of the unit cell

$$\Leftrightarrow \frac{\sigma*}{E*} = \frac{\delta}{L}$$ Because the network's young modulus is defined as: $E^* = \frac{\sigma*}{\epsilon}$

$$\Leftrightarrow \frac{\sigma*}{E*} \propto \frac{FL^3}{E_s I L}$$ Because of the deflection$\delta = \frac{FL^3}{48E_s I} \propto \frac{FL^3}{E_s I}$

$$\Leftrightarrow \frac{\sigma*}{E*} \propto \frac{FL^2}{E_s I}$$

$$\Leftrightarrow \frac{F}{L^2 E*} \propto \frac{FL^3}{E_s I L}$$ Because the stress of the porous network is defined by: $\sigma* = \frac{F}{L^2}$

$$\Leftrightarrow \frac{E_s}{E*} \propto \frac{L^4}{I}$$

$$\Leftrightarrow \frac{E_s}{E*} \propto \frac{L^4}{t^4}$$ Because of the beam moment of inertia: $I = \frac{bh^3}{12} = \frac{t^4}{12} \propto t^4$

$$\Leftrightarrow \frac{E_s}{E*} \propto (\frac{L}{t})^4$$

$$\Leftrightarrow \frac{E_s}{E*} \propto (\frac{\rho*}{\rho_s})^2$$ Because $\begin{cases} \rho* = \frac{m}{V*} = \frac{m}{L^3} \\ \rho_s = \frac{m}{V_s} = \frac{m}{12t^2 L} \end{cases}$ such that $\frac{\rho*}{\rho_s} = \frac{\frac{m}{L^3}}{\frac{m}{12t^2 L}} = \frac{t^2}{12L^2} \propto \frac{t^2}{L^2}$

$$\Leftrightarrow \frac{E_s}{E*} = C_1 * (\frac{\rho_s}{\rho^*})^2$$ Where C_1 is a constant

Starting from this relationship, the relative density can also be linked to the relative

stress $\frac{\sigma^*}{\sigma_s}$ via:

$$\frac{\frac{\sigma^*}{\epsilon}}{\frac{\sigma_s}{\epsilon}} \propto (\frac{\rho*}{\rho_s})^2 \qquad \text{Because } \begin{cases} E^* = \frac{\sigma^*}{\epsilon} \\ E_s = \frac{\sigma_s}{\epsilon} \end{cases}$$

$$\Leftrightarrow \frac{\sigma^*}{\sigma_s} \propto (\frac{\rho*}{\rho_s})^2$$

$$\Leftrightarrow \frac{\sigma^*}{\sigma_s} = C_2 * (\frac{\rho*}{\rho_s})^2 \qquad \text{Where } C_2 \text{ is a constant}$$

This relationship can be used to compute any stress in the linear zone of the structure behaviour, for example to compute the YCS and YTS.

Consequently, the unit cell model presented on Figure E.1 leads to two useful relationships to study the mechanical properties of porous material:

$$\boxed{\begin{array}{c} \frac{E_s}{E^*} = C_1 * (\frac{\rho_s}{\rho^*})^2 \\ \\ \frac{\sigma^*}{\sigma_s} = C_2 * (\frac{\rho^*}{\rho_s})^2 \end{array}}$$

Where C_1 and C_2 are constants to determine experimentally. For porous bone, as it is expected that $E^* = E_s$ and $\sigma^* = \sigma_s$ when $\rho^* = \rho_s$, so $C_1, C_2 \approx 1$ [105]. This speculation is confirmed both by experiments and numerical simulations [105].

Using ρ^* and ρ_s definition, one may notice that:

$$\frac{\rho^*}{\rho_s} = \frac{\frac{m}{V^*}}{\frac{m}{V_s}} = \frac{V_s}{V^*} = V_f$$

Where V_f if the volume fraction, i.e the ratio of solid volume on empty volume. So, the V_f can be used to compute the porosity via:

$$p = 1 - V_f$$

Where p = material porosity.

E.2 Generalized Maxwell model for stress relaxation

Based on the model circuit (Figure E.2), the system stiffness over time, i.e. the stiffness relaxation, can be computed. Computations require the following parameters:

E_∞ = Spring constant of non Maxwell elment $[\frac{N}{m}]$
E_i = Spring constant of spring i $[\frac{N}{m}]$
η_i = Damping constant of damper i $[\frac{Ns}{m^2}]$
α_i = Strain of spring i [-]
ϵ = Total system strain [-]
σ = Applied stress $[\frac{N}{m^2}]$
n = Number of spring-dashpot Maxwell models in parallel [-]

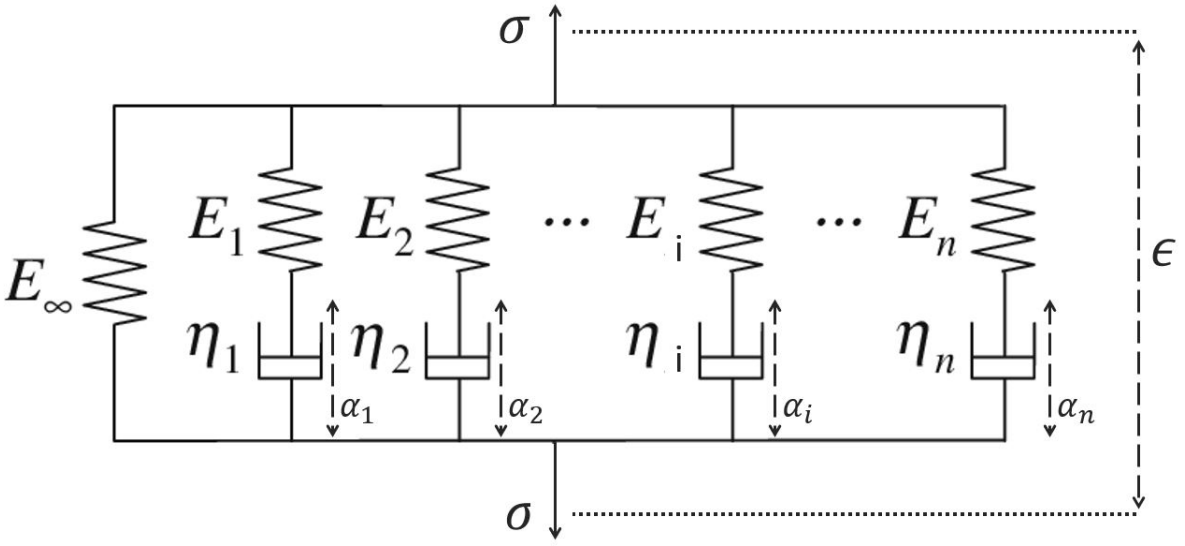

Figure E.2: Generalized Maxwell model for material Young modulus E with one spring and n spring-dashpot Maxwell models in parallel, with a strain α_i for dashpot i and a global system strain ϵ. Please note that lengths showed by dotted lines are proportional to their symbol since a strain is the relative elongation, meaning the ratio between the length variation and the initial length (adapted from [158]).

Based on all these parameters, the system stiffness relaxation can be computed. To do so, the first step is to observe that the force in a spring and a damper in series are equal. Since the force in damper i is given by $\sigma_{\eta_i} = \eta_i \dot{\alpha_i}$ and the one in the spring i by $\sigma_{E_i}(t) = E_i(\epsilon(t) - \alpha_i(t))$, one obtains:

$$\begin{aligned} \eta_i \dot{\alpha_i}(t) &= E_i(\epsilon(t) - \alpha_i(t)) \\ \Leftrightarrow \eta_i \dot{\alpha_i}(t) - E_i(\epsilon(t) - \alpha_i(t)) &= 0 \\ \Leftrightarrow \frac{E_i}{\eta_i}\epsilon(t) &= \dot{\alpha_i}(t) + \frac{E_i}{\eta_i}\alpha_i(t) \end{aligned} \tag{E.1}$$

This first order differential equation of α_i admits

$$(\alpha_i(t))_h = Ae^{\frac{-t}{\tau_i}} \text{ where } \tau_i = \frac{\eta_i}{E_i} \qquad \text{As homogeneous solution}$$

$$(\alpha_i(t))_c = B \qquad \text{As complementary solution}$$

By inserting $(\alpha_i(t))_c$ in Eq. E.1, $B = \epsilon(t)$. Consequently, since $\alpha_i(t) = (\alpha_i(t))_h + (\alpha_i(t))_c$:

$$\alpha_i = Ae^{\frac{-t}{\tau_i}} + \epsilon$$

Using the initial condition stipulating that $\alpha_i(t = 0) = 0$, one could obtain $A = \epsilon(t)$. Eventually, the damper elongation is defined via:

$$\alpha_i(t) = \epsilon(t)(1 - e^{\frac{-t}{\tau_i}})$$

Based on the damper elongation, the stress in each damper can be computed via the previously given equation $\sigma_{\eta_i}(t) = \eta_i \dot{\alpha_i}(t)$:

$$\begin{aligned} \sigma_{\eta_i}(t) &= \eta_i \frac{\epsilon(t) e^{\frac{-t}{\tau_i}}}{\tau_i} \\ \Leftrightarrow \sigma_{\eta_i}(t) &= E_i \epsilon(t) e^{\frac{-t}{\tau_i}} \qquad \text{Since } \frac{\eta_i}{\tau_i} = E_i \text{ by definition of } \tau_i \end{aligned}$$

With this force relationship and observing that the total system stress is equal to the sum of the stresses in all parallel elements and reminding that the force of one spring-damper Maxwell element is equal to the force of the damper (or the spring), one could obtain:

$$\begin{aligned} \sigma(t) &= E_\infty \epsilon(t) + \sum_{i=1}^{n} \sigma_i(t) \\ \Leftrightarrow \sigma(t) &= E_\infty \epsilon(t) + \sum_{i=1}^{n} E_i \epsilon(t) e^{\frac{-t}{\tau_i}} \\ \Leftrightarrow \frac{\sigma(t)}{\epsilon(t)} &= E_\infty + \sum_{i=1}^{n} E_i e^{\frac{-t}{\tau_i}} \\ \Leftrightarrow E(t) &= E_\infty + \sum_{i=1}^{n} E_i e^{\frac{-t}{\tau_i}} \qquad \text{Since } E(t) = \frac{\sigma(t)}{\epsilon(t)} \end{aligned}$$

One alternative form of this equation can be obtained by simply noting that $E(t = 0) = E_0 = E_\infty + \sum_{i=1}^{n} E_i$:

$$\begin{aligned} E(t) &= E_0 - \sum_{i=1}^{n} E_i + \sum_{i=1}^{n} E_i e^{\frac{-t}{\tau_i}} \\ \Leftrightarrow E(t) &= E_0 - \sum_{i=1}^{n} E_i (1 - e^{\frac{-t}{\tau_i}}) \\ \Leftrightarrow E(t) &= E_0 * [1 - \sum_{i=1}^{n} e_i (1 - e^{\frac{-t}{\tau_i}})] \qquad \text{Via defining: } E_i = e_i E_0 \end{aligned} \tag{E.2}$$

This final equation is called the Prony series form, and is often used in simulations since it only requires to know initial material stiffness instead of the stiffness after an infinite time, and the series coefficient e_i and time constant τ_i.

Similar deviations can be conducted for many others mechanical properties provided that they refer to elastic properties. For instance, it can be easily applied to the shear and bulk moduli, which are the only moduli in the relaxation functions asked as input for viscoelastic simulations [108]. Indeed, the shear modulus $G = \frac{\tau_{XY}}{\epsilon_{XY}}$ is the ratio between the stress in direction x applied on a surface of normal y and the deformation in this same direction on the same plane, i.e. a ratio between a stress and and its consequent deformation. So, the parallelism is straightforward. Also, the bulk modulus $K = -V \frac{dp}{dV}$ is similar since it represents the ratio between a pressure and its volume change, multiplied by the the total volume to keep the same units as a stress. Consequently, and defining $G_i = g_i * G_0$ and $K_i = k_i * K_0$ (as for the elastic modulus), one eventually obtains via adapting equation Eq. E.2:

$$G(t) = G_0[1 - \sum_{i=1}^{n} g_i(1 - e^{\frac{-t}{\tau_i^g}})]$$
$$K(t) = K_0[1 - \sum_{i=1}^{n} k_i(1 - e^{\frac{-t}{\tau_i^k}})]$$

Where

$G(t)$	= The shear relaxation function
$G_0 = \frac{E_0}{2*(1+\nu)}$	= The initial shear modulus defined using E_o and ν
g_i	= The ith shear relaxation modulus
τ_i^g	= The ith shear time constant
$K(t)$	= The bulk relaxation function
$K_0 = \frac{E_0}{3*(1-2\nu)}$	= The initial bulk modulus defined using E_o and ν
k_i	= The ith bulk relaxation modulus
τ_i^k	= The ith bulk time constant

E.3 Generalized Kelvin model

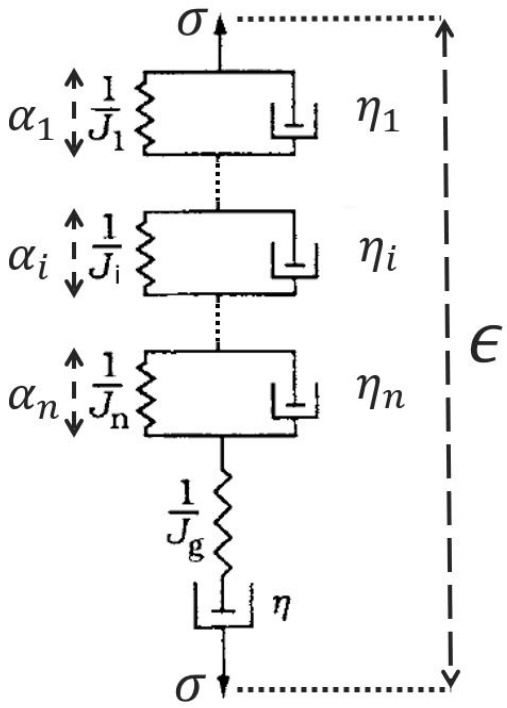

Figure E.3: Generalized Voigt model (adapted from [111]).

The generalized Kelvin model, or generalized Voigt model, is used to model the creep behaviour of viscoelastic material (Figure E.3). As the first step for stress relaxation was to compute the system elongation, for creep relaxation, the first step is computing the system strain under constant stress. To do so, one can observe that the system stress σ is equal to the stress in each element in series σ_i (Voigt elements, Maxwell spring and

damper). On top of that, the stress in one Voigt element is equal to the sum of the forces in the compliant and viscous elements. Consequently:

$$\begin{aligned} & \sigma = \sigma_i \\ \Leftrightarrow\ & \sigma = \sigma_{compliance} + \sigma_{viscous} \\ \Leftrightarrow\ & \sigma = \frac{\alpha_i}{J_i} + \eta \frac{d\alpha_i}{dt} \end{aligned} \tag{E.3}$$

Eq. E.3 is a differential equation that can be solved using the same procedure as for Eq. E.1. Knowing that $\alpha_i(t = o) = 0$, this gives:

$$\alpha_i = \sigma J_i (1 - e^{\frac{-t}{\tau_i}})$$

Where $\tau_i = J_i \eta_i$

Using this equation to define the strain of each Voigt element and observing that the total displacement ϵ is equal to the sum of the displacement of the Voigt elements ϵ_{Voigt_i} and the one of the Maxwell element $\epsilon_{Maxwell}$:

$$\begin{aligned} & \epsilon(t) = \epsilon_{Maxwell} + \sum_{i=1}^{n} \epsilon_{Voigt_i} \\ \Leftrightarrow\ & \epsilon(t) = \sigma J_g + \frac{\sigma t}{\eta_g} + \sum_{i=1}^{n} \sigma J_i (1 - e^{\frac{-t}{\tau_i}}) \\ \Leftrightarrow\ & \frac{\epsilon(t)}{\sigma} = J_g + \frac{t}{\eta_g} + \sum_{i=1}^{n} J_i (1 - e^{\frac{-t}{\tau_i}}) \\ \Leftrightarrow\ & J(t) = J_g + \frac{t}{\eta_g} + \sum_{i=1}^{n} J_i (1 - e^{\frac{-t}{\tau_i}}) \qquad \text{By definition of J(t): } J(t) = \frac{\epsilon(t)}{\sigma} \end{aligned}$$

Where $J_g = \frac{1}{E_g}$ with E_g the initial elastic modulus.

Appendix F

Data

F.1 Study 1: unit cell model

Table F.1: UCM fit for the one lateral hole design with viscoelastic properties corresponding to the longitudinal or transverse properties and anisotropic properties with axial or longitudinal (long.) fibers. Deformation Δz is defined as the mean of the facets deformation where the force is applied [mm]. The structural stiffness k_s is computed by dividing the displacement by the applied force (3.1kN) $[\frac{kN}{mm}]$. The relative stiffness $\frac{k_s}{k^*} = ...$ is defined via $k^* = k_s$ when p = 0.

Volume fraction (porosity)	**Viscoelastic transverse**	**Viscoelastic longitudinal**	**Anisotropic axial fibers**	**Anisotropic long. fibers**
$\frac{\rho^*}{\rho_s} = 0.49$ $(p = 0.51)$	$\Delta z = 0.1152$ $k^* = 26.9097$ $\frac{k^*}{k_s} = 0.0896$	$\Delta z = 0.0617$ $k^* = 50.292$ $\frac{k^*}{k_s} = 0.105$	$\Delta z = 0.1049$ $k^* = 29.552$ $\frac{k^*}{k_s} = 0.1135$	$\Delta z = 0.0664$ $k^* = 46.686$ $\frac{k^*}{k_s} = 0.0833$
$\frac{\rho^*}{\rho_s} = 0.6$ $(p = 0.4)$	$\Delta z = 0.05723$ $k^* = 54.385$ $\frac{k^*}{k_s} = 0.1812$	$\Delta z = 0.03333$ $k^* = 93.0093$ $\frac{k_s}{k^*} = 0.1951$	$\Delta z = 0.06122$ $k^* = 50.287$ $\frac{k^*}{k_s} = 0.1945$	$\Delta z = 0.03214$ $k^* = 96.875$ $\frac{k^*}{k_s} = 0.1729$
$\frac{\rho^*}{\rho_s} = 0.8$ $(p = 0.2)$	$\Delta z = 0.02152$ $k^* = 146.780$ $\frac{k^*}{k_s} = 0.4891$	$\Delta z = 0.01281$ $k^* = 241.995$ $\frac{k^*}{k_s} = 0.5078$	$\Delta z = 0.02403$ $k^* = 129.005$ $\frac{k^*}{k_s} = 0.4956$	$\Delta z = 0.01188$ $k^* = 560.940$ $\frac{k^*}{k_s} = 0.4657$
$\frac{\rho^*}{\rho_s} = 1$ $(p = 0)$	$\Delta z = 0.01033$ $k_s = 300.097$ $\frac{k^*}{k_s} = 1$	$\Delta z = 0.006506$ $k_s = 476.483$ $\frac{k^*}{k_s} = 1$	$\Delta z = 0.01191$ $k_s = 260.285$ $\frac{k^*}{k_s} = 1$	$\Delta z = 0.005533$ $k_s = 560.274$ $\frac{k^*}{k_s} = 1$

Table F.2: UCM fit for the few lateral pores (FLP), one and few axial pore(s) (OAP and FAP respectively) and one and few frontal pore(s) (OFP and FFP respectively) designs with longitudinal (long.) fibers. Deformation Δz is defined as the mean of the facets deformation where the force is applied [mm]. The structural stiffness k_s is computed by dividing the displacement by the applied force (3.1kN) [$\frac{kN}{mm}$]. The relative stiffness $\frac{k_s}{k^*} = ...$ is defined via $k^* = k_s$ when p = 0.

Volume fraction (porosity)	**FLH: Anisotropic long. fibers**	**OAH: Anisotropic long. fibers**	**FAH: Anisotropic long. fibers**	**OFH: Anisotropic long. fibers**	**FFH: Anisotropic long. fibers**
$\frac{\rho^*}{\rho_s} = 0.49$ $(p = 0.51)$	$\Delta z = 0.0472$ $k^* = 65.6501$ $\frac{k^*}{k_s} = 0.2522$	$\Delta z = 0.0236$ $k^* = 131.523$ $\frac{k^*}{k_s} = 0.5053$	$\Delta z = 0.0245$ $k^* = 126.273$ $\frac{k^*}{k_s} = 0.4851$	$\Delta z = 0.6254$ $k^* = 4.9568$ $\frac{k^*}{k_s} = 0.19043$	$\Delta z = 0.0426$ $k^* = 72.7187$ $\frac{k^*}{k_s} = 0.2738$
$\frac{\rho^*}{\rho_s} = 0.6$ $(p = 0.4)$	$\Delta z = 0.0326$ $k^* = 95.238$ $\frac{k^*}{k_s} = 0.365$	$\Delta z = 0.0207$ $k^* = 150.048$ $\frac{k^*}{k_s} = 0.5765$	$\Delta z = 0.0197$ $k^* = 157.441$ $\frac{k^*}{k_s} = 0.6048$	$\Delta z = 0.1699$ $k^* = 18.246$ $\frac{k^*}{k_s} = 0.0701$	$\Delta z = 0.0308$ $k^* = 10.6166$ $\frac{k^*}{k_s} = 0.3865$
$\frac{\rho^*}{\rho_s} = 0.8$ $(p = 0.2)$	$\Delta z = 0.0199$ $k^* = 155.93$ $\frac{k^*}{k_s} = 0.0559$	$\Delta z = 0.0152$ $k^* = 198.463$ $\frac{k^*}{k_s} = 0.76257$	$\Delta z = 0.0156$ $k^* = 0.76257$ $\frac{k^*}{k_s} = 0.76493$	$\Delta z = 0.0388$ $k^* = 80.82$ $\frac{k^*}{k_s} = 0.3088$	$\Delta z = 0.0193$ $k^* = 160.539$ $\frac{k^*}{k_s} = 0.6167$
$\frac{\rho^*}{\rho_s} = 1$ $(p = 0)$			$\Delta z = 0.01191$ $k^* = 260.285$ $\frac{k_s}{k^*} = 1$		

Table F.3: Analysis of the full design under a compressive axial load (superoinferior) of 3100N. Deformation Δz is defined as the mean of the facets deformation where the force is applied. The stiffness is computed by dividing the displacement by the applied force (3.1kN). The $FoS_{stiffness}$ is defined by the cage stiffness k and the vertebral body stiffness k_{VD} via $FoS_{stiffness} = \frac{k}{k_{VB}}$, where $k_{VB} = 7.8\frac{kN}{mm}$ [74]. The stress is defined as the Von Mises stress for isotropic properties, but as the maximal stress is each direction for anisotropic material (x=longitudinal direction, y = frontal direction, z = axial direction). σ_{max} is the absolute maximal stress, reported with its sign. The $FoS_{stress} = \frac{\text{YTS}}{|\sigma_{max}|}$ with a YTS of 52.5MPa and 92.78MPa for the transverse and longitudinal configuration respectively. The unit stress factor (USF) is defined for a 1N compressive force. The yield force is computed via: $_{yield} = \frac{YTS}{|USF|}$ [124].

Design	**Properties**	**Force**	$\boldsymbol{\Delta z[mm]}$ $\boldsymbol{k[\frac{N}{mm}]}$ $\boldsymbol{FoS_{stiffness}}$	$\boldsymbol{\sigma_{max}[MPa]}$ $\boldsymbol{FoS_{stress}}$	$\boldsymbol{USF[MPa]}$ $\boldsymbol{F_{yield}[N]}$
Full	Viscoelastic, transverse	Top	$\Delta z = 0.0225$ $k = 137.65$ $FoS_{stiffness} = 17.65$	$\sigma_{max} = 235.3$ $FoS_{stress} = 22.31\%$	0.07697 $F_{yield} = 682.084$
		All	$\Delta z = 0.0103$ $k = 300.09$ $FoS_{stiffness} = 38.474$	$\sigma_{max} = 39.5$ $FoS_{stress} = 132.91\%$	0.01223 $F_{yield} = 4292.72$
	Viscoelastic, longitudinal	Top	$\Delta z = 0.0106$ $k = 292.18$ $FoS_{stiffness} = 37.459$	$\sigma_{max} = 221.6$ $FoS_{stress} = 41.86\%$	0.07103 $F_{yield} = 1306.2$
		All	$\Delta z = 0.00635$ $k = 488.19$ $FoS_{stiffness} = 62.59$	$\sigma_{max} = 39.92$ $FoS_{stress} = 232.41\%$	0.01415 $F_{yield} = 6556.89$
	Anisotropic, axial fibers	All	$\Delta z = 0.005373$ $k = 576.96$ $FoS_{stiffness} = 73.97$	σ_{max} FoS_{stress} x -36.62 143.36% y -36.11 145.39% z -53.16 174.53%	USF F_{yield} x -0.01181 4445.38 y -0.01165 4506.044 z -0.01715 4826.82
	Anisotropic, longitudinal fibers	All	$\Delta z = 0.01198$ $k = 258.76$ $FoS_{stiffness} = 33.175$	σ_{max} FoS_{stress} x -21.81 425.4% y -24.71 212.46% z -39.62 132.5%	USF F_{yield} x -0.007035 13188.34 y -0.00797 6587.202 z -0.01278 4107.98

Table F.4: Analysis of the one lateral pore (OLP) design with a high porosity (↑p, p=0.5) and low porosity (↓p, p=0.213) under a compressive axial (superoinferior) load of 3.1kN. Axial deformation (Δz) the average axial displacement of the superior surface. The stiffness (k) is computed by dividing the axial displacement by 3.1kN. The $FoS_{stiffness}$ is defined via $FoS_{stiffness} = \frac{\text{cage stiffness}}{\text{vertebral body stiffness}}$, where vertebral body stiffness $= 7.8\frac{kN}{mm}$ [74]. The stresses (σ_{max} and unit stress factor (USF) are defined using the Von Mises stress or maximal stress per direction stress for isotropic and anisotropic properties respectively. $FoS_{stress} = \frac{\text{YCS}}{\text{Maximal Von Mises stress}}$ with a YCS of 52.5MPa and 92.78MPa for the transverse and longitudinal configuration respectively. The yield force is computed via: $_{yield} = \frac{YCS}{Unitstressfactor}$ [124].

Design	**Properties**	**Force**	$\boldsymbol{\Delta z[mm]}$ $\boldsymbol{k[\frac{N}{mm}]}$ $\boldsymbol{FoS_{stiffness}}$	$\boldsymbol{\sigma_{max}[MPa]}$ $\boldsymbol{FoS_{stress}}$	$\boldsymbol{USF[MPa]}$ $\boldsymbol{F_{yield}[N]}$
OLH, ↑p	Viscoelastic, transverse	Top	$\Delta z = 0.223$ $k = 13.9013$ $FoS_{stiffness} = 1.784$	$\sigma_{max} = 1670$ $FoS_{stress} = 3.14\%$	$USF = 0.4812$ $F_{yield} = 109.1022$
		All	$\Delta z = 0.122$ $k = 25.4098$ $FoS_{stiffness} = 3.258$	$\sigma_{max} = 493.8$ $FoS_{stress} =$ 10.63%	$USF = 0.1515$ $F_{yield} = 346.53$
	Viscoelastic, longitudinal	Top	$\Delta z = 0.112$ $k = 27.6786$ $FoS_{stiffness} = 3.548$	$\sigma_{max} = 1308$ $FoS_{stress} = 7.55\%$	$USF = 0.3784$ $F_{yield} = 260.88$
		All	$\Delta z = 0.0671$ $k = 14.365$ $FoS_{stiffness} = 1.842$	$\sigma_{max} = 483.8$ $FoS_{stress} =$ 20.41%	$USF = 0.151$ $F_{yield} = 653.77$
	Anisotropic, axial fibers	All	$\Delta z = 0.07252$ $k = 42.75$ $FoS_{stiffness} = 5.48$	σ_{max} FoS_{stress} x -194.2 27.03% y -394.7 13.301% z -625.9 14.82%	USF F_{yield} x -0.05821 901.907 y -0.1168 449.49 z -0.1965 267.16
	Anisotropic, longitudinal fibers	All	$\Delta z = 0.1297$ $k = 23.901$ $FoS_{stiffness} = 3.064$	σ_{max} FoS_{stress} x 153.8 60.32% y -427.6 12.28% z -442.4 11.87%	USF F_{yield} x 0.04426 1928.898 y -0.1214 779.74 z -0.1313 15558.78
OLH, ↓p	Viscoelastic, transverse	Top	$\Delta z = 0.0424$ $k = 78.113$ $FoS_{stiffness} = 9.373$	$\sigma_{max} = 494.1$ $FoS_{stress} =$ 10.62%	$USF = 0.155$ $F_{max} = 338.71$
		All	$\Delta z = 0.0228$ $k = 135.97$ $FoS_{stiffness} = 17.43$	$\sigma_{max} = 130.8$ $FoS_{stress} =$ 40.14%	$USF = 0.0421$ $F_{max} = 1247.031$
	Viscoelastic, longitudinal	Top	$\Delta z = 0.0024$ $k = 1294.36$ $FoS_{stiffness} =$ 165.944	$\sigma_{max} = 375.6$ $FoS_{stress} =$ 24.70%	$USF = 0.119$ $F_{max} = 779.66$
		All	$\Delta z = 0.0132$ $k = 234.67$ $FoS_{stiffness} =$ 30.085	$\sigma_{max} = 136.4$ $FoS_{stress} =$ 68.021%	$USF = 0.04388$ $F_{max} = 2114.4$
	Anisotropic, axial fibers	All	$\Delta z = 0.01231$ $k = 251.83$ $FoS_{stiffness} = 32.28$	σ_{max} FoS_{stress} x -61.97 84.71% y -66.25 79.24% z -168 55.23%	USF F_{yield} x -0.01995 2631.57 y -0.02135 2459.016 z -0.05368 978.018
	Anisotropic, longitudinal fibers	All	$\Delta z = 0.02488$ $k = 124.60$ $FoS_{stiffness} = 15.97$	σ_{max} FoS_{stress} x -34.7 267.38% y -56.52 92.89% z -124.2 42.27%	USF F_{yield} x -0.01121 8276.54 y -0.01794 2926.42 z -0.0399 1315.79

Table F.5: Analysis of the few lateral holes (FLH) design with a high porosity (↑p, p=0.5) and low porosity (↓p, p=0.213) under a compressive axial (superoinferior) load of 3100N. Axial deformation (Δz) the average axial displacement of the facets edges where the force is applied. The stiffness (k) is computed by dividing the displacement by the applied force (3.1kN). The $FoS_{stiffness}$ is defined via $FoS_{stiffness} = \frac{\text{cage stiffness}}{\text{vertebral body stiffness}}$, where $vertebralbodystiffness = 7.8\frac{kN}{mm}$ [74]. The stresses (σ_{max} and unit stress factor (USF)) are defined as the Von Mises stress or maximal stress per direction stress for isotropic and anisotropic properties respectively (x, y and z are the longitudinal frontal and axial direction respectively). $FoS_{stress} = \frac{\text{YCS}}{\text{Maximal Von Mises stress}}$ with a YCS of 52.5MPa and 92.78MPa for the transverse and longitudinal configuration respectively. The yield force is computed via: $_{yield} = \frac{YCS}{Unitstressfactor}$ [124].

Design	**Properties**	**Force**	$\boldsymbol{\Delta z[mm]}$ $\boldsymbol{k[\frac{N}{mm}]}$ $\boldsymbol{FoS_{stiffness}}$	$\boldsymbol{\sigma_{max}[MPa]}$ $\boldsymbol{FoS_{stress}}$		$\boldsymbol{USF[MPa]}$ $\boldsymbol{F_{yield}[N]}$	
FLH, ↑p	Anisotropic, axial fibers	All	$\Delta z = 0.02207$ $k = 140.462$ $FoS_{stiffness} = 18.008$	σ_{max}	FoS_{stress}	USF	F_{yield}
				x -89.31	58.78%	x -0.0288	1822.92
				y -78.49	66.88%	y -0.02532	2073.46
				z -291.08	33.91%	z -0.09364	990.82
	Anisotropic, longitudinal fibers	All	$\Delta z = 0.04673$ $k = 66.3385$ $FoS_{stiffness} = 8.5049$	σ_{max}	FoS_{stress}	USF	F_{yield}
				x -78.74	117.83%	x -0.0254	3652.76
				y -59.25	86.61%	y -0.01911	2747.25
				z -241.7	21.72%	z -0.07798	673.25
FLH, ↓p	Anisotropic, axial fibers	All	$\Delta z = 0.009641$ $k = 321.54$ $FoS_{stiffness} = 41.22$	σ_{max}	FoS_{stress}	USF	F_{yield}
				x -74.53	70.44%	x -0.02406	2182.044
				y -72.26	72.65%	y -0.02332	2251.28
				z -140.5	66.035%	z -0.04534	1157.92
	Anisotropic, longitudinal fibers	All	$\Delta z = 0.02062$ $k = 150.34$ $FoS_{stiffness} = 19.27$	σ_{max}	FoS_{stress}	USF	F_{yield}
				x -37.8	245.45%	x -0.01219	7611.15
				y -40.42	129.88%	y -0.01304	4026.074
				z -119.6	43.89%	z -0.03857	1361.16

Table F.6: Analysis of the one axial hole (OAH) and few axial holes (FAH) designs with a high porosity (↑p, p=0.5) and low porosity (↓p, p=0.213) under a compressive axial (superoinferior) load of 3100N. Axial deformation (Δz) the average axial displacement of the facets edges where the force is applied. The stiffness (k) is computed by dividing the displacement by the applied force (3.1kN). The $FoS_{stiffness}$ is defined via $FoS_{stiffness} = \frac{\text{cage stiffness}}{\text{vertebral body stiffness}}$, where $vertebralbodystiffness = 7.8\frac{kN}{mm}$ [74]. The stresses (σ_{max} and unit stress factor (USF)) are defined as the Von Mises stress or maximal stress per direction stress for isotropic and anisotropic properties respectively (x, y and z are the longitudinal frontal and axial direction respectively). $FoS_{stress} = \frac{\text{YCS}}{\text{Maximal Von Mises stress}}$ with a YCS of 52.8MPa and 92.78MPa for the transverse and longitudinal configuration respectively. The yield force is computed via: $_{yield} = \frac{YCS}{Unitstressfactor}$ [124]. Note: mesh had been refined for the FAH designs, otherwise SolidWorks was not able to solve the FEM.

Design	**Properties**	**Force**	$\boldsymbol{\Delta z[mm]}$ $\boldsymbol{k[\frac{N}{mm}]}$ $\boldsymbol{FoS_{stiffness}}$	$\boldsymbol{\sigma_{max}[MPa]}$ $\boldsymbol{FoS_{stress}}$	$\boldsymbol{USF[MPa]}$ $\boldsymbol{F_{yield}[N]}$
OAH, ↑p	Anisotropic, axial fibers	All	$\Delta z = 0.01142$ $k = 271.45$ $FoS_{stiffness} = 34.8$	σ_{max} FoS_{stress} x -75.5 69.54% y -69.55 75.48% z -105.2 93.84%	USF F_{yield} x -0.02435 2156.057 y -0.02244 2339.57 z -0.03393 1547.303
	Anisotropic, longitudinal fibers	All	$\Delta z = 0.02455$ $k = 126.27$ $FoS_{stiffness} = 16.1$	σ_{max} FoS_{stress} x -38.87 238.69% y -35.32 148.51% z -70.40 74.57%	USF F_{yield} x -0.01254 7398.72 y -0.0139 3776.97 z -0.02271 2311.76
OAH, ↓p	Anisotropic, axial fibers	All	$\Delta z = 0.00704$ $k = 440.34$ $FoS_{stiffness} = 56.454$	σ_{max} FoS_{stress} x -51.63 101.68% y -51.72 101.508% z -82.78 112.08%	USF F_{yield} x -0.0167 3143.71 y -0.0167 3143.70 z -0.0268 3461.947
	Anisotropic, longitudinal fibers	All	$\Delta z = 0.0154$ $k = 201.298$ $FoS_{stiffness} = 25.807$	σ_{max} FoS_{stress} x -27.06 342.86% y -28.09 186.90% z -56.32 93.21%	USF F_{yield} x -0.008734 10622.85 y -0.009063 5792.783 z -0.01816 2890.97
FAH, ↑p	Anisotropic, axial fibers	All	$\Delta z = 0.01053$ $k = 294.397$ $FoS_{stiffness} = 37.74$	σ_{max} FoS_{stress} x -88.54 59.29% y -83.11 63.17% z -119.8 77.45%	USF F_{yield} x -0.02856 1838.24 y -0.02681 1958.22 z -0.03865 2400.52
	Anisotropic, longitudinal fibers	All	$\Delta z = 0.02254$ $k = 137.53$ $FoS_{stiffness} = 17.63$	σ_{max} FoS_{stress} x 46.82 198.16% y 72.49 72.42% z -70.08 74.91%	USF F_{yield} x 0.0151 6144.37 y 0.02338 3968.35 z -0.02261 4103.49
FAH, ↓p	Anisotropic, axial fibers	All	$\Delta z = 0.00718$ $k = 431.75$ $FoS_{stiffness} = 55.35$	σ_{max} FoS_{stress} x -71.87 73.04% y -82.49 63.64% z -102.9 90.16%	USF F_{yield} x -0.02318 2264.88 y -0.0266 1973.68 z -0.03317 2797.106
	Anisotropic, longitudinal fibers	All	$\Delta z = 0.01524$ $k = 203.41$ $FoS_{stiffness} = 26.078$	σ_{max} FoS_{stress} x -24.29 381.97% y -27.66 189.804% z -50.88 103.18%	USF F_{yield} x -0.007817 11869 y -0.008878 5979.5 z -0.01642 3197.32

Table F.7: Analysis of the one frontal hole (OFH) and few frontal holes (FFH) designs with a high porosity (↑p, p=0.5) and low porosity (↓p, p=0.213) under a compressive axial (superoinferior) load of 3100N. Axial deformation (Δz) the average axial displacement of the facets edges where the force is applied. The stiffness (k) is computed by dividing the displacement by the applied force (3.1kN). The $FoS_{stiffness}$ is defined via $FoS_{stiffness} = \frac{\text{cage stiffness}}{\text{vertebral body stiffness}}$, where $vertebralbodystiffness = 7.8\frac{kN}{mm}$ [74]. The stresses (σ_{max} and unit stress factor (USF)) are defined as the Von Mises stress or maximal stress per direction stress for isotropic and anisotropic properties respectively (x, y and z are the longitudinal frontal and axial direction respectively). $FoS_{stress} = \frac{\text{YCS}}{\text{Maximal Von Mises stress}}$ with a YCS of 52.5MPa and 92.78MPa for the transverse and longitudinal configuration respectively. The yield force is computed via: $_{yield} = \frac{YCS}{Unitstressfactor}$ [124].

Design	**Properties**	**Force**	$\boldsymbol{\Delta z[mm]}$ $\boldsymbol{k[\frac{N}{mm}]}$ $\boldsymbol{FoS_{stiffness}}$	$\boldsymbol{\sigma_{max}[MPa]}$ $\boldsymbol{FoS_{stress}}$	$\boldsymbol{USF[MPa]}$ $\boldsymbol{F_{yield}[N]}$
OFH, ↑p	Anisotropic, axial fibers	All	$\Delta z = 0.6565$ $k = 4.722$ $FoS_{stiffness} = 0.6053$	σ_{max} FoS_{stress} x **-2002** 2.62% y **-1151** 4.56% z **-952.7** 9.74%	USF F_{yield} x -0.4583 114.55 y -0.2154 243.73 z -0.2015 460.45
	Anisotropic, longitudinal fibers	All	$\Delta z = 0.6231$ $k = .975$ $FoS_{stiffness} = 0.637$	σ_{max} FoS_{stress} x **-2697** 3.44% y **-653** 8.039% z **-671** 7.82%	USF F_{yield} x -0.4529 205.86 y -0.08284 633.75 z -0.1009 520.32
OFH, ↓p	Anisotropic, axial fibers	All	$\Delta z = 0.02755$ $k = 112.523$ $FoS_{stiffness} = 14.42$	σ_{max} FoS_{stress} x -189.2 27.75% y -70.86 74.09% z -201.9 45.95%	USF F_{yield} x -0.05948 882.65 y -0.0223 2354.26 z -0.0645 1438.45
	Anisotropic, longitudinal fibers	All	$\Delta z = 0.03753$ $k = 82.60$ $FoS_{stiffness} = 10.59$	σ_{max} FoS_{stress} x -225.2 41.20% y -44.37 113.32% z -129.3 40.60%	USF F_{yield} x -0.07081 1310.27 y -0.01409 3726.047 z 0.04112 1276.75
FFH, ↑p	Anisotropic, axial fibers	All	$\Delta z = 0.0206$ $k = 150.48$ $FoS_{stiffness} = 19.2$	σ_{max} FoS_{stress} x -68.41 76.75% y -110.7 47.43% z -299.8 30.95% Not: x,y,z inside holes	USF F_{yield} x -0.02191 2396.17 y -0.03558 1475.55 z -0.09636 962.84
	Anisotropic, longitudinal fibers	All	$\Delta z = 0.03973$ $k = 78.026$ $FoS_{stiffness} = 10.003$	σ_{max} FoS_{stress} x -43.17 214.92% y -78.46 66.91% z -208.0 25.24%	USF F_{yield} x -0.01393 6660.44 y -0.02531 2074.29 z -0.06711 782.298
FFH, ↓p	Anisotropic, axial fibers	All	$\Delta z = 0.009463$ [149] $k = 327.59$ $FoS_{stiffness} = 41.999$	σ_{max} FoS_{stress} x -46.16 113.7% y -48.67 107.87% z -143.4 64.70%	USF F_{yield} x -0.01488 3528.23 y -0.0158 3322.78 z -0.04647 1956.56
	Anisotropic, longitudinal fibers	All	$\Delta z = 0.01908$, $k = 162.47$ $FoS_{stiffness} = 20.83$	σ_{max} FoS_{stress} x -31.87 295.76% y -34.26 153.24% z -106.5 49.30%	USF F_{yield} x -0.01028 9025.29 y -0.01105 4751.13 z -0.03435 1528.38

Bibliography

[1] Wikipedia. *Spinal disc herniation*. 2019. URL: https://en.wikipedia.org/wiki/Spinal_disc_herniation (visited on Dec. 9, 2019).

[2] U.S; National library of medicine (NIH). *Intervertebral disc disease*. 2019. URL: https://ghr.nlm.nih.gov/condition/intervertebral-disc-disease#statistics (visited on Dec. 12, 2019).

[3] Asia Medical Specialists Limited. *'Slipped Disc' FAQs*. 2017. URL: https://www.asiamedicalspecialists.hk/en/health-info/3/%27Slipped-Disc%27-FAQs (visited on Apr. 13, 2020).

[4] Becker C. "Spine-tingling prospects: artificial disc implants are among the new technologies expected to revolutionize the outcomes of back surgery". In: *Mod Healthc* 33 (Jan. 2013), pp. 30–32.

[5] Well Cornell brain and spine center: Department of Neurological Surgery. *TLIF Minimally Invasive Spine Fusion*. 2020. URL: https://weillcornellbrainandspine.org/procedure/tlif-minimally-invasive-spine-fusion (visited on Apr. 13, 2020).

[6] Sarah Magdy. "Spine biomechanics". In: *Rapoff, MER/BIO soft tissues mechanics* (2018).

[7] Joseph P. Iannotti and Richard D. Parker. *The Netter Collection of medical illustrations: Musculoskeletal System Part II—Spine and Lower Limb*. 1600 John F. Kennedy Blvd., Ste. 1800, Philadelphia, PA 19103-2899: Saunders Elsevier, 2nd edition.

[8] SPINE-health. *Lumbar Osteophytes (Bone Spurs) Video*. 2020. URL: https://www.spine-health.com/video/lumbar-osteophytes-bone-spurs-video (visited on Apr. 13, 2020).

[9] Mayfield Brain Spine. *Facet Joint Syndrome / Arthritis*. 2018. URL: https://www.mayfieldclinic.com/pe-facet.htm (visited on Apr. 13, 2020).

[10] OrthoInfo. *Kyphosis (Roundback) of the Spine*. 2016. URL: https://orthoinfo.aaos.org/en/diseases--conditions/kyphosis-roundback-of-the-spine (visited on Dec. 24, 2019).

[11] Spondylitis Association of America. *Overview of Ankylosing Spondylitis*. 2020. URL: https://spondylitis.org/about-spondylitis/types-of-spondylitis/ankylosing-spondylitis/ (visited on Apr. 13, 2020).

[12] Wikipedia. *Radiculopathy*. 2020. URL: https://en.wikipedia.org/wiki/Radiculopathy (visited on May 21, 2020).

[13] Pine-Health: knowledge from Veritas. *Arthrodesis Definition*. 2019. URL: https://www.spine-health.com/glossary/arthrodesis (visited on Dec. 14, 2019).

[14] Marios G Lykissas and Alexander Aichmair. "Current concepts on spinal arthrodesis in degenerative disorders of the lumbar spine". In: *World J Clin Cases* 01.01 (Apr. 2013), pp. 4–12.

[15] Ralph J. Mobbs, Kevin Phan, Greg Malham, Kevin Seex, and Prashanth J. Rao. "Lumbar interbody fusion: techniques, indications and comparison of interbody fusion options including PLIF, TLIF, MI-TLIF, OLIF/ATP, LLIF and ALIF". In: *Journal of Spine Surgery* 1.1 (Dec. 2015).

[16] Nucleus Medical Art Inc. *Spinal Fusion Surgery C5 6 Anterior Cervical Discectomy (Diskectomy)*. 2001. URL: https://www.alamy.com/spinal-fusion-surgery-c5-6-anterior-cervical-discectomy-diskectomy-image7712702.html (visited on Dec. 31, 2019).

[17] AO Fondation. *Supine position*. 2019. URL: https://www2.aofoundation.org/wps/portal/!ut/p/a0/04_Sj9CPykssy0xPLMnMz0vMAfGjzOKN_A0M3D2DDbz9_UMMDRyDXQ3dw9wMDAzMjfULsh0VAbWjLW0!/?bone=Spine&classification=52-B2&implantstype=&method=Anterior\%20plating&preparation=Supine\%20position&redfix_url=1447245301165&segment=TraumaLowerCervical&showPage=preparation&treatment=&contentUrl=/srg/52/03-Preparation/Pr100_Supine.jsp (visited on Jan. 20, 2020).

[18] Synthes Spine. *Anterior access to the lumbar spine, mini-open, retro-perinal approach*. 1302 Wright Lane East, West Chester, PA 19380, 2006.

[19] Southern Medical. *Caspar Cervical Distractor*. 2020. URL: http://www.southmed.co.za/caspar-cervical-distractor-92 (visited on Jan. 20, 2020).

[20] AO Fondation. *Anterior approach to the cervical spine*. 2019. URL: https://www2.aofoundation.org/wps/portal/!ut/p/a1/04_Sj9CPykssy0xPLMnMz0vMAfGjzOKN_A0M3D2DDbz9_UMMDRyDXQ3dw9wMDAzMjYEKIvEocDQnTr8BDuBoQEh_QW5oKAD4ENaS/dl5/d5/L2dJQSEvUUt3QS80SmlFL1o2XzJPMDBHSVMwS09PVDEwQVNFMUdWRjAwMDcz/?approach=Anterior\%20to\%20cervical\%20spine&bone=Spine&segment=TraumaLowerCervical&showPage=approach&contentUrl=/srg/52/04-Approaches/A001_AntToCervSpine.jsp (visited on Jan. 20, 2020).

[21] Robert Bohinski. *Anterior cervical descectomy and fusion*. 2018. URL: https://mayfieldclinic.com/pe-acdf.htm (visited on Dec. 31, 2019).

[22] Lawrence S. Chin. *Cervical Arthrodesis Technique*. 2018. URL: https://emedicine.medscape.com/article/1999857-technique#c2 (visited on Dec. 31, 2019).

[23] Mark J. Spoonamore. *Posterior Lumbar Interbody Fusion (PLIF) Transforaminal Lumbar Interbody Fusion (TLIF)*. 2019. URL: https://www.uscspine.com/treatement-options/back-treatment/lumbar-interbody-fusion/ (visited on Jan. 5, 2020).

[24] a JhonsonJhonson company: DePuy synthes. *Contact fusion cage: surgical technique*. Eimastrasse 3 4436 Oberdorf Switzerland: Synthes GmbH, 2017.

[25] Stryker spine. *AVS Navigator: TLIF Surgical Technique*. 2 Pearl Court, Allendale, NJ 07401-1677 USA: Stryker SA, 2016.

[26] E. Emel, A. Abdallad, and A. Fahir Ozer. *Principles of spine surgery, chapter 31: posterior approach to the lumbar spine and lumbosacral junction: surgical anatomy*. Intertip Yayinevi, US akademi, 2019.

[27] Charles Branch, Kevin Foley, and Anthony Salerni. *CAPSTONE PEEK Spinal system: PLIF and TLIF surgical technique*. 1800 Pyramid Place, Memphis, TN 38132: Medtronics sofamor danek, 2008.

[28] Richard Wolf: spirit of excellence. *Transforaminal ("Inside Out") Approach*. 2019. URL: https://www.richardwolfusa.com/discipline/spine-surgery/applications-methods/lumbar-decompression/transforaminal-approach.html (visited on Dec. 31, 2019).

[29] Scoliosis and spine associates. *PLIF, ALIF and TLIF Procedures*. 2019. URL: https://www.scoliosisassociates.com/conditions/spondylolisthesis/plif-alif-and-tlif-procedures/ (visited on Jan. 5, 2020).

[30] Ji Woong Park, Hee-Seung Nam, and Yongbum Park. "Usefulness of Posterolateral Transforaminal Approach in Lumbar Radicular Pain". In: *Annals of Rehabilitation Medicine* 35 (2011), pp. 395–404.

[31] Sukrit Jain, Adam E M Eltorai, Roy Ruttiman, and Alan H Daniels. "Advances in Spinal Interbody Cages". In: *Othopaedic Surgery* 8 (Aug. 2016), pp. 278–284.

[32] Alan L. Williams, Matthew F. Gornet, and J. Kenneth Burkus. "Advances in Spinal Interbody Cages". In: *AJNR Am J Neuroradiol* 26 (Sept. 2005), pp. 2057–2066.

[33] Conor P. Delaney. *Netter's surgical anatomy and approaches*. 1600 John F. Kennedy Blvd., Ste. 1800, Philadelphia, PA 19103-2899: Saunders Elsevier, 2014.

[34] D. A. Stroh, B. W. Moatz, and P. J. Tortolani. *Anterior Lumbar Approach*. 2019. URL: https://musculoskeletalkey.com/anterior-lumbar-approach/ (visited on Jan. 3, 2020).

[35] Bijjawara H. Mahesh, Bidre N. Upendra, Rao Raghavendra, Sekharappa Vijay, Kumar Arun, and Reddy Srinivasa. "Transforaminal Approach to Cervical Spine with Use of Cervical Pedicle Screws: Technical Description of a Novel Approach". In: *Indian Spine Journal* 1.1 (2001), pp. 51–60.

[36] Youtube. *Left anterior retroperitoneal approach to the L4-L5 disc*. 2019. URL: https://www.youtube.com/watch?v=EvLky2LMl0U (visited on Jan. 4, 2020).

[37] Jhonson Jhonson. *SYNFIX EVOLUTION System*. 2020. URL: https://www.jnjmedicaldevices.com/en-US/product/synfixr-evolution-system (visited on Feb. 20, 2020).

[38] K. Phan and Ralph J. Mobbs. "Evolution of Design of Interbody Cages for Anterior Lumbar Interbody Fusion". In: *CHINESE ORTHOPAEDIC ASSOCIATION AND JOHN WILEY SONS AUSTRALIA, LTD* 08 (2016), pp. 270–277.

[39] Greet Kerckhofs. *Lecture notes in Biomechanics*. Ecole polytechnique de Louvain, UCLouvain. 2019.

[40] E. B. Van der Houwen, P. Baron, A. G. Veldhuizen, J. G. M. Burgerhof, P. M. A. van Ooijen, and G. J. Verkerke. "Geometry of the Intervertebral Volume and Vertebral Endplates of the Human Spine". In: *Annals of Biomedical Engineering* 38.01 (Jan. 2009), pp. 33–40.

[41] Mar-Bal Inc. *Left anterior retroperitoneal approach to the L4-L5 disc*. 2020. URL: https://www.mar-bal.com/language/en/applications/advantages-of-composites/ (visited on Apr. 16, 2020).

[42] Roel FMR Kersten, Steven M van Gaalen, Mark P Arts, Kit CB Roes, Arthur de Gast, Terry P Corbin, and F Cumhur Öner. "The SNAP trial: a double blind multi-center randomized controlled trial of a silicon nitride versus a PEEK cage in transforaminal lumbar interbody fusion in patients with symptomatic degenerative lumbar disc disorders: study protocol". In: *BMC Musculoskeletal Disorders* 15 (Feb. 2014).

[43] Sukrit Jain, Adam E M Eltorai, Roy Ruttiman, and Alan H Daniels. "Advances in Spinal Interbody Cage". In: *CHINESE ORTHOPAEDIC ASSOCIATION AND JOHN WILEY SONS AUSTRALIA, LTD* 08 (2016), pp. 278–284.

[44] Arts MP, Wolfs JFC, and Corbin TP. "Porous silicon nitride spacers versus PEEK cages for anterior cervical discectomy and fusion: clinical and radiological results of a single-blinded randomized controlled trial". In: *Eur Spine J.* 26.09 (Sept. 2017), pp. 2372–2379.

[45] Hieu T Ball, Bryan McEntire, and Sonny Bal B. "Accelerated Cervical Fusion of Silicon Nitride versus PEEK Spacers: A Comparative Clinical Study". In: *Eur Spine J.* 06.06 (Sept. 2017), pp. 396–401.

[46] wikipedia. *Composite material*. 2020. URL: `https://en.wikipedia.org/wiki/Composite_material` (visited on Apr. 16, 2020).

[47] Mar-Bal Inc. *Left anterior retroperitoneal approach to the L4-L5 disc*. 2020. URL: `https://www.mar-bal.com/language/en/applications/advantages-of-composites/` (visited on Feb. 20, 2020).

[48] D. Daentzer, E. Willbold, K. Kalla, I. Bartsch, W. Masalha, M. Hallbaum, C. Hurschler, T. Kauth, D. Kaltbeitzel, C. Hopmann, and B. Welke; "Bioabsorbable Interbody Magnesium-Polymer Cage: Degradation Kinetics, Biomechanical Stiffness, and Histological Findings From an Ovine Cervical Spine Fusion Model". In: *Spine* 20.39 (Sept. 2014), pp. 1220–1227.

[49] D. Greg Anderson. *The Role of Bone Graft in Spinal Fusion Surgery*. 2020. URL: `https://www.spineuniverse.com/treatments/surgery/role-bone-graft-spinal-fusion-surgery` (visited on Apr. 16, 2020).

[50] Hansraj KK. "Stem Cells in Spine Surgery." In: *Surg Technol Int* 29 (Oct. 2016), pp. 348–358.

[51] Daniel Lubelski, Kalil G. Abdullah, Edward C. Benzel, and Thomas E. Mroz. "The Utility of Allograft Mesenchymal Stem Cells for Spine Fusion: A Literature Review". In: *Global Spine J.* 02.06 (June 2012), pp. 109–114.

[52] Zimmer Biomet Spine. *Avenue T: TLIF Cage*. 13785 Research Boulevard, Suite 200, Austin, TX 78750 USA: LDR Spine, 2017.

[53] Chen Y1, Wang X, Lu X, Yang L, Yang H, Yuan W, and Chen D. "Comparison of titanium and polyetheretherketone (PEEK) cages in the surgical treatment of multilevel cervical spondylotic myelopathy: a prospective, randomized, control study with over 7-year follow-up." In: *European Spine Journal* 22 (July 2013), pp. 1539–1546.

[54] Mecanumeric. *CHARLY4U - CHARLY2U.* 2020. URL: https://www.charlyrobot.com/produits/14-6/cnc-milling-machine-for-training/charly4u-charly2u.html (visited on June 14, 2020).

[55] E. Munting, A. Faundez, and E. Manche. "Vertebral reconstruction with cortical allograft: long-term evaluation". In: *Eur Spine J* 10 (2001), pp. 153–157.

[56] Guido Reina. *Ellipse in polar coordinates.* 2006. URL: https://www.researchgate.net/figure/Ellipse-in-polar-coordinates_fig6_220778370 (visited on May 20, 2020).

[57] Gregory J. Bennett. "Biocompatibility of Metallic Spinal Implants". In: *Holtzman R.N.N., McCormick P.C., Farcy JP.C., Winston H. (eds) Spinal Instability. Contemporary Perspectives in Neurosurgery. Springer, New York, NY* (1993), pp. 63–75.

[58] Yue Wang and Michele C. Battie´and Tapio Videman. "A morphological study of lumbar vertebral endplates: radiographic, visual and digital measurements". In: *Eur Spine J.* 21 (Jan. 2012), pp. 2316–2323.

[59] Samir Zahaf, Bensamine Mansouri, Abderrahmane Belarbi, and Zitouni Azari. "The effect of the eccentric loading on the components of the spine". In: *Open Access Text: Hematology Medical Oncology* 1.2 (2016), pp. 1–10.

[60] S. H. Zhou, I. D. McCarthy, A. H. McGregor, R. R. H. Coombs, and S. P. F. Hughes. "Geometrical dimensions of the lower lumbar vertebrae – analysis of data from digitised CT images". In: *Eur Spine J.* 09 (Jan. 2000), pp. 242–248.

[61] Seyed Mohammad Hadi Mirab, Mohammad Barbarestani, Seyyed Mohammad Tabatabaei, Soodeh Shahsavari, and Mohammad Bagher Minaeii Zangi. "Research Paper: Measuring Dimensions of Lumbar Intervertebral Discs in Normal Subjects". In: *Anatomical Science* 14.01 (Feb. 2017), pp. 3–8.

[62] Brody A. Frost, Sandra Camarero-Espinosa, and E. Johan Foster. "Materials for the Spine: Anatomy, Problems,and Solutions". In: *MDPI, Materials* (Jan. 2019).

[63] Eikelkam. *On the Development of an Artificial Intervertebral Disc. PhD-thesis.* University of Groningen, 2002.

[64] Moshe Nissan and Issachar Gilad. "Dimension of human lumbar vertebrae in the sagittal plane". In: *J. Biomechanics* 19.02 (Feb. 1986), pp. 753–758.

[65] L. H. F. Damansceno, S. R. G. Catarin, A. D. Campos, and H. L. A. Defino. "Lumbar lordosis: a study of angle values and of vertebral bodies and intervertebral discs role". In: *ACTA ORTOP BRAS* 14.04 (Apr. 2006), pp. 193–1999.

[66] P. Goudas, H. Pope, V. Macropoulos, G. Labeas, and L. Goudas. "Development and Analysis of a Finite Element Model of the L5/S1 Disk using a Loading Model Simulating Whole-body Vibration". In: *Presented at the 1st International workshop "Modelling of Spinal Loads Associated with Vibration and Shock - State of the Art, Critical Assessment, Application, and Research Needs, Appendix W3E to Final Report* (May 2001).

[67] E. F. Morgan, G. U. Unnikrisnan, and A. I. Hussein. "Bone Mechanical Properties in Healthy and Diseased States". In: *Annu Rev Biomed Eng* 04.20 (2018), pp. 119–143.

[68] P. H. F. Nicholson, X. G. Cheng, G. Lowet, S. Boonen†, M. W. J. Davie, J. Dequeker, and G. Van der Perre. "Structural and material mechanical properties of human vertebral cancellous bone". In: *Med. Eng. Phys* 19.08 (1997), pp. 729–737.

[69] Wikipedia. *Poisson's ratio*. 2020. URL: `https://en.wikipedia.org/wiki/Poisson%27s_ratio` (visited on Apr. 30, 2020).

[70] M.E.Szabó and P.J.Thurner. "Anisotropy of bovine cortical bone tissue damage properties". In: *Journal of Biomechanics* 01 (Jan. 2013).

[71] H. Schmidt, A. Kettler, F Heuer, U. Simon, L Claes, and H.J. Wilke. "Intradiscal Pressure, Shear Strain, and Fiber Strain in the Intervertebral Disc Under Combined Loading". In: *SPINE* 32.07 (2007), 748—755.

[72] R. F. Heary, N. Parvathreddy, S. Sampath, and N. Agarwal. "Elastic modulus in the selection of interbody implants". In: *Journal of Spine Surgery* 03.02 (2017), pp. 163–167.

[73] X. Banse, T. J. Sims, and A. J. Bailey. "Mechanical Properties of Adult Vertebral Cancellous Bone: Correlation With Collagen Intermolecular Cross-Links". In: *Jounal of bone and mineral research* 17.09 (2002), pp. 1622–1628.

[74] A. Renau, J. Farrerons, B. Yoldi, J. Gil, I. Proubasta, J. Llauger, J. Gonzalez Oliván, and J. Planell. "Yield Point in Prediction of Compressive Behavior of Lumbar Vertebral Body by Dual-Energy X-Ray Absorptiometry". In: *Journal of Clinical Densitometry* 07.04 (Dec. 2004), 382—389.

[75] D.T. Reilly and R. H.Burstein. "The elastic and ultimate properties of compact bone tissue". In: *J. Biomech* 6.08 (1975), pp. 393–396.

[76] X. N. Dong and X. E. Guo. "The dependence of transverselyisotropic elasticityof human femoral cortical bone on porosity". In: *Journal of Biomechanics* 37 (2004), pp. 1281–1287.

[77] David Peter Drabousky. "Prony series representation and interconversion of viscoelastic material functions of equine bone". In: *Submitted in partial fulfillment of the requirements For the degree of Master of Science* (Aug. 2009).

[78] M. J.Mirzaalia, J. Schwiedrzik, S. T. James, P.B. J. Michler, P. K.Zysseta, and U. Wolfram. "Mechanical properties of cortical bone and their relationships with age, gender, composition and microindentation properties in the elderly". In: *Bone* 93 (2016), pp. 196–211.

[79] H. Cezayirlioglu, E. Bahniuk, D.T. Davy, and K.G. Heiple. "Anisotropic yield behavior of bone under combined axial force and torque." In: *J Biomech* 18.01 (Apr. 1985), pp. 61–69.

[80] X Sherry Liu, Adi Cohen, Elizabeth Shane, Perry T Yin, Emily M Stein, Halley Rogers, Shannon L Kokolus, Donald J McMahon, Joan M Lappe, Robert R Recker, Thomas Lang, and X Edward Guo. "Bone Density, Geometry, Microstructure, and Stiffness: Relationships Between Peripheral and Central Skeletal Sites Assessed by DXA, HR-pQCT, and cQCT in Premenopausal Women". In: *Journal of Bone and Mineral Research* 25.10 (2010), 2229—2238.

[81] O. R. Boughton, S. Ma, X. Cai, L. Yan, L. Peralta, P. Laugier, J. Marrow, F. Giuliani, U. Hansen, R. L. Abel, Q. Grimal, and J. P. Cobb. "Computed tomography porosity and spherical indentation for determining cortical bone millimetre-scale mechanical properties." In: *Scientific Report* 09.7416 (May 2019), pp. 1–15.

[82] Saeed Jerbana, Xing Lua, Hyungseok Janga, Behnam Namiraniana Yajun Maa, Nicole Lec, Ying Lid, Eric Y. Changc, and Jiang Du. "Significant correlations between human cortical bone mineral density and quantitative susceptibility mapping (QSM) obtained with 3D Cones ultrashort echo time magnetic resonance imaging (UTE-MRI)". In: *Magnetic Resonance Imaging* 62 (2019), 104—110.

[83] H. A. Hogan. "Micromechanics modeling of Haversian cortical bone properties". In: *J. Biomech* 25.05 (May 1992), pp. 549–556.

[84] Physiopedia. *Lumbosacral Biomechanics*. 2020. URL: `https://www.physiopedia.com/Lumbosacral_Biomechanics` (visited on Feb. 25, 2020).

[85] H.-J. Wilke, K. Wenger, and L. Claes. “Testing criteria for spinal implants: recommendations for the standardization of in vitro stability testing of spinal implants”. In: *Eur Spine J* 7 (1998), 148—154.

[86] A. Rohlmann, L. E. Claes, G. Bergmann, F. Graichen, P. Neef, and H.J. Wilke. “Comparison of intradiscal pressures and spinal fixator loads for different body positions and exercises”. In: *Ergonomics* 44.8 (2001), pp. 781–794.

[87] N. Newella, JP Littleb, A. Christoua, MA Adamsc, CJ Adamb, and SD Masourosa. “Biomechanics of the human intervertebral disc: A review of testing techniques and results”. In: *Journal of the Mechanical Behavior of Biomedical Materials* 69 (2017), 420—434.

[88] S. E. Bezci and G. D. O’Connell. “effect of axial compression preload on intervertebral disc torsional mechanics”. In: ed. by Bioengineering Summer Biomechanics and Biotransport Conference. Snowbird Resort, Utah, USA, June 2015.

[89] S. Mikuckytė and V. Ostaševičius. “Numerical study of lateral bending influence on lumbar intervertebral disc”. In: *JVE Journal* 15 (2017), pp. 71–76.

[90] A. Rohlmann, D. Pohl, A. Bender, F. Graichen, J. Dymke, H. Schmidt, and G. Bergmann. “Activities of Everyday Life with High Spinal Loads”. In: *PLoS ONE* 09.05 (2014), 1—5.

[91] M. Malakoutian, J. Street, H. J. Wilke, I. Stavness, S. Fels, and T. Oxland. “A musculoskeletal model of the lumbar spine using ArtiSynth – development and validation”. In: *Computer Methods in Biomechanics and Biomedical Engineering: Imaging Visualization* (2016), 1—8.

[92] S.M. McGill, R.W. Norman, and J. Cholewicki. “A simple polynomial that predicts low-back compression during complex 3-D tasks.” In: *Ergonomics* 39.09 (Sept. 1996), pp. 1107–1118.

[93] D. M. Hooper, V. K. Goel, A. Aleksiev, K. Spratt, K. M. Bolte, and M. Pope. “Three dimensional moments in the lumbar spine during asymmetric lifting”. In: *Clinical Biomechanics* 13 (1998), pp. 386–393.

[94] H.J. Wilke, P. Neef, M. Caimi, T. Hoogland, and L.E. Claes. “New in vivo measurements of pressures in the intervertebral disc in daily life.” In: *Spine* 24.08 (Apr. 1999), pp. 755–762.

[95] S. Katsuhiko, K. Shinichi, and T. Yonezawa. “In Vivo Intradiscal Pressure Measurement in Healthy Individuals and in Patients With Ongoing Back Problems”. In: *Spine* 24.23 (Apr. 1999), pp. 2468–2474.

[96] A. Nachemson and G. Elfström. "Intravital dynamic pressure measurements in lumbar discs. A study of common movements, maneuvers and exercises." In: *Scand J Rehabil Med Suppl.* 01 (1970), pp. 1–40.

[97] M. A. Rajaee, N. A., A. Shirazi-Adl, A. Plamondon, and H. Schmidt. "Comparative evaluation of six quantitative lifting tools to estimate spine loads during static activities". In: *Applied Ergonomics* 48 (2014), pp. 22–32.

[98] A. Claus, J. Hides, G. L. Moseley, and P. Hodges. "Sitting versus standing: Does the intradiscal pressure cause disc degeneration or low back pain?" In: *Journal of Electromyography and Kinesiology* 18 (2008), 550—558.

[99] Gabriel Abedrabbo Ode. "Quantification of intervertebral efforts using a multibody dynamics approach : application to scoliosis". Prom. : Fisette, Paul and Cartiaux, Olivier. MA thesis. Louvain-la-Neuve, Belgium: UCLouvain, Feb. 2017.

[100] D. W. Wagner, M. P. Reed, and J. Rasmussen. "Assessing the Importance of Motion Dynamics for Ergonomic Analysis of Manual Materials Handling Tasks using the AnyBody Modeling System". In: *SAE TECHNICAL PAPER SERIES* 01.2504 (2007).

[101] S. Kromodihardjo and A. Mital. "Biomechanical analysis of manual lifting tasks". In: *J Biomech Engng* 109.2 (1987), pp. 132–138.

[102] M. Jäger and A. Luttmann. "Load on the lumbar spine during asymmetrical bi-manual materials handling." In: *Ergonomics* 35.7-8 (1992), pp. 783–805.

[103] M. Gagnon and D. Gagnon. "The influence of dynamic factors on triaxial net muscular moments at the L5/S1 joint during asymmetrical lifting and lowering." In: *J. Biomech* 25.8 (Aug. 1992), pp. 891–901.

[104] M. Gagnon, A. Plamondon, and D. Gravel. "Pivoting with the load. An alternative for protecting the back in asymmetrical lifting." In: *Spine* 18.11 (Sept. 1993), pp. 1515–1524.

[105] M.F Ashby. "The properties of foams and lattices". In: *Philosohical transaction of the royal society* 365 (2006), pp. 15–30.

[106] Solidworks. *Meshing Options*. 2018. URL: `https://help.solidworks.com/2018/english/SolidWorks/cworks/c_Meshing_Options.htm` (visited on May 26, 2020).

[107] Wikipedia. *Viscoelasticity*. 2019. URL: `https://en.wikipedia.org/wiki/Viscoelasticity` (visited on Mar. 27, 2020).

[108] Solidworks. *Viscoelastic Model*. 2019. URL: `https://help.solidworks.com/2019/English/SolidWorks/cworks/c_Viscoelastic_Model.htm?format=P&value=` (visited on Mar. 27, 2020).

[109] Rod Lakes. *Viscoelasticity Notes*. 2019. URL: http://silver.neep.wisc.edu/~lakes/VEnotes.html (visited on Mar. 20, 2020).

[110] Wikipedia. *Generalized Maxwell model*. 2019. URL: https://en.wikipedia.org/wiki/Generalized_Maxwell_model (visited on Mar. 27, 2020).

[111] Ton van Vliet and Hans Lyklema. "6. Rheology". In: *Fundamentals of Interface and Colloid Science:* 04 (2005), pp. 1–88.

[112] Adel A. Abdel-Wahaba, K. Alamb, and Vadim V. Silberschmidta. "Analysis of anisotropic viscoelastoplastic properties of cortical bone tissues". In: *Journal of the mechanical behaviour of biomedical materials* 04.04 (July 2011), pp. 807–820.

[113] S. Pandini and A. Pegoretti. "Time and temperature effects on Poisson's ratio of poly(butylene terephthalate)". In: *eXPRESS Polymer Letters* 05.08 (Feb. 2011), pp. 685–697.

[114] D. Raftopoulos, E. Katsamanis, F. Saul, W. Liu, and S. Saddernit. "An intermediate loading rate technique for the determination of mechanical properties of human femoral cortical bone". In: *J Biomech Eng.* 15.01 (Jan. 1993), pp. 60–66.

[115] Byju's. *Poisson's Ratio - Longitudinal Strain and Lateral Strain*. 2020. URL: https://byjus.com/physics/poissons-ratio/ (visited on Mar. 20, 2020).

[116] Engineer Edge. *Poisson's ration definition and equation*. 2020. URL: https://www.engineersedge.com/material_science/poissons_ratio_definition_equation_13159.htm (visited on Mar. 20, 2020).

[117] Rescearch Gate. *Is it really reasonable to set Poisson's ratio as a constant?* 2019. URL: https://byjus.com/physics/poissons-ratio/ (visited on Mar. 20, 2020).

[118] Q.Xu and B. Engquist. "A mathematical and Physical Model Improves Accuracy in Simulating Material Relaxation Modulus and Viscoelastic Responses". In: *Cornell University* (20014), pp. 1–37.

[119] DC. Wirtz DC, Schiffers N, T. Pandorf, K. Radermacherand D. Weichert, and R. Forst. "Critical evaluation of known bone material properties to realize anisotropic FE-simulation of the proximal femur". In: *J Biomech.* 33.10 (Jan. 2000), pp. 1325–1330.

[120] Olivier Cornu, Jérome Boquet, Olivier Nonclercq, Pierre-Louis Docquier, John Van Tomme, Christian Delloye, and Xavier Banse. "Synergetic effect of freeze-drying and gamma irradiation on the mechanical properties of human cancellous bone". In: *Cell Tissue Bank* 02 (2011), pp. 281–288.

[121] N. Sasaki and A. Enyo. "Viscoelastic properties of bone as a function of water content". In: *J Biomech.* 28.07 (July 1995), pp. 809–8015.

[122] Wikipedia. *Yield surface*. 2019. URL: https://en.wikipedia.org/wiki/Yield_surface (visited on May 25, 2020).

[123] Wikipedia. *von Mises yield criterion*. 2020. URL: https://en.wikipedia.org/wiki/Von_Mises_yield_criterion (visited on Apr. 9, 2020).

[124] Solid Solutions Technical Team. *Dassault System: SolidWorks techs blog - Simulation Hacks!* 2016. URL: https://blogs.solidworks.com/tech/2016/06/simulation-hacks.html (visited on May 11, 2020).

[125] Medtronic. *Verte-stack ® crescent PEEK Vertebral Body Spacer*. 1800 Pyramid Place, Memphis, TN 38132: Medtronics sofamor danek, 2008.

[126] D.R. Sumner. "Long-termimplant fixation andstress-shieldingintotalhipreplacement". In: *Journal ofBiomechanics* 18 (Mar. 2015), pp. 797–800.

[127] GraphPad. *Prism - GraphPad, year = 2020, url = https://www.graphpad.com/scientific-software/prism/, urldate = 2020-05-20.*

[128] Siddharth Sharma. *Quora: What is the difference between von Mises Stress and Max Principal Stress?* 2019. URL: https://www.quora.com/What-is-the-difference-between-von-Mises-Stress-and-Max-Principal-Stress (visited on May 15, 2019).

[129] SolidWorks. *Large Displacement Solution*. 2015. URL: https://help.solidworks.com/2015/english/SolidWorks/cworks/c_Large_Displacement_Solution.htm (visited on May 19, 2020).

[130] Captive Spine. *Pivotech TLIF cage*. 2020. URL: https://www.captivaspine.com/lumbar-cervical-spine-fusion-products/pivotec-tlif-cage/ (visited on May 28, 2020).

[131] Captive Spine. *Customizable PLIF/TLIF CAGE instrument set with stainless steel trays/inserts*. 2020. URL: https://rudischhauser.com/fileadmin/user_upload/pdf/Cage_sets/RH_SpineSets_Catalogue_2020_EN_111_web.pdf (visited on May 28, 2020).

[132] Wikipedia. *Tsai Wu criterion*. 2019. URL: https://en.wikipedia.org/wiki/Tsai\%E2\%80\%93Wu_failure_criterion (visited on June 6, 2020).

[133] Garet C. Comer, Anthony Behn, Shashank Ravi, and Ivan Cheng. "A Biomechanical Comparison of Shape Design and Positioning of Transforaminal Lumbar Interbody Fusion Cages". In: *GLOBAL SPINE JOURNAL* 06 (2016), pp. 432–438.

[134] International Organization for Standardization (ISO): Online Browsing Platform (OBP). *ISO 12189:2008(en) Implants for surgery — Mechanical testing of implantable spinal devices — Fatigue test method for spinal implant assemblies using an anterior support*. 2008. URL: https://www.iso.org/obp/ui/#iso:std:iso:12189:ed-1:v1:en (visited on Mar. 9, 2020).

[135] Science Direct. *Spine Implant*. 2019. URL: https://www.sciencedirect.com/topics/nursing-and-health-professions/spine-implant (visited on Jan. 5, 2020).

[136] ASTM International , West Conshohocken , PA. *ASTM F1717-18, Standard Test Methods for Spinal Implant Constructs in a Vertebrectomy Model*. 2018. URL: http://www.astm.org/cgi-bin/resolver.cgi?F1717 (visited on Mar. 9, 2020).

[137] ASTM International , West Conshohocken , PA. *ASTM F2077-18, Test Methods For Intervertebral Body Fusion Devices*. 2018. URL: http://www.astm.org/cgi-bin/resolver.cgi?F2077 (visited on Mar. 9, 2020).

[138] ASTM International , West Conshohocken , PA. *ASTM F1798-13, Standard Test Method for Evaluating the Static and Fatigue Properties of Interconnection Mechanisms and Subassemblies Used in Spinal Arthrodesis Implants*. 2013. URL: http://www.astm.org/cgi-bin/resolver.cgi?F1798 (visited on Mar. 9, 2020).

[139] ASTM International , West Conshohocken , PA. *ASTM F3292-19, Standard Practice for Inspection of Spinal Implants Undergoing Testing*. 2019. URL: http://www.astm.org/cgi-bin/resolver.cgi?F3292 (visited on Mar. 9, 2020).

[140] ASTM International , West Conshohocken , PA. *ASTM F2267-04(2018), Standard Test Method for Measuring Load Induced Subsidence of Intervertebral Body Fusion Device Under Static Axial Compression*. 2018. URL: http://www.astm.org/cgi-bin/resolver.cgi?F2267 (visited on Mar. 9, 2020).

[141] William Maish. *William Maish*. 2019. URL: https://geekymedics.com/the-vertebral-column/ (visited on Dec. 18, 2019).

[142] Frank H. Netter. *Atlas of human anatomy*. 1600 John F. Kennedy Blvd., Ste. 1800, Philadelphia, PA 19103-2899: Saunders Elsevier, 6th edition.

[143] Robert E. Windsor. *Cervical Spine Anatomy*. 2017. URL: https://emedicine.medscape.com/article/1948797-overview#a1 (visited on Dec. 18, 2019).

[144] Oliver Jones. *The Vertebral Column*. 2019. URL: https://teachmeanatomy.info/back/bones/vertebral-column/ (visited on Dec. 18, 2019).

[145] Wikipedia. *Foramen medula*. 2019. URL: https://en.wikipedia.org/wiki/Foramen_magnum (visited on Dec. 19, 2019).

[146] Nachum Dafny. *Chapter 3: Anatomy of the Spinal Cord*. 1997. URL: https://nba.uth.tmc.edu/neuroscience/m/s2/chapter03.html (visited on Dec. 19, 2019).

[147] Wikipedia. *Ventral ramus of spinal nerve*. 2019. URL: https://en.wikipedia.org/wiki/Ventral_ramus_of_spinal_nerve (visited on Dec. 19, 2019).

[148] Ekramul M. Gofur and Paramvir Singh. "Anatomy, Back, Vertebral Canal Blood Supply". In: *StatPearls [Internet]* (Apr. 2019).

[149] GP notebook. *arcuate line (anatomy)*. 2019. URL: https://gpnotebook.com/simplepage.cfm?ID=1751842873 (visited on Jan. 3, 2020).

[150] Doctor. *Atlas of Anatomy, 15 Arteries Veins*. 2019. URL: https://doctorlib.info/medical/anatomy/17.html (visited on Jan. 3, 2020).

[151] Timothy P. Holsgrove, Nikhil R. Nayak, William C. Welch, and Beth A. Winkelstein. "Advanced Multi-Axis Spine Testing: Clinical Relevance and Research Recommendations". In: *International Journal of Spine Surgery* 34.9 (Jan. 2015).

[152] Augustus A. White III and Manohar M. Panjabi. *Clinical Biomechanics of the Spine*. Phidadelphia, Pennysylvania, United States: Lippincott William Wilkins, 1990.

[153] a JhonsonJhonson company: DePuy spine inc. *MIS lateral plateform: surgical technique guide*. 325 Paparamount Drive, Raynham, MA 02767, USA, 2012.

[154] Thomas A. Zdeblivk and J. Kenneth Burkus. *LT-cage: lumbar tempered fusion device, surgical technique*. 1800 Pyramid Place, Memphis, TN 38132: Medtronics sofamor danek, 2000.

[155] Eeric Truumees and Alan S. Waitze. *O.I.C. Cage: PLIF Surgical Technique*. Cité Centre, Grand-Rue 90, 1820 Montreux, Switzerland: Stryker SA, 2008.

[156] D. J. Bell and P. Marsh. *Uncinate process of the cervical spine*. 2019. URL: https://radiopaedia.org/articles/uncinate-process-of-the-cervical-spine (visited on Jan. 2, 2020).

[157] Robert D. Elliott. *Prone Position*. 2020. URL: http://wiki.med.uottawa.ca/display/WIKITHESIA/Prone+Position (visited on Mar. 9, 2020).

[158] Seung-Hyun Chae, Jie-Hua Zhao, Darvin Edwards, and Paul S Ho. "Characterization of the Viscoelasticity of Molding Compounds in the Time Domain". In: *Journal of Electronic Materials* 39.4 (Apr. 2010), pp. 419–425.